Generative Design of Hydrocephalus Shunts

Elizabeth Hayman

Keble College

University of Oxford

A thesis submitted for the degree of

Doctor of Philosophy

Michaelmas 2025

Abstract

The design of medical devices is often a lengthy and costly process, requiring multiple stages of testing through experimental, animal, and human trials. Therefore, computational methods are increasingly used early in the design process both to explore the mechanical-biological interactions which affect device use, and to identify promising new design options in a process known as generative design.

This thesis focusses on improving the design of ventricular catheters used in the treatment of hydrocephalus, a relatively common but serious condition caused by excess cerebrospinal fluid (CSF) in the brain. Current catheters have high failure rates ($\geq$ 40% [1]), often due to blockage by the Choroid Plexus (ChP), the nearby brain tissue that produces CSF. There is consequently an urgent need to improve the design to reduce this risk.

A 3D computational fluid–structure interaction (FSI) model was developed to assess how catheter designs influence ChP deformation. Designs used in the UK were tested and compared, with superior designs defined as those that caused less ChP deformation and hence reduced the likelihood of blockage.

As 3D simulations take days to run, faster, reduced-order models were developed using geometric simplifications and mechanistic approximations. Combined with a predictive machine learning layer, this created a surrogate model able to predict ChP deformation rapidly and accurately, enabling a large-scale optimisation over design space. Promising new catheter designs suggested by this surrogate-aided optimisation were tested in the full FSI model and showed marked improvements in performance when compared to current devices.

This interdisciplinary thesis brings together methods from mathematics and engineering, and applies them to a critical biomedical problem.

The results here focus on ventricular catheters, however the surrogate-aided generative design framework is general, and has the potential to be used more widely. The modular codebases and methodologies developed in this work have all been deliberately designed to ensure they can be applied to other optimisation and design problems, both within the biomedical sphere and beyond.

Dedicated to my parents and to Daniel.

Acknowledgements

I would like to express my deepest gratitude to all my amazing supervisors for their continuous guidance and support throughout this journey: Professor Antoine Jérusalem, Professor Sarah Waters, Professor José-Maria Peña and Mr Jay Jayamohan, all of whose insights and encouragement have been invaluable. I am also grateful to the Oxford Doctoral Training Centre, Lurtis ltd. and the EPSRC (EP/S024093/1) for their financial support in making this research possible.

Special thanks go to Dr Van Dung Nguyen for his patience in recompiling my codebase multiple times without hesitation, and to Hisham Elamin for his invaluable computer support. My sincere appreciation also goes to Dr Pablo Naharro for lengthy debugging sessions and for teaching me the essential lesson of never indiscriminately uninstalling Python.

Finally, to my friends and family: your unwavering encouragement and belief in me have made this thesis possible. Thank you for being my constant source of strength and motivation.

Contents

Table of variables

Variable	Description	Units
Catheter design		
x, y, z	Cartesian coordinates.	mm, mm, mm
r, θ, z	Cylindrical polar coordinates.	mm, -, mm
α	Angle of axial rotation between catheter and ChP	°
k	Index of inlet holes for a given catheter design	-
r_k	Radius of the base of a conical inlet hole	mm
ϕ_k	Inlet hole angle with the positive horizontal axis	°
z_k	Axial position of an inlet hole	mm
n	Number of inlet holes in a circumferential ring	-
$zPos_k$	Axial length between neighbouring inlet holes	mm
Fluid model		
$\boldsymbol{v}$	Fluid velocity field.	$\mathrm{m\,s^{-1}}$
p	Fluid pressure.	mPa
$\boldsymbol{n}$	Unit normal vector.	–
$\boldsymbol{V}$	Discretised velocity vector.	$\mathrm{m\,s^{-1}}$
$\boldsymbol{p}$	Discretised kinematic pressure vector.	mPa
Λ	Effective wall permeability.	$\mathrm{mm^2\ s/g}$
Solid model		
$\boldsymbol{X}$	Reference (material) position.	mm
$\boldsymbol{x}$	Current (spatial) position.	mm
$\boldsymbol{u} = \boldsymbol{x} - \boldsymbol{X}$	Solid displacement.	mm
$\boldsymbol{F} = \partial \boldsymbol{x} / \partial \boldsymbol{X}$	Deformation gradient.	–
$\boldsymbol{\sigma}$	Cauchy stress tensor.	mPa
$\mathbb{B} = \boldsymbol{F} \cdot \boldsymbol{F}^{\top}$	Left Cauchy–Green tensor.	–
$\mathbb{I}$	Identity tensor.	–
$J = \det(\boldsymbol{F})$	Deformation Jacobian.	–
$\boldsymbol{P}$	First Piola–Kirchhoff stress.	mPa
Machine learning		
i	Data point index.	–
$\boldsymbol{x}$	Input vector.	Various
y	Output: maximum equilibrium ChP displacement.	mm
ϵ	Prediction error.	mm
$\boldsymbol{\beta}$	Internal algorithm weights.	–
$\boldsymbol{\lambda}$	Hyperparameters of the algorithm.	–

Table 1: Table of key variables used in this thesis

Chapter 1

Introduction

1.1 Motivation

Traditionally, medical devices are tested for efficacy through lengthy and expensive *in vitro*, *in vivo* and clinical trials, often building incrementally on previous designs with the aim of increasing the performance of a device [2]. The process of device design is becoming more complex, with an increasing number of safety standards and regulations to be considered, and the devices themselves operating in increasingly intricate ways [3]. In addition, clinical trials place a heavy burden both on the participating patients, and the organisations running and funding the work [4]. There is a strong incentive to leverage the increasing availability of computational power to reduce the time and cost of this process.

Currently, computational methods are used primarily in the early stages of the design process [5]. Computational models are invariably an approximation of the true biological scenario and so cannot replace clinical trials, but they can significantly reduce the number of designs being sent to trials, with a corresponding decrease in the cost and failure rate. Models can be used to gain an enhanced understanding of biological mechanisms and domains which impact device use [6], or to test and evaluate proposed designs and explore new design directions, ensuring only the most promising designs pass to the next stage of testing.

In this work, the design of ventricular catheters used in hydrocephalus shunt systems is identified as a problem of interest due to high failure rates, numerous designs in current use, and the lack of any current metric to directly compare the relative performance of different designs. Paediatric hydrocephalus is a serious medical condition where an excess of cerebrospinal fluid (CSF) in the ventric-

ular system of the brain causes a build-up of intra-cranial pressure [7]. If left untreated, the condition worsens, causing headaches, balance problems and potentially proving fatal within years [8]. The most common treatment for severe hydrocephalus is to implant a permanent drainage shunt system connecting a ventricular catheter in the brain to a second catheter in the stomach, allowing excess fluid to be safely cleared [9]. The ventricular catheter is a hollow tube with inlet holes in the side wall clustered around the closed tip of the catheter. This research focusses specifically on the size and placement of inlet holes in the ventricular catheter.

The CSF drainage through shunt systems can cause the Choroid Plexus (ChP), the soft, deformable, vascularised tissue rooted to the base of the ventricles that produces the CSF, to be dragged into the ventricular catheter causing it to block. This requires shunt replacement, which is complicated by the risk of the adhered ChP tissue tearing and haemorrhaging [10]. Blockage due to brain tissues such as ChP is responsible for over half of shunt systems malfunctioning [10]. The aim of an improved catheter design is one that minimises the deformation of the ChP towards the catheter, hence reducing the risk the ChP will reach the catheter and block it.

Each year, 400,000 new cases of paediatric hydrocephalus develop across the world, with a higher incidence rate in low and middle income countries [11]. Latin America, Southeast Asia and Africa carry 75% of the case burden [12, 13]. In the UK, 3,000 to 3,500 shunt surgeries are performed every year, while the annual cost of shunt surgery in the USA was estimated at $1 - 2 billion in 2021 [14, 15]. It is therefore crucial to better understand how to improve catheter design to help mitigate the increasing social and economic costs. For example, a recent innovation impregnating the shunt catheter material with antibodies is estimated to save the UK Health Service £7 million per year by reducing infection and therefore the need for shunt replacement surgery [16].

In this work an idealised, computational model is developed to investigate the impact of catheter design on ChP deformation, incorporating the key parts of the ventricular-catheter domain. The ventricle-catheter-ChP environment is a complex biological system in which ChP deformation is driven by CSF-induced stresses, and this deformation in turn alters the fluid domain and resulting flow. The model therefore captures the fluid-structure interaction (FSI) coupling between the CSF (the fluid component) and the ChP (the solid component). It can

serve as a test bed for candidate catheter designs, with designs causing less ChP deformation being considered more successful.

Ideally, the FSI model would then be combined with computational optimisation techniques to search for improved catheter designs. This integration of computational models and optimisation into a design process is known as generative design. However, while the high-fidelity model which resolves the complex FSI coupling gives detailed mechanistic insight, it is computationally expensive with a runtime of days. Using such a model in a generative design protocol is infeasible, and an investigation into faster models is thus performed.

First, reduced-order models (ROMs) are developed either by considering geometric reductions of the domain or by replacing key mechanisms (such as the FSI) with simplifications. ROMs focus on a specific component of the full FSI model and give a fast, but approximate, model of this component. Different ROMs have different focusses, and do not necessarily model the ChP directly. To be informative for this problem, an output from the ROM needs to be correlated to ChP deformation. Machine learning (ML) algorithms are hence used to establish relationships between outputs of the ROMs and the ChP deformation. This use of data-driven techniques to enhance the predictive power of ROMs is known as mechanistic learning (MxL) [17]. This procedure also identifies which ROMs are the most effective in the problem of predicting ChP deformation. This combination of ROM with a predictive ML layer is defined as a surrogate model. The surrogate model replaces the full FSI model in evaluating the effect of a catheter design on ChP displacement.

Once established, the surrogate model is integrated into a generative design protocol. This creates the surrogate-aided generative design pipeline, where proposed designs are evaluated by the approximate surrogate model. This pipeline identifies candidate designs which are the most successful, as evaluated by the surrogate model. The candidate designs are then tested in the 3D FSI model to ensure they are true improvements over existing designs. All designs suggested by the optimisation are improvements over existing designs, meaning the surrogate model is successful in identifying promising designs.

The structure of this thesis is shown in Figure 1.1. The colours in the Figure indicate where the different sections of the methodology will be discussed in this thesis, with (a), in blue: Chapters 3 and 4; (b), in red: Chapters 5 and 6; and (c), in green: Chapter 7.

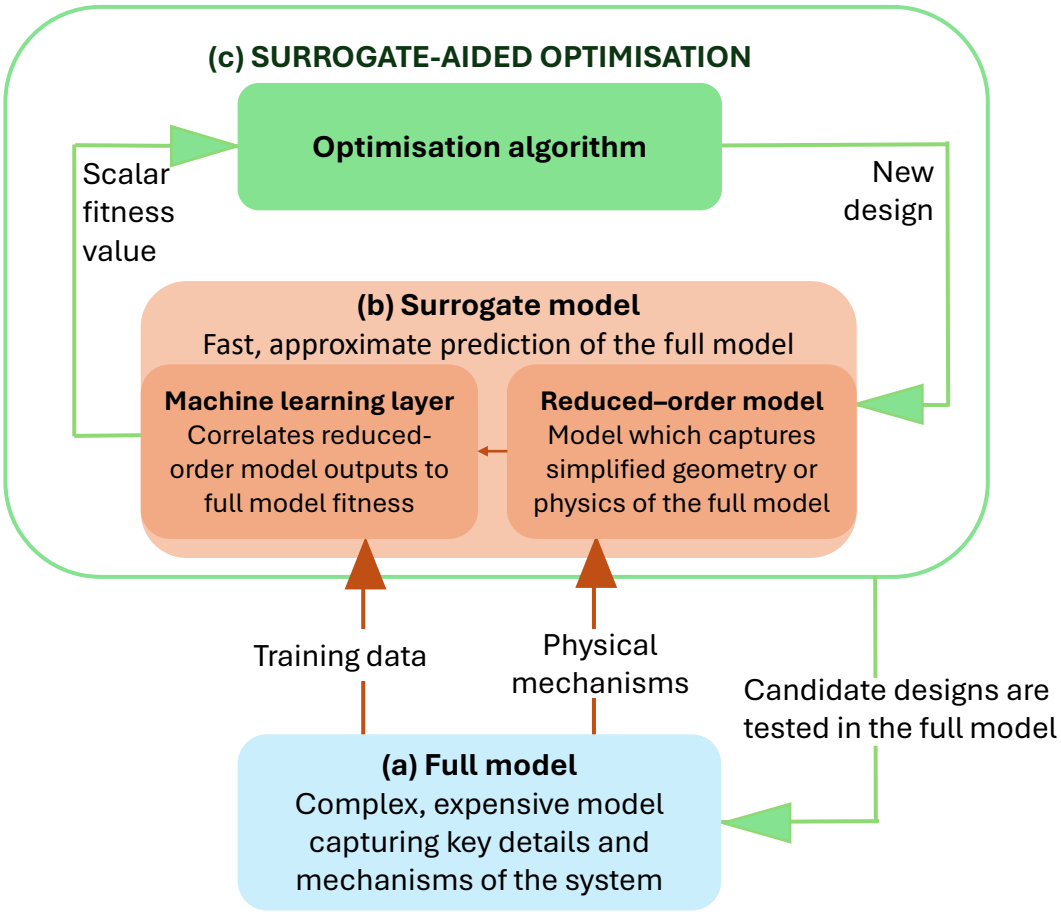

Figure 1.1: Graphic of the surrogate-aided optimisation methodology presented in this work.

This thesis suggests improvements to the design of the ventricular catheter with the specific aim of minimising the risk of ChP blockage. This work both extends the current knowledge of hydrocephalus catheter design and develops highly configurable codebases and methodologies that can potentially be applied to many other design problems. In particular, this work demonstrates how simpler, approximate models can be used successfully in generative design, when ground-truth data may not be available, or the full model is computationally too expensive to be used in a comprehensive optimisation sweep.

1.2 Thesis plan

Chapter 2 provides a background to the catheter problem with a discussion of the physiological and clinical setting of hydrocephalus and previous work on improving shunt system design. The main computational modelling techniques used in this work are introduced. A review of optimisation methods is given, along with a discussion of previous work using surrogates in generative design.

Chapter 3 details the model and method used to create the main 3D FSI simulations. This includes adapting and coupling existing codebases used to model fluids and solids. The model created is the blue component shown in Figure 1.1.

Chapter 4 presents results from the 3D FSI simulation, and compares three examples of current catheter designs. A 2D FSI ROM is introduced and a comprehensive parameter sweep using this model motivates a first improvement to catheter design. Again, the 3D FSI model is shown in Figure 1.1 (a).

Chapter 5 introduces two further ROMs which focus on the fluid field inside the catheter and the stress field on the ChP respectively. A ground-truth dataset curated from the 3D FSI model is introduced and used to quantify the accuracy of the ROMs.

Chapter 6 combines the ROMs introduced in Chapter 5 with ML techniques to create a predictive surrogate model which can be used as an approximation to the full 3D FSI. The chapter focusses on Figure 1.1 (b), taking insights from the 3D FSI model discussed in previous chapters.

Chapter 7 contains results from the structured optimisation of the catheter design space. The surrogate model introduced in Chapter 5 is combined with generative design algorithms to propose new candidate designs. Candidate designs are then simulated in the 3D FSI model, and their ground-truth performance compared to existing catheter designs in Chapter 4. This chapter presents Figure 1.1 (c), both the optimisation protocol and the testing of optimised designs in the 3D FSI model.

Chapter 8 presents the final conclusions of the project and discusses their impact and limitations. Suggested directions for future work are given, and the application of the computational methodology to other problems is discussed.

Chapter 2

Scientific background

This literature review begins with a description of hydrocephalus and current treatments, focussing specifically on the shunt system which is the most common treatment for severe paediatric hydrocephalus. A discussion of the development of the shunt system over the last century follows, with a particular focus on research into optimal placement of the catheter inlet holes. Finite element and finite volume models form the basis of the computational model developed in this thesis, and are introduced next. Computational models have already been used extensively to investigate biomedical problems, and a range of models are reviewed, including fluid models of cerebrospinal fluid (CSF) around the ventricles and nervous system, solid models of brain tissue, and biological fluid-structure interaction models. The second part of this thesis focusses on generative design, which is introduced alongside a review of optimisation techniques. Particular attention is given to the use of surrogate models, which play a central role in this work. The chapter concludes with a discussion of surrogate-aided optimisation.

2.1 Healthy physiology

The nervous system is the body's main communication network, gathering signals from the surrounding environment and transmitting information between the peripheral and central nervous systems (CNS) via a network of neuronal cells [18]. The peripheral nervous system is a system of neurons spread across the body, while the CNS is comprised of the brain and spinal cord [19].

The CSF is a homogeneous, incompressible, Newtonian fluid which forms a critical part of the CNS. With a viscosity of 0.75 mm^2/s and a density of

1000 kg/m^3, CSF is rheologically similar to water [20, 21, 22]. The CSF cushions the brain during the impact of daily activities, and provides a buoyant support reducing the stress of the brain on the spinal cord [19]. The CSF is also the medium for the transport of nutrients around and removal of waste from the CNS [23]. It is produced primarily in the lateral ventricles in the centre of the brain; two identical mirror-image, fluid filled cavities, each with a volume of approximately 5 cm^3 in newborns [24, 25] (see Figure 2.1 a). Within the ventricles, CSF is primarily produced by the Choroid Plexus (ChP) which grows in a fin from the bottom of the lateral ventricles, with the base of the tissue rooted and the upper parts extending into the fluid they produce (see Figure 2.1 b)) [13]. Epithelial cells in the ChP secrete CSF, with the frond-like cross-section of the ChP giving a larger surface area for the transport of CSF into the ventricles.

Multiple studies have used magnetic resonance imaging (MRI) and ultrasound methods to determine the shape of the ChP within the ventricle. Due to the small size of the ChP, and its location deep within the brain, this is a difficult task [26]. Images of the ChP taken from children aged 0-16 years suggest a width of 3.4 mm with little variation by age [27], while a separate study on newborns gave an average width of 5.5 mm [28] (measurements taken of the maximum width of the ChP in the lateral ventricles). The variation between these results suggests significant measurement error, due to the difficulty in imaging the brain and correctly segmenting these images [29]. The frond of ChP is reported to have an average length of approximately 14.15 mm (left hemisphere) and 14.6 mm (right hemisphere) measured in 114 foetuses at 11-13 weeks gestation [30], rising to 22.9 mm (left) to 23.4 mm (right) measured in 50 newborns [28]. These studies give the approximate size of the ChP, but the measurements should be used with care due to the reported amount of measurement error and variation between studies. It is also observed that the size and shape of the ChP vary substantially both between patients, and for any specific paediatric patient the ChP will grow as the child grows and develops.

After production in the lateral ventricles, the CSF drains through apertures called the Foramen of Munro, collecting in the third ventricle, a smaller, triangular space located in the centre of the brain. From there, the fluid flows through the Aqueduct of Sylvius into the fourth and final ventricle [8]. Once the CSF has left the brain's ventricular system it flows either around the spinal cord or to the subarachnoid space surrounding the brain and spinal cord (see Figure 2.1).

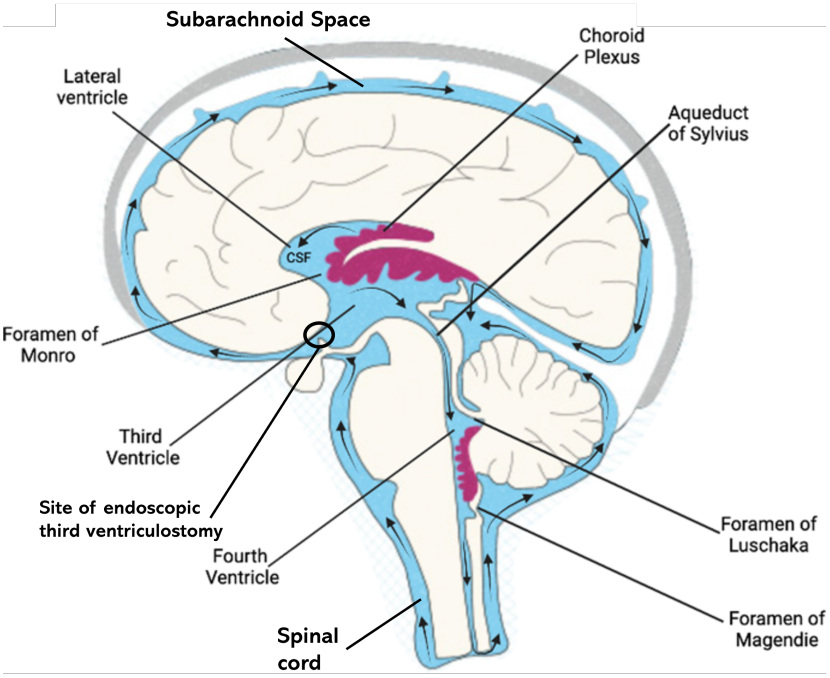

(a)

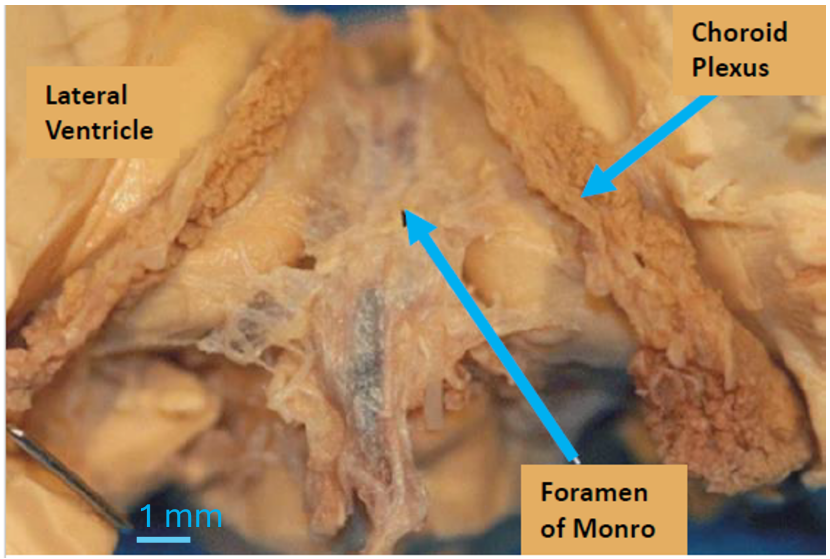

(b)

Figure 2.1: (a) Image adapted from Bitanihirwe, Lizano, and Woo [31] under a Creative Commons Attribution 4.0 International License (CC BY 4.0 [32]) showing key regions of the upper CNS and CSF flow direction. (b) Image from Mortazavi, Griessenauer, Adeeb, Deep, Bavarsad Shahripour, Loukas, Tubbs, and Tubbs [33] with approximate scale added (permission to reproduce obtained from Springer Nature) showing the position of the ChP tissue in the ventricle of a cadaver.

From here, the fluid is reabsorbed into the surrounding tissue [23]. This system is very sensitive to any disturbance in the production or uptake mechanisms as the production rate must always balance the uptake rate to maintain the correct quantity of CSF in the system. Key components of this system are shown in Figure 2.1 a), with the direction of CSF flow shown with arrows [22].

The flow of CSF is influenced by two factors. Firstly, the production of CSF in the brain's ventricular system at a rate of 400-600 mL day^{-1} causes a bulk movement of fluid through the system [34]. There is debate over whether the production of CSF from the ChP is constant (due to an active transport mechanism) [31], or varies with the cardiac cycle [19, 35]. During the cardiac cycle, blood flow into the blood vessels in the head increases the vessels' volume, forcing the volume of the ventricles and other brain tissues to decrease to maintain the overall volume of the skull (Monro-Kellie law) [34]. The incompressible CSF is consequently pushed out of the ventricular system and into the spinal canal, the base of which expands to accommodate the extra fluid. During diastole, all these effects reverse causing a partial change in the direction of flow back into the ventricles [7]. However, as this variation is small when compared with the overall production rate, most models assume constant production rates (and consequently flow rates) of 0.3-0.4 mL min^{-1} [36]. It has been suggested that there may also be some variation in the production rate on a slower, daily cycle, but this has not been well quantified and is a smaller effect [33].

2.2 Pathophysiology

2.2.1 Hydrocephalus

Hydrocephalus describes the condition where an excess of CSF is present in the lateral ventricles. Due to the directional nature of CSF flow, any production imbalance or blockage can lead to a build-up of CSF in the brain, which quickly causes dangerous levels of intracranial pressure [13]. The consequences of severe hydrocephalus include headaches, cognitive changes, and commonly result in severe brain damage and death [8]. Hydrocephalus was recorded by Hippocrates in the 5^{th} century AD, with further mentions of infant hydrocephalus being discussed in anatomical textbooks in 1701 and 1832 [37].

Flow imbalances may be caused by the small apertures connecting different parts of the ventricular system becoming blocked, or by damage to the reabsorption system, meaning the brain is not able to absorb all the CSF produced [7]. Hydrocephalus is commonly divided into three types: in adults, normal-pressure hydrocephalus is most common, where a stroke, injury or changes to the brain during ageing gradually restricts the flow of CSF, while keeping the intra-cranial pressure at a constant level [13, 15]. Hydrocephalus driven by ageing mostly affects adults over 60 and is often misdiagnosed as Alzheimer's disease due to similar symptoms [38]. The second type is acquired hydrocephalus which can develop any time after birth, and is usually the result of a serious head injury or tumour causing a dramatic change in brain shape and pressure [39]. In this project, the focus is on the third type of hydrocephalus, namely congenital hydrocephalus, which is present at birth and which can be caused by haemorrhage or infection during pregnancy or during the rapid development of the infant shortly after birth [13]. Hydrocephalus cases can sometimes be alternatively classed as communicating or non-communicating hydrocephalus [13]. In communicating hydrocephalus, the CSF is able to pass through the ventricular system and into the subarachnoid space with some reabsorption possible at all points. In this project, the focus is on non-communicating hydrocephalus, where a blockage is present within the ventricular system preventing any flow of CSF. Ventricular blockages are particularly dangerous as there are minimal reabsorption surfaces in the central brain, so pressure can build rapidly [38].

Hydrocephalus is clinically diagnosed with a combination of physical signs (primarily, an enlarged head in infants as the excess CSF distorts the flexible skull), and confirmed with MRI imaging and CSF pressure readings [40].

2.2.2 Treatment

Making holes in the skull to ameliorate pressure build-up (decompressive trepanation) was proposed as a treatment for hydrocephalus in a 10^{th} century medical treatise by Abulcasis [41]. Medieval doctors including Vesalius were well aware of the excess of CSF as the cause of hydrocephalus, and so drainage treatments were often attempted [37, 42]. Towards the end of the 19^{th} century, successful insertions of drainage systems between the brain and various parts of the body

were shown to be safer and more effective than open trepanation, as they decreased the risk of infection. Rubber as a material for catheters became popular in the 1940s [43, 44], and shunt surgeries became standard after breakthroughs in the use of silicone and drainage valves in the 1960s [41].

Shunt systems remain a common treatment for severe non-communicating, congenital hydrocephalus, as they effectively restore normal pressure conditions by removing excess fluid [13, 45]. Shunt insertions are one of the most common neurosurgical procedures with over 36,000 shunt surgeries taking place each year in the United States of America [46], 3500 in the United Kingdom [47] and an estimated 160,000 worldwide [48]. Shunt treatment improves survival rates to "70% at one year, 40% at ten years" [9]. The shunt system comprises two catheters, the ventricular catheter positioned in the lateral ventricles, and typically a peritoneal catheter positioned in the peritoneal cavity of the stomach. Alternative outlet catheter positions are possible, with the right atria of the heart or the pleural cavity also common choices [8, 49]. The ventricular catheter has a closed tip (often containing a radiotracer to aid positioning) and a series of inlet holes in the 20 mm of catheter wall closest to the tip. The catheters are connected by a valve positioned towards the back of the skull. Figure 2.2 a) shows the most common placement of the ventricular catheter (entering from the back of the head), with the position of the lateral ventricles and ChP also indicated. Figure 2.2 b-d) show various ventricular catheter designs with a range of inlet hole styles.

Surgical and material improvements in the 2000s reduced the risk of infection during surgery by minimising invasive techniques during the implant procedure and impregnating the shunt tubing with antibiotic properties [44]. There has also been much developmental work done on the valve, looking at pressure or flow driven options, and allowing for programmable behaviour [43].

Modern valves monitor the flow to maintain normal pressure within the brain and prevent backflow [53]. The first valve systems were differential pressure driven mechanisms, used to prevent backflow of CSF or the introduction of other body fluids, such as blood, into the brain [41]. Earlier shunt systems suffered from over-drainage as the user changed position (e.g. from lying down to sitting up), and so more recent valve systems actively control the flow of CSF from the head to prevent the dramatic changes in intra-cranial pressure associated with over-drainage.

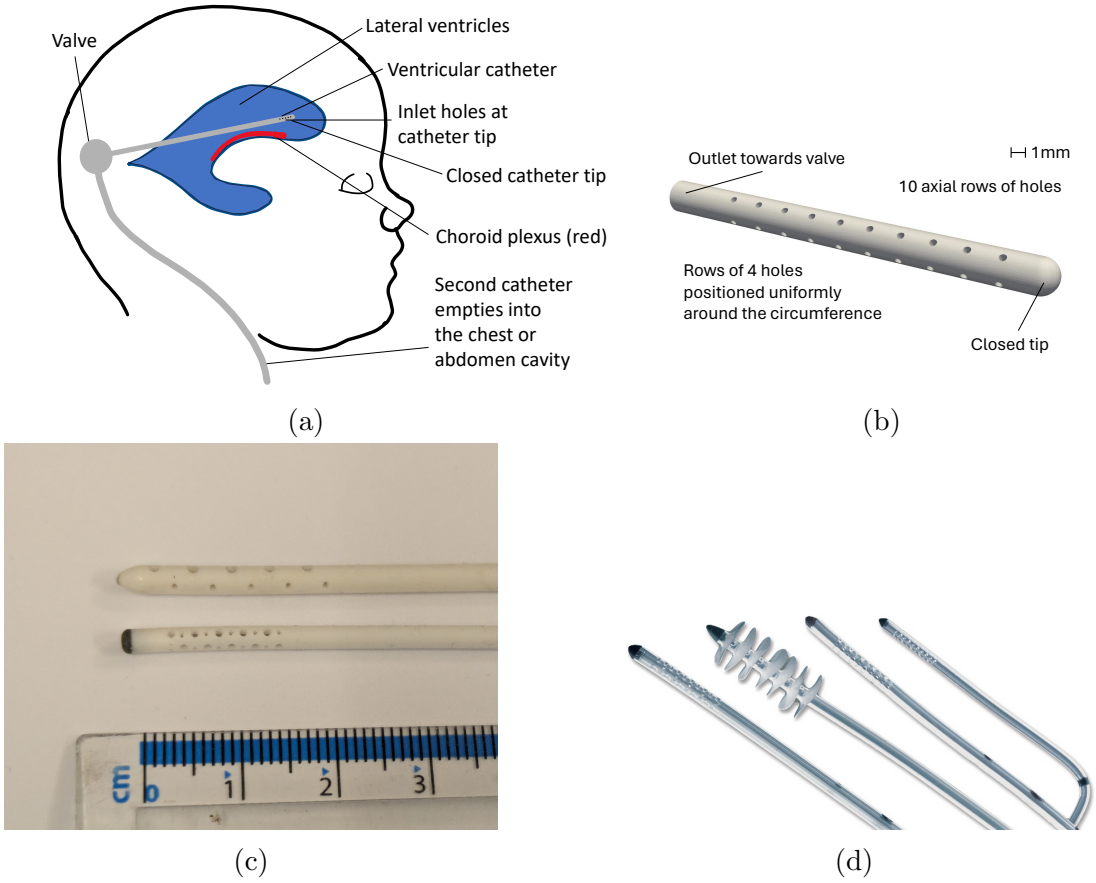

Figure 2.2: (a) Schematic of a shunt system positioned in the ventricle environment (image reproduced from Ref. [50] under a Creative Commons Attribution 4.0 International License (CC BY 4.0 [32]). (b) Close-up visualisation of a ventricular catheter, showing the 30 mm closest to the closed tip. (c) Two example catheters, both manufactured by Codman ® [51], that will be examined in this work. (d) Ventricular catheters currently produced by Natus Medical ® [52], including a flanged design (second left).

More recently, endoscopic third ventriculostomy, the process of making a small drainage channel internally connecting the third ventricle to the sub-arachnoid space, has been used as a hydrocephalus treatment [12, 54]. However, it is an area of much debate as to whether this procedure is safer and more successful than shunting, and for which categories of hydrocephalus it is most effective [55].

2.2.3 Shunt design

While shunt systems effectively deal with the excess of CSF, and can successfully operate for years at a time, they are prone to failure, with 50-85% of patients requiring replacement, and with 2 to 4 shunt replacements expected in the first 10 years of use [15, 56, 57]. There are two main reasons for shunt replacement: infection during initial implant surgery or malfunction of the shunt preventing it from successfully draining CSF. Infections occur due to contamination of the shunt during implant surgery and occur in 5%-15% of all cases [58]. However, the development of antibody-impregnated catheters in the 2000s has been successful at reducing the rate of surgical infection (from 7.1% to 2.6% in a survey of 1800 participants [59]), and catheters made from antibody resistant material have become standard in the industry.

In this research the focus is therefore on the second cause of failure: shunt malfunction. A main cause of mechanical failure in shunt systems is the blockage of the ventricular catheter by the ChP. This is illustrated in a sheep model in Figure 2.3 a). Such ChP blockage further endangers the patient as not only does the build-up of intracranial CSF cause dangerous levels of pressure within hours, but the shunt cannot be easily removed without tearing the vascular ChP and causing bleeding in the brain. Of all shunt replacement surgeries, an estimated 40% are due to the catheter becoming blocked, the second highest cause of failure after surgical infection [1, 60]. To prevent this, the catheter tip (which contains the inlet holes) is placed as far forward in the lateral ventricle as possible, away from the rooted ChP (see Figure 2.2 a). However as infants grow, the length of the ventricle increases relative to the shunt length, and as a result the tip is then closer to the ChP region [45]. Clinical studies of hydrocephalus track the success of shunt treatments and routinely see high rates of shunt revisions. A large scale study following 456 patients who underwent shunt surgery as infants saw 95% requiring shunt revisions, some after a period of 20 years [62]. A second clinical study of 227

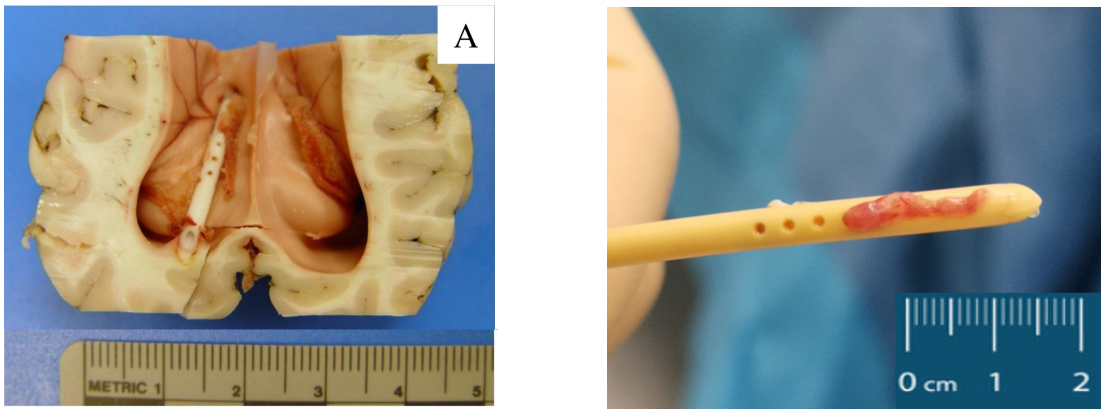

(a) (b)

Figure 2.3: (a) Occlusion of a ventricular catheter by ChP tissue in a sheep model, taken from Johnston, Del Bigio, Drake, Armstrong, Di Curzio, and Bertrand [56] (under a Creative Commons Attribution 2.0 International License CC BY 2.0 [32]) (b) Explanted catheter with ChP growing into inlet hole, taken from Levrini, Czosnyka, Lawes, Kolias, and Mannion [61] with approximate scale added (under a Creative Commons Attribution 4.0 International License CC BY 4.0 [32]).

patients found that 20% of patients required revision surgery, with occlusion by tissues being the leading cause of shunt failure [14], while a third study argued that placing the catheter away from brain tissues was the most promising predictor of catheter success [63]. A 2017 study compared shunt treatments in 434 patients over 40 years and found no significant improvement in infection or revision rates over that time period despite improvement in materials and techniques [45]. A comprehensive review of existing clinical studies of hydrocephalus treatments found high rates of shunt revision surgeries due to occlusion in all studies reviewed [9].

These studies show that the problem of catheter blockage remains. As clinical studies are observational, they do not directly suggest ways to reduce the problem. Various ventricular catheter designs have been proposed to mitigate the risk of blockage by ChP. The flanged design (second left, Figure 2.2 d)) was proposed in the 1970s to physically stop the ChP from reaching the inlet holes, but proved ineffective, and particularly difficult to replace as the ChP became entangled in the flanges [64]. Now, a variety of catheter inlet hole designs are available (Figures 2.2 b-d)) with significant variation between the size and placement of inlet holes, but none are totally successful at preventing blockages.

To gain a deeper understanding of the catheter blockage process, experiments have been performed on animal models. Johnston, Del Bigio, Drake, Armstrong, Di Curzio, and Bertrand [56] demonstrated the limitations of a ventricular catheter in a sheep model, and found that the ventricular catheter was blocked by the ChP within 9 days of insertion in 11 out of 16 subjects. McAllister, Talcott, Isaacs, Zwick, Garcia-Bonilla, Castaneyra-Ruiz, Hartman, Dilger, Fleming, Golden, Morales, Harris, and Limbrick [65] showed similar results in a pig model, additionally measuring a four-fold increase in ventricular volume after hydrocephalus was induced.

The similarity of symptoms seen in animal models and humans aids understanding of the symptoms and treatment of hydrocephalus [34]. However, animal studies can only consider small populations, and hence inter-patient variability makes it difficult to draw generalisable conclusions. This motivates the use of computational models as an inexpensive, fast alternative to animal models which can be used to improve the mechanistic understanding of the problem.

Improving the design of the catheter inlet holes to prevent blockage by ChP has huge potential to improve the performance of the shunt system and minimise the risk to the patient. In this work, an investigation into ventricular catheter hole design is performed, and the impact of different designs on ChP deformation is studied. As this is a complex biological system, modelling the full hydrocephalus problem *in silico* requires intricate techniques based on well-established methods. To this end, a discussion of the computational methods that are used to simulate the ventricle-catheter-ChP domain is presented below, including a summary of previous computational research into various parts of the ventricle-catheter-ChP system.

2.3 Computational models

Computational modelling emerged at the end of the second world war and has since revolutionised research across the sciences [66]. Physical systems can be represented by a set of mathematical governing equations on a geometry, with the governing equations determined either by the laws of nature (e.g. conservation of mass and momentum), or from experimentally observed relationships (e.g. Hodgkin-Huxley's model of action potentials in neuron, derived from experimental observations of a giant squid [67]). Computers are efficient at finding a

good approximation to the solution of a set of governing equations, and benefit from being cheaper, faster and non-intrusive compared to experimental models. Computational models are removed from experimental noise and measurement uncertainty, and can often explore beyond the range of experimental models (e.g. a model input parameter may be limited experimentally by the materials available, but can be easily changed in the computational model simply by altering the value of the parameter). However, models are inherently an abstraction of the real world problem, making simplifications and assumptions to create a closed system of mathematical equations.

Some systems of governing equations apply to many different problems. Here for example, CSF is modelled as an incompressible, Newtonian fluid, and like all incompressible, Newtonian fluids is governed by the incompressible Navier-Stokes equations linking fluid velocity $\boldsymbol{v}$ with fluid pressure p:

$$\nabla \cdot \boldsymbol{v} = 0, \quad \rho_f \Big(\frac{\partial \boldsymbol{v}}{\partial t} + (\boldsymbol{v} \cdot \nabla)\boldsymbol{v} \Big) = -\nabla p + \mu \nabla^2 \boldsymbol{v}, \tag{2.1}$$

where ρ_f and μ are the density and viscosity of the fluid respectively. These equations quantify conservation of mass and momentum in the system. Similarly, a momentum balance in compressible solids leads to the governing equations balancing the Cauchy stress tensor $\boldsymbol{\sigma}$, the solid density ρ_s and the solid displacement vector $\boldsymbol{u}$ (specifically $\boldsymbol{u} = \boldsymbol{x} - \boldsymbol{X}$ is the vector difference between the initial configuration of the solid, $\boldsymbol{X}$, and the current configuration, $\boldsymbol{x}$).

$$\rho_s \frac{D^2 \boldsymbol{u}}{Dt^2} = \nabla \cdot \boldsymbol{\sigma}, \quad \boldsymbol{\sigma} = G(\boldsymbol{u}), \tag{2.2}$$

where D/Dt denotes the material time derivative. The constitutive relation G characterises the material response, governing the association of deformation and stress. As a material property, G must satisfy objectivity, ensuring that the constitutive response is not affected by the observers frame of reference, and hence "are independent of superimposed rigid-body motions" [68].

These governing equations are applicable to a multitude of fluid and solid problems, and consequently the computational finite element and finite volume methods have been developed to efficiently solve these specific systems of equations.

2.3.1 Computational methods

Computational methods transform the governing equations for the fluid and solid (which are non-linear partial differential equations) into large systems of simpler equations. There are two key methods: the finite element method (FEM) and the finite volume method (FVM). These methods are similar in nature, but subtle differences make them better suited to solving different problems. Commonly, FEM is used to simulate the deformation of solid bodies and FVM for simulating the movement of fluids for reasons discussed below.

The FEM dissects the geometry into convex subdomains called elements, with every element defined by the position of its nodes. FEM solves a weak formulation of the governing equations to find the solution at each node. The node solutions are then interpolated across elements, ensuring continuity. FEM is the preferred method for solid dynamics simulations as the node positions can be easily updated during the simulation as the solid deforms. In contrast, FVM divides the geometry into fixed control volumes and solves an integrated form of the governing equations to determine a solution for each volume. FVM therefore intrinsically accounts for conservation laws such as mass and momentum due to the integrated form of the governing equation. FVM is often used to solve fluid dynamics problems due to the inherent conservation laws, but FVM methods do not necessarily give a continuous solution between neighbouring volumes [69]. The strength of both methods is that arbitrarily complex domains can be simulated as long as the element size is small enough to accurately capture the geometry [70].

The first FEM model is often quoted as having been developed in 1941 [71], with Hrennikoff publishing work discretising a 2D domain into a regular lattice of points, and Courant separately working with 2D domains discretised into triangles. The method was successfully used by Boeing in the 1950s, and aerofoil problems are still a standard benchmark in the field [72]. FVM emerged in the 1980s as an adaption of FEM to better suit fluid dynamics problems. In the 1990s, these methods were combined to address fluid-structure interaction (FSI) problems, introducing the arbitrary Lagrangian-Euler formulation to combine FVM and FEM. Some of the first work on FSI problems focussed on blood flow through arteries [73] and on the large deformation of soft biological tissues [74]. Since the 1990s, the increase in available computing power has made FEM and

FVM popular in multiple areas of research, particularly solid mechanics and fluid dynamics.

However, it should be noted that both FEM and FVM are intrinsically approximations, and can have convergence or numerical issues which lead to erroneous solutions [72]. In Appendix A.4.1, an example is presented where two different element types (both superficially giving a good quality discretisation of the geometry) lead to significantly different simulation results. This emphasises the importance of fully understanding all computational methods being used to have full confidence in simulation results.

Previous computational work which has focussed on various parts of the hydrocephalus scenario is now discussed: fluid models of the CSF, solid models of brain tissue and examples of FSI problems.

2.3.2 Fluid models of cerebrospinal fluid

There has been considerable research modelling the flow of CSF (treated as a viscous, Newtonian, incompressible fluid) in various sections of the CNS to better understand flow patterns.

FVM have been commonly used to simulate CSF flow as their discretisation of the domain is well adapted to capturing complex biological geometries. However, these simulations are computationally intensive and most studies thus focus their models on a small subdomain of the CNS. FVM studies of CSF flow dynamics often take boundary geometries from magnetic resonance imaging to recreate a physiological CSF domain, a technique able to account for inter-patient variability [75]. Various studies have focussed on the subarachnoid space [21], the ventricular system [76], and the spinal cord [21]. These numerical simulations confirm experimental results that CSF dynamics are pulsatile with a second order bulk flow through the ventricular system [21, 22]. These studies captured CSF flow in the CNS of a healthy patient. Recovering normal CSF flow is the target outcome of surgical treatment, and hence it is important to understand CSF flow in healthy patients [7].

Computational models have also been used to study the effects of the hydrocephalus condition on CSF flow. Linninger, Xenos, Zhu, Somayaji, Kondapalli, and Penn [77] modelled a 2D vertical slice of the head, reducing the permeability of the system when incorporating the effects of hydrocephalus, and finding

higher CSF velocities throughout the system. Gholampour, Fatouraee, Seddighi, and Seddighi [78] extended these results to 3D, using clinical data to determine healthy and pathological model parameters. They found intracranial pressure was five times higher in hydrocephalus patients than in healthy ones. The same group then extended their model to incorporate a shunt system. They found that shunting rapidly decreased intracranial pressure, but that the pressure and fluid velocity waveforms of shunted models did not reconcile with the healthy models even after 900 days, suggesting that the presence of the shunt systems fundamentally altered the CSF fluid profile [79]. In separate work, Patel, Huang, Dengiz, Pravdivtseva, Jansen, Quandt, and Aizenberg [80] used 2D simulations to study biomolecular transport in a 2D ventricle domain with shunt system.

This body of work has extensively investigated the flow profile of CSF in the ventricular system, taking a high level view to investigate the effect of hydrocephalus on intracranial pressure and CSF flow. This work did not account for the detailed design of catheters, and models do not incorporate the ChP.

A separate body of research does focus on the design of the ventricular catheter. FVM are used to examine the flow of CSF around and through the catheter, usually by isolating the catheter in an infinite fluid domain (often modelled as a large cylinder coaxial to the catheter, Figure 2.4). This removes the catheter from its biological context, and hence never directly investigates the effect of catheter design on ChP. The key focus of these studies is to quantify the different inflow rates through different inlet holes with the assumption that higher rates of inflow will exert greater forces on nearby ChP, hence causing greater deformation towards holes.

Fluid-only models have therefore searched for catheter designs which facilitate identical inflow through each inlet hole. The more complex model created in this project, which does include the ChP, investigates whether this "identical influx into each hole" requirement is a successful proxy for ChP deformation. Previous computational studies have also been concerned with shear stress rates, as higher shear stresses have additionally been linked to higher likelihood of small cells suspended in the CSF adhering to the catheter, a secondary cause of blockage [1, 15, 10]. In contrast, Ref. [81] argued that very low shear stresses are also linked to increased chance of catheter blockage caused by cells adhering to the ventricle walls.

The first study by Lin, Morris, Olivero, F., and Sanford [82] in 2003 used 2D FVM to model a vertical cross-section of a catheter, and showed that over 50% of the total fluid inflow enters the catheter in the most proximal holes. These results were verified experimentally using ink to visualise flow patterns, and a survey of occluded catheters showed that the ChP most often blocked the proximal hole [83]. This work motivated a new catheter design *Rivulet*, manufactured by Medtronic, which varied the size of inlet holes to enforce more uniform inflow. These ideas were expanded by the group of Galarza, Giménez, Valero, Pellicer, and Amigó [84] who first created a 3D FVM model which could be used to study the flow fields inside a catheter [84]. They showed that varying only the number and placement (and not size) of inlet holes could be used to enforce uniform inflow [85]. This is easier to manufacture as only one drill bit size is needed, and prevents the problems of high levels of cell adhesion in small hole diameters (the smallest holes in the *Rivulet* design have a radius of 0.14 mm). They then proposed and studied five prototype designs, showing how different flow profiles could be achieved in different geometries [86]. The group continued to investigate catheter design, investigating conical or tilted holes [87] and rotations of neighbouring rings of holes respective to each other [88]. They summarised their progress in a review [89] and moved to clinical trials with their most promising design [90]. Throughout their work computational results were qualitatively verified using ink methods to visualise flow patterns, and the clinical trial showed promising results as of 2021: of 40 patients implanted with a novel catheter design, none had catheter blockages in the two years following surgery [90].

Separately in 2017, Weisenberg created and studied a fluid model of the catheter (optimised catheter design recreated in Figure 2.4 [15]). As above, she sought a design which would lead to a uniform inflow profile. She identified the inter-hole spacing and hole diameter as important design parameters, and ran a local optimisation search to identify the design parameter values which would give the most uniform flow profile, while keeping the hole arrangement fixed in six axial rows, with each row containing four holes spread equally around the circumference. Her optimised catheter design is similar to the *Rivulet* design [83] with holes decreasing in size towards the outlet of the catheter, see Figure 2.4.

Results from models using 3D patient-specific ventricle geometries were later compared to the work using these large cylindrical domains. The differences in geometry were shown not to significantly influence the flow fields inside the

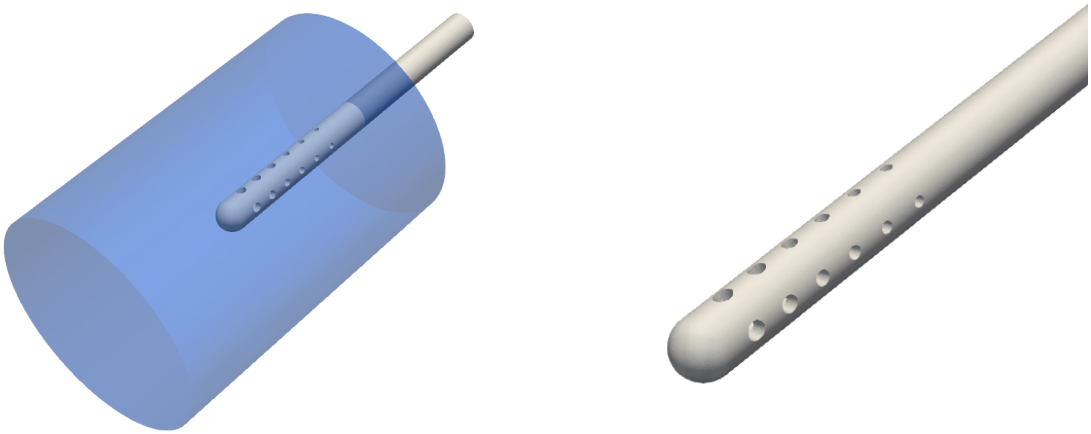

(a) (b)

Figure 2.4: Optimal catheter design found by Weisenberg, recreated from values given in Ref. [15]. The part of the catheter outside of the fluid domain does not contain inlet holes and hence is not modelled. SubFigure (a) catheter situated in modelled fluid domain; (b) close focus on inlet holes. Blue: simulated fluid domain; white: catheter walls.

catheter [91]. In contrast, discrepancies of $\sim 20\%$ were seen when comparing a 2D realistic ventricle geometry to a cross section of the large cylindrical domain [80].

The work by Galarza, Giménez, Valero, Pellicer, and Amigó [84] [85, 86, 88, 89, 90] and Weisenberg [15] provides a detailed exploration into the effect of catheter on hole design on CSF flow, and showed how choices of hole size and spacing could lead to significant differences in the flow field. These models placed a catheter inside a large, cylindrical fluid domain, leading to largely axisymmetric flow fields, and did not include the ChP as part of the model.

This project extends existing work by creating a new model that includes the ChP as a deformable solid, allowing the ChP deformation to be specifically quantified. It is of particular interest in this research to evaluate whether the "identical influx into each hole" metric used previously is sufficient to judge the overall effect of catheter geometry on ChP deformation.

2.3.3 Solid models of brain tissue

In this work the ChP is modelled as a deformable solid, which requires knowledge of its constitutive behaviour and associated material parameters to ensure the model accurately captures the deformation. However, there is very limited work specifically analysing the ChP, and studies that do are typically aiming to understand the biological role and complex substructure of the ChP as part of the blood-brain barrier motivated by attempts to regrow the ChP in an *in vitro* setting [35, 29, 92].

There has been far more investigation into the biomechanical properties of the brain, either as a whole, or focussing on the grey and white matter (as summarised in the reviews [93, 94]). As the specific mechanical properties of ChP are not well understood, existing models of brain tissue are used as a basis for the ChP model: an acceptable first estimate.

Brain tissue is a deformable, porous, composite, heterogeneous material which exhibits a non-linear mechanical behaviour [93, 95], with a complex dependence on the microstructure of cells and proteins [96]. A 2016 review of constitutive models for white and grey matter gave a wide range of models used in current research [94]. This review focussed on simple models which give a good macroscale approximation to brain deformation, and so the most common models were linear elastic models, with various formulations of hyperelastic models also popular. Elastic models have stress tensors that are dependent only on the current deformation of the material and hence are simpler than models incorporating porous and viscous effects. Simpler models have less material-dependent parameters which is a benefit when little is known about the material. Across the models reviewed in Ref. [94] the Poisson's ratio was high ($\geq$0.4 in all of the 21 models which include a Poisson's ratio; $\geq$0.45 in 16/21 cases), with research consistently agreeing that brain tissue is near incompressible. It should be noted that compressible computational models are normally more numerically stable, and hence truly incompressible brain tissue (with Poisson's ratio of 0.5) is frequently modelled using a high, but <0.5, Poisson's ratio. There was much more variation in quoted values of the Young's Modulus, ranging from 0.7 - 44 kPa, suggesting a high degree of uncertainty in this measurement.

The brain is known to also exhibit a visco- and poro-elastic behaviour [97]. Viscoelastic models add time-dependence to the elastic response and can be for-

mulated by representing the mechanical response as a system of springs and dashpots [98], or by taking a decomposition of the stress tensor over the deformation history [99, 100]. Poroelastic models separate the solid and fluid constituents of brain tissue, and model the material as an elastic matrix saturated with viscous fluid [101]. These models combine the microscale detail of the distinct fluid and solid components into one material law which combines the elastic solid stress tensor and the effective pore pressure [97, 102], with more complex models incorporating multiple distinct solid components [103]. Detailed work looking at the microscale arrangement of blood vessels in brain tissue showed how the position and arrangement of fluid vessels can affect the mechanical properties of the overall tissue [104, 105].

Additionally, biological tissues grow over time, which can cause their shape and material properties to change. Models focussing on growth are often composed of an elastic component and a growth component [106], with the growth component leading to complex internal stresses in the material [107].

Many of the above models focus solely on either grey or white matter tissue, and most homogenise the tissue of interest into a uniform material. It is also noted that models fitted to a specific loading scenario often do not capture different loadings, and many models are applicable only for a small range of deformations [93]. While there has been a wealth of research attempting to quantify the mechanical behaviour of brain tissue, very little of it is directly concerned with the ChP, with significant variation between models depending on the testing scenario and research focus. Consequently, and in line with the studies reviewed in Ref. [94], a simple elastic constitutive model is used in this project to quantify the behaviour of the ChP, thereby restricting the number of unknown material parameters. Additionally, the simple model for ChP behaviour neglects tissue growth.

2.3.4 Fluid-structure interaction models

All the models discussed so far have looked at either a fluid or a solid component in isolation. In the ventricle-catheter-ChP domain however, the solid ChP deforms due to the fluid stresses on its surface created by the flow of CSF in the system. In turn, the movement of the ChP affects the fluid flow because of the change to the geometry of the system and the ChP's role in CSF production. It is

therefore essential to include both the fluid and solid components in the model, which then interact during a simulation. This type of behaviour defines a fluid-structure interaction (FSI) problem [108]. FSI models aim at providing a detailed understanding of the multiphysics, but are typically computationally expensive to run, as not only are FEM or FVM needed for the solid and fluid components respectively, but multiple iterations of both components are required to ensure convergence of the full system close to the FSI boundary [109].

To my knowledge, there has been no FSI model used to investigate the deformation of ChP in the ventricle environment. However, there has been other work using FSI methods to understand the flow of CSF in the CNS [21, 75, 76]. As with the fluid-only models, research into the flow of CSF through the CNS incorporating FSI effects is limited to focus on specific sub-systems. Parts of the fluid boundary which have been identified as of interest are modelled as a deformable solid. Previous studies have looked at incorporating deformable effects at the base of the spinal column [110], allowing fluid exchange with brain tissues using a porous model [20], or investigating CSF flow through the aqueduct of Sylvius, modelling the walls as elastic [111].

Simpler, compartment-based FSI models remove the explicit spatial dependence and formulate systems of ODEs relating the pressure, volume and fluid velocity of different regions in the ventricular system [34, 112]. These models are far faster to solve than those containing FEM or FVM, and can replicate *in vivo* measurements. However, by removing the spatial terms, these models cannot replicate detailed flow patterns or tissue deformation. For this reason, FEM and FVM are employed for the solid and fluid domains respectively to fully resolve the spatial features of the system.

In summary, this section reviewed existing computational models of CSF flow (either through the CNS or in detail about a catheter), solid models of brain tissue, and examples of where these areas have been combined to investigate FSI effects in the CNS. Whilst this thesis is the first example of FSI methods being used to analyse the detail of ChP deformation, the FSI model developed here builds on different aspects (mechanisms and material parameters) of existing models thus extending previous research.

2.4 Computational optimisation

The final section of this literature review focusses on the computational methods that are used to improve the catheter design. This section introduces generative design and discusses previous successful applications of this method for biomedical design. The optimisation codebase used in this thesis is introduced, as are the surrogate and ROM techniques which are used to enhance the efficiency of an optimisation.

2.4.1 Generative design

Generative design describes the use computational models and optimisation procedures to produce design improvements [113]. The optimisation "generates" new designs which conform to a set of user prescribed constraints, and computational models are used to test the efficacy of a new design. This process allows a large range of possible designs to be explored efficiently [114, 115].

The first applications of generative methods emerged in architectural problems to improve and refine initial designs [116], and quickly spread to mechanical engineering problems [117, 118]. Generative methods are now integrated into several mainstream software packages including Dassault Systèmes [119] and the Revit [120] and Fusion [121] products of Autodesk. Traditionally, a new design of a medical component must undergo animal testing and finally human trials before being released [4]. New designs are often incremental improvements on existing designs to avoid wasting resources by testing a completely new configuration. Nevertheless, this experimental process is expensive, and components that do well in animal trials may be poorly adapted for human use due to inherent differences in biology [122]. Generative design allows for a more pragmatic approach, with many variations tested quickly *in silico* and only the best designs are passed onto experimental testing. Here, the design process starts by formulating the problem in terms of necessary constraints and practical requirements, before allowing the computer to identify promising designs [119, 123]. This process is cheaper than traditional design approaches in both cost and time. Generative algorithms also have the advantage that they explore design combinations not previously considered, as the generative algorithm has freedom to test a large parameter space.

Generative design techniques have been used effectively in medical contexts to create patient-specific knee implants for osteoarthritis, adjusting the domain of design parameters to account for inter-patient variability. There has also been similar work to improve knee implants [124], skeletal joint replacement [125], elbow orthosis supports [126], and ureteric flow washout devices [6]. In general, using computational optimisation methods removes human bias in design choices and tests designs outside of a previously considered range. The speed and low relative cost of computational testing also makes this approach an efficient method to explore a design space. However, two points must be emphasised. First, generative methods often provide a family of promising designs, instead of a single optimum design [119, 125] allowing the user to evaluate which designs to take forward into experimental testing. Second, a finite search space must be chosen by the user, meaning there will always be some level of parameter constraints on the design algorithm. A larger search space requires either more aggressive stochastic search methods or more computational time to explore, and users must choose a balance between exploring a larger design area and computational efficiency. This process therefore does not ensure optimality, but the best effort, as constrained by a computational budget.

This project on ventricular catheter design can be phrased as a generative design problem by associating a catheter design with a set of input parameters and searching for the parameters which lead to minimal deflection of the ChP.

2.4.2 Lurtis codebase

The optimisation codebase used for this project is provided by collaborators at Lurtis Ltd., and is presented in full detail in Refs. [127] and [128]. The structure of the optimisation sweep is shown in Figure 2.5. The code is highly modular, allowing the same optimisation framework to be applied to many scenarios. The two key parts of the optimisation process are the fitness function (blue) and the optimisation codebase (green).

As seen in Figure 2.5, an optimisation problem consists of two distinct, independent parts. The fitness function f, which is problem specific, takes as input a set of parameter values, interprets these values as a specific design and evaluates the effectiveness of this design. The effectiveness of a design is known as its fitness, and here is a single, scalar value. This value can be used to rank designs,

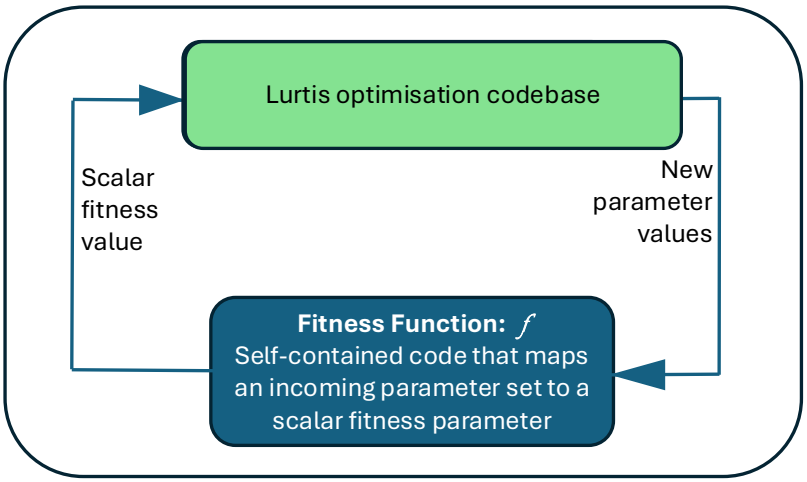

Figure 2.5: Basic optimisation protocol structure using the Lurtis Ltd. codebase.

prioritising those with higher fitness. All models specific to the problem at hand (construction of a design from input parameters, evaluation of the design through FVM or FEM and any postprocessing) are contained within the fitness function.

The second part of the optimisation sweep, the optimisation algorithm, does not interact directly with any methods specific to the design problem. This codebase proposes new designs based on the fitness values evaluated from previous parameter sets. The aim of this code is to find the set of parameter values that minimise the fitness function. It should be noted that a design is characterised both by the vector used by the optimisation algorithm (often known as the genotype) and the physical design implemented in and analysed by the fitness function (often called the phenotype) [123]. The map between the genotype and phenotype is also problem specific, and is known as the encoding [129].

2.4.3 Optimisation methods

This section provides a brief overview of common optimisation methods, with particular detail given to those which appear in the Lurtis codebase.

Optimisation methods focus on efficiently searching a multidimensional parameter space to find the minima of the fitness function. If the space is large, or the dimension of the parameter set is high, then searching the entire space is computationally inefficient. Optimisation methods aim to efficiently search the space by combining two strategies: exploitatory and exploratory. Exploratory

strategies explore the parameter space to find promising regions and exploitatory strategies narrow down on local minima. Most algorithms combine methods from the two strategies to improve overall performance, but may focus more on one or the other.

Methods with good exploitatory behaviour often use local search methods (such as gradient search, pseudo-newton optimisation, or simulated annealing search [117, 130]) to ensure they propose new parameter values with a smaller fitness. Calculating the fitness of a single parameter set can be computationally expensive, and calculating the gradient is an additional cost. Therefore batch or stochastic gradient descent methods are used to approximate the gradient at a point [131]. Previous work by Lurtis Ltd [128] incorporated the more complex methods of limited memory-BFGS-B [132] or multi-trajectory-search (MTS) [133] to efficiently explore the fitness landscape. MTS varies one entry of the parameter vector at a time, and progresses in the direction of decreasing fitness, creating a stepped path. BFGS uses a Newton style approach, using previous fitness evaluations to improve its estimation of the gradient. The limited memory version of this algorithm only stores a fixed number of recent fitness evaluations to save computational memory.

Exploitatory search methods benefit simpler problems where constraints and fitness functions are relatively smooth and simple [131], and can be caught in local minima (any minima has a gradient of zero, which the gradient descent algorithm is searching for, but a local minima does not have the lowest fitness of the search space meaning this is a sub-optimal design). Such methods also depend on the fitness function having a well-defined gradient. For more complex problems with discontinuities, directional, but gradient-free, methods exist, such as the Nelder-Mead downhill simplex method [134] or direct-search methods [135].

In contrast, algorithms with better exploratory capabilities investigate solutions across the whole search space, while incorporating knowledge of the local landscape [136]. Parameter spaces are often large and complex, and so a completely random exploration, such as stochastic sampling (Monte Carlo search), would be prohibitively long. For their exploratory algorithm, Lurtis use differential evolution (DE), a subclass of genetic algorithms [137]. This draws inspiration from biology, using evolutionary approaches to tend towards optimal solutions [138], while maintaining some randomness to ensure space exploration [139]. New population members are constructed by either combining existing

members, introducing new features into existing members (a mutation event), or by combining features from two members to create a new offspring (a recombination event) [137]. If the offspring has a better fit than the parent it replaces the parent in the population [137, 127]. Differential algorithms additionally benefit from only needing a small number of control parameters [140]. An adaption of the general DE method is the success-history based adaptive DE (SHADE), used here, which allows the parameters controlling adaption and mutation to vary, and stores all previous values of these parameters. The historical values are used to guide the selection of the new parameter value, incorporating memory effects into the algorithm [141, 142]. Other extensions of genetic algorithms include probability estimation models [143] which replace the crossover and mutation parameters, instead learning the probability distribution of promising solutions, and consequently have a higher computational cost.

2.4.4 Surrogate-aided optimisation

Optimisation methods require efficient algorithms to explore a parameter space and identify promising minima. However, to understand the shape of the fitness landscape, multiple evaluations of the fitness function must be performed (one for each new parameter value proposed). It has previously been noted that FSI models based on FVM and FEM are computationally expensive, potentially taking of the order of hours or days to run, and a fitness function using these methods will have a comparable runtime. A complete optimisation of a high-dimensional search space requires thousands of parameter evaluations, which is unfeasible with the runtime of the complex models [2]. Various techniques have been developed to improve the efficiency of optimisation algorithms [144, 145, 146]. One of the most successful techniques replaces the computationally intensive fitness evaluation with an approximation to the fitness, through the creation of a surrogate model [147, 148].

The terms "surrogate model" and "ROM" are both used in the literature on computational optimisation, occasionally interchangeably, to refer to approximate models that replace a complex model or fitness function. The complex model is defined as the ground-truth for the fitness function, and the aim of approximate models is to have good agreement with the ground-truth, with faster runtime. Approximate models can be developed in various ways and employed at different

stages of the optimisation process, meaning definitions in the literature are often inconsistent or overlapping. For clarity, this thesis will use "ROM" to refer to a simplified model designed using geometric or mechanistic approximations of the problem. A "surrogate model", is here defined as the combination of a ROM with a predictive ML layer which directly replaces the 3D FSI model [149]. The procedure as a whole, whereby an approximate model is used to speed up an optimisation protocol, is a "surrogate-aided optimisation", consistent with the literature.

A ROM can be a stand-alone replacement to the fitness function, but combining the outputs of a ROM with ML techniques to create a surrogate model often improves the agreements between the fitness (as calculated by the ROM) and the ground-truth fitness (as calculated by the complex model). This combination of data-driven techniques with mechanistic models, known as mechanistic learning (MxL), has been successful in recent applications across quantitative biology [17, 150]. However if there is very little data available to train the ML layer, or if it is very important to maintain interpretability, then adding ML to a ROM may not improve its efficacy. Likewise it is possible to design a truly data-driven surrogate model that has no mechanistic underpinning, and is simply a black box associating input parameters with fitness values. These different approaches all have value and will be more or less applicable depending on the problem at hand.

The approach discussed here, whereby the computationally expensive fitness function is replaced with a cheaper approximation is also known as an offline approach. "Offline" refers to the fact that the surrogate model is built and trained outside of the optimisation protocol [151]. Offline creation allows for much more fine-tuning of the surrogate with potential pitfalls such as overfitting being identified and addressed. Different offline implementations may replace the true fitness completely, or exchange dynamically between true and approximate fitness functions throughout the optimisation [152, 153], as seen in previous work in multi-resolution [154] and island injection genetic algorithms [155] which used both a full and simplified model in their optimisations.

Offline surrogate models are popular within aerospace engineering and have been used successfully in the design of telescope housing [115], aircraft landing gear [156] and automotive design [157]. Surrogate methods are beginning to be leveraged in FSI optimisation problems by creating an approximate solution to the flow and deformation fields in the entire 3D domain [158, 159]. Due

to the complexity of physical fields in intricate domains, these studies required complex ML models to capture the fields to the required accuracy. To successfully approximate large flow fields, ML either needs a large quantity of data from which the underlying physical mechanisms can be deduced, or intricate techniques to incorporate physical laws inherently into the training protocol [160]. Chapter 6 of this thesis is concerned entirely with building and evaluating surrogates to the complex FSI model, with particular consideration given to careful training of the ML algorithms used.

In contrast to offline methods, "online" models are dynamically built during an optimisation. Here, the optimisation first uses the ground-truth fitness function to evaluate a number of initial parameter designs. The initial parameters and their corresponding fitnesses create a training dataset which trains an ML layer as the optimisation runs [161]. Often, an online surrogate model is integrated into the optimisation protocol rather than being the user-set fitness function, and so the surrogate is not exposed to the specifics of the problem and instead acts as a black box, attempting to map parameter values to their fitness value. The parameter space is a subset of n-dimensional Euclidean space (where n is the number of design parameters), and so an online surrogate models the fitness landscape by interpolating between known values of the fitness function [162] using either preset function shapes (linear, quadratic or radial-basis functions) or regression techniques to determine function coefficients [134].

As the optimisation proceeds, the online surrogate acts immediately on all new parameters proposed by the optimisation, discarding those it predicts to be highly unpromising, and only allowing promising design candidates to progress to the expensive fitness evaluation. This reduces the time spent investigating regions of the parameter space with high fitness. At the beginning of the optimisation run, the online surrogate is trained on little data and so is very uncertain in its prediction. To account for this initial uncertainty, and the lack of interpretability inherent to black box ML, the surrogate model is cautious, only discarding parameter combinations that are highly likely (as defined by the surrogate) to be worse than existing designs. This ensures that good designs are not discarded due to an error in the surrogate approximation. However, this caution means that the majority of new candidates proceed to the expensive fitness evaluation [127]. As the optimisation proceeds, the dataset of parameters and associated

fitnesses grows, and the ML can retrain with each new data point. This improves the predictive ability of the online surrogate in the later stages of optimisation.

2.4.4.1 Machine learning

In the above section several references have been made to integrating ML techniques in the development of surrogate models. In the last decade machine learning has penetrated every aspect of research and normal life, with ML models ranging from the simplest linear regression (in essence, a line of best fit) to large language models training on the entire internet [163]. At their heart, all ML algorithms seek to learn relations from a given set of data, either to better understand patterns present in the data, or to predict outputs associated with new data [164]. The specific ML algorithm is chosen to suit the size, data type and intricacy of the dataset under consideration [165, 166]. In this thesis, ML is used in the prediction of the approximate fitness of a new catheter design (specifically, in predicting the deformation of the ChP), making the ML applications here all supervised regression problems, where "supervised" indicates there is an unknown output to be predicted, and "regression" indicating that this output is continuous [167].

ML algorithms rely on the quality and quantity of input data to learn patterns as they do not have any inherent understanding of the context or mechanisms behind the dataset (hence the term black box). Therefore a crucial step in developing an ML model is careful training (the process in which the ML model is fitted to a dataset) and validation (checking that the algorithm has not overfit to the input data) [168]. In particular, the datasets available in this project for ML to learn from are small (where small is defined in this area as ≤ 1000 data points), which precludes the use of more complex algorithms such as deep neural networks [167]. The development and training of ML models is carefully performed in the development of the surrogate model in Chapter 6, with each step of the process being described in detail.

This section has outlined the generative design techniques that will be employed in this thesis to enhance catheter design. It presents the optimisation methods used to explore the design space and introduces reduced-order and surrogate models, discussing their roles in accelerating the optimisation process.

2.5 Summary

This chapter outlined the clinical and biological context that motivates the research project and reviews existing work relevant to its development. It begun by introducing the physiological and clinical background of hydrocephalus, including standard treatment via drainage shunt systems. Particular attention was given to the issue of choroid plexus (ChP) occlusion of the ventricular catheter, a long-standing problem highlighted in several clinical studies, yet one for which the underlying mechanisms remain poorly understood.

A review of computational modelling approaches followed, focussing on FEM and FVM. Prior studies that model cerebrospinal fluid (CSF) flow in the ventricular system and the mechanical behaviour of brain tissue were discussed, as they provide valuable insight into material parameters and constitutive laws that inform the current model. Of direct relevance to catheter design are the fluid-based studies by Galarza, Giménez, Valero, Pellicer, and Amigó [84] [85, 86, 88, 89, 90] and Weisenberg [15], both of which focus on uniform inflow through each catheter inlet hole. This research directly precedes the current project, and Weisenberg's proposed optimal design is re-evaluated using the new fluid–structure interaction (FSI) model developed here.

The chapter concludes with a summary of the optimisation methods developed previously in the group of Professor Jérusalem and with collaborators at Lurtis Ltd. These methods, combined with the FSI model and surrogate modelling techniques, form the framework for identifying optimal catheter designs.

2.6 Statement of originality

This work is, to the best of my knowledge, the first model that directly studies ChP deformation in the hydrocephalus scenario. Chapter 3 presents the codebase used for the model. The 2D FSI coupling code is adapted to the hydrocephalus setting from 2D work by Nguyen, Sanchez Naharro, Pena, and Jerusalem [169] on the aerofoil problem. This required substantial alterations to the methods of Ref. [169], which are discussed in Section 3.4.4.1. The extension of the coupling code to 3D to create the 3D FSI model is new, and is presented as a working example in the in-house codebase `MuPhiSim` [170]. Chapter 4 presents new results using the 3D and adapted 2D FSI models. The ROMs in Chapter 5 are not new

(versions of the permeable fluid model can be seen in Ref. [171, 172]) but are presented in a novel setting. The novel surrogate model created by combining the ROMs with ML is trained on new synthetic data created by the 3D FSI model. The optimisation codebase used in Chapter 7 is created by Lurtis Ltd., and this work provides an original application of the optimisation code to the hydrocephalus problem.

Chapter 3

Materials and methods

This chapter presents the computational FSI model of the hydrocephalus scenario, used here as the ground-truth model within the optimisation framework, see Figure 3.1. This FSI model is used as a testing space to compare different catheter

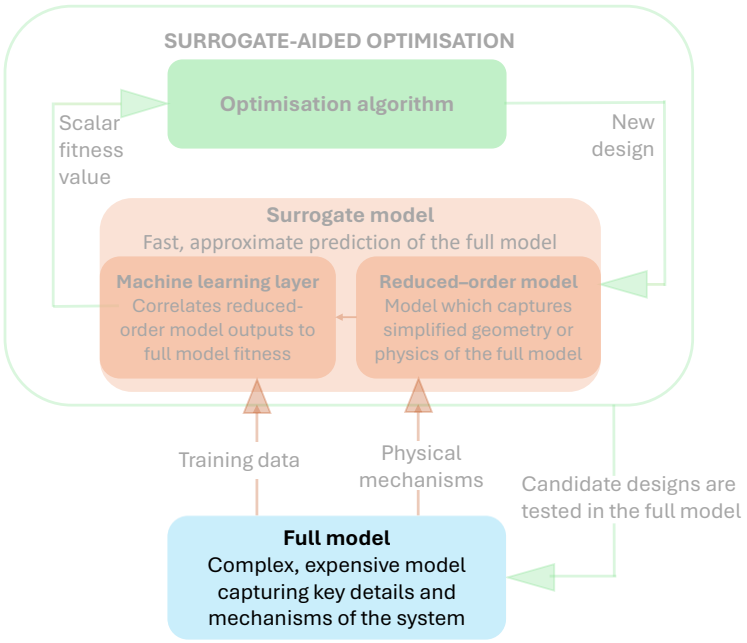

Figure 3.1: Optimisation methodology, highlighting the "full model" component.

designs with a focus on the impact of the design on ChP deformation, hence allowing the designs to be ranked.

The structure of this chapter is as follows. Firstly, the geometry of the ventricle-catheter-ChP environment is presented, followed by the governing equations. The second part of the chapter describes the computational methods used

to simulate and solve the theoretical model. To fully capture the hydrocephalus scenario, existing codebases and FSI coupling methods are adapted to incorporate key mechanisms, focussing in particular on the surface of the ChP that constitutes the FSI boundary while also being the CSF source in the fluid domain. Parts of this chapter are adapted from the Materials and Methods section of Ref. [50] by Hayman et al.

3.1 Hydrocephalus model

The proposed FSI model aims at capturing the ventricle-catheter-ChP environment during hydrocephalus, incorporating the following key components: the CSF, the ventricular domain, the ventricular catheter and the deformable ChP. The area of interest is the region surrounding the inlet holes of the catheter. Figure 3.2 a) shows a realistic foetal ventricle geometry (recreated from data in Ref. [173]) with a catheter and ChP tissue overlaid on the geometry to provide a reference. The box shows the area of interest for this work.

The domain geometry and material properties in the model presented here are chosen to be representative of a realistic scenario, albeit simplified. This idealised model allows for the comparison of different catheter designs and could be adapted to patient-specific geometries or more complex material properties in future research. Figure 3.2 shows the idealised model geometry. Parameter values are taken either from well-established values in the literature (for example, the rheological properties of the well-studied CSF), or are chosen as representative values taken from the range observed in the literature. Characteristic values for lengths are given, as the geometries are curved and irregular. It must be emphasised that there is uncertainty around the ventricle and ChP geometry and the Young's Modulus of the ChP. A summary of parameter values used in the model is given in Table 3.1. The lengths given for the ventricle and ChP are characteristic, as the shapes are irregular. Appendix A.5 gives the results of a parameter sensitivity study which confirmed that the chosen parameter value does not significantly affect the behaviour of the model. This is corroborated by Ref. [91] where varying the ventricle and ChP size, shape and location was shown to not significantly affect catheter performance.

In newly-born infants, the lateral ventricle volume is estimated at slightly under 3000 mm^3 per ventricle using ultrasound [24], or 4500-5000 mm^3 using

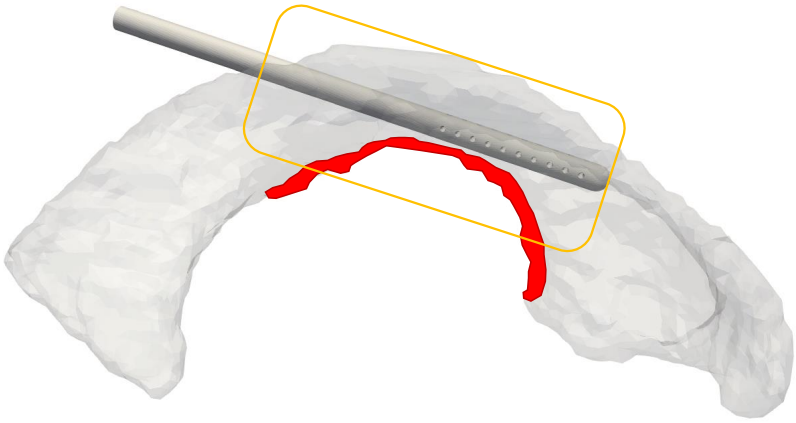

(a)

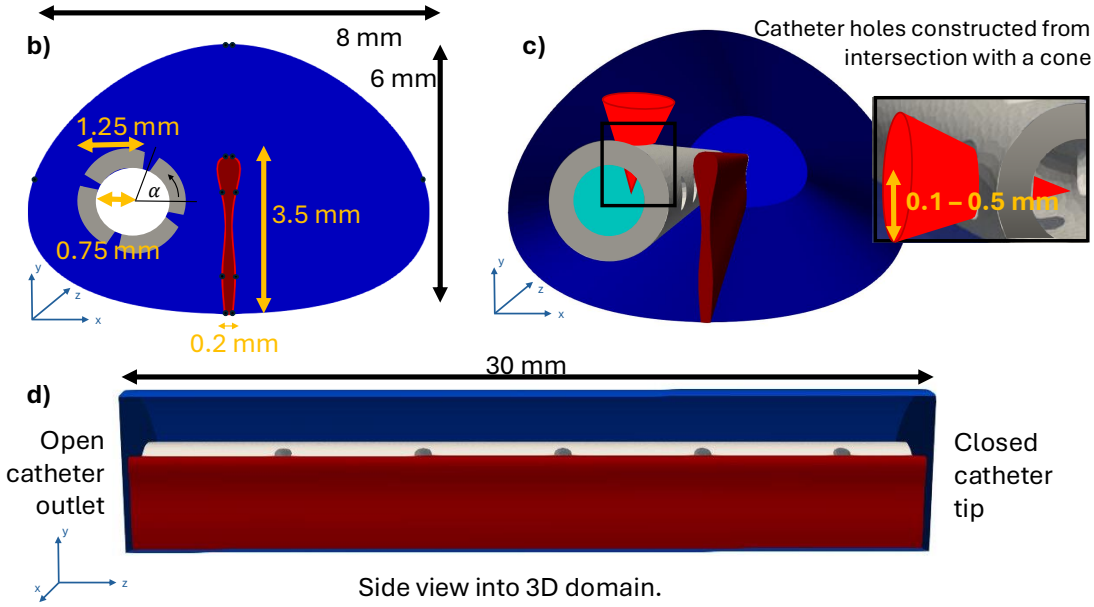

Figure 3.2: (a) Reference visualisation of a foetal ventricle (grey), with catheter and ChP (red). Image created from data in Ref. [173], under a CC BY 4.0 license [32]. An example catheter (dark grey) and Choroid Plexus (red) show relative size and position. (b) Cross-section of the model geometry. Black markers on the boundary of the ventricle and ChP indicate the reference points for the spline curves. (c) 3D geometry front view with front wall boundary removed to show interior surfaces. (d) 3D geometry side view with wall boundary removed: ChP tissue (dark red), catheter (grey).

Table 3.1: Model parameters.

Parameter	**Value**	**Reference**
$L_x \times L_y \times L_z$ Ventricle lengths (characteristic values)	8 mm × 6 mm × 30 mm	[24, 25]
$ChP_x \times ChP_y \times ChP_z$ ChP lengths (characteristic values)	0.2 mm × 3.5 mm × 30 mm	[27, 28]
T Time scale	1 day	[10]
ρ_s Solid density	$1.05 \cdot 10^3$ kg/m^3	[174]
E Young's modulus	50 kg /(m s^2)	[94]
ν Poisson's ratio	0.45	[94]
ρ_f Fluid density	10^3 kg/m^3	[15]
Q Fluid production	6 mm^3/s	[76]
μ Fluid viscosity	$7.5 \cdot 10^{-4}$ kg/(m s)	[175]

MRI [25]. The ventricle shape is complex and varies between patients. The focus of this research is on the interaction between the ChP and catheter inlet holes, both of which sit at the front of the ventricles, see Figure 2.2 a). Accordingly, a sub-domain of the ventricle is modelled, focussing on this key region.

While detailed patient-specific head geometries exist (e.g. Ref. [173]), here the sub-domain is idealised into an asymmetric cylinder of length 30 mm with a volume of 983.8 mm^3 to simplify the model, and provide a view across patient geometries. Comparing patient-specific to idealised ventricle geometries was shown to give $< 1\%$ difference in the volumetric flux into catheter inlet holes [91]. Additionally, the same study investigated different sizes of idealised ventricle and saw $< 0.1\%$ difference in flux, corroborated by a similar study given in [15]. This suggests that effects from the boundary of the fluid domain are not significant, and hence an idealised ventricle geometry is acceptable.

Characteristic domain lengths are nevertheless chosen to be representative of children younger than one year old, consistent with paediatric hydrocephalus. The ventricle cross-section is a curved, irregular shape with maximum width of 8 mm and height of 6 mm. The curved shape is created by using the in-built radial-basis spline functions of `gmsh` [176] to draw a smooth curve through a given set of points, shown as black markers on Figure 3.2 b). The points are: $\{(-\frac{1}{2}ChP_x, 0)$, $(\frac{1}{2}ChP_x, 0), (\frac{1}{2}L_x, \frac{1}{2}L_y), (\frac{1}{2}ChP_x, L_y), (-\frac{1}{2}ChP_x, L_y), (-\frac{1}{2}L_x, \frac{1}{2}L_y)\}$. For reference, a visualisation of an newborn infant ventricle is shown in Figure 3.2 d), created from data provided in Ref. [173].

Growth effects are neglected in this model. The model focusses on the period after a successful catheter implant surgery (any issues arising during surgery would be immediately corrected) as the catheter-ventricle-ChP system reaches equilibrium, a timescale of $\sim$ 1 day. Catheter blockage by the ChP has been reported at any times from 1 day to nearly 4000 days after insertion [10], and the first two years of life is known to be a period of rapid growth and brain development [177]. Looking at the effect of growth on the ventricle domain would be an important effect to include in a more detailed future model, as growth becomes more important over longer timescales. Here, however, growth is neglected as an initial assumption.

In *in vivo* conditions, the walls of the ventricle are deformable brain tissue, which could be modelled as either poro- or viscoelastic, or both. However, during the function of a working catheter the deformation of the brain tissue is minimal

compared to the deformation of the ChP as the Young's modulus of brain tissue is orders of magnitude higher than that of the ChP. Motivated by this, here the ventricle is modelled as a rigid, impermeable, closed box, assuming the most extreme scenario of hydrocephalus without any physiological exit flow (either through apertures into the rest of the ventricular system or through uptake into the permeable brain tissue) which forces all the CSF to drain through the catheter.

The ChP is modelled as a narrow volume of uniform cross-section, with a biologically inspired cross-section created from radial-basis splines extending along the z axis. The width of the base of the ChP cross-section is 0.2 mm, with a height of 3.5 mm [27, 28]. Again the cross section is created by radial-basis splines passing through the set of points: $\{(-\frac{1}{2}ChP_x, 0),\ (\frac{1}{2}ChP_x, 0),\ (\frac{3}{2}ChP_x, \frac{1}{4}ChP_y),\ (\frac{3}{2}ChP_x, \frac{3}{4}ChP_y),\ (\frac{1}{2}ChP_x, ChP_y),\ (-\frac{1}{2}ChP_x, ChP_y),\ (-\frac{3}{2}ChP_x, \frac{3}{4}ChP_y),\ (-\frac{3}{2}ChP_x, \frac{1}{4}ChP_y)\}$, again shown as black markers on Figure 3.2 b). The ChP is rooted to the base of the ventricles and extends beyond the modelled subdomain of the ventricle, Figure 3.2 a). The ChP is therefore fixed at the bottom of the ventricle, with end faces flush against the flat ends of the idealised ventricle. The ChP is a very soft tissue, and so an arbitrarily low Young's modulus of 50 Pa is chosen from the range of 1-1000 Pa [94], see Table 3.1. This value ensures that the ChP is soft enough that collision events can be observed within the model but not so soft that every trial resulted in a collision. Results from different Young's moduli are shown in supplementary Figure A.10 c). The value of 50 Pa shows a large range of ChP responses to the different catheter designs making differentiation between designs more efficient.

The catheter is modelled as a rigid, impermeable, hollow cylinder with circular cross-section, also oriented along the same axis as the ventricle and the ChP. Rigidity is assumed as the Young's modulus of typical catheter material is orders of magnitude greater than that of the ChP [178]. Inlet holes decrease the stiffness of the overall catheter, but, throughout this work, sufficient catheter material to inlet hole area is assumed, to ensure that the catheter remains much stiffer than the ChP (catheters with a stiffness on the order of 50 Pa would not be mechanically sound or surgically useful). The catheter has a closed end at the tip, which is flush with the ventricle wall. Inlet holes for CSF are typically arranged close to the closed tip (within 20 mm of the tip) in a regular formation with ten rows along of the catheter axis of either four or two holes, with holes in each row distributed evenly around the catheter circumference [15]. Only 30

mm of the catheter contained within the idealised ventricle is modelled, as this section contains the inlet holes and is the region of interest.

Physical examples of catheters were examined under an Alicoma microscope (with a resolution of 1 µm) to obtain accurate measurements of the inlet hole radius and shape. Catheters have an outer radius close to 1.25 mm and an inner radius of 0.75 mm, consistent with measurements previously reported [15, 86]. The inlet holes are modelled by removing a conical shape from the wall of the hollow catheter, as Alicoma measurements showed the inlet holes had a conical profile. The orientation of the catheter about its centreline is prescribed by α, the angle between the horizontal and the midpoint of the first hole, see Figure 3.2 b). The angle α is not a design parameter of the catheter and instead captures the relative position of the catheter to the ChP. As such, α is not prescribed in surgery and the behaviour of catheters at multiple values of α thus needs to be investigated.

In Chapter 4, a reduced 2D model is used to gain an understanding of the scenario in a smaller and computationally cheaper domain. Briefly, the 2D model takes a cross-section of the full domain perpendicular to the main cylindrical axis, with the same geometry as shown in Figure 3.2 b). For investigations with the 2D model, the outer and inner catheter radii are fixed at 1.25 mm and 0.75 mm, respectively. In the 2D model, the hollow centre of the catheter is not part of the fluid domain. The outlet boundary is adjusted to account for this, with this change ensuring that the fluid simulation remains purely 2D. In both 2D and 3D, all fluid entering the catheter leaves the ventricular system: the subtle change to boundary conditions is needed only as the 2D model cannot capture fluid flow in the central space of the catheter. In 2D, holes are created by removing a wedge shape from the wall of the hollow catheter.

3.2 Governing equations

3.2.1 Fluid

The CSF within the ventricle volume is modelled as a homogeneous, incompressible, Newtonian fluid with a viscosity of $\mu = 0.75$ mm^2/s and a density of ρ_f =1000 kg/m^3 [20, 21, 22], see Table 3.1 for the parameter values. Body forces are neglected as a less influential driver of flow [36]. The flow is governed by the

continuity and Navier-Stokes equations for the pressure field p and velocity field $\boldsymbol{v}$:

$$\nabla \cdot \boldsymbol{v} = 0, \tag{3.1}$$

$$\rho_f \left(\frac{\partial \boldsymbol{v}}{\partial t} + (\boldsymbol{v} \cdot \nabla)\boldsymbol{v} \right) = -\nabla p + \mu \nabla^2 \boldsymbol{v}. \tag{3.2}$$

3.2.2 Solid

The equations of motion for a solid with no body force is given by Equation (3.3), where $\boldsymbol{\sigma}$ is the Cauchy stress tensor, ρ_s the solid density and $\boldsymbol{u}$ is the displacement vector (where $\boldsymbol{u} = \boldsymbol{x} - \boldsymbol{X}$ is the vector difference between the initial configuration of the solid, $\boldsymbol{X}$, and the current configuration, $\boldsymbol{x}$). Hence:

$$\rho_s \frac{D^2 \boldsymbol{u}}{Dt^2} = \nabla \cdot \boldsymbol{\sigma}, \tag{3.3}$$

where D/Dt denotes the material time derivative. Biologically, the ChP is close to incompressible [94] with a Poisson's ratio of 0.45 used to approximate near-incompressibility. A neo-Hookean hyperelastic model is chosen to describe the constitutive behaviour of the ChP. Although, in line with other complex brain tissues, the ChP has poro- and viscoelastic properties [93], a constitutive law for the ChP is at the moment not established and a simpler model with fewer unknown parameters is favoured here:

$$\boldsymbol{\sigma} = \frac{E}{3(1-2\nu)}(J-1)\mathbb{I} + \frac{E}{2(1+\nu)} J^{-\frac{5}{3}} (\mathbb{B} - \frac{1}{3}(\mathrm{tr}(\mathbb{B}))\mathbb{I}), \tag{3.4}$$

where $\mathbb{B}$ is the left Cauchy-Green tensor, $\mathbb{I}$ is the identity tensor, and $J = \sqrt{\det(\mathbb{B})}$. Equation (3.4) has only two parameter values: the Young's modulus E and Poisson's ratio ν. These equations remain the same in the reduced 2D model, with the additional requirement of plane strain enforcing exclusively in-plane displacement, by setting axial displacement to 0 at all points.

3.2.3 Boundary and interfacial conditions

The model geometry is shown in Figure 3.3, with the relevant volumes and boundary surfaces indicated, both for the 3D (left) and 2D (smaller, right) models. Curved arrows indicated faces which are hidden from view in this visualisation. The fluid domain Ω_f is shown in blues and the solid domain Ω_s is shown in

reds. The ventricle walls, $\partial\Omega_{\text{ventricle}}$, are shown in dark blue, the catheter outlet, $\partial\Omega_{\text{outlet}}$, in bright blue and the catheter walls,$\partial\Omega_{\text{catheter}}$, in grey. The ChP surface, $\partial\Omega_{\text{FSI}}$, the FSI boundary between Ω_f and Ω_s is shown in dark red. The end faces of the ChP, $\partial\Omega_{\text{ChP end}}$ is shown in bright red in the 3D model, and also refers to the face of the ChP at the far end of the domain, hidden in this visualisation (curved arrows). The boundary $\partial\Omega_{\text{ChP end}}$ does not appear in the 2D model. In 3D, the base of the ChP,$\partial\Omega_{\text{ChP end}}$, is hidden under the red solid, but is visible in the 2D visualisation. In 3D $\partial\Omega_{\text{outlet}}$ is the distal end of the catheter tube. As discussed above, in 2D $\partial\Omega_{\text{outlet}}$ is the boundary where flow from the inlet holes enters the catheter interior. The boundary conditions at these locations are given

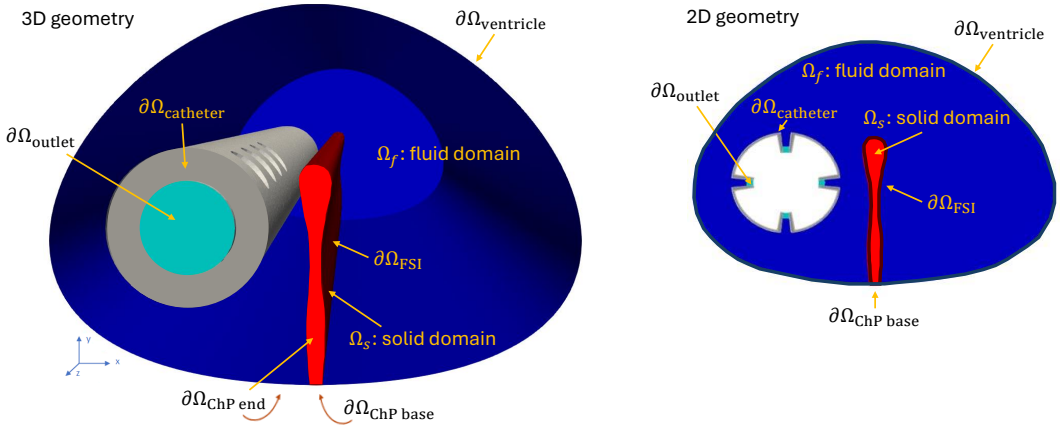

Figure 3.3: Geometry of the ventricle-catheter-ChP system, labelling the fluid and solid domains and all boundaries.

in Table 3.2.

As the most severe hydrocephalus condition is assumed here, where natural pathways out of the ventricles are blocked, a no-flux and no-slip fluid velocity condition is applied on $\partial\Omega_{\text{ventricle}}$, and separately on the impermeable catheter wall $\partial\Omega_{\text{catheter}}$:

$$\boldsymbol{v} = \mathbf{0} \quad \text{on} \quad \partial\Omega_{\text{ventricle}} \quad \text{and} \quad \partial\Omega_{\text{catheter}}. \tag{3.5}$$

The ChP surface, $\partial\Omega_{\text{FSI}}$, simultaneously acts as a fluid source (with total flux Q mm^3/s) into the ventricle domain, and as the deformable FSI boundary. It is assumed the new CSF created by the ChP is passed into the fluid domain in the direction normal to the surface of the ChP and uniformly across the ChP surface:

$$\boldsymbol{v} = \frac{Q}{A_{ChP}}\boldsymbol{n} \quad \text{on} \quad \partial\Omega_{\text{FSI}}, \tag{3.6}$$

where $\boldsymbol{n}$ is the unit normal to the ChP surface, of area A_{ChP}. The uniform velocity profile is motivated by research into the active transport mechanisms that ensure constant CSF production [31]. It has been well established that the CSF in the ventricular system has a production rate of 500-600 mL each day [15, 20, 7]; which is equivalent here to a total flux of $Q = 6$ mm^3/s. In the 2D model, the fluid flux out of the ChP boundary is adjusted so that the fluid flux out of the ChP per unit length is considered: $Q_{2D} = Q/L_z$.

Without loss of generality, the outlet fluid pressure is set to zero (for reference, *in vivo* reference pressure would be around 10 -15 mmHg [110]). *In vivo* CSF flows through the outlet boundary and continues into the rest of the shunt system. A sufficient length of catheter is included in the model away from inlet holes for the fluid to be assumed to be fully developed at the outlet. Therefore zero tangential velocity and continuity of normal stress is imposed on the outlet boundary:

$$\boldsymbol{v} - (\boldsymbol{v} \cdot \boldsymbol{n})\boldsymbol{n} = \boldsymbol{0}, \quad -p + \boldsymbol{n} \cdot \mu \left(\nabla \boldsymbol{v} + (\nabla \boldsymbol{v})^T\right) \cdot \boldsymbol{n} = 0 \ \text{ on } \ \partial\Omega_{\text{outlet}}, \tag{3.7}$$

The fluid stresses exerted on the solid boundary of the ChP by the CSF drives the solid deformation. Continuity of stress is imposed on the ChP boundary so that

$$\left(-p\mathbb{I} + \mu \left(\nabla \boldsymbol{v} + (\nabla \boldsymbol{v})^T\right)\right) \cdot \boldsymbol{n} = \boldsymbol{\sigma} \cdot \boldsymbol{n} \ \text{ on } \ \partial\Omega_{\text{FSI}}. \tag{3.8}$$

The solid problem is closed by imposing zero displacement along the base of the ChP, as biologically the ChP is rooted to the ventricles:

$$\boldsymbol{u} = \boldsymbol{0} \ \text{ on } \ \partial\Omega_{\text{ChP base}}. \tag{3.9}$$

The ChP extends out of the sub-domain of ventricle modelled, and hence the end-faces of the ChP, $\partial\Omega_{\text{ChP end}}$ are constrained to slip freely at the ventricle walls, imposing zero displacement in the direction normal to the end walls and zero tangential stress.

$$\boldsymbol{u} \cdot \boldsymbol{n} = 0 \text{ and } \ \boldsymbol{\sigma} \cdot \boldsymbol{n} - (\boldsymbol{n} \cdot \boldsymbol{\sigma} \cdot \boldsymbol{n})\boldsymbol{n} = \boldsymbol{0} \ \text{ on } \ \partial\Omega_{\text{ChP end}}. \tag{3.10}$$

Table 3.2 summarises the stress and velocity conditions enforced on each boundary region of the fluid and solid problems.

Problem	Boundary	Imposed conditions
Fluid	Choroid plexus	Imposed normal velocity and no slip.
	Catheter outlet	Continuity of normal stress and no tangential fluid velocity.
	Ventricle and catheter walls	No slip and no flux.
Solid	ChP base	Zero displacement.
	ChP end faces	Zero normal displacement and zero tangential stress.
	ChP fluid boundary	Continuity of stress.

Table 3.2: Boundary conditions for the simplified catheter domain.

3.3 Full equations

A non-dimensional analysis of these governing equations is performed for the characteristic scales in the hydrocephalus scenario (see Section A.1) which justifies the decision to neglect time-dependent effects ($\partial/\partial t \approx 0$) in both the fluid and solid governing equations.

The final set of equations is given below, with all variables summarised in

Table 3.3, and parameter values given in Table 3.1.

Fluid equations:

$$\nabla \cdot \boldsymbol{v} = 0, \quad \rho_f(\boldsymbol{v} \cdot \nabla)\boldsymbol{v} = -\nabla p + \mu \nabla^2 \boldsymbol{v} \ \text{ in } \ \Omega_f. \tag{3.11}$$

Solid equations:

$$\nabla \cdot \boldsymbol{\sigma} = \mathbf{0}, \quad \text{where} \quad \boldsymbol{\sigma} = \frac{E}{3(1-2\nu)}(J-1)\mathbb{I} + \frac{E}{2(1+\nu)}J^{-\frac{5}{3}}(\mathbb{B} - \frac{1}{3}(\text{tr}(\mathbb{B}))\mathbb{I}), \tag{3.12}$$

and $\mathbb{B} = (\mathbb{I} + \nabla \boldsymbol{u}) \cdot (\mathbb{I} + \nabla \boldsymbol{u})^T$ in Ω_s.

Fluid boundary conditions:

$$\boldsymbol{v} = \mathbf{0} \ \text{ on } \ \partial\Omega_{\text{ventricle}} \ \text{ and } \ \partial\Omega_{\text{catheter}}, \tag{3.13}$$

$$\boldsymbol{v} = \frac{Q}{A_{ChP}}\boldsymbol{n} \ \text{ on } \ \partial\Omega_{\text{FSI}} \tag{3.14}$$

$$\boldsymbol{v} - (\boldsymbol{v} \cdot \boldsymbol{n})\boldsymbol{n} = \mathbf{0}, \quad -p + \boldsymbol{n} \cdot \mu \left(\nabla \boldsymbol{v} + (\nabla \boldsymbol{v})^T\right) \cdot \boldsymbol{n} = 0 \ \text{ on } \ \partial\Omega_{\text{outlet}}. \tag{3.15}$$

Solid boundary conditions:

$$\boldsymbol{u} = \mathbf{0} \ \text{ on } \ \partial\Omega_{\text{ChP base}}, \tag{3.16}$$

$$\boldsymbol{u} \cdot \boldsymbol{n} = 0 \text{ and } \ \boldsymbol{\sigma} \cdot \boldsymbol{n} - (\boldsymbol{n} \cdot \boldsymbol{\sigma} \cdot \boldsymbol{n})\boldsymbol{n} = \mathbf{0} \ \text{ on } \ \partial\Omega_{\text{ChP end}}, \tag{3.17}$$

$$\left(-p\mathbb{I} + \mu \left(\nabla \boldsymbol{v} + (\nabla \boldsymbol{v})^T\right)\right) \cdot \boldsymbol{n} = \boldsymbol{\sigma} \cdot \boldsymbol{n} \ \text{ on } \ \partial\Omega_{\text{FSI}}. \tag{3.18}$$

Table 3.3: Variables within the full governing equations

Fluid velocity	$\boldsymbol{v}$	Solid displacement	$\boldsymbol{u}$
Fluid pressure	p	Solid stress tensor	$\boldsymbol{\sigma}$
Normal vector	$\boldsymbol{n}$	Solid Jacobian	$J = \det(\mathbb{I} + \nabla \boldsymbol{u})$

3.4 Computational methods

In this section the methods used to build the computational codebase to solve the FSI model are described. Finite element and finite volume methods (FEMs and FVMs) were reviewed in Section 2.3 and are well established for solving complex 3D fluid and solid problems. Four routines are combined to form the computational pipeline to solve the FSI model: meshing, fluid solver, solid solver and coupling code. The fluid and solid solvers draw from pre-existing codebases: `OpenFOAM` [179] for the fluid solver and `MuPhiSim` for the solid solver [170]. Meshes for both parts of the simulation are created in the `openCascade` suite of `gmsh` [176]. The FSI coupling was adapted from the methods in Ref. [169] which are tailored to accommodate the large deformation seen in soft biological tissues. This method is weakly coupled: the fluid and solid solvers are kept separate, and coupled only through the exchange of stress and (relaxed) displacement fields on their mutual boundary. Relaxation is a numerical technique to improve the computational stability of the framework and will be discussed below. A schematic of the computational framework is shown in Figure 3.4.

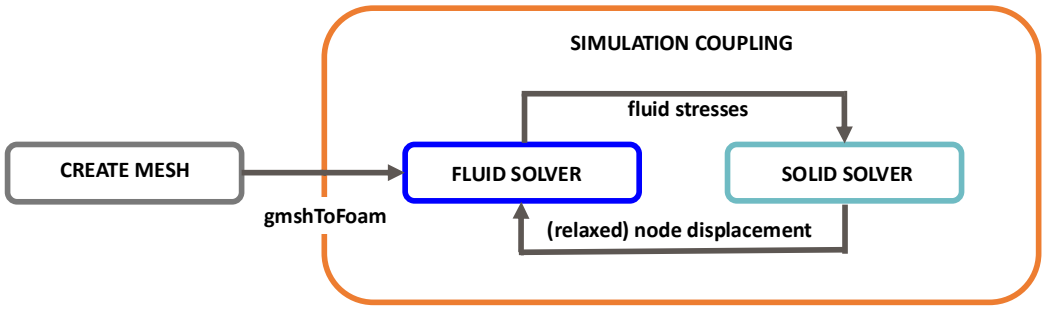

Figure 3.4: Schematic of computational FSI framework.

3.4.1 Meshing software: gmsh

To model a 3D volume (or 2D area) using FEMs or FVMs, the volume (or surface) needs to be broken down into elements which capture the domain geometry but are small enough that a linear or quadrilateral approximation captures the variation of a physical field across the element. The resulting "meshes" are typically composed of tetrahedra or hexahedra (equivalently, in 2D, triangles or quadrilaterals) though many other element types exist.

To create these meshes, the codebase `gmsh` [176] with the `openCascade` kernel [180] is used, as these softwares contain the ability to build or import model geometries and algorithms, and to create meshes from a given geometry. Full details of the mesh types and styles used, mesh quality analysis and mesh postprocessing are given in Section A.2.

In short, the geometry described in Section 3.1 is created in an ASCII file with .geo extension, separately for the fluid and solid domains. For a numerical solver to correctly interact with a geometry, labels must be given to all boundary surfaces to impose the correct boundary conditions on the correct surfaces. The labels are imposed by creating `Physical Surface` groups at the end of the .geo file. Each boundary condition is linked to one label. Multiple, disjoint boundary surfaces can be given the same physical label and this will impose the same boundary condition on all surfaces. Using this approach can be very useful: if a geometry has multiple outlet regions and only the total flux across all outlet is known, then all the outlet surfaces can be grouped under one label "outlet", and the total flux condition applied on this composite surface.

Internal meshing algorithms within `gmsh` are then used to create a conformal mesh. Conformal means that no elements overlap, a critical condition in creating a valid mesh. In this project the Delaunay algorithm [181] is used as it best captures the curved geometry of the biological surface. This creates tetrahedral elements for both the solid and fluid domains. As errors on the fluid validation study are over 10%, the mesh was transformed to its polyhedral dual using the `polyDualMesh` function of `OpenFOAM`. The mesh created is shown in Figure 3.5 showing both the fluid, subfigure a), and solid, subfigure b) meshes. Figure 3.5 c) shows the mesh refinement near the inlet holes on the surface of the catheter, with the smaller elements needed to capture the regions of high curvature near the inlet holes. A detailed discussion of the standard methods used in mesh creation, analysis and validation is given in Appendix A.2.

Further detail on the mesh styles available in `gmsh` and the mesh quality analyses are discussed in Section A.2.2 and A.2.3.

3.4.2 Fluid solver: OpenFOAM

Fluid modelling is a complex task and the choice of solver is highly dependent on the specific problem being addressed. `OpenFOAM` [179] is used for fluid simulations

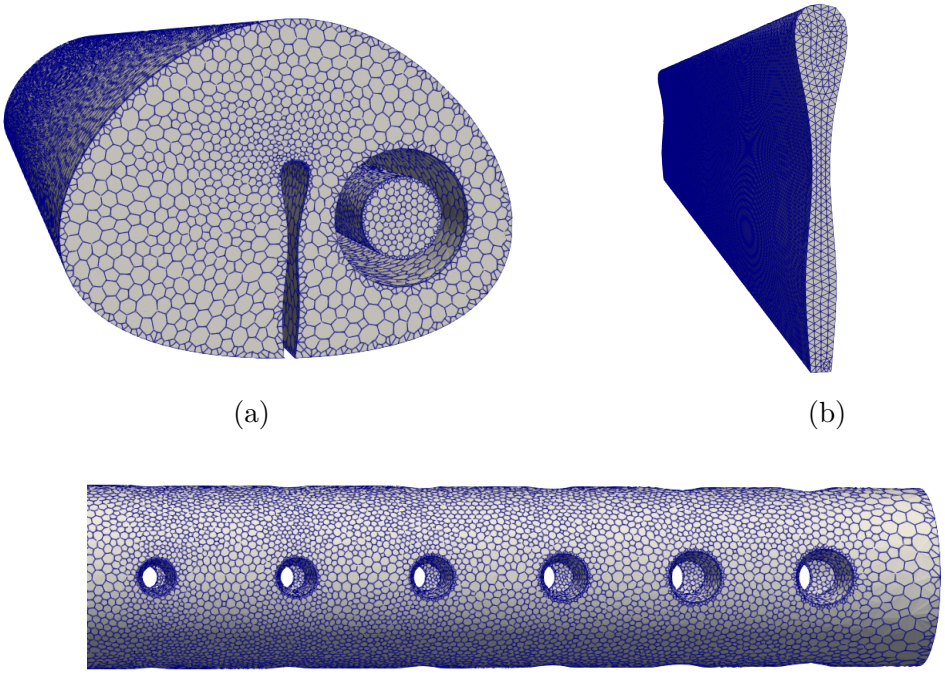

(a) (b)

(c)

Figure 3.5: Mesh visualisation of (a) the polyhedral fluid mesh, (b) the tetrahedral solid mesh and (c) close-up of mesh refinement near the inlet holes on the surface of the catheter.

as it is highly configurable and well established. In this section the setup for the fluid solver and the numerical methods used by `OpenFOAM` are discussed. To validate results from `OpenFOAM`, and to further justify the use of a time-independent solver, validation and time-independence studies are performed, and results given in Appendices A.4.1 and A.4.2. The time-independence study compared the results of a time dependent solver after sufficiently long time with results of the steady fluid solver, and showed, consistent with the non-dimensional analysis performed in Section A.1, the steady and time dependent flow profile results matched in the parameter regime being considered in this problem.

Appendix A.3 gives the folder structure and files needed to run a fluid simulation, and Algorithm 1 gives the commands that configure, initialise and run a fluid simulation. These commands are contained in the `run.sh` script placed in the fluid folder, allowing them to be executed automatically.

Algorithm 1 Commands to run a complete fluid simulation

`gmsh fluidGeometry.geo -3` ← use `gmsh` to create 3D fluid geometry and mesh with tetrahedra,
`gmshToFoam fluidMesh.msh` ← create an `OpenFOAM` compatible mesh structure from the fluid mesh,
`polyDualMesh 60 -overwrite` ← create a polyhedral mesh from the existing tetrahedral mesh and overwrite into the file structure,
if running in parallel on n cores **then**
    `decomposePar` ← subdivide domain into n self-contained sub-domains,
    `mpirun -np n simpleFoam -parallel` ← run the simulation on n cores,
    `reconstructPar` ← reconstruct the fluid domain from subdomain solutions,
else
    `simpleFoam` ← run the simulation on one core,
end if

3.4.2.1 SimpleFOAM algorithm

In Section A.1 the CSF is established as a incompressible, Newtonian, viscous fluid with constant density. The flows are steady and laminar (non-turbulent), which motivates the use of the `simpleFOAM` solver [182], the only time-independent, incompressible solver offered by `OpenFOAM`. `simpleFOAM` implements the SIMPLE (Semi-Implicit Method for Pressure Linked Equations) algorithm to solve static,

incompressible, Newtonian flow scenarios. `simpleFOAM` assumes a constant density throughout the fluid and consequently considers the kinematic pressure p/ρ_f, so that the fluid behaviour is controlled by only one physical parameter, the kinematic viscosity $\nu = \mu/\rho_f$. The equations to be solved are:

$$\nabla \cdot \boldsymbol{v} = \mathbf{0}, \tag{3.19}$$

$$(\boldsymbol{v} \cdot \nabla)\boldsymbol{v} = -\nabla \left(\frac{p}{\rho_f} \right) + \nu \nabla^2 \boldsymbol{v}. \tag{3.20}$$

The Navier-Stokes equations lead to four coupled equations for the four unknown variables (kinematic pressure and the three velocity components). However, numerical solvers are challenged by the fact that pressure never arises explicitly in the equation, only through a gradient, as the pressure field can be considered a Lagrange multiplier enforcing incompressibility on the velocity field. To obtain an equation for p/ρ_f, the `simpleFOAM` algorithm rearranges Equations (3.19) and (3.20). A brief overview of the `simpleFOAM` algorithm is given in Algorithm 2, with a complete description given in Ref. [183]. The first step discretises the system, introducing the vectors $\boldsymbol{V}$ and $\boldsymbol{p}$ contain the velocity and kinematic pressure in each of the finite volumes. For these vectors, Equation (3.20) takes the form

$$\boldsymbol{A} \cdot \boldsymbol{V} - \boldsymbol{H}(\boldsymbol{V}) = -\nabla_d \boldsymbol{p}, \tag{3.21}$$

where ∇_d is the discretised analogue of the gradient operator, the diagonal matrix $\boldsymbol{A}$ is independent of $\boldsymbol{V}$ and $\boldsymbol{p}$, and $\boldsymbol{H}$ is a matrix function of $\boldsymbol{V}$ that contains the non-linear terms of the momentum equation. As a diagonal, non-singular matrix $\boldsymbol{A}$ can be easily inverted to give an explicit expression for $\boldsymbol{V}$:

$$\boldsymbol{V} = \boldsymbol{A}^{-1}(-\nabla_d \boldsymbol{p} + \boldsymbol{H}(\boldsymbol{V})). \tag{3.22}$$

From mass conservation $\boldsymbol{V}$ has no divergence and so:

$$\nabla_d \cdot (\boldsymbol{A}^{-1}(\nabla_d \boldsymbol{p})) = \nabla_d \cdot (\boldsymbol{A}^{-1}\boldsymbol{H}(\boldsymbol{V})). \tag{3.23}$$

This is the pressure Poisson equation and is an inhomogeneous elliptic equation for $\boldsymbol{p}$ with a known $\boldsymbol{V}$. This formulation inherently preserves mass conservation, but represents the pressure and velocity fields in each element with a single value for each value, meaning that there are inherently discontinuities in the physical fields between neighbouring elements.

Algorithm 2 Sketch code for `simpleFOAM` solver

Initially set $\boldsymbol{V}_0 = \boldsymbol{0}$ and $\boldsymbol{p}_0 = \boldsymbol{0}$ everywhere,
while Not converged **do**
  Use Equation (3.22) to update $\boldsymbol{V}_{\text{new}} = \boldsymbol{A}^{-1}(-\nabla_d \boldsymbol{p}_{\text{old}} + \boldsymbol{H}(\boldsymbol{V}_{\text{old}}))$,
  Solve Equation (3.23) for $\boldsymbol{p}_{\text{new}}$ in terms of $\boldsymbol{V}_{\text{new}}$,
  Apply relaxation factors to assist convergence.
end while

3.4.2.2 Numerical parameters

To ensure the `simpleFOAM` algorithm produces an accurate and complete solution, several choices of numerical parameters and numerical methods need to be made. These are contained in the files `fvSchemes` and `fvSolutions`. `fvSchemes` stores the numerical methods used to calculate the derivatives of the velocity and pressure fields, see Appendix A.3. These methods need to be chosen carefully, accounting for the local mesh structure, but for most derivatives the default Gaussian schemes used by `OpenFOAM` are sufficient. However in the gradient calculation the `leastSquares` scheme is used as this is far more accurate when calculating gradients on unstructured meshes [184]. The `leastSquares` method takes an average over neighbouring cells, and hence has a higher accuracy when elements have a high number of neighbours, which is true of the polyhedral mesh.

The numerical tolerances are applied to the residuals of the individual steps of the `simpleFOAM` algorithm, and need to be satisfied for that step to be considered converged. Each step of the `simpleFOAM` algorithm solves a matrix system $\boldsymbol{A} \cdot \boldsymbol{x} = \boldsymbol{b}$ for some matrix $\boldsymbol{A}$ and vectors $\boldsymbol{b}$, $\boldsymbol{x}$ where $\boldsymbol{x}$ is unknown. This system is solved using iterative methods which are cheaper than matrix inversion, and the residual is defined as $\boldsymbol{b} - \boldsymbol{A}\boldsymbol{x}_{\text{sol}}$ for a current proposed solution vector $\boldsymbol{x}_{\text{sol}}$. Here, the tolerances are set to an absolute tolerance of 10^{-6} and relative tolerance of 10^{-3}. The absolute tolerance is normalised by the average value of the field being calculated, making both tolerance values dimensionless. Relaxation factors are used to scale the update to the pressure and velocity fields to ensure smoother convergence and are kept at the standard values of 0.3 for pressure and 0.7 for velocity. The restrictions on the pressure field are usually tighter than those on the velocity, as the `simpleFOAM` algorithm calculates velocity as an explicit function of pressure.

A suitably large bound on the number of allowed iterations is set at 2500, ensuring that the convergence is attained. Two non-orthogonal corrector loops are incorporated for the pressure equation to correct for the shape of mesh elements (last step of Algorithm 2) [184].

3.4.2.3 Boundary conditions

`simpleFOAM` requires a boundary condition (or a consistent placeholder) on every boundary, for both (kinematic) pressure and velocity. It is important to emphasise that this does not overprescribe the mathematical problem, but is necessary as the `simpleFOAM` solver reforms the governing equations as an elliptic equation for pressure, an equation form that requires conditions on every boundary. In many cases the condition is a placeholder, which directs the solver to look to the other field for the true condition.

Table 3.4 gives the boundary conditions imposed on the fluid solver, defined by a keyword designating the boundary type and a second line giving additional information about the boundary condition. These boundary conditions give the same mathematical system as Table 3.2.

Table 3.4: Boundary conditions used in the `OpenFOAM` solver.

Boundary	Pressure	Velocity
ChP surface	`fixedFluxPressure`	`flowRateOutletVelocity` `volumetricFlowRate constant 6`
Catheter outlet	`fixedValue` `value uniform 0`	`pressureInletOutletVelocity` `tangentialVelocity uniform (0 0 0)`
Ventricle and catheter walls	`fixedFluxPressure`	`noSlip`

The `noSlip` velocity condition on the ventricle and catheter walls imposes a zero value of the velocity at the surface, and similarly the `fixedValue` condition

sets the pressure value to 0 on the catheter outlet. `flowRateOutletVelocity` imposes a set total outflux from the surface, here the `volumetricFlowRate` keyword is used to prescribe the total volumetric outflux in mm^3/s. Without any further keywords, `flowRateOutletVelocity` imposes the velocity uniformly over the surface and in the normal direction to the surface.

`fixedFluxPressure` is the complementary condition imposed on kinematic pressure when the velocity field is known. This condition combines Equation (3.22) with the known velocity on the boundary to derive an expression for the pressure gradient at the wall in terms of the known velocity on this boundary. This ensures the solution to the pressure Poisson equation is compatible with an incompressible velocity field.

Similarly, `pressureInletOutletVelocity` is the complementary condition for the velocity at an inlet or outlet when the pressure value is known, and is equivalent to $\partial \boldsymbol{v}/\partial \boldsymbol{n} = 0$.

3.4.3 Solid solver: MuPhiSim

The deformation of the ChP is simulated in `MuPhiSim`, an in-house FEM codebase specialising in large deformations [170]. A tetrahedral mesh is used for the ChP solid model, taking advantage of the ability of tetrahedra to capture curved geometry. However, non-quadratic tetrahedral elements can be problematic in incompressible solid simulations, motivating the use of a compressible formulation with high, but < 0.5, Poisson's ratio. Here, the ChP is modelled with a compressible formulation and Poisson's ratio 0.45 to improve numerical stability. A validation study for this mesh style is presented in Appendices A.4.3 and A.4.4.

3.4.3.1 Large deformation FEM

The following gives a brief description of the methods used by `MuPhiSim` to solve for the solid problem with no body forces, with a full description given in Ref. [185], or in the `MuPhiSim` documentation available at `https://github.com/muphisim`. Solid deformation problems seek to find the map between the initial configuration of the solid, given by $\boldsymbol{X}$ and the current configuration $\boldsymbol{x} = \boldsymbol{x}(\boldsymbol{X})$.

The displacement vector of a point used in the governing Equation (3.3) is $\boldsymbol{u} = \boldsymbol{x} - \boldsymbol{X}$. The deformation gradient $\boldsymbol{F} := \partial \boldsymbol{x}/\partial \boldsymbol{X}$ is hence related to the

displacement vector by $\boldsymbol{F} = \mathbb{I} + \nabla_{\boldsymbol{X}} \boldsymbol{u}$ where the subscript on $\nabla_{\boldsymbol{X}}$ indicates the gradient is being taking with respect to coordinates in the initial configuration.

Here, the stress as presented in Equations (3.3) is designated by the Cauchy stress $\boldsymbol{\sigma}$, related to the first Piola-Kirchhoff stress $\boldsymbol{P}$ by $\boldsymbol{\sigma} = (\det \boldsymbol{F})^{-1} \boldsymbol{P} \boldsymbol{F}^{\boldsymbol{T}}$.

In short, `MuPhiSim` considers the weak form of the solid governing equations, looking at possible perturbations $\boldsymbol{\eta}$ to the deformation vector $\boldsymbol{x}$. Known shape functions related to each mesh element e are then used to approximate $\boldsymbol{x}$ and $\boldsymbol{\eta}$ in each element by

$$\boldsymbol{x}^e = \sum_{a \in \text{ element } e} N_a^e(\boldsymbol{\xi}^{\boldsymbol{e}}) \boldsymbol{x}^a, \quad \boldsymbol{\eta}^e = \sum_{a \in \text{ element } e} N_a^e(\boldsymbol{\xi}^{\boldsymbol{e}}) \boldsymbol{\eta}^a \tag{3.24}$$

where $\boldsymbol{x}_a$ is the position of node a in element e and $N_a^e(\boldsymbol{\xi}^{\boldsymbol{e}})$ is the polynomial shape function approximation for new coordinates $\boldsymbol{\xi}^e$ also specific to the element. Here the linear tetrahedral meshes use linear equations for the shape functions.

Combining the shape functions with the weak form of the governing equation gives

$$\sum_e \sum_{a,b \in e} \left(\int_{\Omega_0^e} \rho_{s,0} N_a^e N_b^e dV \right) \frac{d^2 \boldsymbol{x}^a}{dt^2} \cdot \boldsymbol{\eta}^b + \sum_e \sum_{b \in e} \int_{\Omega_0^e} (\boldsymbol{P} \cdot \boldsymbol{\nabla}_{\boldsymbol{X}} N_b^e) \cdot \boldsymbol{\eta}^b \, dV \tag{3.25}$$

$$= \sum_e \sum_{b \in e} \int_{\partial \Omega_{0,n}^e} N_b^e \boldsymbol{T} \cdot \boldsymbol{\eta}^b \, dS, \tag{3.26}$$

where a, b index nodes in element e. Traction boundary conditions are captured by $\boldsymbol{T}$, and the 0 subscript in $\rho_{s,0}$ indicate this is the solid density in the initial configuration.

As discussed above, solid problems are closed by imposing a constitutive relation $\boldsymbol{\sigma} = \boldsymbol{\sigma}(\boldsymbol{u})$ or $\boldsymbol{P} = \boldsymbol{P}(\boldsymbol{F})$. This relation must hold for all admissible displacements at all nodes $\boldsymbol{\eta}_b$, and hence Equation (3.25) looks to find values $\boldsymbol{x}^a$ such that

$$\sum_e M_{a,b}^e \frac{d^2 \boldsymbol{x}^a}{dt^2} + \sum_e f_b^{e,\text{int}}(\boldsymbol{x}^a) = \sum_e f_b^{e,\text{ext}} \tag{3.27}$$

is true for all b. Here,

$$M_{a,b}^e = \sum_{a \in e} \int_{\Omega_0^e} \rho_{s,0} N_a^e N_b^e dV, \; f^{e,\text{int}} = \int_{\Omega_0^e} \boldsymbol{P} \cdot \boldsymbol{\nabla}_{\boldsymbol{X}} N_b^e \, dV \text{ and } f^{e,\text{ext}} = \int_{\partial \Omega_{0,n}^e} N_b^e \boldsymbol{T} \, dS.$$

$f^{e,\text{int}}$ gives the interior stresses in element e arising from the constitutive relation, and $f^{e,\text{ext}}$ gives the stresses arises from the traction boundary conditions.

These, alongside $M^e_{a,b}$, are calculated from the known shape equations, giving a matrix system to solve for $\boldsymbol{x}^a$.

The static formulation of the problem is then

$$\sum_e f_b^{e,\text{int}}(\boldsymbol{x}^a) = \sum_e f_b^{e,\text{ext}} \tag{3.28}$$

with all variables defined as above.

3.4.3.2 Static and dynamic solvers

The dynamic and static versions of the problem use different numerical methods to find their solution, either iterating to converge on the equilibrium solution (in the static case), or solving the system at each time point using an implicit Newton-Raphson algorithm (in the dynamic case). A full description of the processes can be found in the appendix of the `MuPhiSim` documentation [170]. Here, it suffices to remark that dynamic solvers have the advantage of being more numerically stable than static solvers due to the influence of the time step dt, which appears as a $1/dt$ component on the diagonal of the matrix $\boldsymbol{M}$, increasing the relative weight of the diagonal, and making the matrix more stable during the inversion procedure.

For this reason, the dynamic solver is sometimes used instead of the static solver in this project, when large deformation of the ChP leads to the static solver not converging. The dynamic solver has time dependence, and in this case the solid solver was run for time steps of 0.1 s for time between 0 and 100 s. These time values were chosen as sufficiently long in comparison to the natural timescale or internal elastic oscillations, making dynamic effects negligible. The static and dynamic methods are compared in Appendix A.4.4 and are shown to be indistinguishable for these choices of time parameters, ensuring this is a quasi-static implementation of the dynamic solver.

3.4.4 Fluid-structure interaction coupling

The FSI coupling algorithm that combines the solvers `OpenFOAM` and `MuPhiSim` is now introduced. Existing FSI frameworks such as preCICE [186] can be configured to couple the `OpenFOAM` and `MuPhiSim` solvers, but struggle to numerically converge in scenarios where the fluid and solid densities are similar [187], or when the solid deformation is large. Both are the case in the hydrocephalus scenario,

and hence the static nature of the problem is leveraged in the creation of a new coupling code which solves for the equilibrium configuration of the hydrocephalus system. This codebase containing the FSI coupling is presented as an application in the `MuPhiSim` repository `https://github.com/muphisim`.

The overall approach of the FSI framework, described below in detail, is shown in Figure 3.4. The method is weakly coupled and partitioned, keeping the fluid and solid solvers self-contained and independent within the simulation. The solid and fluid regions are distinct and coupled through their common boundary, the ChP surface, over which stress or displacement data are passed iteratively. The simulation solves for the equilibrium state of the FSI system. Intermediate iterations are therefore non-physical, with only the last, converged iteration having a physical interpretation as the equilibrium state of the FSI system.

At each iteration, the equilibrium state of, first, the fluid and then the solid system is found for the current domain boundaries (fluid part) or FSI boundary condition stress (solid part). This equilibrium state then produces the updated condition on the FSI boundary that will be passed to the next solver. The full system is considered converged when the update to the displacement field of the solid part is below a relative tolerance, here set to 0.01. A relaxation factor, ω, scales the update to the solid displacement field to improve numerical convergence. A value of 0.5 is used for ω in the majority of simulations presented, which balances computational speed with numerical stability. Simulations are scrutinised to ensure that there are no numerical oscillations and the system has converged smoothly to its true equilibrium. If such oscillations are detected then the simulation is rerun with a lower value $\omega = 0.25$, which in all cases was sufficient to see smooth convergence to equilibrium. A sketch of the coupling algorithm is given below in Algorithm 3.

3.4.4.1 Novel coupling method

The FSI coupling mechanism is adapted from the methods used in Ref. [169], which consider the 2D scenario of airflow past an aerofoil. To adapt this method to the hydrocephalus scenario three adjustments needed to be made:

- adapt the method to 3D,
- impose a non-trivial source condition on the FSI boundary,

Algorithm 3 Sketch code for the FSI simulation

$\omega \leftarrow$ relaxation factor ($\omega \leq 1$),
Create a list of points describing the FSI boundary,
while Not converged **do**
    Build solid and fluid geometries using boundary points,
    Run fluid simulation in `simpleFOAM`,
    Extract fluid pressure and stress at the boundary nodes,
    Impose stress boundary condition on the FSI interface,
    Run solid simulation in `MuPhiSim` with stress boundary conditions,
    Extract the deformed positions of the boundary nodes.
    Boundary nodes positions are scaled by ω and updated.
    The maximum change in position is calculated, and compared to the convergence tolerance = 0.01.
end while

- incorporate viscous fluid stresses.

The FSI boundary is generated by first creating a suitably small mesh with `gmsh` from the idealised geometry file. In Ref. [169], the boundary is a 1D closed loop and an ordered list of boundary nodes is used to track nodal connectivity. The deformation of the boundary nodes combined with nodal connectivity information gives the deformed FSI boundary. To extend this method to 3D, the list of elements creating the FSI surface is stored, and the nodes creating each surface element are saved. This stores the nodal connectivities, and tracking the displacements of these nodes during solid deformation allows the position of the boundary to be tracked.

In this model, the ChP surface is a source of CSF into the fluid domain, in addition to acting as the interface boundary between solid and fluid components. In a dynamic simulation, the fluid velocity imposed on the ChP surface would need to incorporate the velocity of the moving boundary as well as the flux from the source term. In this coupling method all parts of the domain are assumed to have achieved their static equilibrium and hence the velocity of the boundary is $\mathbf{0}$. Therefore, it is sufficient to impose only the CSF outflux as the fluid boundary condition on the ChP surface.

In the aerofoil work of Ref. [169], viscous stresses are negligible and the deformation of the solid is driven by pressure. In the hydrocephalus scenario, viscous stresses are significant and so it is important to include both effects. Thus,

the fluid stresses from `OpenFOAM` are extracted, and drive the solid deformation through the novel stress boundary condition discussed in Section 3.4.4.3.

The coupling code is written in `python3`. For reference, it is included as the example "`py-FSI-3D`" in `MuPhiSim`, accessible at `https://github.com/muphisim`. To test the accuracy of this code a validation study was completed, replicating a benchmark problem considering flow through a deformable pipe (results given in Appendix A.4.5).

3.4.4.2 Extracting the fluid stress field

In the FSI model, fluid stresses on the boundary of the ChP drive the solid deformation. The weakly coupled FSI solver therefore requires the stress field on the surface of the ChP to be extracted from the `simpleFOAM` solver. The fluid stress field is defined as $(-p\mathbb{I} + \mu(\nabla \boldsymbol{v} + (\nabla \boldsymbol{v})^T)$.

`OpenFOAM` contains functionality to extract the pressure of each element on a given boundary surface. This is implemented in the `functions` dictionary of the `system/controlDict` file. `OpenFOAM` does not have an in-built function to calculate the full stress tensor, and hence a specific extraction code was written to extract the value of $\mu(\nabla \boldsymbol{v} + (\nabla \boldsymbol{v})^T)$ at any boundary surface. It is possible to write novel code in a separate local folder, which is then compiled, and dynamically linked to the `simpleFOAM` run folder with the command `libs ("libstressTensor.so")`, written in the `system/controlDict` file. To keep all the fluid code contained within one folder, here the stress tensor extraction was written directly into the `functions` dictionary of the `system/controlDict` file. While this implementation required the stress extraction code to be recompiled every time it is used, the compile time is on the order of seconds, and consequently does not significantly affect the overall run time of the FSI model.

3.4.4.3 Solid boundary condition

For each iteration of the weakly coupled FSI methodology, the solid deformation resulting from the fluid stress field on the FSI boundary, $\boldsymbol{\sigma}_{FSI} := -p\mathbb{I} + \mu\left(\nabla \boldsymbol{v} + (\nabla \boldsymbol{v})^T\right)$ is found. To correctly solve this problem, in each solid iteration the solid starts in its initial, relaxed state, and its equilibrium displacement under the current fluid stress field are found. There may be large deformations between

the relaxed and equilibrium positions of the ChP, meaning that the normal vector to the ChP surface $\boldsymbol{n}$ changes significantly as the solid solver converges to equilibrium.

The FSI boundary condition is imposed via a prescribed stress tensor: $\boldsymbol{\sigma}_{FSI} \cdot \boldsymbol{n}$ on the ChP surface. This incorporates both the viscous stress components and the effect of large changes in the normal vector throughout the deformation.

The Cauchy stress in the current configuration $\boldsymbol{\sigma}$, is related to the first Piola-Kirchhoff stress in the initial configuration $\boldsymbol{P}$ (used in the solid solver) via $\boldsymbol{\sigma} = J^{-1}\boldsymbol{P}\boldsymbol{F}^{\boldsymbol{T}}$.

To impose this condition, a new boundary condition was required in `MuPhiSim`, written in the `src/solvers/classNeumannBCs` file. This class requires six numerical values that define the symmetric Cauchy stress tensor, automatically computes the current normal vector of the solid surface to find the traction vector $\boldsymbol{\sigma}_{FSI} \cdot \boldsymbol{n}$ and applies this vector in the Neumann traction condition.

3.4.5 Computation

For the simulations in this project, the code was run on a combination of i7 core laptop and university cluster with 60 CPU cores. The 2D model did not need to be parallelised because of its efficiency, with each fluid-solid coupling iteration taking $\sim$20 s. The fluid and solid simulations within the 3D model were parallelised over six cores to speed up runtime as a full simulation takes over 24 hours. Six cores were chosen to maximise efficiency while allowing multiple independent simulations to be run concurrently on the cluster. The coupling between the fluid and solid simulations is kept on one core for simplicity as coupling takes significantly less time than the solid and fluid simulations.

Investigating the run time of each component of Algorithm 3 for the 3D model showed that the slowest steps by far were the solid simulation (75% of runtime), followed by the fluid remeshing step (20% of runtime). In contrast, the fluid simulation took $< 1\%$ of runtime.

3.4.6 Visualisation and data extraction: ParaView

Visualisation of the model output was done in `ParaView` [188]. `ParaView` was also used for data extraction, configured and automated using python-like scripts which must be executed through `ParaView`'s in-house version of python, `pvpython`.

3.5 Chapter summary

This chapter introduces a model for the hydrocephalus ventricle-catheter-ChP system. While idealised, the model incorporates all key biological components: CSF, ChP, ventricle and the catheter. Model parameters were selected based on established literature values or chosen within biologically plausible ranges. When exact values were uncertain, a parameter sensitivity study was conducted, which demonstrated that the model consistently preserved the ranking of different catheter designs across the range of parameters considered.

The second part of the chapter presents the computational framework used to determine the model's equilibrium configuration. The FSI framework consists of four components: the fluid solver, solid solver, meshing, and coupling. Each of these components is discussed in detail, with attention given to numerical considerations affecting accuracy.

Validation studies for the fluid, solid, and FSI solvers (detailed in the Appendices) confirm the accuracy of the individual solvers and the overall codebase. With this validation, the FSI model can be used to simulate ChP deformation in an idealised hydrocephalus scenario.

Chapter 4

FSI model results

The framework presented in Chapter 3, the "full model" component of the optimisation methodology, Figure 3.1, is used in this chapter. These FSI simulations allow for an examination of the detailed flow structures and solid deformation in the ventricle-catheter-ChP environment during hydrocephalus. Two existing catheter designs manufactured by Codman® [51], along with the design proposed by Weisenberg [15] are considered. The Codman® designs were chosen as they are routinely used in the UK National Health Service and have two very different hole configurations. Weisenberg's design, which aims to take in the same quantity of CSF through each inlet hole, was chosen as it is similar in style to Medtronic's Rivulet catheter, currently in clinical use, and was created through a computer-guided design process combining an optimisation sweep with CFD methods [15].

For the design of Codman catheter A, the FSI simulation is visualised, with results from different subdomains of the ventricular-catheter-ChP system highlighted. Various quantitative metrics which could be used to assess catheter performance are introduced and discussed. A selection of these metrics are then evaluated for each existing catheter design for a range of rotation angles of the catheter about its centre axis.

In particular, the maximum equilibrium ChP deflection is computed. This quantity is of particular interest, as designs that produce equilibrium ChP positions close to the catheter are more likely to result in blockage, whereas designs maintaining greater separation are less susceptible. The model neglects additional biological processes such as growth and cell adhesion, which would further increase the likelihood of blockage when the ChP approaches the catheter. In

particular, configurations in which the ChP comes into direct contact with the catheter are treated as worst-case scenarios. A design that results in less ChP deflection across the range of rotation angles is considered a better design within the framework of this model.

The 3D FSI model contains all the detail of the ventricle-catheter-ChP domain, but has a long runtime of $\geq$3 days. This motivates the development of a geometrically reduced-order model (ROM) considering a 2D cross-section of the 3D domain. This ROM neglects axial effects occurring along the centreline of the catheter, but has a significantly reduced computational time and maintains the key FSI mechanism. The 2D ROM is used to systematically explore the space of hole parameters (size and circumferential position), and shows that a high number of large, equally sized holes positioned uniformly around the circumference of the catheter lead to the minimum ChP deflection. Results from this ROM are compared to the full 3D FSI model in Appendix B.1, and shown to quantitatively agree.

Results from the 2D parameter sweep are consequently used to motivate a new 3D design, which is then modelled in the 3D FSI model, and the resulting equilibrium ChP deformation is compared to results using the three existing designs. Selected material from this chapter is published in Ref. [50] by Hayman et al.

4.1 Existing designs

Codman's catheter A, shown in Figure 4.1 a), has ten axial rows of holes with two holes in each row, where the holes are positioned circumferentially opposite each other. Each row contains one large hole and one small hole, diametrically opposite, with rows offset along the catheter length. Codman's catheter B, also shown in Figure 4.1 a), has holes positioned much closer along the axis of the catheter, with each of the ten axial rows containing four holes each: two large, two small. Rows are again offset, so that large and small holes alternate along the catheter axis. The example catheters were examined with a focus-variation Alicona microscope to obtain measurements of hole diameter to the nearest 10 µm, see Table 4.1. Weisenberg's design parameters are given in page 68 of Ref. [15] and feature six rows of holes with four equally spaced holes per row. Holes on

each row have the same radius, and the radius decreases along the catheter with holes at the tip having the largest radius.

Table 4.1: Existing catheter design model parameters.

Catheter example	**Catheter diameter**	**Largest hole diameter**	**Smallest hole diameter**
Catheter A	Outer diameter: 2.77 mm Inner diameter: 1.43 mm	0.97 mm	0.61 mm
Catheter B	Outer diameter: 2.50 mm Inner diameter: 1.27 mm	0.80 mm	0.50 mm
Weisenberg	Outer diameter: 2.70 mm Inner diameter: 1.5 mm	0.85 mm	0.524 mm

4.1.1 3D simulation visualisation

The 3D FSI model enables visualisation of the detailed flow structures and ChP deformation arising during the simulation. Figure 4.2 examines Catheter A, focusing on the region near the inlet holes. Different panels in the figure show the range of information that can be extracted and quantified from the 3D model. Figure 4.2 a) shows the equilibrium deformation of the ChP. The "tip" of the ChP, defined as the set of points satisfying $x = 0, y = 3.5$mm in the undeformed configuration, is indicated by a gold line. The maximum displacement of the ChP occurs at this tip in the vicinity of the holes closest to the outlet (red colour). Figure 4.2 c) shows the displacement along the ChP tip, plotting both the magnitude of the displacement field, $|\boldsymbol{u}|$ and its x-component, $\boldsymbol{u} \cdot \boldsymbol{e}_x$. The close agreement between these curves indicates that deformation is predominantly in the x direction, with negligible contributions in y and z. The results also show that the ChP comes into contact with the catheter for all points with $z > 15$ mm (red markers). The ChP moves slightly away from the catheter for $z < 4$ mm, and here $|\boldsymbol{u}| \approx -\boldsymbol{u} \cdot \boldsymbol{e}_x$. While it is positive to see the ChP moving away from

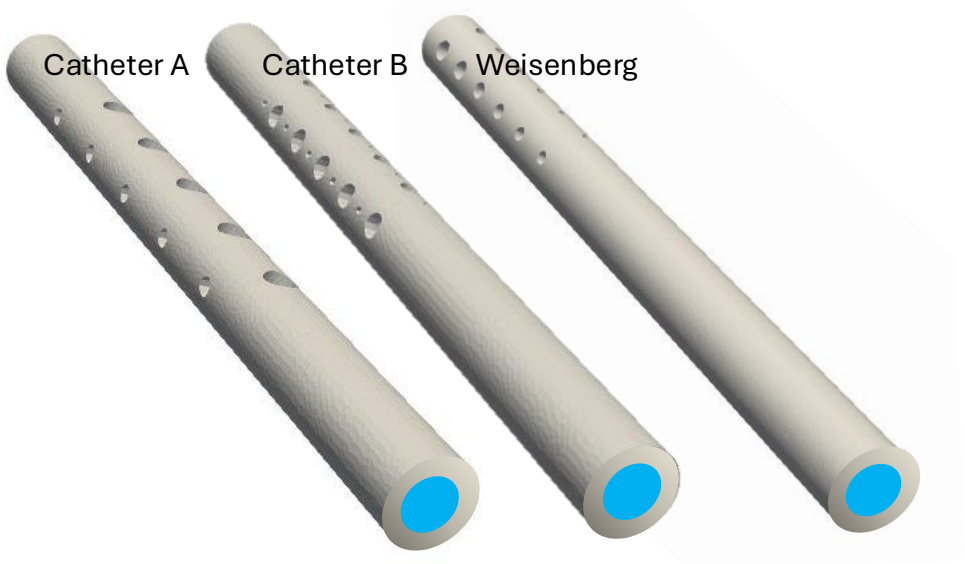

Figure 4.1: Geometries of existing catheter designs. Image adapted from Ref. [50], reproduced under a Creative Commons Attribution 4.0 International License (CC BY 4.0 [32]).

the catheter, the blockage of holes near the closed tip of the catheter is less of a concern as the remaining downstream holes are still able to take in CSF. In contrast, the large deformation towards the outlet holes suggests blockage at these downstream holes is likely, which will cause the catheter to stop working entirely if they block. To further quantify this risk, the minimum distance between the ChP surface and the catheter holes can be evaluated. In this case, parts of the ChP overlap with a catheter hole, giving a minimum distance of 0 mm, suggesting a high likelihood of potential blockage.

Figure 4.2 b) shows the pressure field and the axial fluid flux ($:= \int\int_{x,y} \boldsymbol{v} \cdot \boldsymbol{e_z}, dx, dy$) along the centreline of the catheter. Jumps in the flux curve indicate the axial positions of the inlet holes; the magnitude of each jump corresponds to the influx of fluid entering the catheter at that location. Holes closer to the outlet (at $z = 30$ mm) draw a greater proportion of the total influx. A total of 6 mm^3/s enters the domain from the ChP, and, due to incompressibility and the static domain of each fluid iteration, the same flux exits through the catheter outlet. In this case, the holes nearest the outlet, at $z = 25.4$ mm, admit a flux of 2.16 mm^3/s, accounting for over one third of the total influx.

The mean and standard deviation of the influx across the ten axial rings of

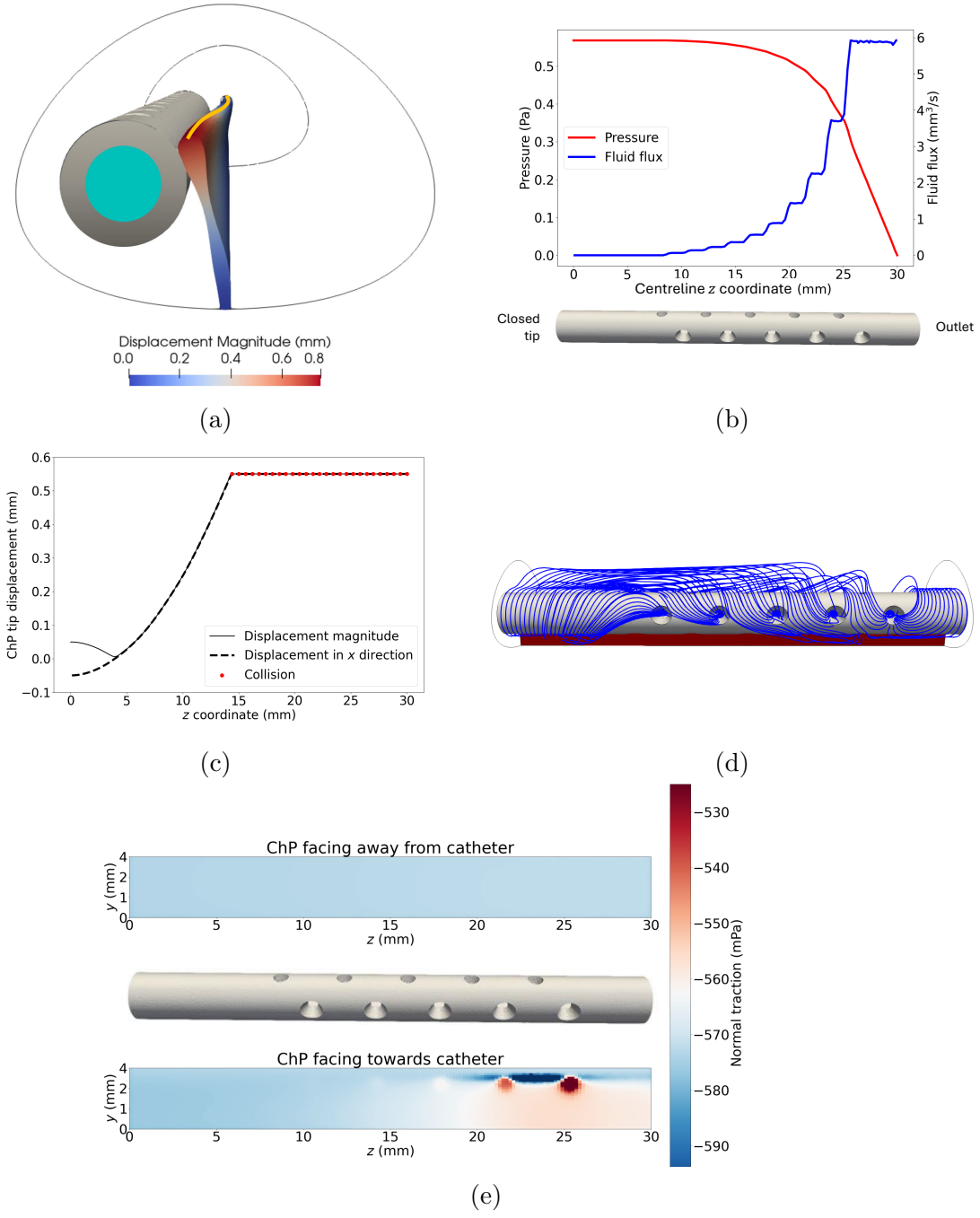

Figure 4.2: (a) Equilibrium configuration of ventricle-catheter environment, view into ventricle domain from outlet. (b) Fluid flux and pressure along the centreline of the catheter. (c) Displacement of the tip of the ChP, showing both the magnitude (solid line), and the displacement in the x direction (dashed line). (d) Side view of the ventricle-catheter domain, with selected streamlines shown entering the catheter holes. (e) Normal traction exerted by the fluid on the surface of the ChP, showing both the faces towards (upper) and away from the catheter (lower). Image reproduced from Ref. [50] under a Creative Commons Attribution 4.0 International License (CC BY 4.0 [32]).

inlet holes are 0.586 mm^3/s and 0.706 mm^3/s, respectively. For comparison, an equal influx into each axial ring of holes would yield (6 mm^3/s) / 10 = 0.6 mm^3/s per ring, which is close to the mean value obtained. However, the large standard deviation highlights the strong non-uniformity in influx evident in Figure 4.2 b). Previous studies have emphasised redistributing flux across axial hole bands, making the standard deviation of influx a key performance metric. This catheter design performs poorly under both criteria, exhibiting both large ChP deformation and highly non-uniform inlet flux.

The imbalance in influx is due to the pressure in the catheter interior dropping from ∼0.6 Pa at the closed tip to the reference pressure of 0 Pa at the outlet end. The pressure away from the catheter in the ventricle domain is approximately uniform (and comparable to the pressure at the closed tip) and so there is a greater pressure difference over the catheter holes near the outlet, driving the flow of fluid. Figure 4.2 c) shows selected streamlines in the ventricle-catheter-ChP domain. Again, a greater number of streamlines can be seen entering to inlet hole closest to the outlet (right), consistent with the graph of Figure 4.2 b).

It is also of interest to evaluate the fluid stress field exerted on different parts of the domain, as this field underpins the dominant FSI mechanisms: fluid stresses acting on the ChP surface drive its deformation. In Figure 4.2 e), the normal component of the fluid stress vector (referred to here as the normal traction), $\boldsymbol{n} \cdot \left(-p\, \boldsymbol{n} + \mu \left(\nabla \boldsymbol{v} + (\nabla \boldsymbol{v})^\top\right) \cdot \boldsymbol{n}\right)$ is visualised on the ChP surface. Dark blue regions indicate lower values of the normal traction on the surface of the ChP, and the ChP will deform away from regions. Analogously, red values indicate higher values of normal traction and the ChP will deform towards these regions. Dark blue regions on the side of the ChP facing the catheter lead to ChP deformation towards the catheter, which is undesirable. On the surface of the ChP facing away from the catheter, the traction is spatially uniform and dominated by the pressure contribution, $-p$, which is itself approximately homogeneous. In contrast, on the side facing the catheter, the normal traction exhibits significant spatial variation, with extreme values localised near the inlet holes, particularly those closest to the outlet. The pressure on the near side of the ChP ranges between 500 and 701 mPa, while the viscous contribution, $\boldsymbol{n} \cdot \left(\mu \left(\nabla \boldsymbol{v} + (\nabla \boldsymbol{v})^\top\right) \cdot \boldsymbol{n}\right)$ lies between -3.76 and 3.03 mPa. This indicates that, although viscous stresses contribute to the local structure of the traction field, the overall the normal traction is strongly pressure dominated.

Tracking intraventricular pressure is a key objective in the study of hydrocephalus, as excess CSF can lead to dangerous increases in intracranial pressure. In the model, the reference pressure is set to 0 mPa at the outlet, which therefore corresponds to the minimum pressure within the fluid domain. The maximum pressure in this equilibrium solution is 717.6 mPa, occurring on the ChP surface facing the catheter at $z = 25.5$ mm, where the ChP approaches contact with the catheter. These values are taken from the final iteration prior to collision, at which point a very narrow gap exists between the ChP and catheter, leading to locally elevated pressures required to drive the flow.

To provide a more global characterisation of the pressure field, the 10^{th}, 50^{th}, and 90^{th} percentiles of the pressure distribution are computed as 561.3, 572.3, and 573.4 mPa, respectively. This indicates that the majority of the domain is at a relatively uniform pressure, with deformation driven primarily by localised high-pressure regions near the catheter interface. The maximum pressure at the ventricular wall is 578.6 mPa, slightly above the 90^{th} percentile, suggesting limited spatial variation in pressure away from the catheter. The pressure distribution along the ventricular wall is of particular interest, as localised increases may influence the surrounding brain tissue. However, it is important to note that fluctuations of less than 1 Pa are several orders of magnitude smaller than the intracranial pressure variations observed during the cardiac cycle, which have amplitudes on the order of 5000 Pa [189].

4.1.2 Comparison of existing designs

The 3D FSI model is used to simulate the equilibrium configuration of the ventricle-catheter-ChP system for each catheter shown in Figure 4.1.As catheters are not always inserted with the same orientation, the results are compared for various axial rotations α. Figure 3.2 b) shows the placement of α, with $\alpha = 0°$ placing a row of holes horizontally to the right of the centreline, and increasing α rotating the placement clockwise. The choice of $\alpha = 0°$ is an arbitrary decision, and so results should not be compared at specific values of α but viewed holistically. Fifteen simulations spanning the full 360° were run for each catheter example, changing the axial rotation α by 24° each iteration. The results of Figure 4.2 are taken from Catheter A at $\alpha = 0°$.

Each simulation takes ~ 3 days to run, when parallelised optimally across six cores. With 60 cores on a shared university cluster available, this configuration allowed 10 different simulations to be run concurrently. Nevertheless, the simulations used to obtain the data plotted in Figure 4.1 required over two weeks to create.

Maximum ChP deformation (mm)																		
α (°)	0	24	48	72	96	120	144	168	192	216	240	264	288	312	336	360	mean	std
Catheter A	0.55	0.55	0.314	0.330	0.297	0.132	0.134	0.55	0.55	0.55	0.55	0.55	0.55	0.55	0.55	0.55	0.468	0.158
Catheter B	0.507	0.396	0.240	0.292	0.455	0.259	0.342	0.457	0.444	0.313	0.291	0.464	0.510	0.310	0.362	0.507	0.324	0.072
Weisenberg	0.55	0.55	0.456	0.55	0.55	0.55	0.440	0.55	0.55	0.542	0.452	0.55	0.55	0.486	0.505	0.55	0.542	0.017
Maximum influx over axial rings of holes (mm^3/s)																		
α (°)	0	24	48	72	96	120	144	168	192	216	240	264	288	312	336	360	mean	std
Catheter A	2.313	2.395	2.383	2.392	2.401	2.415	2.430	2.253	2.266	2.274	2.483	2.550	2.376	2.366	2.356	2.346	2.372	0.089
Catheter B	2.002	1.986	2.051	2.032	1.96	2.013	2.085	2.057	2.094	2.035	2.118	2.081	2.009	2.08	2.051	2.002	2.047	0.044
Weisenberg	1.062	1.049	1.033	1.065	1.047	1.036	1.035	1.07	1.052	1.045	1.04	1.046	1.046	1.034	1.053	1.062	1.048	0.011
Mean influx over axial rings of holes (mm^3/s)																		
α (°)	0	24	48	72	96	120	144	168	192	216	240	264	288	312	336	360	mean	std
Catheter A	0.617	0.614	0.615	0.613	0.61	0.613	0.617	0.612	0.615	0.617	0.617	0.617	0.617	0.615	0.617	0.617	0.615	0.002
Catheter B	0.614	0.613	0.615	0.612	0.613	0.613	0.614	0.615	0.614	0.617	0.618	0.617	0.614	0.618	0.616	0.614	0.615	0.002
Weisenberg	1.015	1.017	1.014	1.015	1.015	1.014	1.013	1.016	1.016	1.014	1.014	1.014	1.015	1.014	1.014	1.015	1.015	0.001
Standard deviation of influx over axial rings of holes (mm^3/s)																		
α (°)	0	24	48	72	96	120	144	168	192	216	240	264	288	312	336	360	mean	std
Catheter A	0.712	0.728	0.723	0.726	0.73	0.736	0.743	0.703	0.706	0.707	0.74	0.735	0.715	0.714	0.714	0.715	0.721	0.014
Catheter B	0.598	0.592	0.604	0.598	0.582	0.596	0.613	0.606	0.614	0.61	0.624	0.615	0.597	0.611	0.611	0.598	0.605	0.011
Weisenberg	0.027	0.017	0.02	0.04	0.019	0.015	0.014	0.034	0.021	0.022	0.017	0.023	0.018	0.012	0.028	0.027	0.022	0.008
Maximum pressure on ventricle walls (mPa)																		
α (°)	0	24	48	72	96	120	144	168	192	216	240	264	288	312	336	360	mean	std
Catheter A	575.2	567.4	567.0	564.6	562.2	560.250	558.3	572.1	570.5	575.5	567.3	580.1	579.1	577.3	575.5	573.7	570.7	6.572
Catheter B	580.9	581.1	585.5	580.7	591.1	583.9	578.9	579.8	583.6	580.1	578.9	582.3	584.3	583	580.4	580.9	582.4	3.247
Weisenberg	917.7	914.8	913.9	921.2	916.9	915.1	914.2	917.5	915.2	913.6	913.6	918.8	914.6	912.7	915.3	917.7	915.7	2.315
Maximum normal traction on ChP surface (mPa)																		
α (°)	0	24	48	72	96	120	144	168	192	216	240	264	288	312	336	360	mean	std
Catheter A	-520.7	-552.9	-557.3	-555.0	-552.7	-551.350	-550.0	-533.9	-530.4	-555.5	-543.6	-516.0	-549.4	-546.6	-543.8	-541.0	-541.9	13.83
Catheter B	-517.2	-571.3	-578	-571.4	-580.5	-575.7	-572.2	-564.8	-572.6	-571.7	-570.7	-563.9	-572.7	-574.3	-570.9	-517.2	-572.2	4.369
Weisenberg	-887.1	-899.9	-902.3	-873	-891.5	-900.9	-903	-889.3	-896.7	-900.3	-898.6	-888.1	-898.9	-900.5	-887.6	-887.1	-894.5	8.262
z position of maximum normal traction on ChP surface (mm)																		
α (°)	0	24	48	72	96	120	144	168	192	216	240	264	288	312	336	360	mean	std
Catheter A	25.49	25.49	25.49	24.49	23.49	24.59	25.69	25.09	25.49	25.29	23.29	23.29	23.09	23.757	24.423	25.09	24.69	1.051
Catheter B	23.14	23.09	24.09	23.69	23.29	23.09	24.09	24.49	24.09	24.09	24.49	24.49	24.49	24.09	23.29	23.14	23.92	0.531
Weisenberg	7.106	1.709	1.709	8.904	7.106	1.709	1.909	8.904	3.308	1.709	10.7	8.904	5.307	1.709	8.904	7.106	5.307	3.46

Table 4.2: Comparison of quantitative metrics for different catheter designs across $\alpha \in [0, \ldots, 360]$. The mean and standard deviation computed over α are also given.

Table 4.2 summarises some of the key metrics discussed above, for each catheter design and at each value of α. For each metric, the mean and standard deviation (std) across α are also given in the right-most columns. Table 4.2 provides a basis for ranking the catheter designs. The maximum ChP deformation varies significantly both between designs and across values of α. Weisenberg's design exhibits deformation exceeding 0.55 mm (indicating contact) for the majority of cases, while Catheter A also shows multiple instances of contact. In contrast, Catheter B exhibits no contact for any value of α and has the lowest mean deformation (0.324 mm). These trends are illustrated in Figure 4.3. Displacements greater than 0.55 mm, indicating contact between the ChP and catheter, are marked with red dots. Although Weisenberg's catheter was designed to enforce uniform influx through each inlet hole (as confirmed in Figure 4.4), it exhibits collisions for most values of α. This highlights that uniformity of inflow alone is not sufficient to rank catheter performance. Overall, Catheter B provides the most robust performance across all values of α, despite Catheter A achieving the minimum deformation at $\alpha = 120°$.

There remains a strong dependence of ChP deformation on α for all designs. As this orientation is not controlled during implantation, reducing sensitivity to α is a key consideration in catheter design.

Previous work has focussed on influx into the catheter, particularly the standard deviation of influx across axial rings of inlet holes. Catheters A and B have relatively large standard deviations (with the mean over α of the standard deviation over axial rings of holes of 0.721 and 0.605 mm^3/s respectively), whereas Weisenberg's design is very successful at minimising this value (mean 0.022 mm^3/s), see Figure 4.4 a). This is also reflected in the close agreement between maximum and mean influx values for Weisenberg's design, indicating that flow is distributed more evenly across all rings of inlet holes. It is notable that for each catheter design, the influx metrics vary very little with α, suggesting that flow within the catheter lumen is relatively insensitive to catheter orientation within the ventricle. This supports the findings of Ref. [91], who also observed limited dependence of lumen flow metrics on ventricle geometry. Figure 4.4 a) shows the fluid centreline fields for the catheter developed in Weisenberg's computational study. This design was chosen to enforce uniformity of flow into each inlet hole, which can clearly observed.Nevertheless, Figure 4.3 shows that this design results in large equilibrium ChP deformation for all values of α, performing

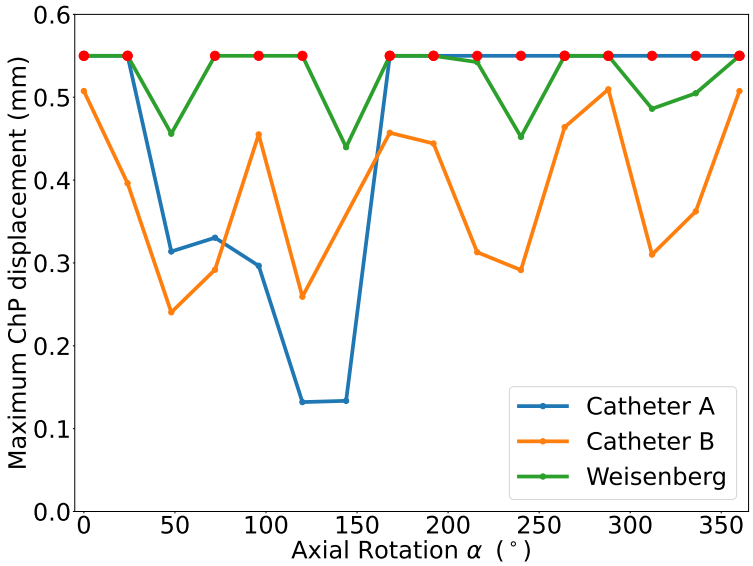

Figure 4.3: Maximum ChP displacement (mm) against axial rotation. Collision events between the catheter and ChP are shown by a red dot. Image adapted from Ref. [50], focussing on the existing designs, reproduced under a Creative Commons Attribution 4.0 International License (CC BY 4.0 [32]).

worse than both Codman examples. This demonstrates that uniformity of inflow alone is not a sufficient design criterion.

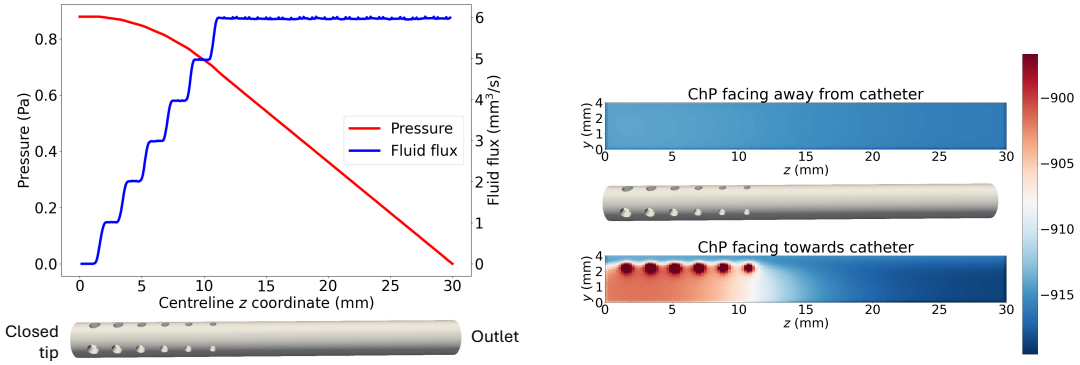

(a) (b)

Figure 4.4: (a) Velocity flux and pressure along the centreline of Weisenberg's catheter [15]. (b) Normal traction on the surface of the ChP.

The maximum pressure on the ventricular wall is also recorded. There is relatively little pressure variation in the ventricle domain, so this maximum pressure is comparable to pressure values throughout the ventricle. Catheters A and B

both exhibit maximum pressures around 570–580 mPa (means of 570.7 mPa and 582.4 mPa respectively), while Weisenberg's design requires a significantly higher pressure (mean 915.7 mPa) to drive flow through the catheter. Although this is notably larger, it remains below 1 Pa and is therefore small compared to daily intracranial pressure variations. This increase is likely due to Weisenberg's inlet holes being positioned further from the outlet, resulting in a longer section of catheter lumen over which fluid must travel before reaching the outlet boundary at 0 mPa. It should be noted that the model assumes rigid ventricular walls, whereas in reality the surrounding brain tissue would deform, reducing local pressure increases. As with other metrics, there is very little variation in maximum pressure across α, and the z-location of maximum pressure is consistently at $z = 0$ for all α and for all designs, corresponding to the region furthest from the outlet.

Also of interest is the maximum (least negative) normal traction on the ChP surface, and the z position at which this occurs. From Figure 4.2 e), the maximum normal traction occurs on the surface facing the catheter and is highly localised near specific inlet holes. For Catheters A and B, the inlet hole closest to the outlet admits the largest influx and exerts the strongest traction on the nearby ChP. This is reflected in the relatively consistent z-position of maximum traction (means of 24.69 mm and 23.92 mm respectively) which correspond to the z position of the inlet hole nearest to the catheter outlet. In contrast, the z-position of maximum traction for Weisenberg's design varies more significantly (mean 5.307 mm, std 3.46 mm), indicating that multiple inlet rings contribute comparably to the local traction field. Inspection of simulation results, Figure 4.4 b), shows that each of the six axial rings of holes produces a strong local traction, and small changes in α shift the location of the maximum between these different rings.

Given the range of metrics considered, it is clear that different measures capture different aspects of catheter performance, and a multi-objective approach could incorporate several of these simultaneously. For this work, the maximum equilibrium ChP deformation is used to quantify catheter performance, as it directly captures the strength of the FSI and identifies cases where the ChP comes into contact with the catheter, corresponding to a high likelihood of occlusion. It also shows sensitivity to α not captured by other metrics discussed. While fluid-based metrics such as influx uniformity and pressure provide useful complementary information, they do not consistently reflect this failure mechanism.

Maximum ChP deformation therefore provides a simple, robust, and clinically meaningful basis for initial design comparison and optimisation in this work.

This section showed that the 3D FSI model is effective at comparing existing catheter designs, and ranking their performance by considering the maximum equilibrium ChP deformation seen. The 3D FSI model also gives detailed insight into the complex flow fields and ChP deformation in the ventricle-catheter-ChP system. A range of further metrics can be extracted from the 3D FSI model, including fluid flow structure within the catheter lumen, intraventricular pressure values and the spatial structure of surface traction exerted by the fluid.

However, each 3D FSI simulation takes over 3 days to run, even with internal parallelisation. To explore and improve catheter design and assess a large range of catheter design parameters, a simpler ROM is developed, applying the same FSI model and codebase to a 2D cross-section of the ventricle-catheter-ChP system. This model geometry is described in Section 3.1, and the ROM has the advantage of a considerably reduced computational time (2D model taking $\sim$10 min on one core of an i7 laptop), which allows large sweeps over parameter regimes to be completed. Whilst the ROM neglects effects occurring along the axis of the catheter, results from the ROM can nevertheless be used to identify promising design directions which can be reinterpreted back into 3D.

4.2 Reduction to cross-section

Figure 4.5 shows results from the 2D model for two sizes of catheter hole radii: 0.11 mm and 0.87 mm. The subfigures a) and c) show ChP displacement for the two hole sizes. The highest displacement is around the tip of the ChP, as expected, in both simulations, with the maximum displacement being a factor of three higher for the smaller hole configuration. Selected streamlines show that the flow field pattern is similar for both simulations, with streamlines joining the ChP source to drainage at the catheter holes. Holding the catheter hole pressure at 0, but reducing the area across which fluid can drain causes an increase in the fluid velocity within the catheter inlet holes. To drive this, a higher relative pressure is needed in the ventricle (see subfigures b) and d)). The scenario with smaller holes generates a pressure drop across the catheter holes of 50 mPa, while the larger holes need only 2 mPa. These pressures are approximately uniform across different angles α for the same hole size. Maintaining a normal intracranial

pressure is a key aim of hydrocephalus treatments, so hole configurations which cause a lesser increase in pressure are *a priori* desirable. The pressures seen in the 2D model results are smaller than those seen in the 3D model as removing the third dimension significantly shortens the path length of fluid particles travelling from the ChP to the outlet. As discussed above, 50 mPa is a small increase compared to the normal range of intracranial pressure.

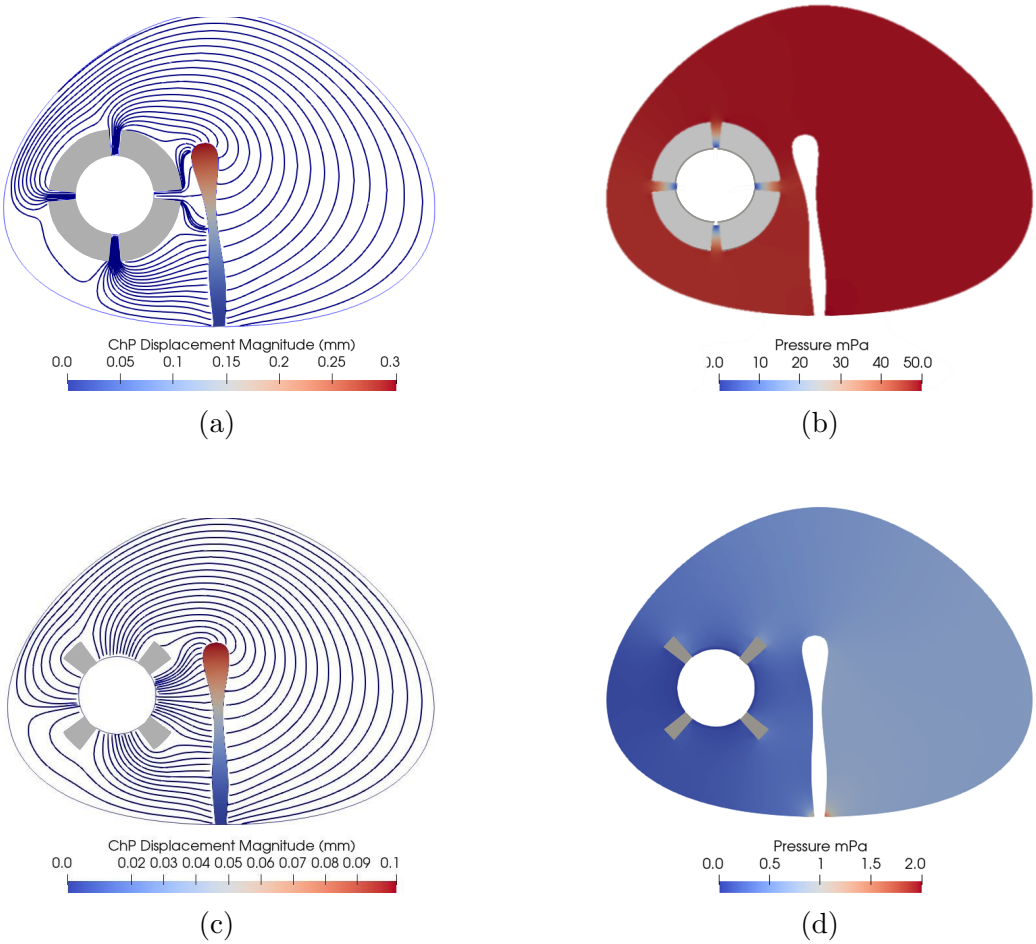

Figure 4.5: Representative cross-section model simulations for two different hole widths (a), (b) 0.11 mm hole radius; (c), (d) 0.87 mm hole radius for the same $\alpha = 0$. (a), (c) Streamlines which flow out of the ChP and into the outlet holes of the catheter, and the displacement field on the ChP tissue in mm (red high, blue low). (b), (d) Fluid pressure field in mPa (red high, blue low). Note the different pressure scales in (b) and (d). Image reproduced from Ref. [50] under a Creative Commons Attribution 4.0 International License (CC BY 4.0 [32]).

The 2D model is not able to capture the z dependence seen in the streamlines and hence flow field of Figure 4.2 c) or in the ChP deformation of Figure 4.2 a). Loss of detail is expected with the reduced dimensionality of the solver. However, both the 2D and 3D models have qualitative similarities, with the point of maximum deformation of the ChP occurring at the upper tip. Appendix B.1 gives further results on the comparison between the 2D and 3D FSI models.

4.2.1 2D parameter sweep

The 2D ROM is used to perform a systematic investigation into the response of the ChP deflection to changes in hole size and circumferential position. As the axial rotation α is not clinically imposed, it is necessary to test catheter designs for multiple values of α. Figure 4.6 shows how α, and the hole radius r are determined.

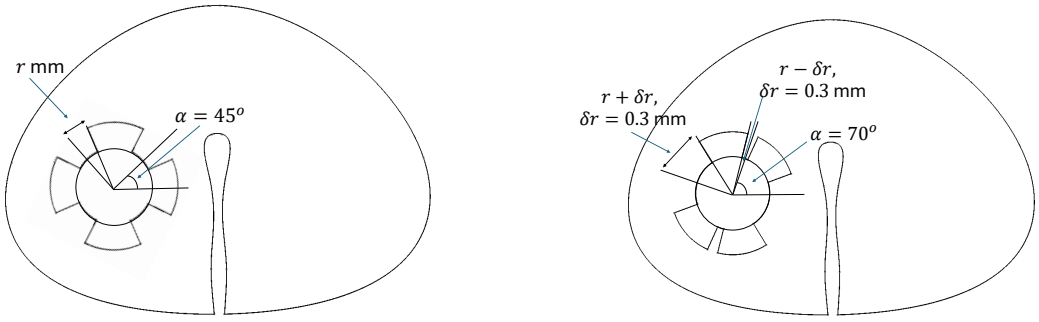

(a) (b)

Figure 4.6: (a) Radius r and offset angle α shown on two representative outlines of the cross-section model. Each catheter has four symmetrically positioned holes. (a) Catheter with equal sized holes, (b) catheter with two larger and two smaller holes, with radius $r + \delta r$ and $r - \delta r$. Image reproduced from Ref. [50] under a Creative Commons Attribution 4.0 International License (CC BY 4.0 [32]).

Results from the parameter sweep are shown in Figure 4.7; panels on the left of the Figure show variation of the parameter of interest. The range of ChP displacement over α are shown as light blue shading, with the average displacement for that parameter value also indicated. Panels on the right show the impact of α on the maximum displacement of the ChP boundary (some with reduced ranges due to symmetry in the hole position). Light colours show lower values of the parameter, and darker for the high colours.

The first sweep (Figure 4.7 a), b)) considers the effect of hole radius. Four equally sized symmetrically positioned holes are modelled. The hole radius ranges between 0.04 mm and 0.96 mm to quantify the effect of larger or smaller inlet hole area on the ChP displacement. The results show that a smaller hole results in higher deflection of the ChP. In addition, the axial angle α has significant influence on the deflection of the ChP, particularly for smaller holes. Previous work has linked higher wall shear stresses (associated with smaller holes) with an increased chance of cell and debris adhesion [90], an additional factor in favour of larger inlet holes.

For the second sweep (Figure 4.7 c), d)), the effect of unequal hole sizes is tested. To quantify a measure of hole discrepancy, δr is introduced, see Figure 4.6 b). Two (diametrically opposite) holes have radius $r + \delta r$, and the other two holes are smaller with $r - \delta r$ for δr taking values between 0 mm (equal holes) and 0.436 mm (greatest disparity), and r held fixed at 0.54 mm. This form was chosen so that the total area for fluid to enter the catheter remains the same. Here, there is a two-fold symmetry so values of α between 0° and 180° are plotted. The average ChP deflection was approximately uniform for different values of δr, but larger values of δr are more affected by varying α.

The third sweep, Figure 4.7 e), f), fixes the total area of the inlet holes and considers different numbers of equally sized holes positioned at symmetric intervals around the circumference of the catheter. A larger number of holes reduces both the average ChP deflection and the sensitivity to changes in α. However, the catheter designs presented in this sweep, and in Figure 4.5, do not account for physical manufacturing and structural constraints. To maintain structural integrity, a catheter requires a sufficient amount of material between adjacent holes, which is not the case for larger values of r in Figure 4.7 a) and b), or in the example visualisations of Figure 4.5 c) and d). Extremely small holes are also undesirable from a manufacturing perspective, both due to the limitations of drill bit size and the increased likelihood of blockage by cellular debris suspended in the ventricles.

The 2D model cannot resolve axial variations in the same way as the 3D FSI model. Nevertheless, it still provides useful insight into alternative performance metrics beyond maximum ChP displacement. Figure 4.8 shows the maximum pressure (on a logarithmic scale) in the equilibrium configuration for the catheter designs in the first sweep, where four equally sized holes of constant radius are

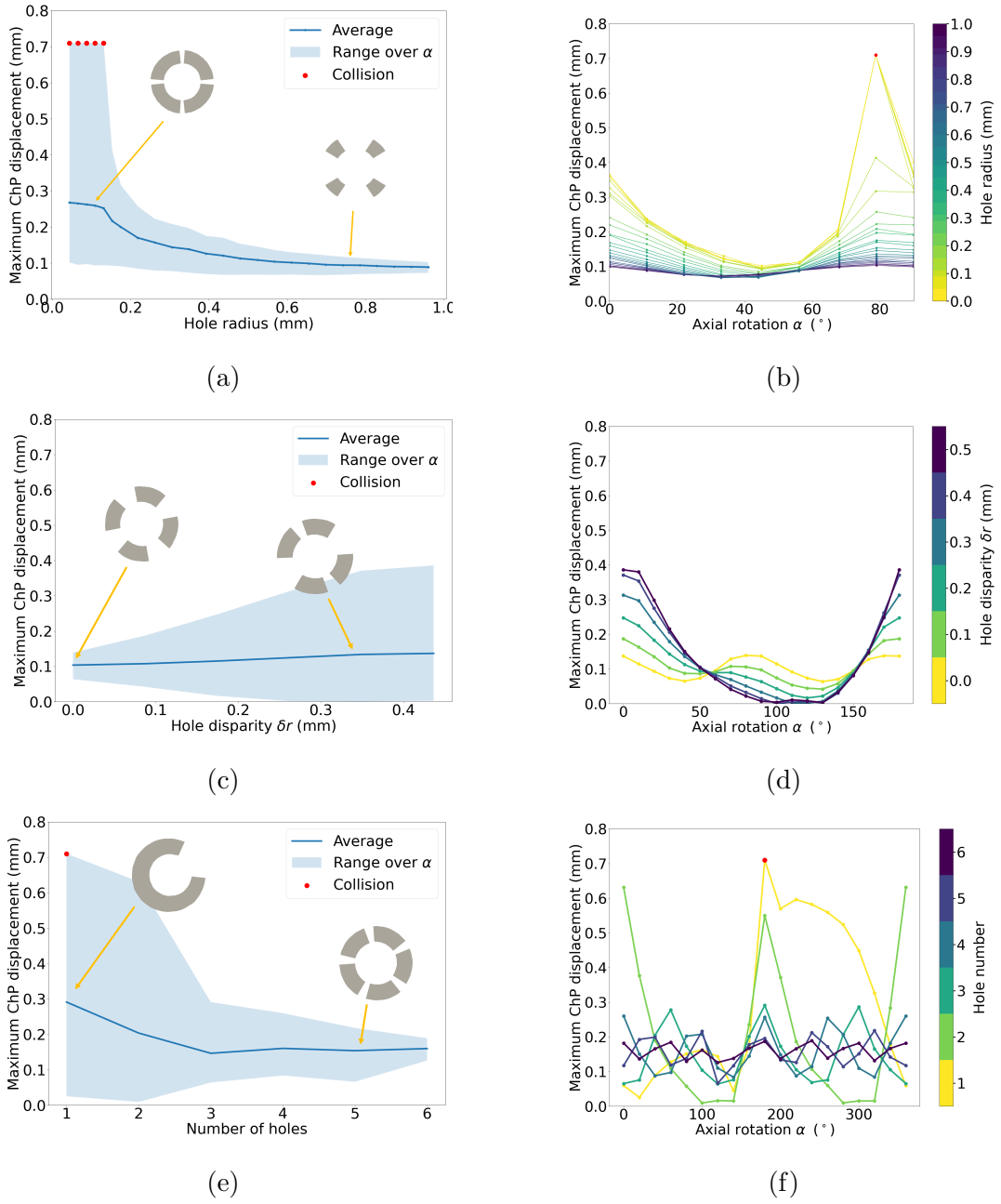

Figure 4.7: Maximum ChP displacement at equilibrium. Figures (a) and (b): impact of hole size, (c) and (d) impact of unequal holes, (e) and (f) impact of multiple holes. (a), (c) and (e) ChP displacement averaged over α (dark line), and the full range over α (light shading). Example catheter geometries overlaid in grey. (b), (d) and (f) same data with α on the x-axis, and colours showing model parameter (light - small, dark - large). Image reproduced from Ref. [50] under a Creative Commons Attribution 4.0 International License (CC BY 4.0 [32]).

distributed uniformly around the circumference of the catheter. Figure 4.8 rein-

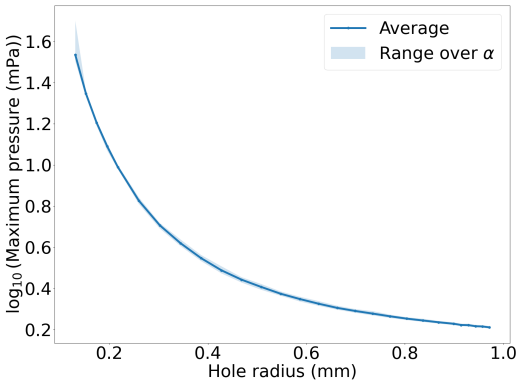

Figure 4.8: Maximum pressure (log scale) for various hole radius, for the catheter designs tested in Figure 4.7 a) and b).

forces the observation from Figure 4.5 that higher pressures are required to drive flow through smaller inlet holes. Even on a logarithmic scale, the increase in maximum pressure for decreasing hole size is pronounced. For each hole radius, there is minimal variation with respect to α, consistent with the weak dependence of ventricle pressure on catheter orientation observed in the 3D results (Table 4.2). Although the observed pressure increase for the smallest 2D holes (on the order of 50 mPa) is not clinically significant in isolation, these results further support the conclusion that larger inlet holes are preferable.

This analysis using the 2D ROM indicates that catheter designs with larger inlet holes, combined with a greater number of holes distributed uniformly around the circumference, lead to reduced ChP deflection and exhibit less sensitivity to α. However, it is important to recognise the manufacturing and clinical constraints that limit the feasible design space from the wider range of configurations explored here.

4.3 Initial design improvement

Results from the 2D parameter sweep suggest potentially promising design directions for catheters that motivate further interrogation. In this section a new 3D catheter design is proposed, motivated by the parameter sweep of the 2D ROM. Larger, equally sized holes result in smaller deflections in the 2D ROM and less dependency on α. However, this must be balanced with the possibility

that a large number of closely placed large holes is likely to reduce the structural integrity of the catheter.

To allow for such manufacturing constraints and structural stability, the hole proportion of the catheter design is considered, again defined as the fraction of surface that is hole (see Section B.1). The hole proportion of the improved catheter is matched to the average of the existing examples (0.15 for Catheter A and 0.05 for Catheter B), i.e., 0.1. A hole diameter of 0.9 mm is chosen, comparable to the largest hole diameter seen in physical examples. This diameter is far smaller than the optimal radius identified above in the 2D model, but balances the need to take practical structural considerations into account. Equally sized holes are noted to be easier to manufacture, as only one size drill bit is needed [86]. This choice of hole radius and total hole proportion permits 24 holes in the catheter. The 2D sweep informed that a large number of holes placed circumferentially would be beneficial for reducing ChP displacement, A hole arrangement is chosen with four rows of holes and six holes in each row, as a higher hole number in each axial slice was shown to reduce ChP deflection (Figure 4.7 e)). To improve structural stability the rows of holes are placed at an axial offset, to place more catheter wall between each hole placement. The geometry of this newly proposed catheter design is shown in Figure 4.9 a).

Figure 4.9 b) compares the maximum ChP deflection for the three existing geometries (blue, orange, and green) and the new design (red). The new design leads, on average, to lower ChP deformation than the existing designs, exhibits reduced sensitivity to α, and shows no collision events, making it more robust overall. This is further supported by the visualisation in Figure 4.9, which examines the improved design at $\alpha = 72°$, corresponding to its worst performance. Figure 4.9 c) shows the displacement magnitude and x-component of the ChP tip, with the maximum displacement occurring at $z = 20.50$ mm.

Further details of this configuration are shown in Figure 4.9 d), which illustrates the fluid fields within the catheter lumen. As with Codman catheters A and B, this design exhibits an imbalanced flux across axial rows of holes. The mean influx is 0.767 mm^3/s (noting that for eight axial rows, a uniform distribution would correspond to 6 mm^3/s / 8 = 0.75 mm^3/s), while the standard deviation is 0.890 mm^3/s, indicating no improvement in flow uniformity relative to the Codman designs. This is consistent with the design objective, which prioritised minimising ChP deformation rather than enforcing uniform inflow.

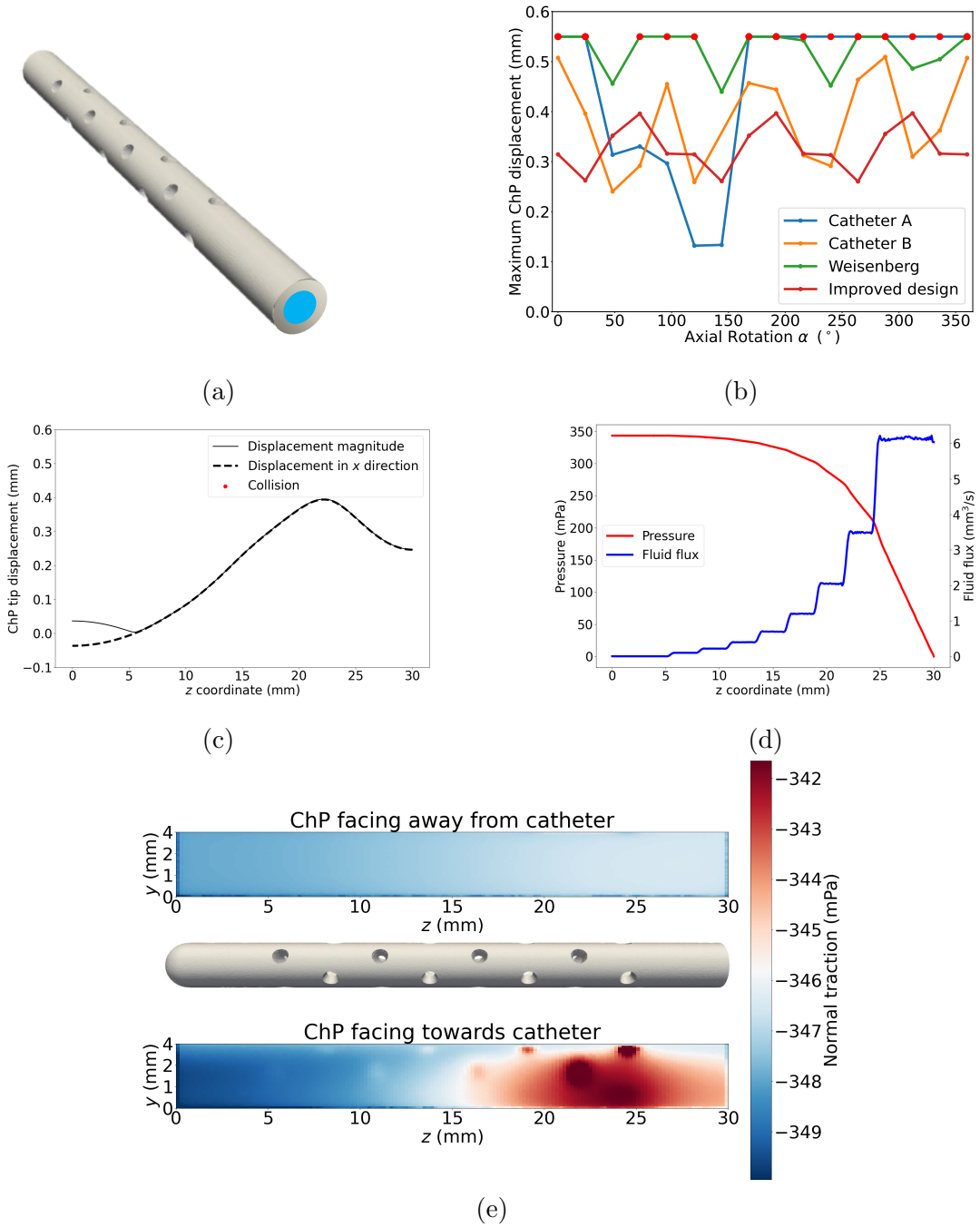

Figure 4.9: (a) Improved design geometry. (b) Maximum ChP deflection plotted against axial angle for the improved and existing designs. Image adapted from Ref. [50], focussing on the initial improved design, reproduced under a Creative Commons Attribution 4.0 International License (CC BY 4.0 [32]). (c) ChP tip displacement. (d) Fluid fields in the catheter lumen. (e) Normal traction on the surface of the ChP.

Of all the designs considered, this configuration exhibits the lowest pressure and traction values. The maximum pressure on the ventricle wall is 351 mPa (again occurring at $z = 0$ mm), suggesting reduced resistance to flow through the catheter. Figure 4.9 e) shows the normal traction field on the ChP surface, with values in the range -350 mPa to -340 mPa, representing smaller absolute magnitudes than those observed in the previous catheter designs. As before, localised regions of elevated traction occur near specific inlet holes, particularly in the range $20 < z < 25$ mm, coinciding with the region of maximum ChP deformation.

Consistent with the trends observed in Table 4.2, the fluid, pressure, and stress metrics show minimal variation with respect to α. Figure 4.9 b) shows that there is still variation in the maximum ChP deformation for this improved design, and there is potential for further improvements to be made in this area.

4.4 Chapter summary

This chapter presents results from the 3D FSI model, demonstrating its ability to discriminate between various catheter designs and highlighting those that reduce the likelihood of obstruction by the ChP. Results from the 3D FSI simulation give a detailed investigation into the flow fields and deformation patterns of the ventricular-catheter-ChP system and allow a range of relevant metrics to be quantified, including maximum ventricular pressure, uniformity of influx into different catheter holes and axial position of maximum traction on the ChP surface.

A 2D FSI ROM is also introduced, which offers a significantly shorter runtime. This model is used to perform a comprehensive investigation into the effects of hole size, differences in hole width, and hole number. Whilst the 2D model can only be used to investigate circumferential design variables, its short runtime allows a comprehensive exploration of these variables. A larger total hole area distributed across evenly spaced, equally sized holes is found to reduce ChP deflection and to produce designs less sensitive to α. Results from the 2D model, combined with manufacturing constraints, are used to motivate a candidate geometry for an improved catheter. This design is then tested *in silico* in the full 3D model and shown to outperform the Codman designs, Catheters A and B, and the catheter proposed in Ref. [15].

While the 2D model has assisted in motivating a design that reduces maximum equilibrium ChP displacement, the results in Figure 4.9 show only a modest improvement over Catheter B. Detailed analysis of the 3D FSI simulation reveals that the improved design still produces localised regions of high traction on the ChP near inlet holes at the outlet end of the catheter. The 2D model does not provide information on the axial placement of inlet holes, which in this case were chosen to ensure sufficient material between successive hole rings. However, these results suggest that a more optimal axial arrangement of inlet holes likely exists, and that further improvements may be achieved by considering axial positioning within a higher-fidelity model.

Nevertheless these results illustrate how a ROM, despite its simplifications, can be efficiently leveraged to inform and improve 3D design. The use of the 2D model to guide catheter development, followed by validation in the 3D model, represents a first step toward the optimisation methodology outlined in Figure 1.1. While no formal optimisation is presented in this chapter, results from the 2D FSI model are successful when translated back into the 3D model, highlighting the promise of ROMs in catheter design. The following chapters build on this approach by introducing additional ROMs that can be leveraged to further improve catheter design.

Chapter 5

Reduced-order models

In Chapter 4, the fluid-structure interaction (FSI) model is shown to successfully simulate the hydrocephalus scenario, with the finite element and finite volume methods allowing the fine detail of the flow fields and ChP deformation to be determined. However, the long runtime of the 3D FSI model makes it infeasible to use when performing a systematic search over catheter design space. In Chapter 4 results from a reduced-order model (ROM), in this case a 2D version of the FSI model, were shown to moderately improve the catheter design when translated back into 3D.

This motivates the exploration of other ROMs for use in the generative design of catheters. In the remainder of the thesis, the aim is to systematically optimise over the space of catheter designs. Due to the computational cost of the 3D FSI model, it is infeasible to use it directly within an optimisation framework. The objective is therefore to develop ROMs that are reliable predictors of catheter performance, while offering significantly reduced computational cost. For use in subsequent optimisation studies (expected to require the evaluation of thousands of designs) a ROM should ideally have a runtime of under 10 minutes.

In this chapter, two further ROMs are presented, motivated by insights from the results of the detailed FSI model presented in Chapter 4, with a view to combine them with machine learning (ML) techniques in later chapters to create a surrogate model. This chapter therefore focusses on the ROM component of the optimisation methodology, as shown in Figure 5.1.

The first ROM aims at capturing the fluid flow within the catheter interior. Approximations of axisymmetric flow fields and a long, thin catheter geometry are combined with a permeable wall approximation to derive a 1D linear model

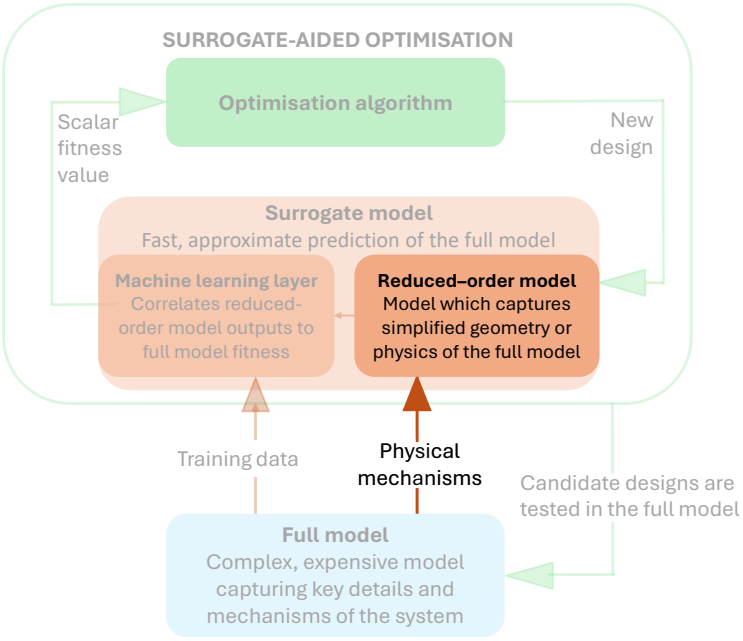

Figure 5.1: Optimisation methodology, highlighting the ROM component which will be the focus of this chapter.

for fluid pressure in the catheter interior. This ROM is compared to results from the 3D FSI model and shown to agree well. The second proposed ROM approximates the equilibrium fluid stress field on the ChP using a rigid wall model. The permeable wall ROM is the subject of Ref. [190], and the stress field ROM is part of the surrogate model development presented in the Methods section of Ref. [191].

5.1 Ground-truth dataset

To test the accuracy of the ROMs and to train and tune the machine learning (ML) layer of the surrogate model in later chapters, a ground-truth dataset is needed. Within this research, the 3D FSI model is the ground-truth for ChP deformation.

The 3D FSI model was used to create a dataset of 180 simulations. The catheter designs contained in the ground-truth dataset are representative of all catheter designs. In the physical examples of catheters examined previously, holes are placed in regular arrangements with a set number of two or four holes per ring. It is possible, however, that an optimal hole arrangement will not have

such a design, and so the ground-truth dataset is curated to contain a mix of catheter designs with regular hole arrangements, and designs with holes placed more generally. For all designs, inlet holes are placed in the 30 mm of catheter nearest the tip. This is required to ensure that inlet holes remain contained in the ventricle and do not interact with the surrounding brain tissue. An additional constraint of a maximum of 40 inlet holes is imposed to match the maximum number of inlet holes seen in physical examples.

The position and size of an inlet hole can be identified by three variables: a radius r (specifically, the radius of the base of the conical section of catheter which is removed to form the inlet hole), the z coordinate of the centre of the inlet hole and a value ϕ as the angle between the hole and the horizontal (e.g. $\phi = 0$ places a hole horizontally to the right of the centreline, while increasing ϕ rotates the placement clockwise). Note that ϕ is a design dependent parameter that is different for each inlet hole, whereas α is not prescribed in design, but measures the relative position between an inlet hole and the ventricle environment. When looking at various values of α therefore, the actual angular offset of a specific inlet hole is $\phi + \alpha$.

Figure 5.2 provides a visualisation of this ring-based encoding. Design parameters controlling the first two inlet holes are indicated. Inlet holes are described in order of decreasing hole radius (i.e., the first inlet hole of a design is the one with largest radius, the second hole has the second-largest radius and so on).

New designs are generated by independent and identically distributed random sampling across the design space. Given the high dimensionality of the problem (120 design variables) and the substantial runtime of the 3D FSI model, any sampling strategy that is computationally feasible will necessarily be very sparse. Consequently, simple random sampling is considered sufficient, rather than more sophisticated space-filling approaches such as Sobol sampling [192]. For each new design the number of inlet holes is first chosen as a random integer between 1 and 40. For each inlet hole the radius, z position and ϕ are then chosen uniformly and independently at random using the `np.random.uniform` function from the ranges given in Table 5.1. Each new design is preprocessed to ensure that holes do not overlap. Overlapping holes may appear due to the independence of parameter choice when choosing the position and size of inlet holes, and these designs are discarded as non-physical.

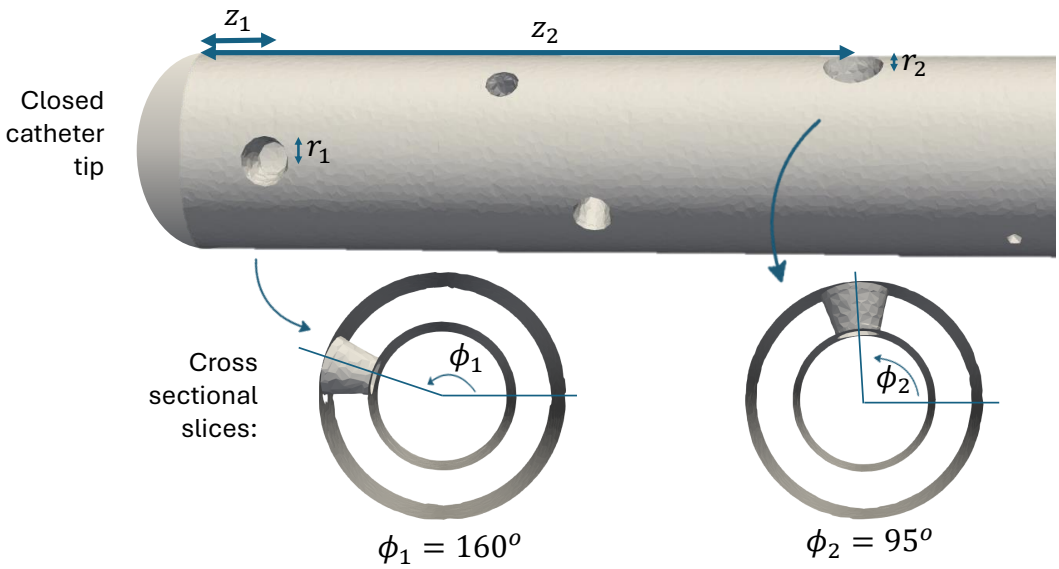

Figure 5.2: Schematic of the design encoding used in the creation of the ground-truth dataset. The design parameters for the two largest holes are indicated: r, z and ϕ.

Table 5.1: Parameter value ranges for the ground-truth dataset.

Variable	**Lower bound**	**Upper bound**
z position	0.5 mm	29.5 mm
ϕ	0°	360°
Hole radius	0.05 mm	0.6 mm

From the results of Chapter 4, particularly Figure 4.1, the value of α, which prescribes the relative axial orientation of the catheter to the ChP, is seen to have a significant effect on the maximum ChP deformation. Therefore several catheter designs are tested at different values of α and included as separate data points in the ground-truth dataset. This helps separate the influence of inlet hole design from the influence of α. When searching for improvement to catheter design in later chapters, it is important that improvements are due to the inlet hole design rather than a fortuitous choice of α.

Figure 5.3 shows a histogram of the number of values of α tested for each catheter design. Where $\alpha > 1$ the values of α are chosen uniformly in the range (0°, 360°). Most designs have have between 1 and 4 values of α tested (with the number of α values to test at also chosen uniformly at random), which balances the need to investigate a large variety of catheter designs, while explicitly including α dependence into the dataset. In total, 65 distinct catheter designs were simulated.

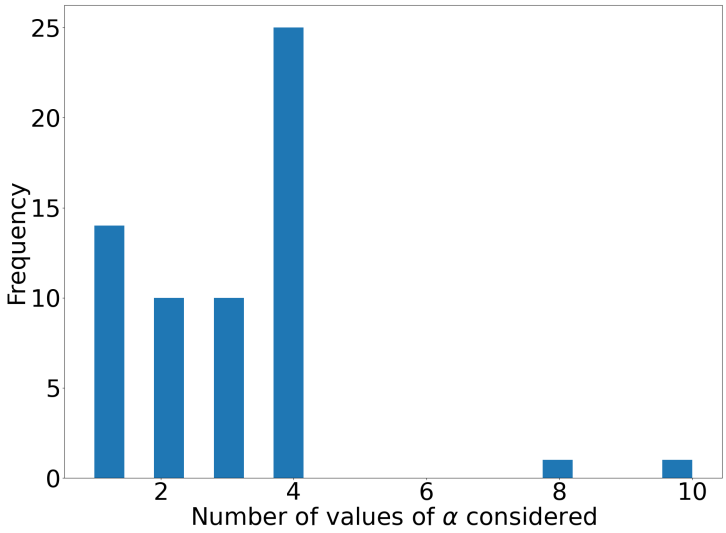

Figure 5.3: Frequency histogram showing the number of α values considered for different catheter designs in the ground-truth dataset.

5.2 Permeable fluid model

In this section, the first ROM is presented. In Chapter 4, the 3D FSI model is used to simulate the hydrocephalus scenario, giving a detailed view of the CSF flow. Certain characteristics of the flow field were common across all catheter designs tested. In particular, there is a distinct difference in the behaviour of the CSF within the catheter, and in the ventricular domain exterior to the catheter:

- **catheter exterior**: the pressure field is approximately constant (relative variation of $\sim 1\%$). The magnitude of the velocity field is approximately constant and low compared to velocities in the catheter lumen (average velocity magnitude external to the catheter is 0.05 mm/s, whereas the average velocity at the catheter outlet is 3.4 mm/s),
- **catheter interior**: the pressure field decreases rapidly and monotonically towards the outlet, and the velocities have a larger magnitude, reaching greatest magnitude at the catheter outlet.

Previous work on catheter design also focussed primarily on the fluid flow through the inlet holes of the catheter [15, 86]. The observations from the FSI model therefore motivate a set of assumptions from which a simple, linear, 1D model of the CSF fluid fields within the catheter interior is derived. The assumptions used in the derivation of the model are as follows:

- Fluid external to the catheter is modelled at a constant, unknown pressure p_0. This neglects the detail of the ventricle geometry and FSI effects from interaction with the ChP.
- The detailed geometry of the inlet holes is replaced with an axisymmetric permeable boundary condition. Subsequently, only the fluid flow within the central lumen of the catheter is modelled.
- The cylindrical geometry of the catheter motivates an axisymmetric flow approximation for flow with the catheter lumen.
- The long, thin geometry of the catheter motivates the use of the lubrication equations to govern leading order flow [193].

These assumptions introduce modelling errors that depend on catheter geometry. The assumption of axisymmetry is most accurate for geometries with many uniformly distributed inlet holes; configurations with fewer or irregularly spaced holes are expected to exhibit 3D flow effects. The lubrication approximation relies on a small aspect ratio, here ($r_i/L \sim 1/40$), which implies neglected terms of order ($\mathcal{O}(1/40)$), corresponding to errors of approximately 2.5%. Lubrication theory also assumes radial inflow through the inlet holes is small compared to axial flow in the lumen. This holds when many inlet holes are present to distribute the inflow, but may break down when only a few holes are present.

The permeable boundary condition replaces the detailed 3D flow through individual inlet holes with an axisymmetric approximation, in which the normal velocity is linearly related to the pressure difference. The proportionality constant is derived from Poiseuille flow, and is therefore most accurate when the inlet holes behave like short tubes with fully developed profiles. Given the fixed catheter wall thickness of 0.5 mm here, this approximation is more valid for small-radius holes. Overall, the ROM is expected to perform best for geometries with many small, evenly distributed inlet holes. Despite these simplifications, the model remains tractable and is shown to predict centreline pressure to within approximately 3.5% of the full FSI solution for the majority of catheter geometries considered.

This model is the subject of Ref. [190] where it is presented in more detail in non-dimensional form, allowing assumptions to be formally justified through a rigorous small-parameter approximations. In this thesis the model is directly applied to the hydrocephalus catheter and so a briefer derivation is given, with all equations presented in dimensional form.

5.2.1 Model derivation

As presented in Section 3.3, the catheter is modelled as a hollow, rigid tube with cylindrical cross-section, of length $L = 30$ mm, inner radius $r_i = 0.75$ mm and outer radius $r_o = 1.25$ mm. The wall is punctured by inlet holes distributed along the length of the catheter. For this model, a cylindrical polar coordinate system is used: (r, θ, z), with corresponding coordinate directions $(\boldsymbol{e_r}, \boldsymbol{e_\theta}, \boldsymbol{e_z})$ with $\boldsymbol{e_z}$ aligned along the catheter centreline. The catheter tip at $z = 0$ is closed and the outlet at $z = L$ is open to fluid. Each catheter has a set of inlet holes indexed by n, where the n^{th} inlet hole has a radius $r_h^{(n)}$ and sits with its centre at axial

position $z_h^{(n)}$. In previous chapters, inlet holes are established as conical. For simplicity here, inlet holes are modelled as cylinders with radius r_h, and height equal to the width of the catheter wall, $r_o - r_i$.

5.2.1.1 External fluid at constant pressure

Motivated by observations from the 3D FSI, this ROM assumes that the catheter sits in a fluid volume where the fluid external to the catheter is spatially constant, with unknown constant value p_0. The ROM therefore models only the fluid internal to the catheter, accounting for the effect of fluid external to the catheter only through a boundary condition involving p_0 at the entrance of the inlet holes. This assumption is motivated by results in Chapter 4 and has been used in previous work, e.g., Ref. [171]. As in the 3D FSI model presented in Chapter 3, the zero value of pressure is set at the catheter outlet.

The boundary of the ROM fluid domain is divided into three parts: the solid impermeable walls Γ_w, the outlet of the catheter Γ_o, and the entrances of the inlet holes Γ_i. A schematic of this geometry is given in Figure 5.4, top subfigure, with boundary areas indicated.

As in Chapter 3, the fluid is modelled as an incompressible, Newtonian, viscous fluid with density ρ and dynamic viscosity μ, with parameter values as in Table 3.1. The fluid velocity $\boldsymbol{v}$ and the fluid pressure p are modelled using the steady, incompressible Navier-Stokes equations:

$$\nabla \cdot \boldsymbol{v} = 0 \;\text{ and }\; \rho(\boldsymbol{v} \cdot \nabla)\boldsymbol{v} = -\nabla p + \mu \nabla^2 \boldsymbol{v}, \tag{5.1}$$

subject to the boundary conditions:

$$\boldsymbol{v} = \boldsymbol{0} \quad \text{on } \Gamma_w, \tag{5.2}$$

$$\boldsymbol{v} - (\boldsymbol{v} \cdot \boldsymbol{n})\boldsymbol{n} = \boldsymbol{0}, \quad -p + \boldsymbol{n} \cdot \boldsymbol{\sigma} \cdot \boldsymbol{n} = -p_0 \quad \text{on } \Gamma_i, \tag{5.3}$$

$$\boldsymbol{v} - (\boldsymbol{v} \cdot \boldsymbol{n})\boldsymbol{n} = \boldsymbol{0}, \quad -p + \boldsymbol{n} \cdot \boldsymbol{\sigma} \cdot \boldsymbol{n} = 0, \quad \int_{\Gamma_o} \boldsymbol{v} \cdot \boldsymbol{n} \, dA = Q \quad \text{on } \Gamma_o. \tag{5.4}$$

where $\boldsymbol{n}$ is the outward-pointing unit normal vector to a boundary surface. On Γ_o, $\boldsymbol{n} = \boldsymbol{e}_z$ everywhere, whereas on Γ_i the normal vector varies for different inlet holes. The fluid stress tensor is $\boldsymbol{\sigma} = \frac{1}{2}\mu(\nabla \boldsymbol{v} + (\nabla \boldsymbol{v})^T)$. These conditions are equivalent to no-slip conditions on every solid wall, with continuity of normal stress and no tangential velocity on the inlet and outlet boundaries. The zero-value of p is imposed at the outlet, and the total flux through the catheter outlet is

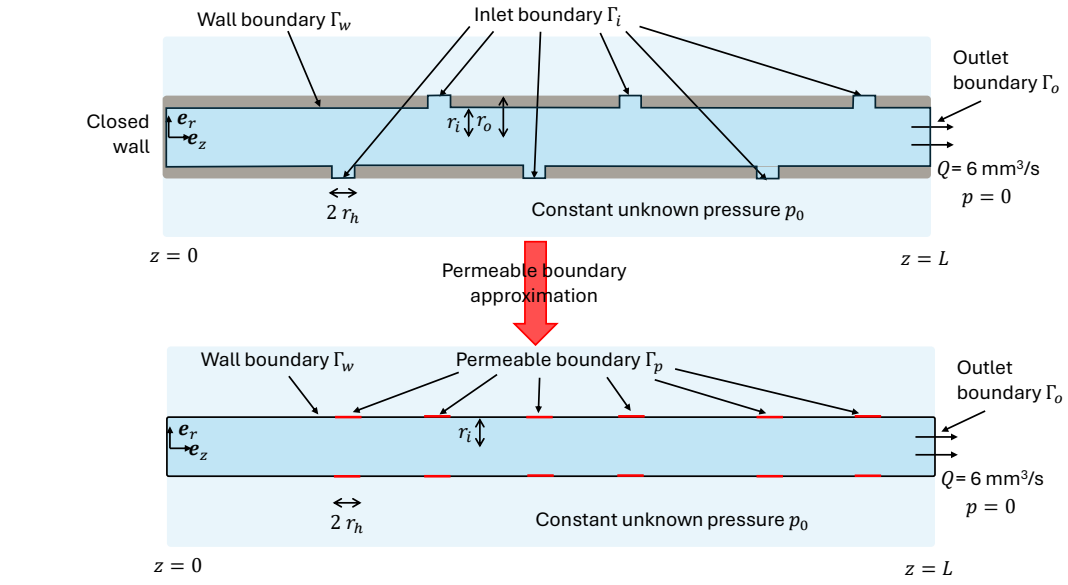

(a)

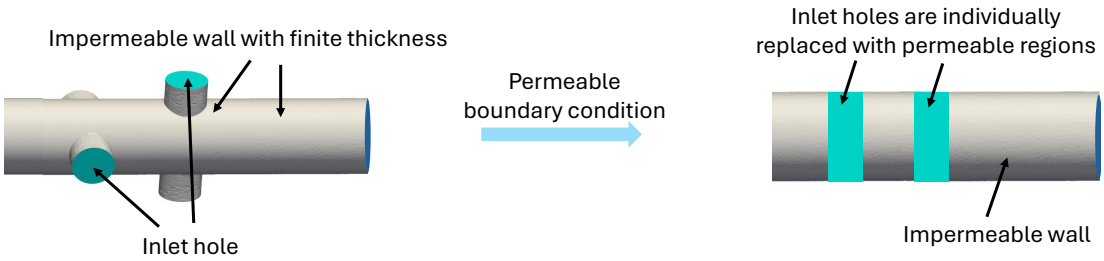

(b)

Figure 5.4: (a) Cross section of the catheter geometry used in the permeable model, with key dimensions shown, and boundary regions labelled. Dark blue: modelled fluid domain, black lines: domain boundary; light blue: fluid external to the catheter, not part of the modelled fluid domain and assumed to be at constant pressure p_0; grey: catheter wall. Lower figure: detail of inlet holes is replaced by a permeable boundary condition. (b) Inlet holes in the catheter, with a height equal to the thickness of the catheter wall, are modelled as axisymmetric permeable regions.

prescribed. The majority of the model governing equations are identical to those presented for the full FSI model in Section 3.3, with the only new conditions at Γ_i which is a new boundary of the reduced fluid domain. The value of p_0 is related to the catheter geometry and Q, and will be a key output of the model (p_0 thus acts as the exterior pressure needed to drive the prescribed flux through the system).

5.2.1.2 Permeable boundary condition

The key simplification of the model is an axisymmetric permeable wall approximation whereby the detailed geometry of the inlet holes, which have a finite height equal to the width of the catheter walls, is replaced with an axisymmetric permeable boundary region Γ_p, Figure 5.4 b). The width of each permeable region is equal to the diameter of the inlet hole it replaces, allowing the ROM to maintain some knowledge of inlet hole placement.

This process is shown in Figure 5.4 b), and subsequently the ROM models only fluid in the central lumen of the catheter, the cylindrical volume with circular cross section $\{0 \leq r \leq r_i, \;\; 0 \leq z \leq L\}$. This ROM does not resolve the flow field in a permeable catheter wall (as is done in, e.g., Ref. [194]), but instead uses a permeable model as a boundary condition to understand the flow in the catheter interior.

The boundary conditions at Γ_i in Equation (5.3) are replaced with

$$\boldsymbol{v} = \Lambda(p - p_0)\boldsymbol{n} \;\; \text{on } \Gamma_p. \tag{5.5}$$

This new condition states that the total influx per unit axial length into the catheter is proportional to the pressure difference between the catheter interior and exterior, as used by Refs. [171, 172]. Here, Λ is the effective wall permeability factor that quantifies the permeability to influx across the catheter wall, accounting for the wall and inlet hole geometry. With this formation, the no-slip and no-flux conditions on the wall boundary region Γ_w can be obtained from the condition on Γ_p by setting $\Lambda = 0$. The union of regions Γ_w and Γ_p is precisely the boundary region $r = r_i$. In the following, any permeability measure Λ defined on Γ_p can be extended to the entire boundary $r = r_i$ by setting $\Lambda = 0$ in suitable regions.

5.2.1.3 Axisymmetry and long, thin geometry

To make the governing equation tractable, the axisymmetric and long, thin geometry of the catheter lumen is leveraged to identify dominant terms. An axisymmetric flow profile of $\boldsymbol{v} = u(r,z)\boldsymbol{e}_r + w(r,z)\boldsymbol{e}_z$ is assumed.

The geometry of the catheter has a small aspect ratio: $\epsilon = r_i/L \sim 0.01$, and the Reynolds number $Re \approx 4$, see Section A.1. Therefore $\epsilon^2 Re$ and ϵ^2 are both small and terms of this order in the governing equations can be neglected. For example, the inertial terms $(\boldsymbol{v}\cdot\nabla)\boldsymbol{v}$ scale with $\epsilon^2 Re$ and are consequently neglected. It is well established by lubrication theory (see Refs. [190] or [193]) that the leading order equations for axisymmetric flow in this parameter domain are:

$$0 = \frac{\partial p}{\partial r}, \quad 0 = -\frac{\partial p}{\partial z} + \mu\frac{1}{r}\frac{\partial}{\partial r}\left(r\frac{\partial w}{\partial r}\right), \quad \frac{1}{r}\frac{\partial}{\partial r}(ru) + \frac{\partial w}{\partial z} = 0, \tag{5.6}$$

which are solved subject to the following boundary conditions (neglecting the terms involving the fluid stress tensor which is of order $o(\epsilon^2)$)

$$u = 0 = w \quad \text{at} \quad z = 0, \tag{5.7}$$

$$w = 0, \quad u = \Lambda(z)(p - p_0) \quad \text{at} \quad r = r_i, \tag{5.8}$$

$$p = 0, \quad 2\pi\int_{r=0}^{r_i} wr\,dr = Q \quad \text{at} \quad z = L, \tag{5.9}$$

along with regularity of all fields at $r = 0$. These conditions correspond to static fluid at the closed catheter tip at $z = 0$, unidirectional fluid flow at the outlet with the integral equation giving the total prescribed flux, and with the pressure set to zero. Flow into the permeable boundary ($r = r_i$) is solely in a direction normal to the boundary, with magnitude determined by the wall permeability, and the pressure difference across the wall.

This system can be solved for a given $\Lambda(z)$, with the unknown p_0 calculated as a solution of the problem. Solving Equations (5.6) with boundary conditions given in Equations (5.7) generates a second order ordinary differential equation for p:

$$\frac{d^2p}{dz^2} = \frac{16\mu}{r_i^3}\Lambda(z)(p - p_0), \tag{5.10}$$

$$\frac{dp}{dz} = 0 \quad \text{at } z = 0, \quad \text{and} \quad \frac{dp}{dz} = -\frac{8\mu}{\pi r_i^4}Q, \quad p = 0 \quad \text{at } z = L. \tag{5.11}$$

The fluid velocity components w and u are defined in terms of p as follows

$$w = \frac{1}{4\mu}\frac{dp}{dz}(r^2 - r_i^2) \quad \text{and} \quad u = \frac{1}{16\mu}\frac{d^2p}{dz^2}(2rr_i^2 - r^3). \tag{5.12}$$

The axial flux through a cross-section of the catheter at any point z (defined as $q(z)$) can also be calculated:

$$q(z) = 2\pi \int_0^{r_i} wr dr = -\frac{\pi r_i^4}{8\mu}\frac{dp}{dz}. \tag{5.13}$$

5.2.1.4 Permeability formulation

Here, a form of the permeability factor $\Lambda(z)$ is established which reconciles the ROM with realistic catheter designs while avoiding introducing new parameters which require calibration. Assuming parabolic Poiseuille flow through each inlet hole, in line with the work of Ref. [171], an expression for Λ is calculated which combines each inlet hole's contribution linearly.

A cylindrical inlet hole with cross section radius $r_h^{(n)}$, height $r_o - r_i$ and positioned at axial position $z_h^{(n)}$ has a resistance to flow proportional to the fourth power of its radius, and inversely proportional to its height [193]. The inlet hole experiences a pressure differential of $(p_0 - p(z_h^{(n)}))$ and therefore permits a influx q_{hole} of

$$q_{\text{hole}} = \frac{\pi r_h^4}{8\mu(r_o - r_i)}(p_0 - p(z_h^{(n)})). \tag{5.14}$$

The inlet hole occupies part of the catheter wall within the region $z \in [z_h^{(n)} - r_h^{(n)}, z_h^{(n)} + r_h^{(n)}]$. In the ROM, this inlet hole is replaced by an axisymmetric permeable boundary region occupying all of $\{z \in [z_h^{(n)} - r_h^{(n)}, z_h^{(n)} + r_h^{(n)}], \theta \in [0, 2\pi]\}$. The flux into the catheter lumen over this section of the catheter boundary is given by

$$q_{\text{ROM}} = \int_z \int_\theta u(r = r_i, z)\, r d\theta dz \approx 2r_h \cdot 2\pi r_i \cdot u(r = r_i, z = z_h^{(n)}), \tag{5.15}$$

with the approximation assuming the fluid velocity does not change significantly in the interval $z \in [z_h^{(n)} - r_h^{(n)}, z_h^{(n)} + r_h^{(n)}]$. This is an approximation which will be more valid with small-radius inlet holes, when $r_h^{(n)}$ is small.

An expression for Λ is derived by equating Equations (5.14) and (5.15), so that the ROM permits the same influx into the catheter lumen as a cylindrical

inlet hole. Substituting in for u using the permeable wall boundary condition in Equation (5.5) gives

$$2r_h^{(n)} \cdot 2\pi r_i u(r = r_i, z = z_h^{(n)}) = 4\pi r_i r_h^{(n)} \ \Lambda(p - p_0) = q_{\text{hole}} = \frac{\pi (r_h^{(n)})^4}{8\mu(r_o - r_i)}(p - p_0), \tag{5.16}$$

hence

$$\Lambda(z) = \frac{1}{32\mu r_i (r_o - r_i)}(r_h^{(n)})^3 \quad \text{for } z \in [z_h^{(n)} - r_h^{(n)}, z_h^{(n)} + r_h^{(n)}]. \tag{5.17}$$

The contributions from each hole are summed linearly over n to account for all inlet holes in the catheter design, hence

$$\Lambda(z) = \sum_n \frac{1}{32\mu r_i (r_o - r_i)} \left(r_h^{(n)}\right)^3 \mathcal{I}_{[z_h^{(n)} - r_h^{(n)},\, z_h^{(n)} + r_h^{(n)}]}, \tag{5.18}$$

where $\mathcal{I}_{[a,b]}$ indicates the indicator function taking value 1 between a and b, and 0 elsewhere.

This form of Λ gives a step function, with Λ taking positive values in regions of the catheter where inlet holes are present, and $\Lambda = 0$ in regions of the catheter where no holes are present. This expression for Λ therefore holds for all $z \in [0, L]$, maintains detail of hole placement, and is simple to calculate, with no unknown parameters to calibrate. It does, however, make several approximations on the fluid flow in the junction region between inlet hole and catheter: inlet holes are modelled as cylinders with circular cross section, height equal to the width of the catheter wall $(r_o - r_i)$, and small aspect ratio (inlet hole radius $r_h^{(n)}$ is much less than inlet hole height $(r_o - r_i)$). In the ventricular catheter examples in the ground-truth dataset, inlet holes are conical, and may have a hole radius close to that of the catheter wall width. Disagreement between simple models incorporating Poiseuille assumptions (like the ROM here) and models resolving full flow detail have been previously observed, with discrepancies of up to 30% when considering the flux in a branching channel [195, 196, 197], with effects such as eddies, flow reversal and recirculation seen in the junction region of more complex models [198, 199, 200].

To attempt to reconcile the simple model presented in the ROM with the more complex flow behaviours seen in fully resolved models, the behaviour of a fluid particle entering an inlet hole is considered. In the ROM, the fluid particle travels in the radial direction while in an inlet hole, but upon entering the lumen

of the catheter immediately switches to travelling in a purely axial direction. In contrast, Figure 5.5 shows the fluid streamlines entering the catheter through an inlet hole in a 3D FSI simulation. Colour shows the length of the streamline, as measured from the top of the inlet hole. The height of the inlet hole is 0.5 mm, but the majority of the fluid travels a longer path, before making a 90° turn and joining the main flow at the black line which shows the edge of the inlet hole. The extra length of this path is not currently included in in the ROM.

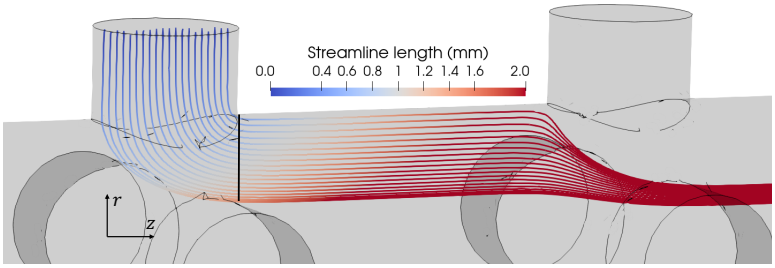

Figure 5.5: Visualisation of 20 selected streamlines entering the catheter through a single inlet hole. Colours shows the length of the streamline as measured from the top of the inlet hole. The black vertical line indicates the edge of the inlet hole.

To account for this extra length, a heuristic adjustment to the permeability expression is suggested as follows:

$$\Lambda(z) = \sum_n \frac{1}{32\mu r_i(r_o - r_i + r_h/2)} \left(r_h^{(n)}\right)^3 \mathcal{I}_{[z_h^{(n)} - r_h^{(n)},\, z_h^{(n)} + r_h^{(n)}]}. \tag{5.19}$$

The additional factor of $r_h/2$ accounts for the extra length the fluid particles travel when entering the catheter lumen from an inlet hole. Appendix B.2 contains further justification of this choice of heuristic, using material and results that will be published in Ref. [190].

5.2.2 Permeable model agreement

In this section the accuracy of the permeable ROM is tested by comparing the permeable model results (using the augmented permeability expression from Equation (5.19)) with results from the flow fields of the 3D FSI model, with governing equations presented in Section 3.3. Specifically, the pressure taken along the centreline of the catheter lumen $p(r = 0, z)$ and the axial flux $q(z)$ are calculated from both models and compared.

For a specific catheter design, the arrangement and size of inlet holes can be translated to the effective wall permeability function $\Lambda(z)$. This function is non-zero at z values corresponding to inlet holes. The r_h^3 term in the expression for permeability, Equation (5.19), means that larger inlet holes dominate the function.

Figure 5.7 shows the FSI and permeable model results for three catheter designs. Subfigures a), c), and e) show the effective wall permeability (left), the centreline pressure (middle) and the cross-section flux (right). Subfigures b), d), f) show visualisations of the corresponding catheter designs. The catheter geometries shown are taken from the ground-truth dataset described in Section 5.1, and the inlet hole parameters of the three examples are given in Appendix B.3. In the three designs shown in Figure 5.6 the agreement is very good between the permeable model and FSI results. The three designs portrayed show a range of permeability profiles: the first design shown in subfigures a) and b) has a large number of inlet holes across the length of the catheter. The second and third designs have many more sparsely positioned inlet holes, with clear "jumps" in the flux profile that correspond to the position of the inlet holes. The second design has smaller holes, with the permeability values never above 0.05 $\text{mm}^2\text{s/g}$, while the third design has a maximum permeability of 0.5 $\text{mm}^2\text{s/g}$.

Agreement between the model and simulation is quantified for designs across the ground-truth dataset by calculating the relative percentage error (RPE) of the cross-section flux. As seen in the derivation of the model, the cross-section flux is proportional to the derivative of the pressure curve so this measure captures the agreement of both flux and pressure. The RPE is

$$\text{RPE} = 100\ \frac{\int_{z=0}^{L}(q_{\text{permeable}} - q_{\text{FSI}})\ dz}{\int_{z=0}^{L} q_{\text{FSI}}\ dz}\%. \tag{5.20}$$

This is nevertheless an integrated quantity, with the axial flux itself being integrated over the radial coordinate. The RPE therefore provides an overall view of model agreement across the whole catheter with less focus on spatial fluctuations in the radial direction. In particular, there is likely to be higher level of model disagreement near the junction of the inlet holes and catheter lumen, which may not be highlighted in the RPE measure.

Figure 5.7 shows the RPE between the permeable and FSI models for all catheter designs in the ground-truth dataset. The agreement with the permeable

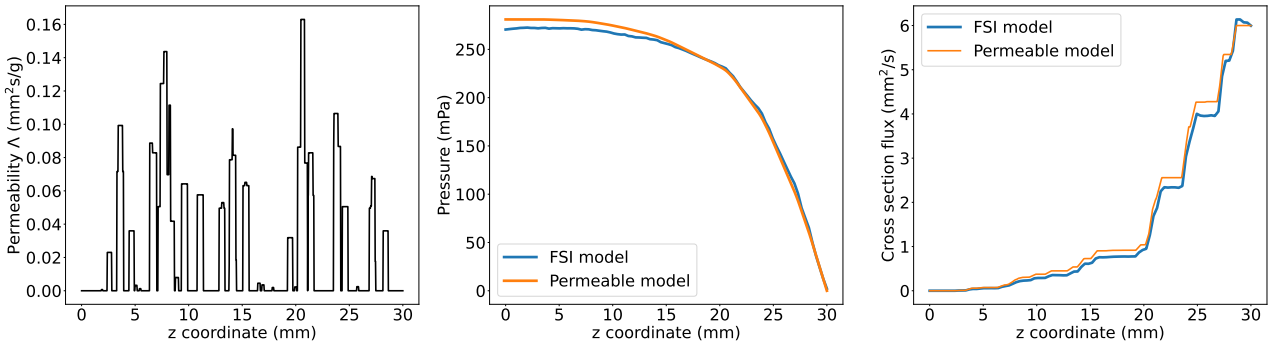

(a)

(b)

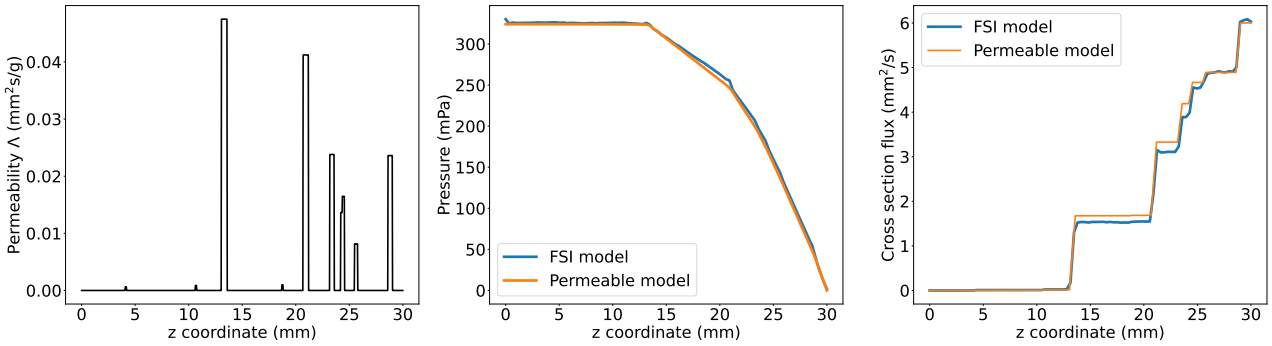

(c)

(d)

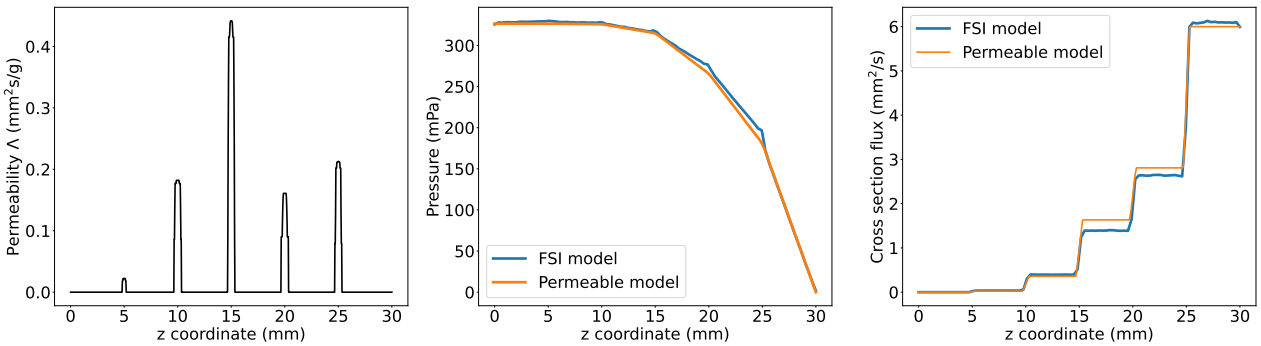

(e)

(f)

Figure 5.6: Examples of agreement between 3D FSI model and permeable model for three different catheters.

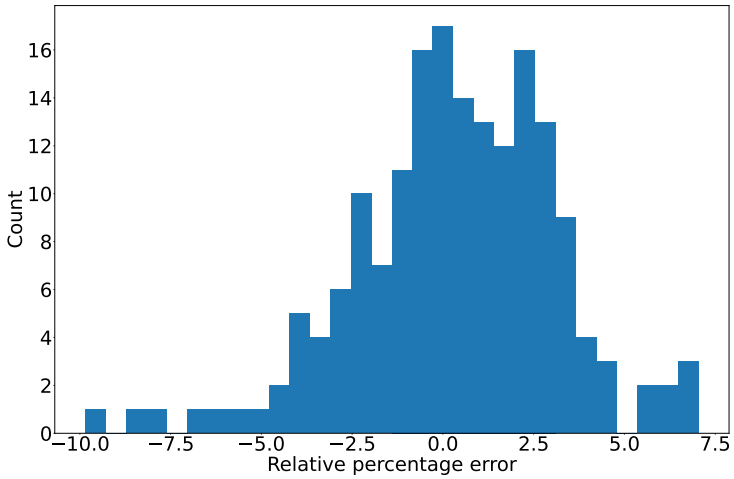

Figure 5.7: Relative percentage error between the permeable model and 3D FSI model results for every design in the ground-truth dataset.

model is good, with all the dataset within 10% relative error, and 80% of the data has a RPE of less than 3.4% (the 10^{th} and 90^{th} quartiles are, respectively, -3.07% and 3.37%). This agreement is very good, particularly considering the number of simplifying assumptions within the permeable model (constant external pressure, axisymmetric flow, narrow aspect ratio of inlet holes) which do not necessarily hold in the computational FSI model. The RPE is an integrated metric evaluated along the catheter centreline of the FSI model. Discrepancies between the ROM and FSI model are expected to be largest near the inlet hole–lumen junctions, where significant radial velocities and inherently three-dimensional, non-axisymmetric flow structures arise, violating the assumptions of the ROM. However, the strong agreement in centreline RPE indicates that such localised errors at the catheter wall, Γ_p, do not propagate significantly into the core lumen flow.

Additionally, model errors are concentrated in the junction regions where inflow from the inlet holes merges with the axial lumen flow. These regions occupy only a small fraction of the total catheter length L, and are consequently downweighted in the integrated RPE.

The permeable model evaluates in under one second, providing a rapid and sufficiently accurate approximation of the catheter flow field. While discrepancies are expected near inlet junctions, the ROM accurately captures centreline quantities such as pressure, as well as integrated measures such as axial flux. Previous

studies on catheter design have focused on achieving uniform CSF influx across inlet holes, using this as a proxy for reduced ChP deformation, and have relied on computationally expensive finite volume methods (FVM). The strong agreement in axial flux between the permeable model and the FSI model (which employs FVM for the fluid phase) suggests that the ROM is an effective *a priori* surrogate for optimisation studies focused on metrics derived from fluid flux, as in [15].

5.3 Stress field on the Choroid Plexus

Here, a second ROM using physical reductions motivated by the 3D FSI model, is introduced. The FSI is critical to predictions of the full model, but is computationally expensive, requiring 5-10 iterations of the fluid and solid parts to converge to the static equilibrium position, with each iteration taking $\sim$8 hours to complete.

As the ChP deformation is driven by the stress exerted by the surrounding fluid on the surface of the ChP, the fluid stress field can be thought of as a reasonable proxy for ChP displacement. In fact, at the first iteration of the 3D FSI model, the deformation of the solid is driven solely by the initial fluid stress field on the ChP surface as the geometry of the ChP is still in its initial configuration, i.e., undeformed.

This ROM is proposed to focus on the initial fluid stress field, with the ChP in its initial, upright position. Solving for the initial fluid stress field requires a fluid-only model, with the same governing equations as the fluid part presented in Section 3.3. All fluid domain boundaries are modelled as rigid as FSI effects are discarded. This model requires a single `openFOAM` simulation (configured in the same way as the fluid part of the FSI model, as discussed in Chapter 3), which has a runtime of under 10 minutes, significantly below the computational requirements of the full 3D FSI model.

The initial fluid stress field drives initial ChP deformation, and Figure 5.8 shows a strong correlation between the maximum displacement of the ChP at equilibrium, and the maximum displacement of the ChP after one iteration of fluid and solid parts has been performed, with a data point for each simulation in the ground-truth dataset. As discussed in Chapter 4, collision events occur for displacement $\geq$0.55 mm. If this occurs then the simulation terminates with a maximum equilibrium ChP displacement of 0.55 mm, which can be seen in

the horizontal line of points at the top of the figure. Calculating the Pearson's

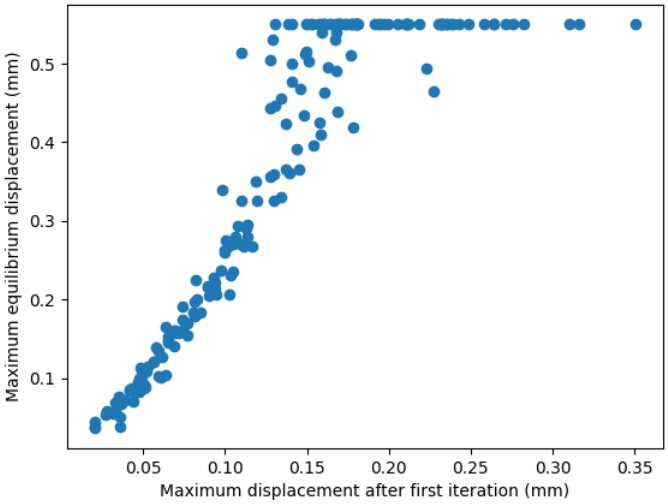

Figure 5.8: Maximum ChP displacement at equilibrium against maximum displacement after one iteration for every 3D FSI simulation in the ground truth dataset.

correlation coefficient for all points in the ground-truth dataset gives a value of 0.90. Examination of Figure 5.8 shows 58 of the simulations in the ground-truth dataset underwent a collision between the catheter and ChP (indicated by a maximum equilibrium ChP displacement of 0.55 mm). The points which have not undergone a collision event (indicated by a maximum equilibrium ChP displacement less than 0.55 mm) show a strong linear trend between the initial and equilibrium ChP displacement, and evaluating Pearson's correlation coefficient on data with maximum equilibrium displacement < 0.55 mm gives a value of 0.94.

Intermediary iterations in the FSI model are non-physical, but the strong correlation seen in Figure 5.8 suggests that the ChP displacement after the first iteration is strongly related to the maximum equilibrium displacement. Therefore the initial fluid stress field on the ChP surface is also expected to be informative for equilibrium ChP displacement.

The correlation between initial and equilibrium maximum displacements is particularly strong when the maximum displacement is low. In the optimisation of future chapters, a low maximum ChP displacement at equilibrium defines a more successful catheter and hence it is particularly important to design ROMs

which are informative in regions of low maximum equilibrium displacement. The initial stress field is therefore particularly appropriate for this optimisation as the correlation is stronger in this area.

This relationship is emphasised in Figure 5.9, which shows visualisations of an example catheter (Figure 5.6 d), with parameters given in Appendix B.3) taken from the ground-truth dataset. The Figure shows the boundary of the ventricle domain and catheter (black lines) with the magnitude of the initial deviatoric stress vector (subfigure a)) and the equilibrium displacement of the ChP (subfigure b)) shown on the ChP surface. The region of high initial fluid stress in Figure 5.9 a) corresponds to the region of highest equilibrium displacement in Figure 5.9 b). The region of high stress can be seen to correspond to one inlet hole, which is neither the largest nor the closest to the outlet, but does have significant effect on the deformation of the ChP.

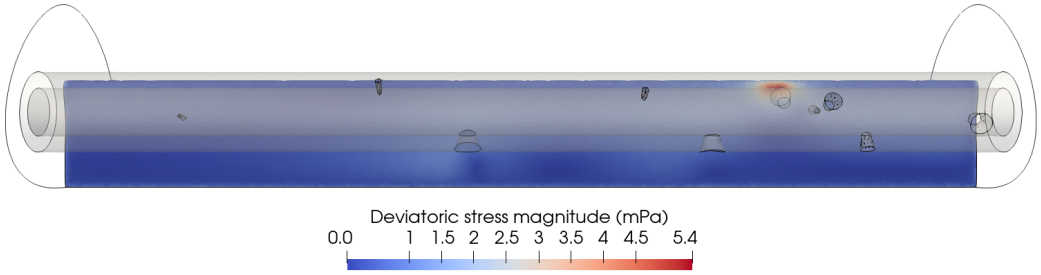

(a)

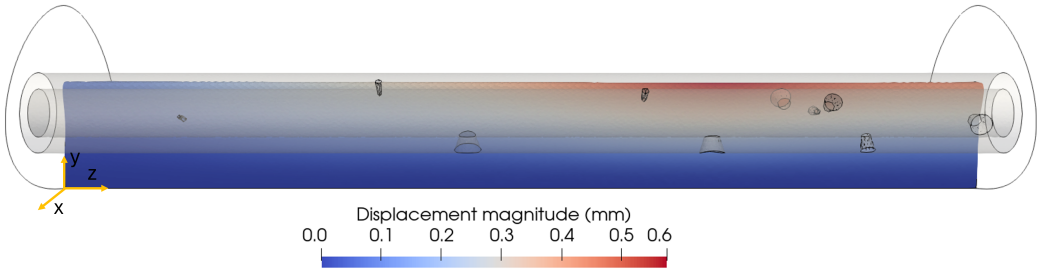

(b)

Figure 5.9: Side view visualisation of the initial fluid stress (a) and equilibrium displacement (b) fields for an example catheter. Ventricle domain and catheter outline shown in black, mutual coordinates shown on the lower figure.

5.4 Chapter summary

This chapter developed two ROMs motivated by the results of the 3D FSI model. The CSF flow through the inlet holes and down the centre of the catheter have previously been a focus of computational studies to improve hydrocephalus design [15, 86]. Motivated by this, a permeable wall ROM is developed and employed in a simple, 1D linear model for flow through the catheter interior. Several assumptions are required to complete the model: assuming that the flow is axisymmetric with the fluid external to the catheter held at a constant pressure and the fluid in the catheter inlet holes taking a parabolic, Poiseuille profile. These assumptions are all simplifications of the detailed 3D FSI model, but, nevertheless, agreement between the fluid pressure and velocity fields was shown to be good when comparing between the ROM and FSI simulations.

The second ROM presented discards the FSI, and focusses on the initial fluid stress field on the surface of the ChP, treating the ChP as a rigid boundary of the fluid domain. The high correlation seen between the maximum equilibrium ChP displacement, and the maximum displacement after one solid iteration suggests that the initial stress field is directly related to the maximum equilibrium ChP displacement. In the following chapter, ML is used to establish and quantify this relation.

Chapter 6

Surrogate model development

The creation of a surrogate model that will replace the full FSI model in the optimisation process needs to be done carefully. Any approximation of the full domain will, by definition, not contain all the available information, and must balance the need for simplicity and speed with a model that contains sufficient information to discriminate between designs. The surrogate model created for this thesis therefore has three requirements:

- accurate predictor (either directly or indirectly) of ChP deformation,
- computationally fast to run,
- mechanistically motivated.

Being able to accurately predict the results of the 3D FSI model is the main requirement of a surrogate. For the optimisation to run in a realistic computational time, the surrogate model must also be fast to evaluate. A comprehensive optimisation will require at least 1,000 designs to be assessed, and multiple fitness evaluations may be needed for any one design (for instance, to test different values of α, as seen in Figure 4.1). Being mechanistically motivated is not a strict requirement of a surrogate model, but helps to improve the interpretability, particularly in models incorporating ML methods, which often operate as black boxes. Interpretability gives confidence that the ML is identifying key mechanisms of the domain instead of focussing solely on correlated patterns in the data. Incorporating the predictive power of ML into mechanistically-motivated ROMs is a process known as mechanistic learning (MxL), and will be implemented here.

To satisfy these requirements of the surrogate model, a ML layer is combined with the reduced-order models (ROMs) presented in the previous chapter to create a strong predictor of ChP displacement. Unlike the 2D FSI presented previously, the ROMs proposed in Chapter 5 cannot be used to directly examine the ChP, as they focus on different areas and mechanisms of the system and do not directly give the fitness value required by the optimisation. A ML layer is therefore used to establish and quantify possible correlations between outputs of the ROM and the fitness value, i.e., the ChP displacement. This composite model (ROM and ML layer) is referred to as the surrogate model, as seen in light red in Figure 6.1.

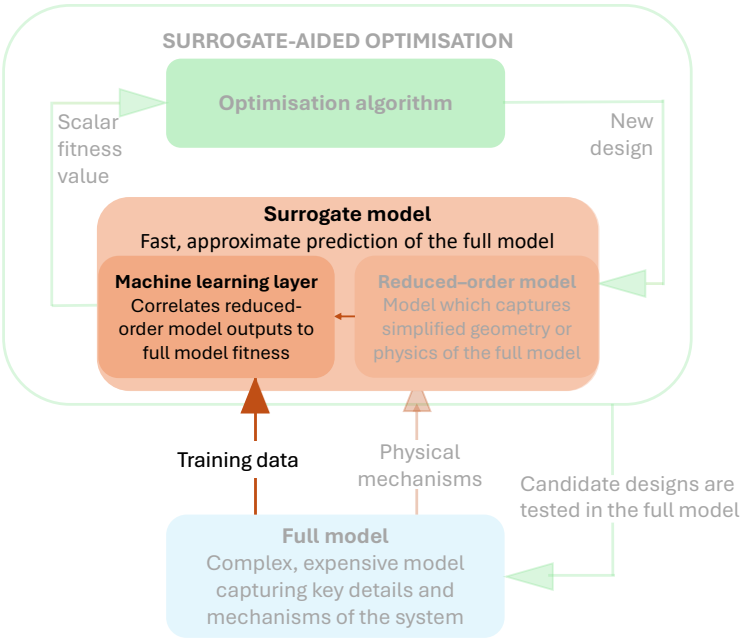

Figure 6.1: Optimisation methodology, highlighting the surrogate model component, which combines ROMs and an ML layer and is the focus of this chapter.

6.1 Machine learning language

The surrogate models presented in this chapter predict the maximum equilibrium displacement over the surface of the ChP for a given catheter design. The maximum displacement takes values in the interval [0 mm, 0.55 mm] (a range which spans from no movement of the ChP, up to collision with the catheter). Hence

predicting this value is a regression problem, in which known input data $\boldsymbol{x}$ are used to predict an output scalar y. Here, y is always the maximum equilibrium displacement of the ChP. In this chapter, the effect of different input vectors $\boldsymbol{x}$ is explored. The input data could be simply the parameters determining catheter design, or could be more complex data taken from one of the ROMs of the previous chapter: for example, $\boldsymbol{x}$ could be the values of the fluid pressure field sampled along the centreline of the catheter from the permeable wall ROM. Whatever the source, the input data $\boldsymbol{x}$ must be formatted as a 1D vector of constant length, whose components are called "features".

Regression problems can be phrased as searching for the best function f such that the error ϵ, defined as

$$\epsilon := ||y - f(\boldsymbol{x}, \boldsymbol{\beta}, \boldsymbol{\lambda})||$$

is minimised, for some norm $||\cdot||$, typically L_2. In this research, the form of f is predetermined by the ML algorithm being investigated, but the internal parameters $\boldsymbol{\beta}$ and $\boldsymbol{\lambda}$ are *a priori* not. The vector of hyperparameters $\boldsymbol{\lambda}$ are user-set and constant, and control factors such as the learning rate or penalty costs of the algorithm. The weights vector $\boldsymbol{\beta}$ is selected by the algorithm to minimise ϵ in a process known as "training" or "fitting" an ML model to a specific set of data. This process is itself an optimisation, with constraints imposed through the choice of $\boldsymbol{\lambda}$. The optimal $\boldsymbol{\beta}$ is also affected by the choice of $\boldsymbol{x}$ and y used in training.

In this chapter, the various input datasets considered are derived from the ground-truth dataset, described in Section 5.1. The ground-truth dataset is indexed by i, where each i represents a different 3D FSI simulation ($i \in \{1, ..., 180\}$) with $\boldsymbol{x}_i$ and y_i thus being the input and output data associated with the i^{th} ground-truth simulation.

The 3D FSI simulations with accompanying ROM results contain a large amount of information. Consequently $\boldsymbol{x}_i$ need to be defined, e.g., the input data $\boldsymbol{x}_i$ could be the vector of design parameters associated with the catheter in simulation i. Alternatively, $\boldsymbol{x}_i$ could be a vector of fluid velocity values along the catheter centreline, as calculated by the permeable model ROM for the catheter design used in ground-truth simulation i. The components of the vector $\boldsymbol{x}_i$ are

commonly called features. For all input datasets considered, the output y_i remains the same, as the aim is always to predict the maximum equilibrium ChP displacement.

This chapter now looks to identify the most promising combination of ML algorithm (with associated hyperparameters) and input data $\boldsymbol{x}_i$ to create a strong prediction layer for the surrogate model.

6.2 Machine learning algorithms

The choice of input data, ML algorithm and ML hyperparameters are found by testing for best fit to the ground-truth dataset. The majority of ML algorithms tested are taken from the `python3` module `scikit-learn`[201], with the exception of the extreme gradient boosted regressor XGBoost which is taken from the package `XGBoost` [202].

Given the small size of the ground-truth dataset (180 data points), it is especially important to ensure that models do not overfit to the data. Overfitting is the detrimental hyper-specialisation of the model, which often occurs with an overly complex model with a high number of internal parameters capturing too much of the details of the training data, and consequently being less able to generalise to new data points. To prevent overfitting, a robust validation process with nested layers of cross-validation is used, described in detail below. The simplest ML models are tested first, as simpler models with fewer internal parameters are less likely to overfit the data. The most complex model tested is a multi-layer perceptron (MLP), a neural network model with a larger number of hyperparameters compared to the other models tested. It was not found to outperform simpler models (due to its high number of internal parameters which makes it more susceptible to overfitting), and so more complex deep neural networks are not investigated.

Below is a summary of the ML models tested, with a brief description of each. These are roughly arranged in order of increasing complexity, and consequently increasing runtime and number of hyperparameters. For more information about the precise formulation, benefits and drawbacks of each method, Ref. [203] is one of many detailed works on the subject.

- **Linear regression:** simple model where all features contribute linearly to the prediction [204].

- **Ridge regression:** linear regression with a penalty term of $\lambda_1||\boldsymbol{\beta}||$ using the L_2 norm [205].
- **Lasso regression:** linear regression with a penalty term of $\lambda_1||\boldsymbol{\beta}||$ using the L_1 norm [206].
- **Support vector regression:** uses hyperplanes to divide data into regions associated with a specific output [207].
- **Bayesian ridge regression**: ridge regression with additional Bayesian techniques to quantify uncertainty in the parameter estimates [208].
- **Decision tree regressor**: graphical method using a tree structure to separate data into different leaf nodes, each associated with a specific output [209].
- **Random forest regressor**: ensemble of (small), randomly initiated decision trees, each contributing information to the output value [210].
- **Gradient boosted regressor**: random forest method with extra optimisation layer in the initialisation step. XGBoost is a version of this [202].
- **Multi-layer perceptron**: simple neural network with one or two hidden layers and connections between all hidden layers [211].

6.3 Input data

The 3D FSI simulation i from the ground-truth dataset provides the value of y_i. The surrogate model used in the optimisation of future chapters must be rapid to execute, and therefore the input data of the ML layer must be quick to generate. This precludes the use of the 3D FSI model in generating input data. However the ROMs described in Chapter 5 are both sufficiently fast, and can be used to generate the input data $\boldsymbol{x}_i$. The aim of this chapter is to identify the form of $\boldsymbol{x}_i$ that gives the best predictions.

The length, and components (features) of $\boldsymbol{x}_i$ are not *a priori* determined. In general, more features will always increase predictive power, and any non-informative feature can be ignored by the algorithm when creating the prediction

of y_i (for example by having its coefficient set to zero in the contribution). However, each new feature adds a further dimension to the input space. It is always desirable to have more ground-truth data points than features, to allow for good estimation of the weight vector $\boldsymbol{\beta}$, and to reduce overfitting. Here, the number of ground-truth data points is fixed at 180, as discussed in Section 5.1.

Table 6.1 shows examples of potential input data that can be extracted from the ROMs, also noting the corresponding number of features for each input data. This selection of input data form is by no means exhaustive. For example, the

Table 6.1: Model parameters.

Preposed ROMs	**Data features**	**Feature size**
Catheter design parameters	Radius, z position and offset angle ϕ for each inlet hole	$3 \times 40 = 120$
Permeable fluid model	Flux and pressure fields sampled down the catheter centreline	$2 \times 100 = 200$
Initial fluid stress field on ChP	Pressure and three components of viscous fluid stress sampled across the ChP surface	$(9 \times 99) \times 4 = 3564$
All input data	All of the above	3884

fluid stress field on the ChP requires one fluid simulation to be run, which contains data from all the fluid fields such as the fluid velocity and pressure at every point in the domain. The choice to extract only data from the ChP surface is motivated by a mechanistic understanding of the domain: that the stress field on this subdomain strongly influences ChP deformation. The set of catheter design parameters is included as an ML input option, though this dataset is not the result of a mechanistically driven model.

6.3.1 Data preprocessing

Before beginning to train a ML model, input data should be analysed, and if necessary, preprocessed. Input data may contain missing values or outliers, which need to be removed to prevent them skewing the model prediction. Here

the ground-truth data is derived from deterministic models, and convergence is checked through internal methods in the FSI model. There are therefore no missing values in the set y_i. All catheter designs in the ground-truth dataset are feasible designs, and therefore not outliers, and so the dataset is kept complete.

In certain applications, the features of a given input dataset are modelled as mutually dependent random variables, with $\boldsymbol{x}_i$ representing the i^{th} sample of the features. Under this interpretation, the dataset comprises independent samples drawn from the underlying feature distribution. For input data with continuous values, as is always the case here, it is advisable to scale each feature such that the sample set for any one feature has a sample mean of 0 and sample standard deviation of 1. This ensures that different features contribute the same weight to parameter estimations and allows the features weights to be directly compared when determining feature importance.

A second preprocessing step undertaken here is dimensionality reduction. Working in a low-dimensional feature space is generally beneficial for ML models. Each ground-truth simulation corresponds to a single point in this feature space, for which the target value y_i is known. When the number of simulations is large relative to the dimensionality of the feature space, the relationship between the features and y_i is more densely sampled, improving the ML model's ability to learn the underlying mapping. Dimensionality reduction algorithms seek to find a low-dimensioned representation (often a projection) of an input dataset that maintains key relationships such as variance. Principal component analysis (PCA) [212] is a common choice of dimensionality reduction, and will be used here, though other algorithms such as uniform manifold approximation and projection (UMAP) and t-distributed stochastic neighbor embedding (t-SNE) are well established [213].

Using the random variable formulation of input data discussed above, the sample covariance matrix is the matrix with (j, k) entry equal to the covariance between features j and k. The j^{th} diagonal entry corresponds to the sample variance of feature j and the total sample variance is the sum of the diagonal. PCA projects the input data through an orthogonal transformation onto component vectors that maximise the sample variance (i.e., the first PCA component is the linear combination of features that itself has the greatest sample variance, the second PCA component is the linear combination of features that has the next greatest sample variance and is orthogonal to the first component etc.).

This preserves total sample variance as the trace of a matrix is preserved under orthogonal transform. As PCA seeks to maximise variance, it is especially important to scale all features to unit variance first, to prevent the PCA artificially prioritising features taking larger values.

The "explanatory" dimension of the input data is defined here as the number of PCA components that contains the majority of the sample variance. By definition, PCA components are ordered so that the first component has the largest variance, the second component the second largest and so on. For highly correlated data, such as is seen on the fluid stress field model (where neighbouring features will have highly related values), the explanatory dimension can reduce drastically after an application of PCA. This is useful as it gives a better sense of the ratio of dataset size to feature dimension. Table 6.2 shows the number of PCA components required to explain 95% and 99% of the total sample variance, for each of the input datasets. In each case, the explanatory dimension is now smaller than the size of the ground-truth dataset (180). This increases confidence that the ML models will be able to predict from the training set without overfitting.

Table 6.2: PCA on input data.

Input data	Total number of features	Number of features required to explain	
		95% of variance	99% of variance
Catheter design parameters	120	11	24
Permeable fluid model	200	11	22
Fluid stress field on ChP	3564	57	101
All input data	3884	61	108

Figure 6.2 shows the variance of the PCA components (given cumulatively as a fraction of the total sample variance), for the data taken from the fluid stress model. The number of components needed to explain 95% and 99% are shown by vertical lines. By design, the first PCA component explains the maximum

possible variance, and each subsequent component explains a smaller fraction of the total variance. This is particularly noticeable in Table 6.2 where the 4% difference in variance between 99% and 95% requires nearly the same number of extra components as the first 95%.

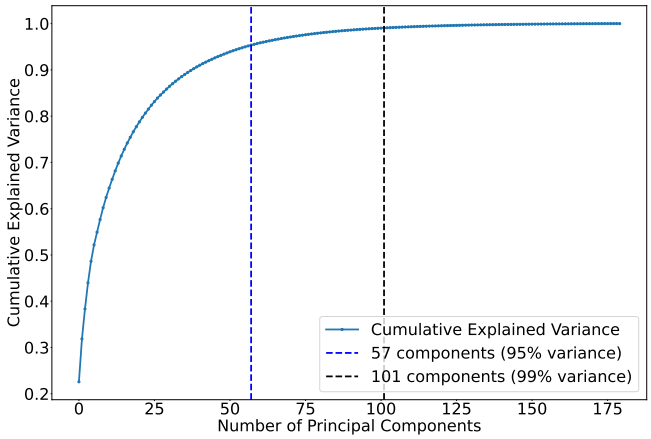

Figure 6.2: Cumulative variance explained by subsequent PCA component vectors for fluid stress dataset, normalised to a total variance of 1.

PCA is successful at investigating the explanatory dimension of a dataset. Separately, it is sometimes beneficial to take the low-dimension projection (the projection onto the first PCA component vectors that contain, for example, 95% of the sample variance) instead of the raw data as input into a ML model. Using PCA transformed data reduces the impact of highly correlated features (which can lead to unstable estimates of $\boldsymbol{\beta}$). However, PCA-transformed data is less interpretable as each new feature is a linear combination of all existing features and therefore lacks a direct physical interpretation.

This chapter has, so far, described the various input datasets available from the ground-truth dataset and the machine learning algorithms that are appropriate for use on this input data. The chapter now turns to identifying the combination of ML algorithm and input data which is best able to predict the maximum ChP displacement.

6.4 Assessing machine learning models

6.4.1 Accuracy metrics

Above, a selection of ML algorithms and input datasets have been presented. To decide the optimal combination of model and dataset for the surrogate model the fit of each combination needs to be evaluated. Various accuracy metrics are used to assess the efficacy of an ML model for specific input data.

A popular accuracy metric is the R^2 score (coefficient of determination), defined as

$$R^2 = 1 - \frac{\sum_i (y_i - f(\boldsymbol{x}_i))^2}{\sum_i (y_i - \overline{y})^2}, \tag{6.1}$$

where $\overline{y}$ is the mean of y_i, and $f(\boldsymbol{x}_i)$ is the ML model applied to input data $\boldsymbol{x}_i$ (the ML approximation of the output data). If $R^2 = 1$, the data is perfectly explained by the model, and $R^2 = 0$ means that the ML model has the same efficacy as a model that returns the mean for any input values (i.e., $f(\boldsymbol{x}) = \overline{y}$ for all $\boldsymbol{x}$). Negative R^2 scores indicate a model that performs very poorly, and should be discarded.

A second metric is Spearman's correlation coefficient ρ, which focusses on the order of the y_i, as opposed to the specific value obtained. The y_i are ordered by value into an ordered list, and the rank of a y_i is the position in the list. Spearman's correlation coefficient is defined as

$$\rho = 1 - \frac{6}{n(n^2-1)} \sum_i d_i^2, \tag{6.2}$$

where d_i is the difference between the rank of the true value y_i and the rank of the prediction $f(\boldsymbol{x}_i)$, and n is the dataset size. A value of $\rho = 1$ indicates perfect preservation of the ranking, while $\rho = 0$ indicates no monotonic relationship. Unlike R^2, Spearman's coefficient detects any monotonic trend, not just linear relationships. Rank-based metrics such as Spearman's ρ are most commonly used to compare relative performance between methods across multiple cases; while they can be used as an accuracy metric, this is not their primary application and other metrics such as R^2 are better. As ρ depends only on ranks, it provides no information about the magnitude of prediction errors.

Other popular metrics for assessing the fit of a ML model are root mean squared error (RMSE) and mean absolute error (MAE) which are defined respectively as:

$$\text{RMSE} = \frac{1}{n}\sqrt{\sum_i (y_i - f(\boldsymbol{x}_i))^2}, \quad \text{MAE} = \frac{1}{n}\sum_i |y_i - f(\boldsymbol{x}_i)|. \tag{6.3}$$

RMSE uses the L_2-norm, and is significantly influenced by outliers, whereas MAE gives a more balanced view that does not penalise outliers. Both of these metrics have the same dimension as y_i, here (mm).

All four of these metrics can be calculated for an ML model, and a good model will have ρ and R^2 close to 1, and low RMSE and MAE scores. Going forward, R^2 is selected as the metric as it gives a view of both model accuracy and rank preservation, and is directly interpretable (R^2 scores of 0.7 or more always indicate a good model, for example, whereas, e.g., MAE = 0.01 mm is dependent on the scale of the problem and thus is harder to evaluate as a "good" or "bad" score).

6.4.2 Cross-validation

To compare the ML models outlined above, the standard cross-validation algorithm is used [167]. A summary of this algorithm is given below.

Algorithm 4 Cross-validation

for ML model with hyperparameters $\boldsymbol{\lambda}$, **do**
  Initialise five folds: splitting the data into five equally (or close to equally) sized, distinct groups,
  for $i \in \{1 \dots 5\}$ **do**
    Select fold i to be the test set,
    The remaining four folds becoming the training set.
    Fit the ML model to the training data,
    Make predictions on the inputs of the test data,
    Compare predictions with outputs of the test data,
    Calculate the R^2 score for the fold.
  end for
  Calculate the mean and standard deviation of all fold scores.
end for
Identify the best ML models from the fold scores.

In short, this algorithm splits the input dataset into equally sized subsets called "folds". Here, the standard choice of five folds is used. For each fold, a ML model with known hyperparameters is fitted (the optimal $\boldsymbol{\beta}$ is identified) using the only the $\boldsymbol{x}_i$ and y_i in the remaining four folds. The trained model is then evaluated on the held-out ("test") fold by comparing its predictions with the corresponding y_i values. This procedure yields one R^2 score per fold, with model performance assessed on data that were not used during training.

Cross-validation makes efficient use of the available data, with each data point used four times for training and once for testing. This reduces sensitivity to any single train–test split and helps to prevent overfitting. Consistently high accuracy metrics across folds indicate that the model is identifying features that generalise well to unseen data and that similar features are deemed informative in each fold. Under these conditions, the model may be retrained using the full dataset to maximise the use of available information, as the dominant features are expected to remain unchanged.

6.5 Selection of machine learning models

Above, a range of ML models and input datasets have been proposed. To identify promising combinations the ML models are trained on each input dataset separately, and their predictive power compared. However, the ML algorithm is further influenced by the choice of user-set hyperparameters $\boldsymbol{\lambda}$. To correctly evaluate the best performance of each ML algorithm, the optimal hyperparameters $\boldsymbol{\lambda}$ for that model first need to be found.

The hyperparameters are model-specific, user-set parameters that control how the ML model trains on a dataset. These vary greatly in value and nature depending on the ML model used. For example in ensemble tree-based algorithms the hyperparameters give bounds on the depth and number of features allowed for any individual tree. Alternatively, a regularised regression model has hyperparameters controlling the relative weight of feature coefficient size to model accuracy.

To tune the hyperparameters the `GridSearchCV` function of `scikit-learn` is used. This function takes in a grid of potential hyperparameters and tests each combination to find the one that maximises the R^2 score for the dataset. The algorithm is outlined in Algorithm 5. This method is similar to Algorithm 4, but

contains an extra step in separating the data initially into training and validation sets.

Algorithm 5 Hyperparameter testing

Split the dataset into ten external validation folds.
for i $\in \{1, \ldots, 10\}$ **do**
  Fold i is the validation set.
  The remaining nine folds form the training set.
  for hyperparameter combination in `GridSearchCV` **do**
    Perform an internal five-fold cross-validation as outlined in Algorithm 4 on the training set (the nine remaining external folds),
  end for
  Save the hyperparameter combination with the best R^2 score,
  Retrain the model with optimal hyperparameters on all the training set,
  Evaluate model performance by calculating the R^2 score on the external validation fold.
end for
Models are ranked by the mean R^2 score across validation folds.

The withholding of the validation dataset throughout the hyperparameter testing allows the final, optimised ML model to be tested on a completely unseen set of data. This separation ensures that the model is not tested on any data which has influenced the choice of hyperparameters, and hence gives an unbiased view of the efficacy of the model. Given the limited size of the ground-truth dataset, allocating a single fixed 10% hold-out would leave too few examples for a reliable validation set. Therefore, a nested cross-validation procedure is used (Algorithm 5): the data are partitioned into ten external folds. In each round, one fold serves as the validation set while the remaining nine provide training data for internal cross-validation and hyperparameter tuning (Algorithm 4). After all ten rounds, models are ranked by the mean R^2 across the external validation sets. This gives a better view on the generalised performance of the algorithm. Full details of the tested hyperparameter ranges are provided in Appendix Tables C.1 and C.2.

Figure 6.3 shows the average R^2 score for the best hyperparameter configuration of each ML model applied to each dataset. Negative R^2 scores are truncated and given a value of 0, as any score ≤ 0 indicates poor performance and that the model should be discarded.

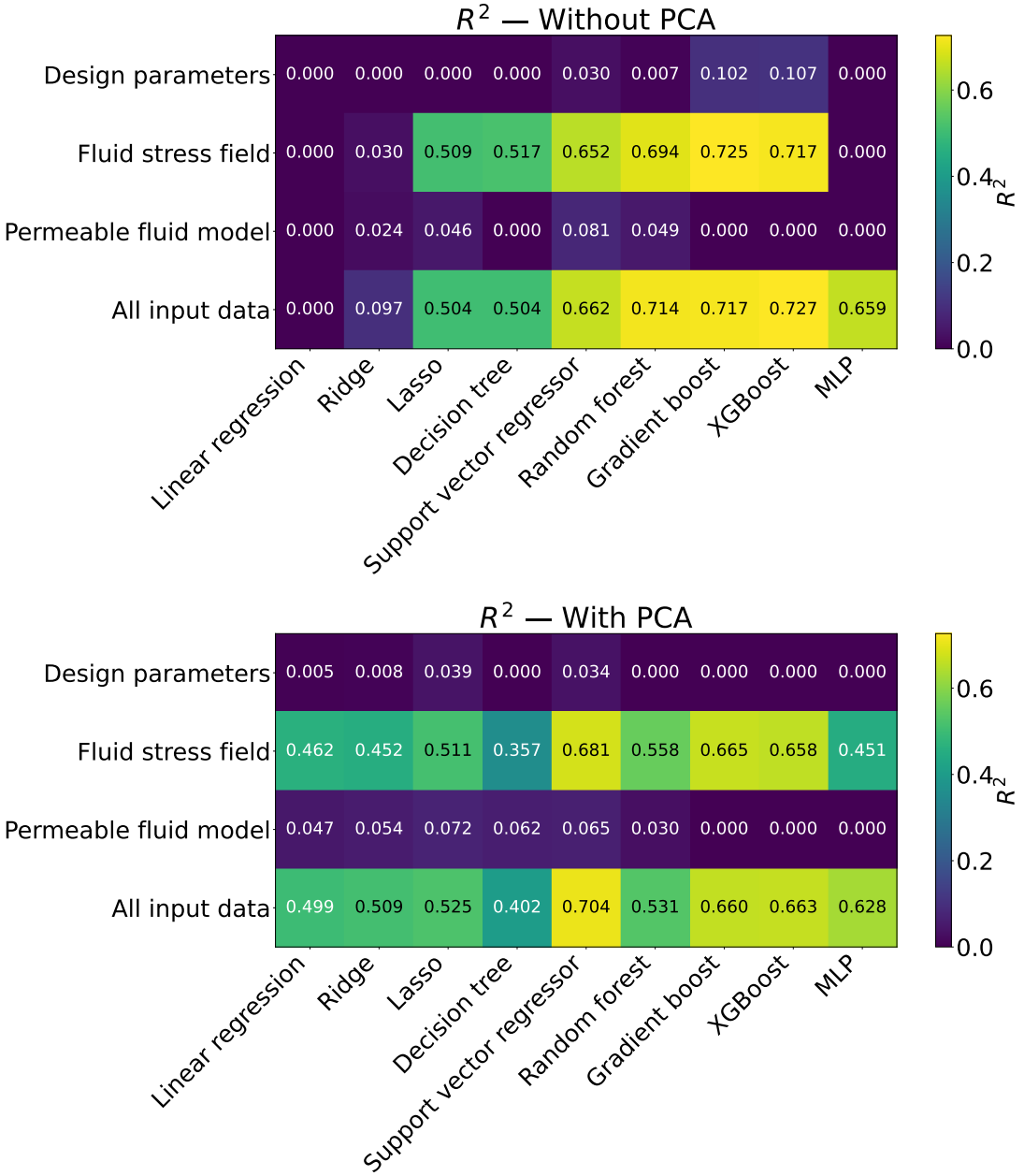

Figure 6.3: Average R^2 score for each ML model applied to each dataset, without (a), and with (b) PCA preprocessing.

The initial exploration indicates that the catheter design parameters, and the permeable fluid model are not informative for ChP deformation, as none of the ML models are able to predict an R^2 score of more than 0.1. This matches the results of Chapter 4, where α was seen to be a highly influential parameter. Neither the catheter design parameters (which are independent of the ventricle domain) nor the permeable fluid model (which is axisymmetric) has any α dependence. In itself this is a key result, as previous computational studies focussed on the flow patterns within a hydrocephalus catheter as a proxy metric for ChP deformation. The results of Figure 6.3, however, suggest that flow fields alone are not good predictors.

The fluid stress field is more promising, with several models giving R^2 scores of greater than 0.6. The tree-based ensembles, i.e., random forests and gradient boosted methods, perform best. The results for the "all input data" dataset are very similar to the fluid stress field, as the stress features are by far the most informative features in the full dataset.

Figure 6.3 b) shows the same investigation, performed on the datasets after a PCA transformation which projects onto the component vectors that explain 95% of the variance. Again, the design parameters and permeable fluid are less informative. PCA preprocessing improves the performance of regression-based models, as it mitigates multicollinearity in the input data, which harms the performance of linear models. In contrast, PCA slightly reduces the efficacy of tree-based models, which rely on recursive data partitioning rather than linear projections and are therefore less naturally aligned with PCA representations. This explains why random forests and XGBoost perform better without PCA preprocessing, and suggests that the underlying problem is not inherently well suited to PCA-based dimensionality reduction.

Going forward, the fluid stress field will be used as the input data for ML models, and no PCA preprocessing will be used. The design parameters and permeable model are uninformative in all cases. In most cases the "all models" dataset slightly outperforms the fluid stress field dataset, as it has access to a greater variety of data. However, to keep the number of input data features small, future models use only data from the fluid stress field as input data.

Table 6.3 gives all the accuracy metrics for all the models applied to the fluid stress field data. Again, the mean over the ten validation datasets is shown, for each of the accuracy metrics after hyperparameter optimisation. A good model

has high R^2 and ρ scores and low RMSE and MAE. The best value for each metric is highlighted in **bold**.

Model	R^2	RMSE (mm)	MAE (mm)	ρ
Linear regression	-2.411 ± 4.308	0.462	0.296	-0.073
Ridge	0.030 ± 1.131	0.252	0.177	0.714
Lasso	0.509 ± 0.126	0.194	0.160	0.796
Decision tree	0.517 ± 0.201	0.189	0.143	0.750
Support vector regressor	0.652 ± 0.139	0.162	0.132	0.824
Random forest	0.694 ± 0.092	0.153	0.119	**0.867**
Gradient boost	**0.725 ± 0.095**	**0.143**	**0.108**	0.857
XGBoost	0.717 ± 0.105	0.145	0.113	0.851
MLP	-0.064 ± 0.974	0.261	0.197	0.625

Table 6.3: Mean of performance metrics on input data derived from the stress field ROM, across-validation folds. R^2 shows mean±std; RMSE/MAE/ρ show fold means.

The highest validation R^2 was achieved by the gradient boosted algorithm, which also produced the lowest RMSE and MAE. The strongest correlation metric (ρ) was obtained by the random forest, while XGBoost performed comparably across all metrics. Across these three methods, the between-fold standard deviation of R^2 (on the order of 0.09–0.10) is similar to or larger than the differences in mean R^2, rendering the models statistically indistinguishable. All three are tree-based learners, only differing in ensemble strategy: random forests use bagging, whereas gradient boosting and XGBoost are boosting methods. These three algorithms were therefore identified as the most promising to take forward.

A single hyperparameter optimisation search (Algorithm 5) was then rerun for each of the best models, now without reserving a separate validation set. This

allows all observations to contribute to both fitting and validation across folds which is useful for small datasets. The structure of the five-fold cross-validation continues to ensure that metrics are evaluated on unseen data within each fold. Table 6.4 reports the fold-averaged scores, showing that further hyperparameter tuning improved the accuracy metrics in every case. Gradient boosting and XGBoost behave similarly, as expected for two gradient-boosted tree implementations. The random forest performs slightly worse than the boosted methods.

Model	R^2	RMSE (mm)	MAE (mm)	ρ
Random forest	0.718 ± 0.051	0.149	0.116	0.860
Gradient boost	0.763 ± 0.048	0.136	0.105	0.879
XGBoost	0.764 ± 0.057	0.136	0.105	0.879

Table 6.4: Mean of performance metrics across cross-validation folds. R^2 shows mean$\pm$ standard deviation across folds; RMSE/MAE/ρ show fold means.

6.6 Final surrogate model

To create the final ML model to integrate into the surrogate, the best algorithms with their optimal hyperparameters (as selected above) were retrained on the full dataset. This maximises training data for the final surrogate, improving predictive performance. The accuracy metrics are calculated again for the final model, analysing the accuracy of the models performance on the whole dataset. In this case only, the model is tested on the same data that it is trained on ("in-sample"). Figure 6.4 shows a visualisation of these models' performance, with the predicted values $f(\boldsymbol{x}_i)$ plotted against the ground-truth value y_i for all data points i in the training dataset. Points lying close to the red line $f(\boldsymbol{x}_i) = y_i$ indicate good predictions. Results are shown for the three models (columns) using cross-validated (out-of-fold) predictions (top row) and after refitting in-sample on the full dataset (bottom row). The top row reflects performance on

data that are distinct from training folds, whereas the bottom row reflects in-sample performance.

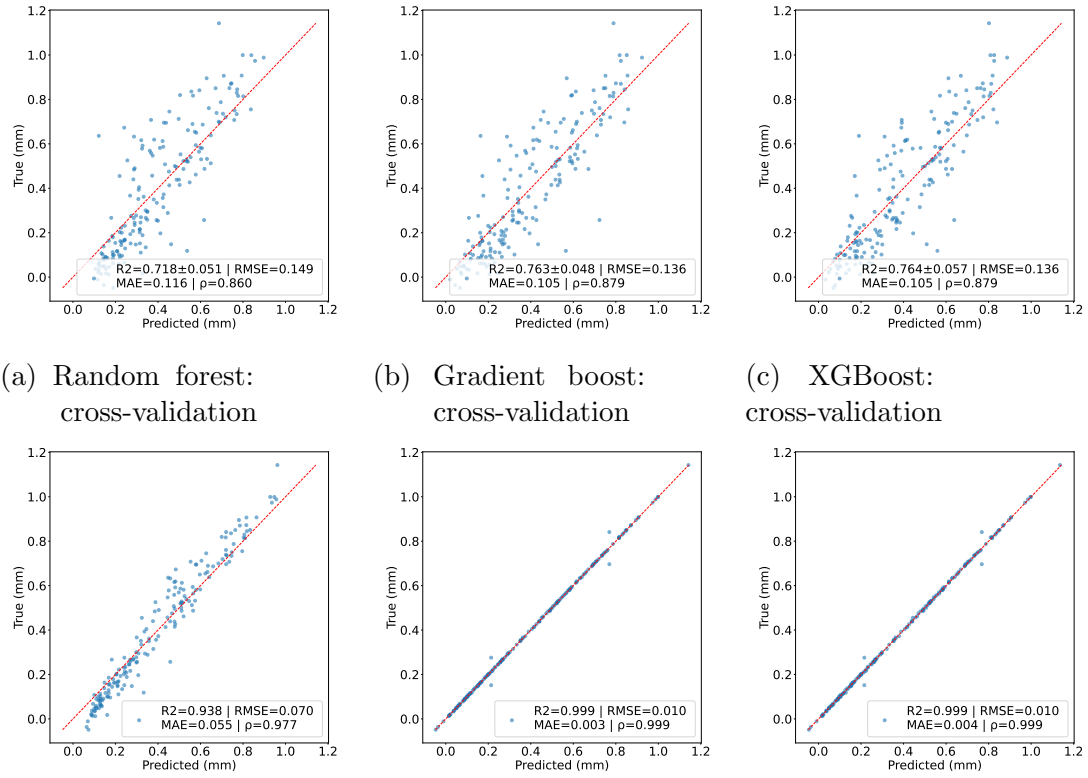

(a) Random forest: cross-validation

(b) Gradient boost: cross-validation

(c) XGBoost: cross-validation

(d) Random forest: in sample

(e) Gradient boost: in sample

(f) XGBoost: in sample

Figure 6.4: Predicted vs. ground-truth of the final ML models with optimal hyperparameters for the cross-validation: a), b), c) and when retrained on the full dataset: d), e), f). Red line, prediction=ground-truth.

The extreme improvement of the boosted models to $R^2 \geq 0.999$ suggests overfitting to the training data, which is a particular concern given the small dataset size. This is further justified below in the feature importance analysis. As such, the random forest model is selected for the surrogate, sacrificing a small amount of accuracy (slightly lower R^2) to reduce the risk of deploying an overfitted model. The optimal hyperparameters of this random forest are given in Table 6.5.

Table 6.5: Optimised hyperparameters for the random forest.

Hyperparameter	**Optimal value**
`n_estimators`	200
`min_samples_split`	3
`min_samples_leaf`	4
`max_features`	`sqrt`
`max_depth`	5

6.6.1 Feature importance

Feature importance is a useful metric to examine the internal workings of an ML layer, and will be used here to further justify the choice of the random forest model. Each entry of the feature importance vector gives a measure of how important the corresponding feature is for the model predictions. In ensemble tree-based models, a feature importance is based on how often that feature is a decision node in any one tree. Analysing feature importance can therefore give some mechanistic insight into a physical problem. Feature importance only shows correlation, and further studies are required to confirm causation. Here, each feature corresponds to the value of a fluid stress field at a specific point on the ChP surface. Features being identified as important therefore identifies specific locations of the stress field on the ChP surface that are decisive in determining ChP deformation. Figure 6.5 a) shows that the random forest attributes greatest importance to the pressure field, with a particularly influential region between 25 and 30 mm. The y-component of the fluid stress field also has elevated importance in this range. This aligns with results seen in Chapter 4, where the largest ChP deformations occurred near the catheter outlet. The most informative features form spatial clusters instead of single hot spots. This is expected as the underlying pressure and stress fields change smoothly across the surface, so neighbouring locations tend to carry similar information. This means the random forest is detecting physically consistent patterns, not just individual pixels.

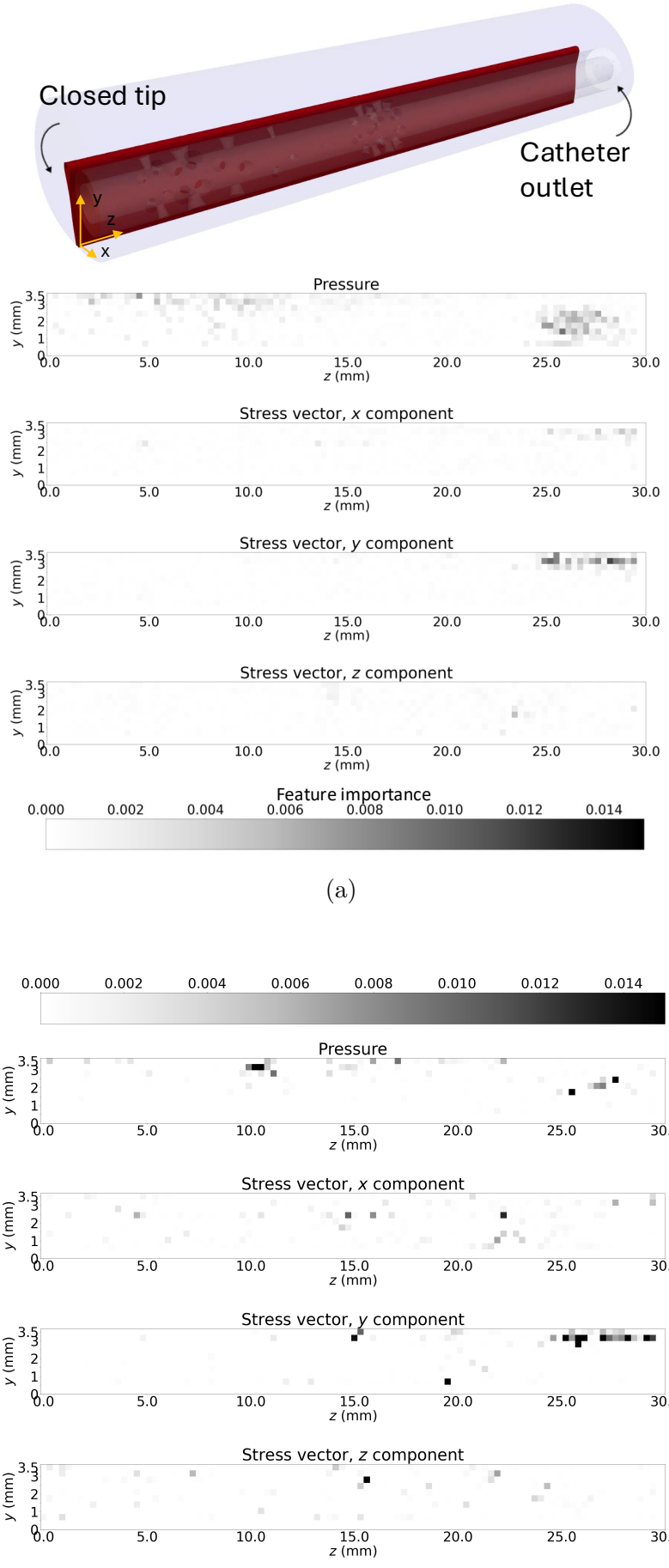

(a)

(b)

Figure 6.5: Feature importance plotted on the projected ChP surface for (a) random forest and (b) XGBoost (common scale). Dark pixels show areas of the stress field on the ChP which are significant in determining ChP displacement.

In contrast, Figure 6.5 b) shows the gradient boosted model's feature importances, which exhibit sharp, isolated peaks. This is yet again consistent with overfitting in small datasets, where a few features can dominate the algorithm and correspond to noise specific to the training data.

The random forest surrogate (comprised of feature weights and tree structures) is saved in a `pickle` file (∼5 MB). The file is small and can be moved and reloaded easily. Given a new instance of fluid stress data, the model returns a ChP deformation prediction in under 1 ms on a single core of an i7 core laptop.

6.7 Chapter summary

This chapter created a surrogate model for ChP displacement, drawing from MxL techniques by combining outputs of the mechanistic ROMs presented in the previous chapter with a predictive ML layer. The stress field ROM was identified as the most informative for prediction, and in combination with a random forest ML method, created an accurate and fast surrogate model. Feature identification plots highlighted the key areas of the ChP that are particularly informative for the model. These areas matched observations made in Chapter 4, giving confidence that the ML model was identifying physical mechanisms within the domain which will generalise well when applied to new input data in an optimisation.

ML methods establish correlations between the various input data forms tested and the prediction target of maximum equilibrium ChP displacement. A secondary result of this chapter establishes that there is very little correlation between the ChP displacement, and the catheter design parameters alone, and separately very little correlation between the ChP displacement and the fluid fields internal to the catheter, suggesting that both these input data forms are unpromising. Previous work on catheter design focusses on using characteristics of the fluid field within the catheter when models did not account for ChP displacement. The results of this chapter suggest that this is not a good metric to use.

The surrogate model created in this chapter is well correlated with the maximum equilibrium ChP displacement and has a fast run time. This makes it an appropriate model for use as a surrogate fitness function in a generative design procedure. In the next chapter this surrogate model is integrated with an optimisation protocol and used to rigorously search for improved catheter designs.

Chapter 7

Generative design

This chapter presents the results of the catheter design optimisation, the green component of the methodology shown in Figure 7.1. This chapter directly applies generative design to the catheter problem, bringing together the work of the previous chapters. In this research, catheter designs are evaluated based on their impact on choroid plexus (ChP) displacement with the fitness of a catheter defined as the maximum equilibrium displacement of the ChP. The optimal catheter design minimises this displacement, assuming that the lower the fitness value, the better the design.

The 3D fluid-structure interaction (FSI) model is treated as the ground-truth for evaluating ChP displacement. However, as seen in Chapter 4, each 3D FSI simulation has a runtime of over three days, making it computationally impractical to use the full model for every fitness evaluation during optimisation. Therefore, faster surrogate models are required which approximate the behaviour of the full model while enabling efficient computational exploration of the design space.

The surrogate model for ChP displacement developed in Chapter 6 is used here to determine the fitness function utilised within the generative design framework. Since this surrogate can only approximate the ground-truth, fitness values are only accurate to the extent that the surrogate model itself is accurate. Therefore one cannot *a priori* expect to find the true global minimum of the full model while using a surrogate. The surrogate-aided generative design methodology presented here does not therefore aim to find the global minimum; instead the results from the surrogate-aided optimisation are used to suggest promising new design directions. These candidate designs are then tested using the full 3D FSI model to assess their true performance. It should also be noted that the accuracy of

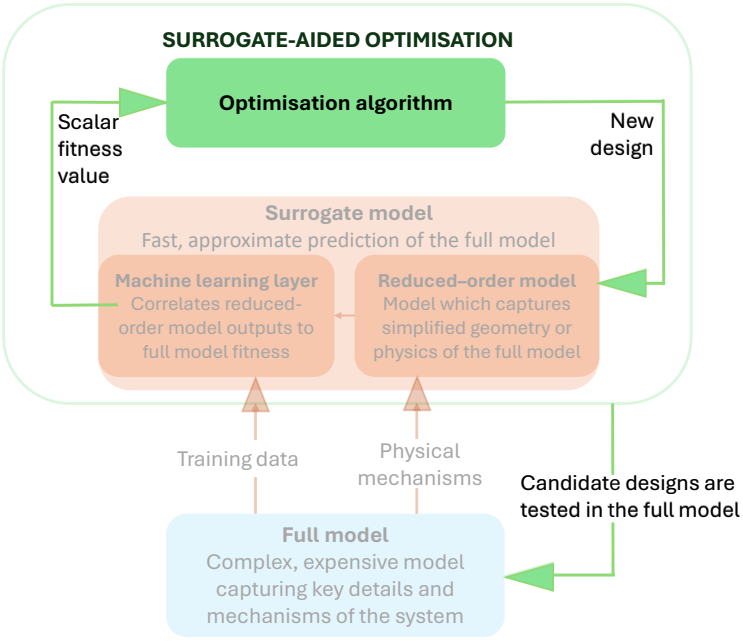

Figure 7.1: Generative design methodology, highlighting the green "optimisation" components, which are the focus of this chapter.

the machine learning (ML) layer, and hence of the surrogate, is influenced by the quality and quantity of its training data.

The optimisation results presented in this chapter are also discussed in detail in Ref. [191].

7.1 Optimisation

7.1.1 Optimisation algorithm

The generative procedure used here builds on the softFEM framework introduced in Refs. [128, 169, 137]. In this framework a multiple offspring sampling (MOS) method is employed [214]. MOS is a hybrid self-adaptive strategy that combines multiple optimisation techniques to dynamically balance exploration and exploitation to efficiently search the design space.

Specifically, the multi-trajectory search (MTS) is used as the algorithm which focusses on exploitatory techniques. MTS progresses step by step, varying one design parameter at a time to descend the fitness landscape [133]. The algorithm chosen to provide a more exploratory strategy is the success-history based

adaptive differential evolutionary algorithm (SHADE), where the parameters controlling adaption and mutation vary throughout the optimisation leading to improved performance [141, 142]. By dynamically balancing these complementary methods, MOS efficiently searches the space of designs parameters. MOS is self-adaptive, dynamically switching between the exploratory SHADE [127, 137] and the exploitatory MTS [133] to efficiently identify local minimum, while maintaining good coverage of the space. This method is described in full detail in Ref. [169].

The optimisation codebase used here is the python-bound `PyMOS` package [127]. Figure 1.1 c) illustrates the optimisation process, with the optimisation protocol interacting with a surrogate fitness function. Before evaluating a new parameter set, a user-defined filter ensures that the parameters correspond to a physically valid catheter design. This filter is closely linked to the choice of parameter encoding and is discussed in Section 7.1.2.

At each stage of the protocol, a population of candidate designs and their associated fitnesses is active. At each step, new candidates are proposed by either MTS or SHADE and replace existing population members if they improve the overall fitness. MOS therefore requires only two hyperparameters:

- **Population size**, the number of candidate designs held in memory during optimisation,
- **Fitness budget**, the total number of times the fitness function may be evaluated.

Here, the population size is set to be of 15, in line with default values used in Ref. [127]. This population size balances two competing factors: a larger population helps maintain genetic diversity, while a smaller population allows for quicker adaptation and mobility within the design space. Having few hyperparameters is a strength of the MOS protocol, and of the internal algorithms MTS and SHADE as fewer hyperparameters reduces concern that the specific choice of hyperparameter value is influencing the results of the optimisation. The fitness budget is equally split between the two component algorithms, MTS and SHADE. SHADE is initialised using default hyperparameters (history of 100 population members, initial mutation and cross over rates of 0.5 for all population members

as described in Ref. [142]). MTS does not require any hyperparameters to be initialised, as discussed in Ref. [169].

`PyMOS` also includes a built-in online surrogate model, as described in Section 2.4. To focus solely on the surrogate created using mechanistic learning (MxL) techniques in Chapter 6, this additional online surrogate is disabled here.

7.1.2 Parameter encoding

An encoding defines the mapping between the parameter vector proposed by the optimisation algorithm and a catheter design evaluated by the fitness function. In `PyMOS`, parameter inputs must be provided as a fixed-length vector of decimal values. This structure naturally accommodates continuous variables, which can take any value within a specified range, but can also be adapted to represent discrete inputs. For example, the number of inlet holes is inherently an integer variable. This can be represented by rounding a continuous value to the nearest integer.

Different encoding schemes may require different types and numbers of parameters to represent a catheter design. One example used in the creation of the ground-truth dataset discussed in Chapter 5 represents each inlet hole individually using three parameters: the radius r_h, circumferential position ϕ, and axial position z. For designs with up to 40 inlet holes, this results in a 120-dimensional parameter space and requires preprocessing to avoid overlapping holes. Physical constraints on these parameters are given in Table 5.1.

The 2D FSI model results presented in Chapter 4 indicate that larger, uniformly distributed inlet holes arranged uniformly around the circumference of the catheter reduce both ChP displacement and sensitivity to α. This insight motivates an alternative encoding based on circumferential rings of inlet holes. In this revised scheme for use in the generative design procedure, a catheter design is constructed by defining multiple rings of inlet holes. Each ring i is described by four parameters:

- Hole radius r_i, identical for all holes on the ring,
- Number of holes n_i (a discrete input), spaced evenly around the circumference,

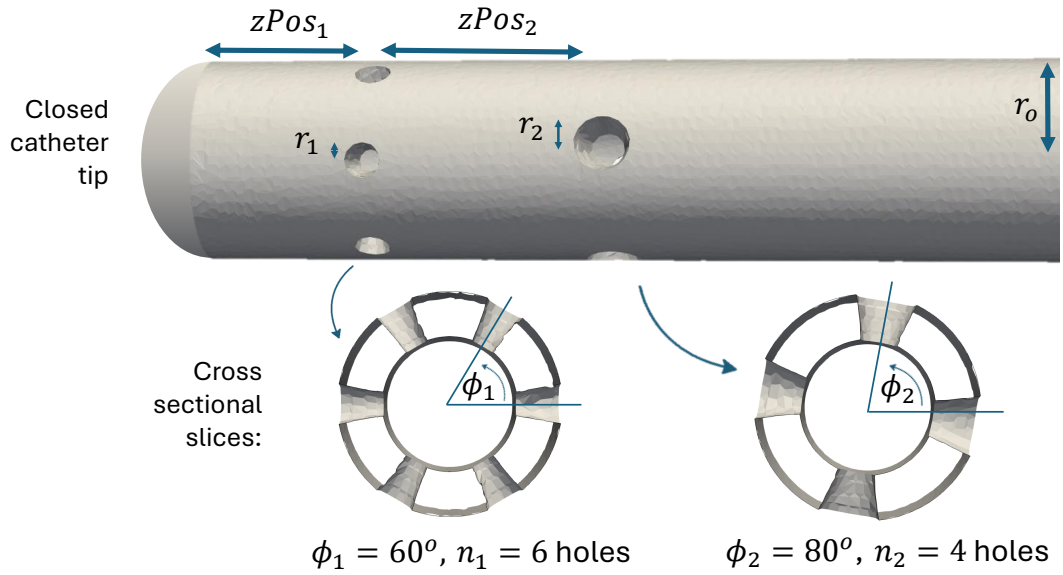

Figure 7.2: Graphic of the design encoding used in optimisation.

- Offset angle ϕ_i, the angle between the first hole and the positive horizontal axis,
- Pitch length $zPos_i$, the axial distance from the previous ring.

As seen previously in physical examples, inlet holes are conical, and r_i refers to the radius of the base of the cone, on the exterior wall of the catheter. Figure 7.2 provides a visualisation of this ring-based encoding. As shown, $\phi_i = 0$ places a hole horizontally to the right of the centreline, and increasing ϕ_i rotates the placement clockwise. As discussed in Section 5.1, as various values of α (which determines the relative orientation of the catheter compared to the ChP) are considered, the actual angular offset of the first inlet hole is $\phi_i + \alpha$. The permissible ranges for each design parameter are listed in Table 7.1. Enforcing constraints on the size of each design parameter makes this a constrained optimisation.

By allowing both the hole radius and the number of holes to be zero, the encoding enables the optimisation to effectively remove a ring of holes from a design if this proves beneficial. Inlet holes with radius <0.1 mm are difficult to manufacture (and not seen on physical examples). Furthermore, results of the permeable wall ROM separately showed that fluid uptake into an inlet holes is arguably proportional to r_i^3, meaning that holes with $r_i \leq 0.1$ mm have minimal

Table 7.1: Parameter bounds for the optimisation encoding.

Variable	**Lower bound**	**Upper bound**
Hole radius r_i	0 mm	0.6 mm
Number of holes n_i	0	10
Offset angle ϕ_i	0°	360°
Pitch length $zPos_i$	0.05 mm	10 mm

influence on inflow into the catheter. Therefore all proposed $r_i < 0.1$ mm are mapped to zero (in effect, removing the ring of holes).

The upper bounds were chosen based on physical examples while allowing room for novel configurations, thus expanding the design space beyond known designs. A maximum of six rings is allowed, in line with prior computational and physical investigations [15, 86]. This results in a 24-dimension design space (six rings × four parameters), but allows up to 60 holes on a design, a 50% increase over the previous encoding.

7.1.2.1 Parameter preprocessing

Two preprocessing steps are applied to ensure that a new vector of parameters corresponds to a physical catheter design:

Hole overlap prevention: Holes must not overlap around the catheter's circumference. As such, for each ring, the condition

$$2r_i \cdot n_i < c \cdot 2\pi r_o, \quad \forall i$$

must be satisfied, where $r_o = 1.25$ mm is the catheter's external radius, and $c = \frac{2}{3}$ reflects manufacturing constraints and ensures sufficient material between holes. This value is based on physical examples in Chapter 4 and can be updated as manufacturing processes evolve.

Placement constraint: All inlet holes must lie within 15 mm of the catheter tip. This is enforced by

$$\sum_i zPos_i \leq 15.$$

This requirement is also based on examination of available specimens and previous work [15, 86], ensuring that inlet holes remain contained within the ventricle and do not interact with the surrounding brain tissue.

The three types of constraints described above are implemented differently within the optimisation code:

- The maximum number of rings determines the length of the parameter vector proposed by `PyMOS`.
- Parameter bounds constrain the range of values that `PyMOS` can propose.
- The preprocessing checks apply problem-specific constraints after parameter generation but before fitness evaluation. This allows the tracking of how many proposed designs are rejected prior to evaluation, offering insight into the encoding's efficiency.

Each design that fails these checks is immediately assigned an infinite fitness, and the optimisation passes to the next proposed design. The modular nature of the `PyMOS` codebase makes it easy to alter the preprocessing function if new information on the biomedical or manufacturing requirements needs to be incorporated.

7.1.3 Fitness function

In this chapter, the fitness function is the surrogate model developed in Chapter 6, which approximates the true maximum equilibrium ChP displacement for each proposed parameter set. Chapter 4 identified α, the rotation of the catheter around its central axis, as a key factor influencing ChP displacement. To ensure good coverage of α, 15 evenly spaced values are tested within the range $(0°, 360°)$. Since α is not surgically prescribed, the worst-case scenario (defined as the maximum predicted ChP displacement across all values of α) is used as the fitness value for each design, see Algorithm 6.

The fitness evaluation is easily parallelised, running each value of α concurrently, and additionally parallelising each `OpenFOAM` simulation (the ROM integrated into the surrogate model requires one fluid simulation to extract the initial stress field) using built-in methods. For this work each `OpenFOAM` simulation is parallelised over four cores, i.e., each optimisation run requires $4 \times 15 = 60$

Algorithm 6 Fitness function for optimisation

New parameter vector is proposed by `PyMOS`,
Preprocess parameter to test for a physically reasonable design,
if not physically reasonable **then**:
    Return fitness = infinity
else:
    for $\alpha \in [0°, 360°)$ **do**,
        Create the catheter geometry for given α and inlet hole design,
        Run a fluid simulation in openFOAM,
        Extract fluid pressure and stress at the ChP surface,
        Use the pre-trained random forest to predict ChP displacement,
    end for
    Return fitness = maximum predicted ChP displacement across all α.
end if

cores. The optimisations are run on the shared University PowerEdge R7525 cluster node, using an allocation of 60 AMD EPYC CPU cores, with each fitness evaluation taking 15 minutes, with the full optimisation of 1000 evaluations taking approximately two weeks.

7.2 Results

7.2.1 Optimisation convergence

When performing an optimisation over a large design space, a key challenge is achieving sufficient exploration while controlling computational cost. Optimisation algorithms aim to search efficiently without neglecting promising regions of the design space and, in principle, seek the global minimum of the fitness function. However, the true global minimum of the ground-truth fitness (as defined here by the 3D FSI model) cannot be guaranteed when using a surrogate fitness function, due to uncertainty in surrogate predictions.

Moreover, the numerical precision achievable during optimisation often exceeds the tolerances relevant to physical manufacture, such as in the catheter design considered here. In such cases, refining design parameters beyond a few decimal places does not lead to any meaningful change in the realised design. Consequently, pursuing extremely small improvements in the surrogate fitness proposed here below this manufacturing resolution has no physical significance, and hence the optimisation should be stopped before this point.

The optimisation algorithm includes stochastic elements, and multiple realisations therefore rely on different random seeds. Figure 7.3 a) shows the convergence histories of these runs. In all cases, the fitness decreases rapidly during the first 200 iterations, followed by smaller, incremental improvements. Despite different initial conditions, the runs converge to similar final fitness values of approximately 0.2 mm, indicating that a budget of 1,000 fitness evaluations is sufficient for this problem. Figure 7.3 b) shows the performance of a single optimisation realisation,

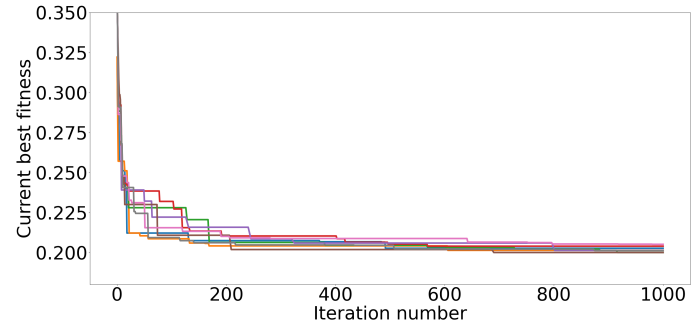

(a)

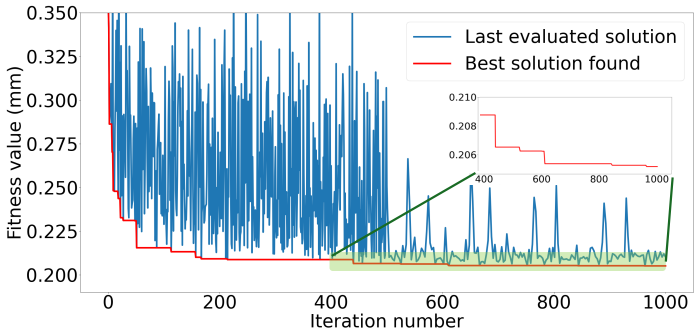

(b)

Figure 7.3: (a) Optimisation convergence history: current minimum fitness for each iteration number. Colours: different optimisation realisations, run concurrently from different seeds. (b) Algorithm performance for a particular realisation. Blue: current iteration fitness; red: current minimum fitness. The minimum fitness for the final 500 iterations is amplified in the cut out.

with the blue line showing the fitness at each iteration. For the first 500 iterations, the explorative SHADE algorithm is used, which searches a large area of the fitness landscape. This can be seen in the large spread of fitness values in this section of the optimisation. In the second half of the optimisation, MTS is used, which leverages exploitative techniques to improve the current fitness. This can

be seen with the blue trajectory, with values much closer to the red line, as the MTS algorithm looks for nearby designs with small incremental improvements to the current fitness. The cut out shows the current best fitness in the second half of the optimisation, amplified to show that fitness improvements are made throughout the optimisation, though the most significant gains in fitness occur in the first 200 iterations.

7.2.2 First optimisation

The optimisation identifies catheter designs that minimise ChP deformation, as evaluated by the surrogate model. Each completed optimisation realisation suggests a new candidate design that the surrogate-aided optimisation has identified as having the lowest fitness. Figure 7.3 shows that all the optimisation realisations suggest candidate designs with fitnesses of around 0.2 mm. However, the ML layer of the surrogate model has an average MAE of 0.1 mm when tested on unseen data (Table 6.4), and Figure 6.4 top left shows that the random forest is particularly uncertain on predictions with low fitness (towards the boundary of its training region), and tends to overestimate its prediction when the true value is less than 0.2 mm.

The multiple concurrent optimisation realisations therefore produce a set of candidate designs which are predicted to have low fitness, but with an uncertainty of approximately 50% on that prediction. To confirm and quantify the improved performance of these designs the full FSI model is used. The three candidate designs with the lowest fitness are taken forward for further investigation. Visualisations of these candidate designs are presented in Figure 7.4. The design parameters for each proposed design are given, respectively, in Appendix D.1.

Each optimisation realisation generated a distinct catheter design, yet all three candidate designs share structural similarities suggesting the the optimisation realisations all identified important design structures. Each design has large n_i values, consistent with the findings of the 2D reduced model in Chapter 4 that designs with a high number of holes placed circumferentially are desirable. Each design additionally has one cluster of large-radius holes near the closed catheter tip and a second cluster of large-radius holes near the midpoint ($z = 15$ mm), with relative few, much smaller holes in between.

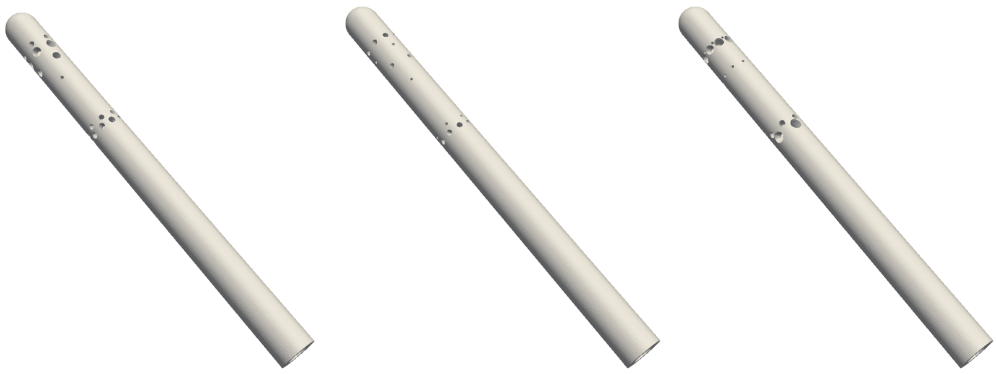

(a) (b) (c)

Figure 7.4: Candidate catheter designs identified by the optimisation realisation. Design parameters given in Tables D.1-D.3.

The large number of circumferential holes reduces the material between adjacent holes, which could compromise the structural integrity of the catheter and increase the risk of damage during insertion. This was partially accounted for in the optimisation through a circumferential spacing constraint, but the tendency to form two closely packed axial clusters suggests this constraint may need to be tightened, or extended to include an axial spacing constraint.

The clusters of large-radius holes may also locally weaken the catheter wall, particularly near the tip where mechanical stresses during placement are highest. The smaller holes between clusters present further challenges, both in terms of manufacturing tolerances and increased likelihood of blockage by cellular debris. The variation in hole size along the catheter also adds complexity to fabrication, likely requiring multiple drilling steps or more advanced manufacturing techniques. It is encouraging that multiple optimisation realisations produced very similar designs, suggesting that small geometric variations are not particularly important, and that extremely high precision may not be required in practice.

7.2.2.1 Optimised designs: ChP deformation

The optimised designs are then tested using the full 3D FSI model to determine their effect on ChP displacement. Figure 7.5 compares the performance of the candidate designs in the full FSI model (green, solid) with the prediction of the surrogate on these candidate designs (green, dashed), with previously tested designs (Chapter 4) shown in blue for reference. As before, each design is tested

for multiple values of α.

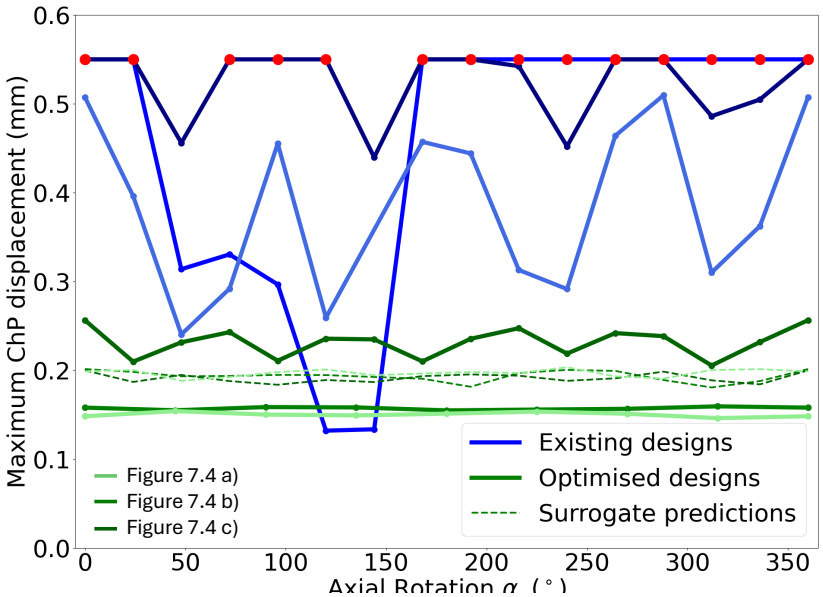

Figure 7.5: Maximum ChP displacement as a function of rotation angle α, comparing optimised designs (green) to those investigated in Chapter 4 (blue). The surrogate model predictions for the new designs are shown in dashed green. Red dots mark collisions with the ChP.

The optimised designs outperform all three of the previous designs at almost every value of α. There are no ChP collision events, and two of the optimised designs (light and middle green) additionally show close to no sensitivity to α, a highly desirable characteristic, as α is not prescribed during implant surgery. This Figure shows the surrogate-aided optimisation methodology has been successful in generated an improved catheter design.

For all of the three candidate optimised designs the surrogate prediction is a flat curve with value of 0.2 mm, consistent with Figure 7.3. However, the performance of the three candidate designs in the full FSI model is not uniform. The two designs shown in Figure 7.4 a) and b) lead to very similar ChP displacements despite differences in their inlet holes. This suggests that the fitness function is very flat across large region of design space, and that other designs could be equally effective. From a manufacturing standpoint, this is highly beneficial. A flat surface implies robustness to small variations in geometry, so minor deviations during production are unlikely to significantly impact performance.

The design shown in Figure 7.4 c), however, shows a different behaviour, with higher ChP displacements than suggested by the surrogate. Inspecting the hole design of Figure 7.4 c) shows that the final ring of inlet holes has parameters $r_6 = 0.427$ mm, $n_6 = 5, \phi_6 = 337°$ and is positioned at $z = 11.7$ mm. The ChP displacement curve associated with this design (Figure 7.5 dark green) shows five-fold periodicity, suggesting that this ring of inlet holes is particularly influential on ChP displacement. Further, it is reasonable to expect that this design could be improved by increasing the value of n_6, thereby reducing the α-dependence of this ring of inlet holes. This contrasts with the designs shown in Figure 7.4 a) and b), for which $n_6 = 9$ and the resulting ChP displacement exhibits substantially lower sensitivity to α. This design direction was not explored by the optimisation algorithm for the design in Figure 7.4 c), likely due to the inherent uncertainty in the surrogate fitness functions, and increasing n_6 may not be identified as beneficial by the surrogate. In this case, insight gained from the ground-truth FSI model enables further design refinement beyond the capabilities of the surrogate-aided generative design framework.

This example shows the importance of exploring designs suggested by the surrogate-aided optimisation methodology. While the three designs shown in Figure 7.4 all have similar performances according to the surrogate model, differences between designs lead to different performances in the full model. Figure 7.5 suggests the designs of Figure 7.4 a) and b) should be taken forward to manufacturing and further testing, while the design in Figure 7.4 c) (while still more successful than any existing designs) should be discarded.

Figure 7.5 demonstrates that the designs identified by the surrogate model indeed lead to performance improvements in the full 3D FSI model. This validates the overall optimisation methodology introduced in Figure 1.1. In all cases the true performance of the designs is within 0.05 mm of the surrogate prediction. In Chapter 6, the uncertainty in the surrogate prediction was quantified, with the MAE for the ML layer $\sim$0.1 mm (see Table 6.4), and hence this discrepancy is unsurprising, but re-emphasises the important of testing promising designs in the full model.

7.2.2.2 Optimised designs: additional metrics

The candidate designs shown in Figure 7.4 all perform better than previous designs when tested in the full 3D FSI model, and all share two distinctive design features: a large number of inlet holes on each circumferential ring of holes, and two distinctive groups of holes, one near the closed tip and one near the catheter midpoint. A high circumferential number of inlet holes was seen in the 2D model parameter investigation in Chapter 4 to reduce ChP displacement, and this feature is also seen in the candidate designs of Figure 7.4. The second common design feature seen in Figure 7.4 is a split between a grouping of larger holes near the closed end of the catheter, and a grouping of larger holes near the axial midpoint, with a relatively large section of catheter with few, smaller holes in between. This configuration has not been reported in previous studies, which instead favoured designs with larger holes near the closed tip that progressively decrease in size towards the catheter outlet, prioritising uniform inflow through each inlet hole [15, 86, 89].

To investigate the potential mechanisms behind this design choice, the results of the 3D FSI models are analysed and compared to previous designs discussed in Chapter 4. Figure 7.6 a) shows the fluid fields down the centre of the catheter. This is a very different profile to previous catheters, where the aim has been to make the influx profile as uniform as possible. Here the maximum influx of 2.268 mm^3/s through an axial hole again occurs at the band of holes at z =15 mm, those nearest the outlet. Across the six axial hole positions that average fluid influx is 1.015 mm^3/s and the standard deviation is 0.867 mm^3/s, a larger range standard deviation of influx than any of the designs presented in Chapter 4. However, if the catheter design is instead interpreted as having two key groups of inlet holes, those near z = 5 mm, and those near z = 15 mm, the group located around z =5 mm take a total influx of 2.984 mm^3/s, meaning that the total influx into the catheter is roughly split in half between the two key groups.

Figure 7.6 b) shows the ChP tip displacement. The maximum displacement is at z=6.27 mm, with regions of the ChP in $z < 10$ mm moving ~ 0.15 mm towards the catheter, and regions of the ChP with $z > 15$ mm moving away from the catheter. As before, the greatest movement of the ChP towards the catheter occurs in the region surrounding the inlet holes.

Figure 7.6 c) shows the normal traction, $\boldsymbol{n} \cdot \left(-p\,\boldsymbol{n} + \mu\left(\nabla \boldsymbol{v} + (\nabla \boldsymbol{v})^{\top}\right) \cdot \boldsymbol{n}\right)$, on the ChP surface facing the catheter (lower) and on the opposite side (upper), evaluated at the equilibrium configuration obtained from the 3D FSI model. A visualisation of the catheter is shown between the two subfigures, with its centreline aligned with the z axis, allowing the inlet hole placement to be seen.

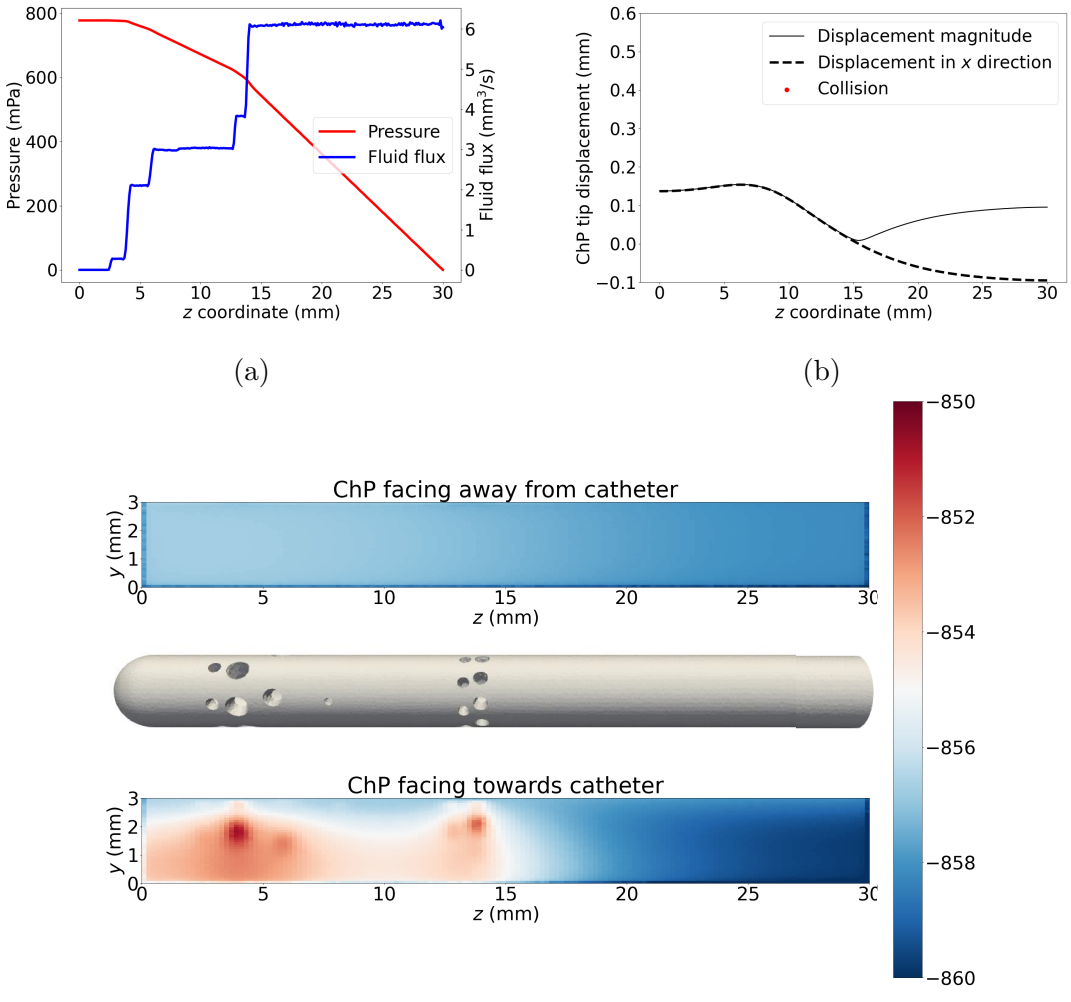

Figure 7.6: (a) Fluid pressure and axial flux along the lumen of the catheter design shown in Figure 7.4 a). (b) ChP tip displacement. (c) The normal component of the traction vector. Blue shows lower than average traction, and red higher than average traction.

Several features of the normal traction are consistent with the traction visualisations presented in Chapter 4. On the side of the ChP facing the catheter, the

normal traction is spatially heterogeneous, while the opposite side experiences an approximately uniform traction field.

Regions of high traction on the catheter-facing side of the ChP can again be consistently associated with nearby inlet holes, in agreement with previous results. The fluid traction on the ChP surface ranges between -850 and -860 mPa, lying within the range observed for the existing catheter designs in Chapter 4. The variation in traction, of approximately 10 mPa, is also comparable to that seen in earlier configurations.

Taken together, Figure 7.6 provides a possible explanation for why the optimisation consistently favours designs with two distinct groups of inlet holes. The candidate design shown in Figure 7.6 a) separates the dominant inlet holes into two axially distinct regions, each admitting approximately 50% of the total fluid influx. This results in two corresponding regions of elevated traction on the ChP surface, which may act to distribute loading on the ChP more evenly and reduce maximum deformation.

Finally, Figure 7.6 a) shows that the smaller holes located between the two main inlet hole groups have negligible impact on ChP deformation, as there is little discernible traction on the ChP surface. This observation is consistent with the permeable reduced-order model presented in Chapter 5, in which the influx through the catheter wall scales with the cube of the hole radius. As a result, small inlet holes contribute minimally to the local flow field and could potentially be removed, if preferred by manufacturing constraints, without significantly affecting catheter performance.

7.2.3 Four-hole designs

In the encoding described above, each ring may have up to ten holes and an arbitrary angular offset ϕ_i. However, both physical prototypes (Chapter 4) and prior computational studies [15, 86, 88] only consider designs with exactly four holes per ring and no offset between rings.

It is of interest to consider an optimisation on this reduced design space: i) for comparison against previous work, ii) because of the likelihood that the current manufacturing process has a preference for four-hole designs, and iii) to evaluate whether designs generated with this restriction can perform as well as the more general designs that were previously identified. In this setting, each ring has

$n_i = 4,\ \phi_i = 0\ \ \forall i$. This reduces the dimensionality of the design space to 12, considering only variation in hole radius and axial spacing between rings.

Figure 7.7 a) and b) shows two designs with the four-hole configuration generated from two separate runs of the optimisation algorithm, with design parameters given in Appendix D.1. As with the designs presented in Figure 7.4, both four-hole designs have one group of large holes clustered close to the closed tip and another group close to the axial midpoint of the catheter, near $z = 15$ mm.

Figure 7.7 c) compares the four-hole designs to the optimised designs above, and to the example catheters used currently. The red curves represent the four-hole designs, which show four-fold rotational symmetry in displacement. As expected, this periodicity is reflected in a 90° period for α. Both four-hole designs achieve a minimum displacement near 0.2 mm and a maximum just under 0.3 mm. While the variation due to α is less for the four-hole design than for the previous examples, this optimisation suggests it is not possible to completely remove the sensitivity to α with a four-hole design. Again, despite differences in the design of the catheters identified as optimal, the ChP displacement curve is very similar, suggesting a variety of designs lead to similar improvement in catheter performance.

The best design produced by the general encoding outperforms the four-hole configurations at all values of α. This aligns with the 2D FSI results from Chapter 4, which showed that increasing the number of inlet holes reduced the sensitivity of ChP displacement to catheter rotation. Figures 7.4 a) and b) confirm that the optimisation algorithm also identifies this trend, with both designs incorporating a large number of inlet holes per ring.

7.2.4 Improving the surrogate model

Testing the new designs in the 3D FSI model allows the assessment of ground-truth performance, but additionally gives a new dataset of ground-truth ChP displacement. These new data are combined with the ground-truth dataset presented in Section 5.1, and are used to improve the surrogate model.

Testing design candidates in the full FSI model above contributes 24 new data points to the ground-truth dataset, a 13% increase in the size of the dataset. Importantly, these new data points all have low fitness values, and improve the predictive power of the surrogate fitness function in this region.

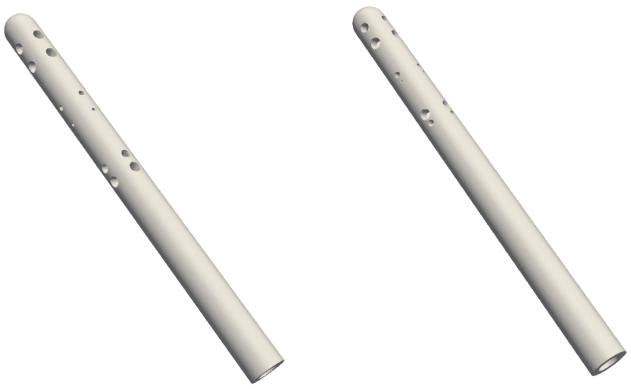

(a) (b)

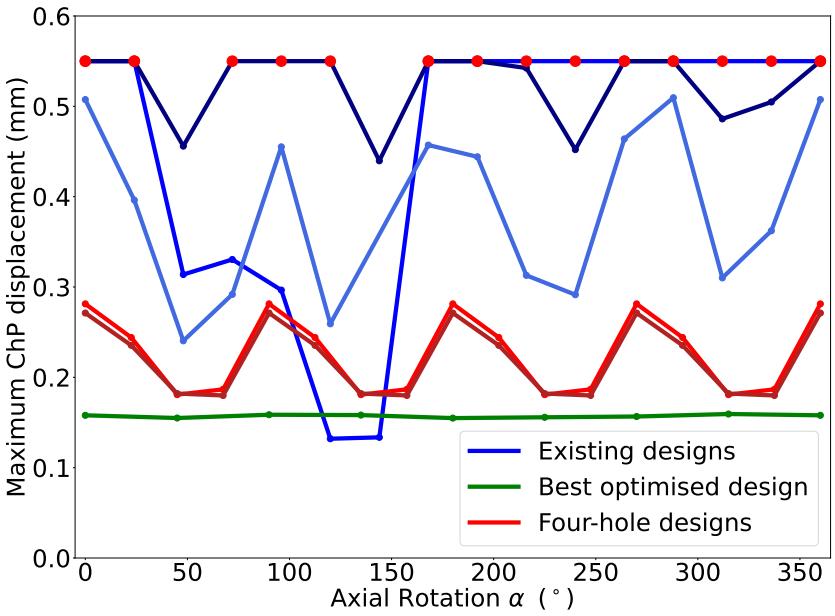

(c)

Figure 7.7: Maximum ChP displacement as a function of rotation angle α, comparing optimised four hole designs (red) to the best performing candidate from Figure 7.4 (green) to those investigated in Chapter 4 (blue). Red dots mark collisions with the ChP.

As in Chapter 5, the same design with a different value of α is considered a separate data point and treated independently. Due to the four-fold rotational symmetry of the new four-hole designs, only values of $\alpha \in [0°, 90°]$ are included in the extended dataset. This is because the symmetry of the design means that the geometry of the catheter-ventricle environment is identical after a rotation of 90°, leading to the same stress distribution on the ChP wall, and the same ChP displacement (as can be seen in Figure 7.7, red lines). Consequently, including data values of these catheter designs for multiples of 90° will duplicate samples in the dataset, unfairly biasing the model towards these data points. The optimal designs taken from the general encoding do not have an exact rotational symmetry, and so all values of α are included in the addition to the dataset.

With the extended dataset, an improved surrogate model is created by training a random forest algorithm. As described in Chapter 6, a hyperparameter optimisation is performed using five-fold cross validation with a 10% validation sample. The same hyperparameters as Table 6.5 were identified as the optimal combination, providing confidence in the model's robustness to new data. Testing on the reserved validation set leads to an R^2 score of 0.831, an improvement over the R^2 score of 0.783 seen in the same process when creating the surrogate (Figure 6.3, middle left).

As described in Chapter 6, the surrogate model is then retrained on the entire dataset for maximal information. This results in accuracy metrics of $R^2 = 0.908$, MAE = 0.060 mm, RMSE=0.083 mm and Spearman's correlation coefficient of 0.953, in all cases giving slight improvements over the model presented in Section 6.6.

Figure 7.8 shows the predicted value for each data point using the improved surrogate model. This should be compared to Figure 6.5 a). The improved surrogate has better predictive power (points closer to the red line), particularly for data points with small fitness, a critical area. The feature importance visualisation shown in Figure 7.9 is similar to that of the original surrogate, (Figure 6.5 b)). The revised ML model gives slightly more importance to the pressure values, and less to the y component of the stress vector (note the different scale used in the stress vector components). This could be due to the added data points all having a restriction of inlet holes to the 15 mm of the catheter closest to the closed tip. The area of importance identified in the y component of the stress tensor for the first surrogate model (Figure 6.5), is between 25 mm and 30 mm.

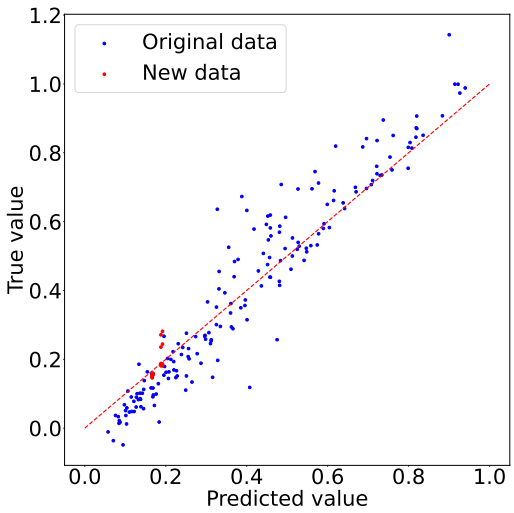

Figure 7.8: Predicted vs ground-truth of the surrogate fitness, with new FSI data. Red line, prediction=ground-truth. Red points: new data points; blue points: original data points.

The new designs interact less with this region as their inlet holes are positioned at the other end of the modelled domain, and so reduce the importance of this region for the improved ML model given here.

7.2.5 Second optimisation

With the improved surrogate model, a second set of optimisation realisations can be run. The optimisation setup, parameter encoding and hyperparameter choices remain the same, with the only change being the new surrogate model to allow direct comparison.

Figure 7.10 a) and b) shows two designs proposed by the optimisation using the improved surrogate, with design parameters given in Appendix D.1. These designs, tested in the 3D FSI model, are shown in Figure 7.10 c) in purple. Surrogate predictions, and previous designs explored are also shown for comparison. As with the first optimisation, designs with high numbers of inlet holes on each circumferential ring, and one group of large-radius holes near the closed tip, and a second group near the axial midpoint are identified as promising. In both the designs identified in the second optimisation, the algorithm takes advantage of the encoding's ability to remove rings of inlet holes, and both designs have only three rings of holes. This is consistent with the observation made earlier that the

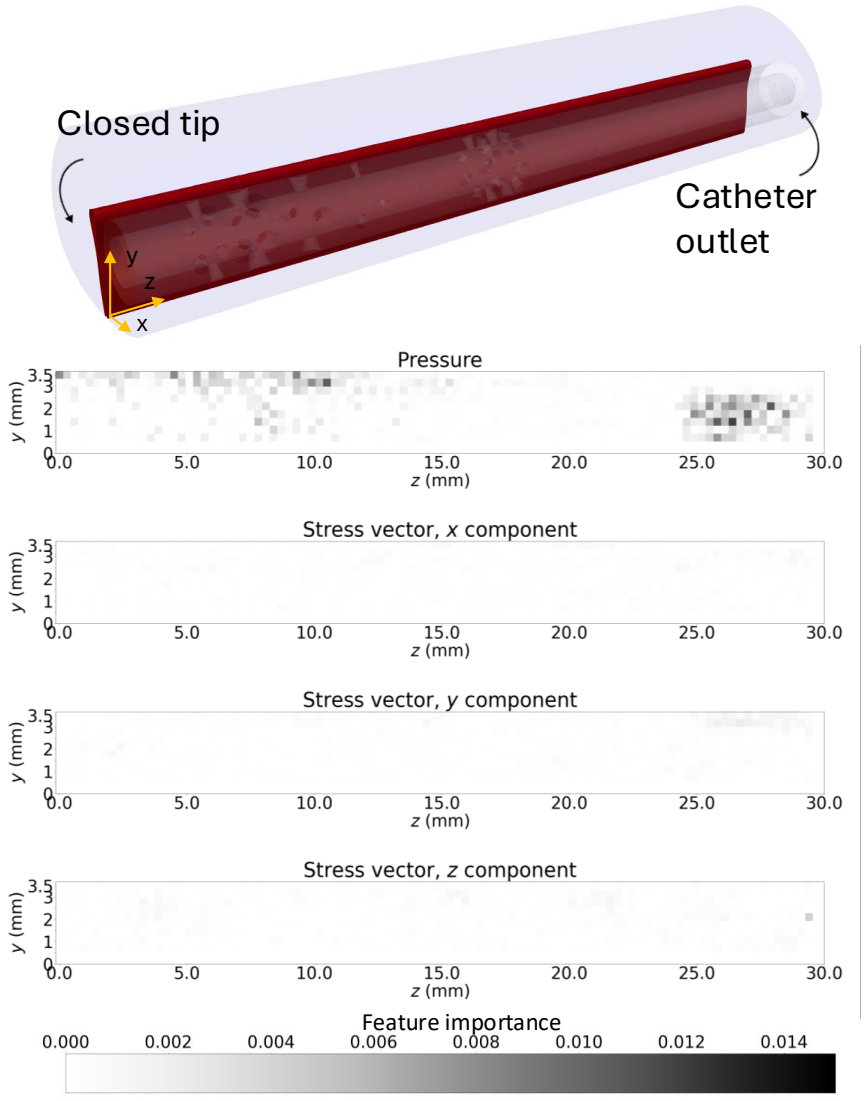

Figure 7.9: Updated feature importance visualisations for different stress components at different locations on the ChP.

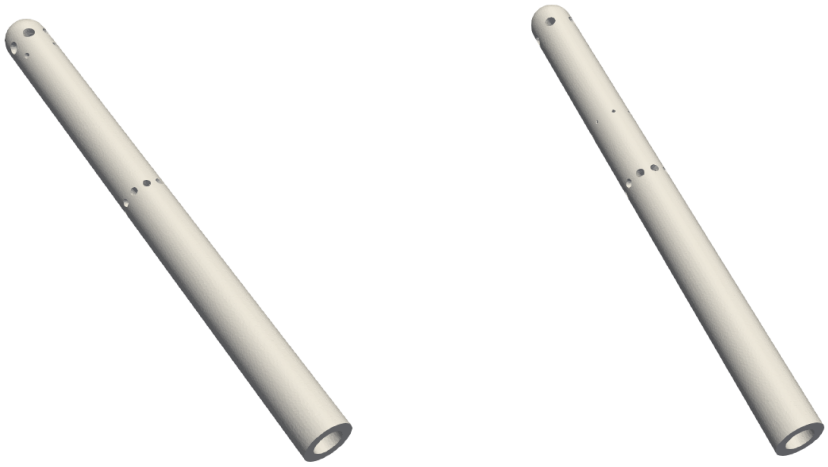

(a)

(b)

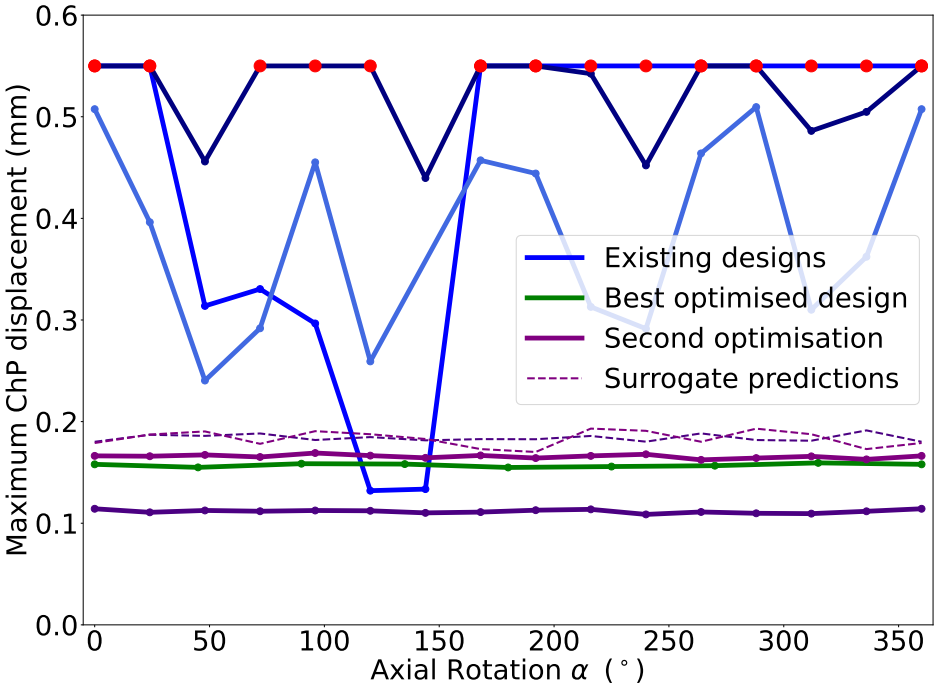

(c)

Figure 7.10: (a), (b): Two catheter designs identified during the second optimisation algorithm. (c) Designs compared in the 3D FSI model, new designs in purple (dashed lines showing surrogate predictions), previous optimised design in green, previous physical examples in blue.

large ring of holes near the catheter midpoint, and the large ring near the closed tip are the most significant design features.

The optimisation protocol presented here does not impose any penalty on the number of inlet holes (which could be enforced, for example, by adding a penalty term proportional to the total number of inlet holes to the design fitness). The fact that the protocol nevertheless identifies less rings as optimal, shows that any further rings in addition to the important ones at the midpoint and closed tip do not contribute to improved catheter performance.

As seen in Figure 7.10 the surrogate predictions are similar, giving fitnesses slightly under 0.2 mm. Again there is discrepancy between the surrogate predictions and the full model performance, comparable to the improved surrogate MAE of 0.08 mm.

One design from the second optimisation (in maroon) performs similarly to the previous best design (green), while the other significantly outperforms it (purple). This both shows the improvement that can be obtained by iteratively improving the surrogate, and also the need to test all new proposed designs in the 3D FSI model, as designs identified as equally promising by the surrogate can perform differently in the ground-truth.

This improvement could be continued, iterating between generating optimal designs, testing in the ground-truth model and using new additions to the ground truth dataset to refine the surrogate. This is a continuous process of improvement, approaching an online surrogate formulation. As with all aspects of generative design, this process should be terminated when the computational time involved in the process outweighs the diminishing returns of improving the surrogate.

7.3 Chapter summary

This chapter presents results from the generative design protocol, which is combined with the surrogate model for ChP displacement introduced in Chapter 6 to search for improved catheter designs. Insights from the full model results, discussed in Chapter 4, also inform the choice of parameter encoding.

The generative design process successfully proposed new catheter designs, which are subsequently confirmed as design improvements when tested using the detailed 3D FSI model. These results complete the surrogate-aided optimisation

methodology outlined in Figure 1.1. The FSI model is then further used to understand why certain design traits are identified as promising by the optimisation, giving a deeper understanding of the design process.

Manufacturing considerations are incorporated into the design process in a parameter preprocessing step. These focus on ensuring a structurally sound catheter with sufficient material between inlet holes, and as such, place limits on size and number of holes that can be present in any one axial ring. As the results from Chapter 4 suggest that catheter designs with large holes perform well when minimising ChP displacement, this was an important consideration to include in the optimisation process to ensure structurally sound designs were produced.

With the generative design methodology established, two extensions to the methodology are presented. The first restricts the design space to examine only designs with regular arrangements of four circumferential holes, a common feature of existing designs. The generative design process still produces improvements over existing designs, but the four-hole designs do not outperform those found by optimising the whole space.

The second extension leverages the need to test promising surrogate-identified designs in the full ground-truth model to determine their true performance. These validated simulations can additionally be used to expand the training dataset for the surrogate model, enabling its refinement and improved results in subsequent optimisation iterations.

This chapter completes the surrogate-aided generative design methodology outlined in Figure 1.1. Each chapter has contributed a distinct component of this framework, which are here successfully combined to generate demonstrable improvements in hydrocephalus catheter design. In the final chapter, the broader implications of this work are discussed, along with its limitations and directions for future research.

Chapter 8

Conclusions

This chapter summarises the key findings of the thesis and reflects on contributions to the field. Limitations of the work are evaluated and areas of possible future research discussed.

8.1 Thesis summary

The primary objective of this thesis was to improve the design of the ventricular catheters used in the treatment of hydrocephalus, with the aim of minimising the chance of ChP blockage. This has been successfully achieved with several new catheter designs proposed. The research also contributes to the broader field of medical device design by developing a generalisable surrogate-aided design methodology based on a combination of mechanistic insight and machine learning (ML) applicable to a wide range of biomedical and engineering problems.

The design of medical devices is often a slow and expensive process, with all new instruments required to pass through a range of clinical trials before being deemed safe for use. While modelling to date still relies on clinical trials, computational models can be effectively leveraged to address the high failure rate seen in clinical trials, as they can act as a filter to screen and remove unpromising designs, or motivate new design directions.

Recently, the growth in computing power has enabled an increase in model complexity. While finite element and finite volume methods to solve fluid and solid problems have existed for over 70 years [69, 70], only recently has the required computational power and memory reached a level that can accommodate

the incorporation of complex effects, including multiphysics and multiscale mechanisms, interdependence between systems and fluid-structure interaction (FSI). However, while these detailed computational models can provide impressive resolution of a problem, they remain computationally very expensive, thus often prohibiting comprehensive parameter exploration or optimisation studies. To overcome this reduced-order models (ROMs) are needed, which capture the key mechanisms of a simulation, but run in a fraction of the time.

This thesis presented the development and application of a generalisable surrogate-aided design methodology, applied to the problem of hydrocephalus shunt design, specifically the design and placement of inlet holes in the ventricular catheter component. Despite recent improvements in antibacterial shunt materials, which have successfully reduced post-surgical infection rates, studies indicate no significant improvement in long-term patient outcomes over the past forty years, suggesting that advances in shunt design may still have life-saving potential [11]. Previous computational studies have proposed design improvements based on achieving uniform influx across inlet holes. However, to date, no model has incorporated the ChP, requiring catheter performance to be inferred solely from fluid flow.

A complex FSI model of the design problem was presented in Chapter 3, with detailed results of the ventricle-catheter-ChP system presented in Chapter 4. This model is successful in capturing the interplay between underpinning mechanisms of the system, but has a runtime of over three days, making it infeasible for incorporation into an optimisation protocol. Therefore several ROMs are proposed. In Chapter 4 a *geometrical* reduction was presented, considering a 2D cross-section of the full model.

This reduction of the FSI setting to 2D proved effective in evaluating the circumferential position and size of inlet holes in the catheter. As there are a limited number of inlet hole configurations possible in 2D, it is feasible to consider an exhaustive search across all possible designs. It therefore was possible to identify the optimum inlet hole configuration in 2D, and this catheter design, when reinterpreted back into 3D was shown to outperform existing examples. However, this reduced-order model was restricted to 2D and could not capture more general three-dimensional effects, motivating the development of additional ROMs.

Chapter 5 introduced two further reduced-order models based on *physical* reductions, in which key mechanisms are approximated or neglected. The first model addressed the flow field within the catheter, exploiting assumptions of axisymmetry and a long, thin catheter geometry to motivate a 1D reduction. The flux through the inlet holes was modelled using a permeable-wall boundary condition, and the resulting model showed good agreement with full computational simulations. The second model focussed on the initial fluid stress field on the surface of the ChP in its undeformed, upright configuration. In this case, FSI effects were neglected, focussing on the initial fluid stresses which drives initial ChP displacement. Since the initial and equilibrium displacements are strongly correlated, the initial fluid stress field was expected to be a strong predictor of the equilibrium ChP displacement.

These ROMs are informative in their own right, but to be useful for design optimisation, they needed to be capable of accurately predicting the maximum equilibrium ChP displacement, here used to quantify the fitness of a catheter design. A mechanistic learning (MxL) approach is therefore implemented, combining a predictive ML layer with the ROMs, which transformed outputs of the ROMs into an approximation for the maximum equilibrium ChP displacement. A range of ML algorithms and input data was considered and the highest predictive accuracies were obtained by combining the stress field model with a random forest predictor. This composite model was successful at predicting ChP displacement and was consequently carried forward as a surrogate fitness function for use in the optimisation.

The integration of surrogate models with an optimisation codebase using multiple offspring sampling was successfully used to generate improved catheter designs through a generative design procedure. These designs were then tested in the full 3D FSI model which confirmed that they were a true improvement over existing devices.

8.2 Summary of accomplishments

This thesis has achieved two main objectives: direct improvements to hydrocephalus shunt system design, and the development of surrogate-aided generative design methodologies. These are discussed separately below.

8.2.1 Hydrocephalus shunt design

Clinical solutions to the medical problem of hydrocephalus have been sought since antiquity [41], with shunt drainage systems becoming standard from the early 20th century [215]. Despite over 36,000 shunt surgeries taking place each year in the United States alone, the failure rate of devices remains stubbornly high, with severe consequences for the patient [46].

Shunt design has been the focus of previous computational studies, notably the extensive work of the group of Galarza and Giménez (Refs. [86, 87] etc.), and separately the doctoral thesis of Weisenberg, Ref. [15]. These studies also focussed on ChP occlusion of the ventricular catheter component, and investigated the effect of the size, position and relative angle of inlet holes. They explored how variations in the size, position, and angle of inlet holes affected flow patterns and, by inference, the likelihood of obstruction.

However, these earlier works modelled only the fluid domain, positioning the catheter inside a large, axisymmetric region of cerebrospinal fluid (CSF) (Figure 2.4) and employing computational fluid methods to study the resultant flow fields. While informative, such fluid-only models necessarily rely on indirect metrics, here the uniformity of flow through inlet holes, as a proxy for design success. Designs that distributed CSF inflow more evenly were considered preferable, based on the heuristic observation that inlet holes near the outlet tend to receive disproportionately high inflow and are more frequently blocked.

This thesis marks a significant extension of that literature by being the first to incorporate a solid model of the ChP, and capture the interplay between the ChP and surrounding fluid, enabling direct simulation of the FSI between the ChP and the catheter. This advancement allows for a more realistic representation of the biological environment in which the catheter operates, capturing not just fluid dynamics but also the physical deformation of the ChP in response to catheter placement and flow. The 3D FSI model developed here confirms prior findings (that inlet holes near the outlet often dominate the influx of CSF and that the ChP often deforms more towards inlet holes near the fluid outlet).

In Chapter 7 several new catheter designs are found through the generative design procedure, all of which are shown to be improvements over existing designs when compared in the 3D FSI model. Consistent with the findings of the 2D reduced model, all designs proposed have a high number of inlet holes positioned

around the circumference of the catheter. Additionally, the proposed designs all prioritise a circumferential ring of large inlet holes near the closed tip, and a separate ring of large inlet holes near the midpoint of the catheter.

This represents a clear departure from previous computational studies of hydrocephalus catheter design, which enforced uniform inflow through each inlet hole and therefore favoured designs with larger holes at the closed tip and progressively smaller holes towards the catheter outlet [15, 216]. Analysis of the fluid stress field acting on the ChP surface shows that the designs proposed here distribute fluid stress more evenly across the ChP than earlier designs, highlighting the critical role of FSI in capturing the interaction between the ChP and its surrounding fluid environment.

This work therefore represents a significant advancement in both the understanding of the interaction between hydrocephalus catheters and their environment, and in the tools available for future design.

8.2.1.1 Limitations

The 3D FSI model presented here was used effectively to discriminate between existing and new catheter designs, but remains an idealised representation of the brain's ventricular environment. Several simplifications were made to ensure computational tractability:

- **Geometry:** the ventricular and ChP domains were modelled using smooth, idealised shapes. This was necessary due to the difficulty in obtaining high-resolution, segmented anatomical data, particularly for the relatively small ChP. As a result, the model lacks patient-specific detail or anatomical variability.

- **Material properties:** mechanical parameters such as the Young's modulus of the ChP were not taken from direct measurements, as such data is currently unavailable in the literature. Instead, values were selected from a biologically plausible range based on related soft biological tissues. The ChP was modelled as a hyperelastic material with a near-incompressible response, which, although a reasonable assumption, is an approximation of true tissue behaviour. Additionally, the deformation of the surrounding brain tissue was not included in the model, nor were growth effects or fluid

absorption at ventricle boundaries. The model the only exit for the CSF is through the catheter, as is true in the most severe hydrocephalus cases.

- **Lack of experimental validation:** the model predictions have not yet been directly validated against experimental or clinical data. This includes both the fluid dynamics and the mechanical deformation fields. While the model shows consistent and biologically plausible trends, quantitative validation remains an essential step.

Nevertheless, the above model simplifications were chosen to balance the complexity of the crucial FSI mechanism with a feasible computational runtime. The model was successful at clearly differentiating between catheter designs in the ventricle environment.

8.2.1.2 Recommended future extensions

This work offers several promising directions for future research into hydrocephalus shunt design, both experimental and computational. An important direction for future work is the validation of the newly proposed catheter designs. While these designs performed well in the 3D FSI model, experimental testing, such as experiments using physical ventricular replicas or *in vitro* systems incorporating synthetic or porcine ChP tissue, would provide important confirmation of their efficacy. Longer-term goals include collaboration with clinical researchers to enable retrospective analysis or clinical trials.

From a computational perspective, future models could incorporate patient-specific geometries derived from high-resolution imaging data such as MRI or CT scans, such as those presented in Ref. [173]. Improvements in image segmentation, especially for soft, small and irregular tissues like the ChP, would enable more anatomically faithful simulations and allow investigation into variability between patients. Alongside this, more sophisticated constitutive models could be developed. The incorporation of growth effects is an important future step to investigate the effect of changes in the ventricle and ChP geometry on catheter occlusion. The current use of a hyperelastic material model for the ChP is a simplification; future work could instead explore poroelastic or viscoelastic descriptions that incorporate the porous nature of brain tissues. Similarly, the assumption that all natural CSF exit pathways are closed could be relaxed.

Given the current lack of understanding into the mechanical properties of the ChP, it would be valuable to explore targeted experimental testing of these properties. This tissue is poorly characterised in the literature, and measurements of stiffness, deformation thresholds, and dynamic response to loading would significantly enhance the accuracy and credibility of future models. Techniques like indentation testing or high-resolution imaging during controlled deformation could be used to inform the derivation of more accurate models.

Finally, as more complex geometries and material behaviours are introduced, ensuring numerical stability and convergence of the computational models will be essential. This may require refinement of meshing strategies or solver strategies. However, the modular design of the simulation framework developed in this thesis makes it easy to make changes in the geometry or material properties under investigation.

8.2.2 Surrogate-aided generative design

While this research has been applied directly to the problem of hydrocephalus catheter design, the surrogate-aided generative design methodology is generalisable and could be applied to a wide range of design problems, particularly those with a dominant FSI component. The value of the methodology (shown in Figure 1.1) has been demonstrated, with the improved catheter designs produced by the surrogate approach showing true improvements when tested in the 3D FSI model.

The idea of using reduced models to improve optimisation algorithm performance is not new, with research on this topic dating back to at least 2001 [152]. As discussed in Section 2.4, previous work often integrated ML techniques directly into the optimisation algorithm, whereas in this research, the approach presented constructs and trains the surrogate model offline (i.e., outside of the optimisation algorithm), enabling the careful curation of a ground-truth dataset, selection and integration of appropriate ROMs, and more careful tuning of the ML layer, for example in avoiding overfitting.

Testing the new designs using the 3D FSI model allowed their efficacy to be assessed with full consideration of FSI effects. This represents a crucial final step in the optimisation procedure, as up to this point the designs have only been

evaluated by the surrogate model, which is inherently an approximation of the 3D FSI model.

The surrogate-aided methodology consists of three core components: the optimisation codebase, the expensive high-fidelity model, and the faster surrogate model which combines ROMs with a predictive ML layer. Figure 1.1 illustrates the exchange of information between these components over the course of a single optimisation run, as implemented in Chapter 7. However, this flow of information need not be limited to a single iteration. As described in Section 7.2.4, testing promising designs in the full 3D FSI model not only validates their performance but also yields a new dataset of ground-truth ChP displacement. This data can be combined with the original training set to enhance the accuracy of the surrogate model.

This iterative enrichment is particularly valuable when access to ground-truth data is limited, due to the high computational cost of full-model simulations. In the present case, the four new designs contributed 24 additional FSI runs—representing a 13% increase in dataset size. Retraining the surrogate model on this extended dataset results in improved predictive performance and offers a further opportunity to test its robustness: for example, evaluating whether the original ML hyperparameter choices generalise well to new data.

Once retrained, the improved surrogate can replace the previous version within the optimisation loop and be used in subsequent iterations. This continuous feedback loop is illustrated in Figure 8.1: each iteration proposes new designs via the surrogate model, evaluates them using the high-fidelity simulation, and incorporates the results into a progressively more accurate surrogate. Because the newly added data points are typically located in low-fitness regions (where the surrogate initially extrapolates with limited confidence in its predictions) this process also improves accuracy in precisely the areas where it is most needed. This iterative process approaches an "online" surrogate training formulation, in which the surrogate model is progressively developed and refined by each new design proposed in an optimisation protocol. Unlike a fully automated online surrogate approach, the procedure here is manual at each stage, with the surrogate model kept the same for each optimisation realisation of Figure 8.1. This allows failures to be identified and further surrogate refinements to be made only when potential improvements are explicitly observed.

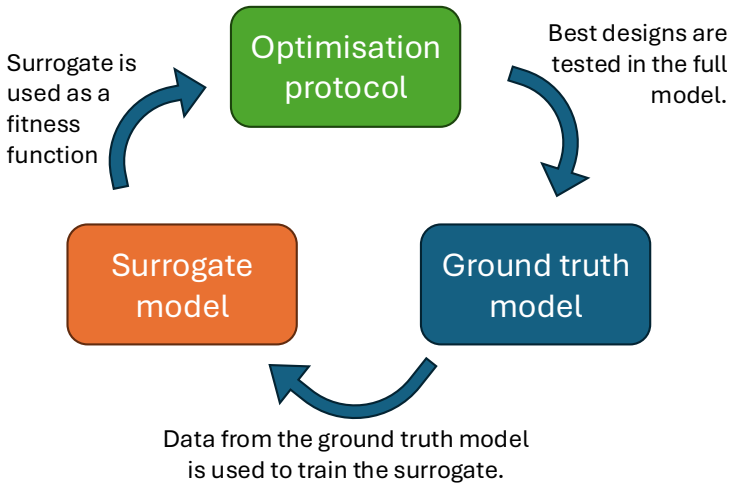

Figure 8.1: The optimisation protocol, the ground-truth model and the surrogate model form a feedback loop allowing for continuous improvement.

8.2.2.1 Limitations

Because the surrogate model is an approximation of the ground-truth physics, the fitness values it provides are limited by the accuracy of the model itself. As a result, identification of the true global optimum, or the globally optimal catheter design, cannot be guaranteed using the surrogate alone. Instead, the optimisation results should be interpreted as identifying promising regions of the design space. Candidate designs can then be evaluated using the full ground-truth model to determine their true performance.

The generative design methodology also relies on the availability of a surrogate model that is both sufficiently fast and sufficiently accurate. In this work, the surrogate runtime was under 10 minutes and achieved an R^2 value exceeding 0.75. For other applications, however, it may not be possible to achieve this balance between computational efficiency and predictive accuracy. These limitations are inherent to the framework and must be considered when applying the method and interpreting its results.

8.2.2.2 Recommended future work

A natural extension of this methodology would be the development of a general-purpose computational package, enabling other researchers to apply these techniques to their own problems. Such a tool could include automated training and

validation routines, in-built model selection tools, and integration with common optimisation frameworks. Additionally, experimental validation of the surrogate-predicted designs, as discussed above, would help demonstrate the effectiveness of the protocol.

8.3 Closing remarks

This research presents a generalisable surrogate methodology, which can be leveraged to speed up the investigation of design problems with a significant FSI component. In this thesis, the methodology is successfully applied to improving hydrocephalus shunt design, a medically important and computationally challenging problem. A detailed 3D finite element and finite volume model was constructed to capture the complex interplay between the ChP and ventricular catheter. Although highly informative, this model was computationally expensive, motivating the development of ROMs including a geometrical reduction to 2D that effectively constrained the design space, and a physically simplified fluid stress model that serves as a fast and accurate surrogate fitness function.

These components were integrated into a comprehensive design optimisation framework, which yielded novel catheter configurations with improved performance when tested in the full 3D model. This work contributes to the advancement of hydrocephalus catheter design, an area that lacks systematic analysis and standardisation of current devices. More broadly, it offers a framework for leveraging detailed, high-fidelity simulations to inform the creation of efficient surrogate models, enabling rapid exploration of design spaces. In doing so, this research responds to the growing need for scalable, adaptable optimisation tools in biomedical and engineering applications, especially as modelling capabilities continue to expand with advances in computational power.

References

[1] C. Harris and J. McAllister. "What We Should Know About the Cellular and Tissue Response Causing Catheter Obstruction in the Treatment of Hydrocephalus." *Neurosurg.* (2012). DOI: 10.1227/NEU.0b013e318244695f.

[2] A. Kapoor, T. Ray, N. Jepson, and S. Beier. "A Surrogate-Assisted Multiconcept Optimization Framework for Real-World Engineering Design". *J. Mech. Des.* (2025). DOI: 10.1115/1.4068404.

[3] P. Ogrodnik. *Medical device design: innovation from concept to market*. Academic Press, 2019. ISBN: 978-0443403187.

[4] D. Fogel. "Factors associated with clinical trials that fail and opportunities for improving the likelihood of success: A review." *Contemp. Clin. Trials Commun.* (2018). DOI: 10.1016/j.conctc.2018.08.001.

[5] L. Jiang, X. Gu, and S. Chen. "Generative Design of Bionic Structures Via Concurrent Multiscale Topology Optimization and Conformal Geometry Method". *J. Mech. Des.* (2020). DOI: 10.1115/1.4047345.

[6] J. Williams, F. Wechsung, B. Turney, S. Waters, and D. Moulton. "Shape optimisation for faster washout in recirculating flows". *J. Fluid Mech.* (2021). DOI: 10.1017/jfm.2020.1119.

[7] A. Linninger, K. Tangen, C-Y. Hsu, and D. Frim. "Cerebrospinal Fluid Mechanics and Its Coupling to Cerebrovascular Dynamics". *Annu. Rev. Fluid Mech.* (2016). DOI: 10.1146/annurev-fluid-122414-034321.

[8] R. Bonow, B. Hanak, and S. Browd. *Principles of Neurological Surgery*. Elsevier, 2018. ISBN: 9780323431408.

[9] M. Vinchon, H. Rekate, and A. Kulkarni. "Pediatric hydrocephalus outcomes: a review." *Fluids Barriers CNS* (2012). DOI: 10.1186/2045-8118-9-18.

[10] B. Hanak, E. Ross, C. Harris, S. Browd, and W. Shain. "Toward a better understanding of the cellular basis for cerebrospinal fluid shunt obstruction: report on the construction of a bank of explanted hydrocephalus devices". *J. Neurosurg. Pediatr.* (2016). DOI: 10.3171/2016.2.PEDS15531.

[11] M. Dewan, A. Rattani, R. Mekary, L. Glancz, I. Yunusa, R. Baticulon, G. Fieggen, J. Wellons, K. Park, and B. Warf. "Global hydrocephalus epidemiology and incidence: systematic review and meta-analysis". *J. Neurosurg.* (2019). DOI: 10.3171/2017.10.JNS17439.

[12] A. Kulkarni, S. Schiff, E. Mbabazi-Kabachelor, J. Mugamba, P. Ssenyonga, R. Donnelly, J. Levenbach, V. Monga, M. Peterson, M. MacDonald, V. Cherukuri, and B. Warf. "Endoscopic Treatment versus Shunting for Infant Hydrocephalus in Uganda." *N. Engl. J. Med.* (2017). DOI: 10.1056/NEJMoa1707568.

[13] M. Koleva and O. De Jesus. *Hydrocephalus.* 2023. URL: www.ncbi.nlm.nih.gov/books/NBK560875/ (visited on 06/14/2023).

[14] N. Mansoor, O. Solheim, O. A. Fredriksli, and S. Gulati. "Revision and complication rates in adult shunt surgery: a single-institution study." *Acta Neurochir.* (2021). DOI: 10.1007/s00701-020-04526-z.

[15] S. Weisenberg. "Improving ventricular catheter design through computational fluid dynamics". Thesis submission. University of Tennessee, 2016. URL: trace.tennessee.edu/utk_gradthes/3817.

[16] C. Mallucci, M. D. Jenkinson, E. Conroy, J. Hartley, M. Brown, T. Moitt, J. Dalton, T. Kearns, M. Griffiths, G. Culeddu, T. Solomon, D. Hughes, C. Gamble, and BASICS study collaborators. "Silver-impregnated, antibiotic-impregnated or non-impregnated ventriculoperitoneal shunts to prevent shunt infection: the BASICS three-arm RCT." *Health Technol. Assess.* (2020). DOI: 10.3310/hta24170.

[17] J. Metzcar, C. Jutzeler, P. Macklin, A. Köhn-Luque, and S. Brüningk. "A review of mechanistic learning in mathematical oncology". *Front. Immunol.* (2024). DOI: 10.3389/fimmu.2024.1363144.

[18] U. S. National Institutes of Health. *Introduction to the Nervous System.* URL: training.seer.cancer.gov/anatomy/nervous/ (visited on 06/14/2023).

[19] T. Wichmann, D. Overgaard, H. Helle, and M. Pedersen. "A Brief Overview of the Cerebrospinal Fluid System and Its Implications for Brain and Spinal Cord Diseases". *Front. Hum. Neurosci.* (2022). DOI: 10.3389/fnhum.2021.737217.

[20] B. Sweetman and A. Linninger. "Cerebrospinal Fluid Flow Dynamics in the Central Nervous System". *Ann. Biomed. Eng.* (2010). DOI: 10.1007/s10439-010-0141-0.

[21] S. Gupta, M. Soellinger, P. Boesiger, D. Poulikakos, and V. Kurtcuoglu. "Three-Dimensional Computational Modeling of Subject-Specific Cerebrospinal Fluid Flow in the Subarachnoid Space." *J. Biomech. Eng.* (2008). DOI: 10.1115/1.3005171.

[22] A. Sánchez, C. Martínez-Bazán, C. Gutiérrez-Montes, and E. Criado-Hidalgo. "On the bulk motion of the cerebrospinal fluid in the spinal canal". *J. Fluid Mech.* (2018). DOI: 10.1017/jfm.2018.67.

[23] M. Lun, E. Monuki, and M. Lehtinen. "Development and functions of the choroid plexus-cerebrospinal fluid system." *Nat. Rev. Neurosci.* (2015). DOI: 10.1038/nrn3921.

[24] M-A. Boucher, S. Lippé, C. Dupont, I. Knoth, G. Lopez, R. Shams, R. El-Jalbout, A. Damphousse, and S. Kadoury. "Computer-aided lateral ventricular and brain volume measurements in 3D ultrasound for assessing growth trajectories in newborns and neonates". *Phys. Med. Biol.* (2018). DOI: 10.1088/1361-6560/aaea85.

[25] Z. Lu, J. He, Y. Yu, Z. Li, Z. Li, and J. Gong. "Measurement of lateral ventricle volume of normal infant based on magnetic resonance imaging." *Chin. Neurosurg. J.* (2019). DOI: 10.1186/s41016-019-0156-9.

[26] V. Hubert, F. Chauveau, C. Dumot, E. Ong, L. Berner, E. Canet-Soulas, J. Ghersi-Egea, and M. Wiart. "Clinical Imaging of Choroid Plexus in Health and in Brain Disorders: A Mini-Review." *Front Mol Neurosci.* (2019). DOI: 10.3389/fnmol.2019.00034.

[27] M. Madhukar, A. Choudhary, D. Boal, M. Dias, and M. Iantosca. "Choroid plexus: normal size criteria on neuroimaging." *Surg. Radiol. Anat.* (2012). DOI: 10.1007/s00276-012-0980-5.

[28] M. Segura and R. Enríquez. "Measurement of the choroid plexus of the lateral ventricles in full-term newborns using ultrasonics." *Bol. Med. Hosp. Infant. Mex.* 47 (1990), pp. 382–4.

[29] K. Kalluri, W. Segars, S. Pells, Phillip Kuo, Lars Furenlid, Matthew Kupinski, Shiva Abbaszadeh, and Michael King. "Simulated imaging of an anthropomorphic model of the choroid plexus with brain-dedicated MPH-SPECT". *J. Nucl. Med.* 65 (2024). Issue Supplement 2.

[30] R. Abu-Rustum, M. Ziade, and S. Abu-Rustum. "Reference Values for the Right and Left Fetal Choroid Plexus at 11 to 13 Weeks". *J. Ultrasound Med.* (2013). DOI: 10.7863/ultra.32.9.1623.

[31] B. Bitanihirwe, P. Lizano, and T. Woo. "Deconstructing the functional neuroanatomy of the choroid plexus: an ontogenetic perspective for studying neurodevelopmental and neuropsychiatric disorders." *Mol. Psychiatry.* (2022). DOI: 10.1038/s41380-022-01623-6.

[32] http://creativecommons.org/licenses/by/4.0/. Accessed: 2025-10-03.

[33] M. Mortazavi, C. Griessenauer, N. Adeeb, A. Deep, R. Bavarsad Shahripour, M. Loukas, R. Tubbs, and R. Tubbs. "The choroid plexus: A comprehensive review of its history, anatomy, function, histology, embryology, and surgical considerations". *Childs Nerv. Syst.* (2013). DOI: 10.1007/s00381-013-2326-y.

[34] A. Linninger, C. Tsakiris, D. Zhu, M. Xenos, P. Roycewicz, Z. Danziger, and R. Penn. "Pulsatile cerebrospinal fluid dynamics in the human brain". *IEEE Trans. Biomed. Eng.* (2005). DOI: 10.1109/TBME.2005.844021.

[35] J. Lim, S. Rhee, H. Choi, J. Lee, S. Kuttappan, T. Tho, S. Choi, Y. Kim, and N-L. Jeon. "Engineering choroid plexus-on-a-chip with oscillatory flow for modeling brain metastasis". *Materials Today Bio* (2023). DOI: 10.1016/j.mtbio.2023.100773.

[36] A. Linninger, M. Xenos, B. Sweetman, S. Ponkshe, X. Guo, and R. Penn. "A mathematical model of blood, cerebrospinal fluid and brain dynamics". *J. Math. Biol.* (2009). DOI: 10.1007/s00285-009-0250-2.

[37] A. Demerdash, R. Singh, M. Loukas, and R. Tubbs. "A historical glimpse into treating childhood hydrocephalus." *Childs Nerv. Syst.* (2016). DOI: 10.1007/s00381-015-2652-3.

[38] R. Schwamb, A. Dalpiaz, Y. Miao, J. Gonka, and S. Khan. "Clinical manifestations of hydrocephalus: A review". *Neurol. Clin. Neurosci.* (2014). DOI: 10.1111/ncn3.117.

[39] National Health Service. *Hydrocephalus*. 2023. URL: www.nhs.uk/conditions/hydrocephalus (visited on 04/04/2023).

[40] A. Hopkins, E. DeSimone, K. Chwalek, and D. Kaplan. "3D in vitro modeling of the central nervous system". *Prog. Neurobiol.* (2015). DOI: 10.1016/j.pneurobio.2014.11.003.

[41] A. Aschoff, P. Kremer, B. Hashemi, and S. Kunze. "The scientific history of hydrocephalus and its treatment." *Neurosurg. Rev.* (1999). DOI: 10.1007/s101430050035.

[42] D. Srinivas, G. Tyagi, and G. Singh. "Shunt Implants – Past, Present and Future." *Neurol. India* (2021). DOI: 10.4103/0028-3886.332263.

[43] S. Suresh. "Development of an Alternative Ventricular Catheter and an In Vitro Model of its Obstruction". PhD thesis. University of Strathclyde, 2014. URL: stax.strath.ac.uk/concern/theses/1r66j128n.

[44] K. Tomei. "The Evolution of Cerebrospinal Fluid Shunts: Advances in Technology and Technique." *Pediatr. Neurosurg.* (2017). DOI: 10.1159/000477174.

[45] P. Kofoed Månsson, S. Johansson, M. Ziebell, and M. Juhler. "Forty years of shunt surgery at Rigshospitalet, Denmark: a retrospective study comparing past and present rates and causes of revision and infection." *BMJ Open* (2017). DOI: 10.1136/bmjopen-2016-013389.

[46] A. Vlasak, H. Okechi, D. Horinek, and A. Albright. "Pediatric Ventriculoperitoneal Shunts Revision Rate and Costs in High-Volume sub-Saharan Department". *World Neurosurg.* (2019). DOI: 10.1016/j.wneu.2019.07.059.

[47] J. Stewart, J. Warner-Levy, S. Bate, C. McMahon, D. Slade, and M. Bailey. "Determinants of adult Ventriculoperitoneal Shunt failure: Insights from a large neurosurgical centre". *Clin. Neurol. Neurosurg.* (2025). DOI: 10.1016/j.clineuro.2025.109013.

[48] S. Sgouros. *Spina Bifida Hydrocephalus and Shunts*. 2023. URL: emedicine.medscape.com/article/937979 (visited on 12/21/2025).

[49] John Hopkins Medicine. *Hydrocephalus in children*. 2022. URL: www.hopkinsmedicine.org/health/conditions-and-diseases/hydrocephalus (visited on 05/30/2022).

[50] E. Hayman, V.-D. Nguyan, I. McFarlane, J. Pech, J. Jayamohan, J-M. Peña Sánchez, S. Waters, and A. Jerusalem. "Reduced model aided fluid-structure interaction design framework for shunt systems". *Med. Eng. Phys.* (2025). DOI: 10.1016/j.medengphy.2025.104403.

[51] Integra Life. *Neurocritical care, Ventricular catheters.* URL: www.integralife.com/codman-ventricular-catheter/ (visited on 05/19/2023).

[52] Natus Global. *Shunt CSF catheters.* URL: natus.com/products-services/shunt-catheters (visited on 05/31/2023).

[53] R. Hoshide, H. Meltzer, C. Dalle-Ore, D. Gonda, D. Guillaume, and C. C. Chen. "Impact of ventricular-peritoneal shunt valve design on clinical outcome of pediatric patients with hydrocephalus: Lessons learned from randomized controlled trials." *Surg. Neurol. Int.* (2017). DOI: 10.4103/sni.sni_11_17.

[54] A. Tasiou, A.G. Brotis, F. Esposito, and K. Paterakis. "Endoscopic third ventriculostomy in the treatment of idiopathic normal pressure hydrocephalus: a review study." *Neurosurg. Rev.* (2016). DOI: 10.1007/s10143-015-0685-4.

[55] S. Gholampour and M. Bahmani. "Hydrodynamic comparison of shunt and endoscopic third ventriculostomy in adult hydrocephalus using in vitro models and fluid-structure interaction simulation". *Comput. Methods. Programs Biomed.* (2021). DOI: 10.1016/j.cmpb.2021.106049.

[56] M. Johnston, M. Del Bigio, J. Drake, D. Armstrong, D. Di Curzio, and J. Bertrand. "Pre- and post-shunting observations in adult sheep with kaolin-induced hydrocephalus". *Fluids Barriers CNS* (2013). DOI: 10.1186/2045-8118-10-24.

[57] J. Scarff. "Evaluation of Treatment of Hydrocephalus: Results of Third Ventriculostomy and Endoscopic Cauterization of Choroid Plexuses Compared With Mechanical Shunts". *Arch. Neurol.* (1966). DOI: 10.1001/archneur.1966.00470100038005.

[58] T. Simon, J. Schaffzin, C. Stevenson, K. Willebrand, M. Parsek, and L. Hoffman. "Cerebrospinal Fluid Shunt Infection: Emerging Paradigms in Pathogenesis that Affect Prevention and Treatment." *J. Pediatr.* (2019). DOI: 10.1016/j.jpeds.2018.11.026.

[59] S. Parker, M. McGirt, J. Murphy, J. Megerian, M. Stout, and L. Engelhart. "Comparative effectiveness of antibiotic-impregnated shunt catheters in the treatment of adult and pediatric hydrocephalus: analysis of 12,589 consecutive cases from 287 US hospital systems." *J. Neurosurg.* (2015). DOI: 10.3171/2014.10.JNS13395.

[60] J. Kast, D. Duong, F. Nowzari, W. Chadduck, and S. Schiff. "Time-related patterns of ventricular shunt failure." *Childs Nerv. Syst.* (1994). DOI: 10.1007/BF00335075.

[61] V. Levrini, Z. Czosnyka, I. Lawes, A. Kolias, and R. Mannion. "Shunt Testing In Vivo: Illustration of Partially Obstructed Ventricular Catheter by In-Growing Choroid Plexus." *Cureus* (2020). DOI: 10.7759/cureus.9287.

[62] M. Vinchon, M. Baroncini, and I. Delestret. "Adult outcome of pediatric hydrocephalus." *Childs Nerv. Syst.* (2012). DOI: 10.1007/s00381-012-1723-y.

[63] B. Tuli S. and; O'Hayon, J. Drake, M. Clarke, and J. Kestle. "Change in Ventricular Size and Effect of Ventricular Catheter Placement in Pediatric Patients with Shunted Hydrocephalus." *Neurosurg.* (1999).

[64] M. Babadagli, D. Cooke, S. Walling, and P. McNeely. "Endoscopic Retrieval of Flanged Ventricular Catheters". *Can. J. Neurol. Sci.* (2018). DOI: 10.1017/cjn.2018.336.

[65] J. McAllister, M. Talcott, A. Isaacs, S. Zwick, M. Garcia-Bonilla, L. Castaneyra-Ruiz, A. Hartman, R. Dilger, S. A. Fleming, R. Golden, D. Morales, C. Harris, and D. Limbrick. "A novel model of acquired hydrocephalus for evaluation of neurosurgical treatments." *Fluids Barriers CNS* (2021). DOI: 10.1186/s12987-021-00281-0.

[66] A. Borrelli and J. Wellmann. "Computer Simulations Then and Now: an Introduction and Historical Reassessment." *N.T.M.* (2019). DOI: 10.1007/s00048-019-00227-6.

[67] A. Hodgkin and A. Huxley. "Currents carried by sodium and potassium ions through the membrane of the giant axon of Loligo." *J. Physiol.* (1952). DOI: 10.1113/jphysiol.1952.sp004717.

[68] A. Goriely. *Solid Mechanics*. 2025. URL: %7Bcourses.maths.ox.ac.uk/pluginfile.php/115507/mod_resource/content/2/Solids-2025.pdf%7D (visited on 04/15/2026).

[69] P. Cardiff and I. Demirdzic. "Thirty years of the finite volume method for solid mechanics". *Arch. Computat. Methods Eng.* (2021). DOI: 10.1007/s11831-020-09523-0.

[70] I. Erhunmwun and U. Ikponmwosa. "Review on finite element method". *J. Appl. Sci. Environ. Manage.* (2017). DOI: 10.4314/jasem.v21i5.30.

[71] W. Liu, S. Li, and H. Park. "Eighty Years of the Finite Element Method: Birth, Evolution, and Future." *Arch. Computat. Methods Eng.* (2022). DOI: 10.1007/s11831-022-09740-9.

[72] R. Clough. "Original formulation of the finite element method". *Finite Elem. Anal. Des.* (1990). DOI: 10.1016/0168-874X(90)90001-U.

[73] C. Taylor, T. Hughes, and C. Zarins. "Finite element modeling of blood flow in arteries." *Comput. Methods Appl. Mech. Eng.* (1998). DOI: 10.1016/S0045-7825(98)80008-X.

[74] G. Holzapfel, R. Eberlein, P. Wriggers, and H. Weizsäcker. "Large strain analysis of soft biological membranes: formulation and finite element analysis." *Comput. Methods Appl. Mech. Eng.* (1996). DOI: 10.1016/0045-7825(96)00999-1.

[75] E. Hadzri, K. Osman, M. Kadir, and A. Aziz. "Computational investigation on CSF flow analysis in the third ventricle and aqueduct of sylvius". *IIUM Eng. J.* (2011). DOI: 10.31436/iiumej.v12i3.158.

[76] B. Sweetman, M. Xenos, L. Zitella, and A. Linninger. "Three-dimensional computational prediction of cerebrospinal fluid flow in the human brain". *Comput. Biol. Med.* (2011). DOI: 10.1016/j.compbiomed.2010.12.001.

[77] A. Linninger, M. Xenos, D. Zhu, M. Somayaji, S. Kondapalli, and R. Penn. "Cerebrospinal fluid flow in the normal and hydrocephalic human brain." *IEEE Trans. Biomed. Eng.* (2007). DOI: 10.1109/TBME.2006.886853.

[78] S. Gholampour, N. Fatouraee, A. Seddighi, and A. Seddighi. "Evaluating the effect of hydrocephalus cause on the manner of changes in the effective parameters and clinical symptoms of the disease." *J. Clin. Neurosci.* (2017). DOI: 10.1016/j.jocn.2016.09.012.

[79] S. Gholampour. "FSI simulation of CSF hydrodynamic changes in a large population of non-communicating hydrocephalus patients during treatment process with regard to their clinical symptoms". *PLoS One* (2018). DOI: 10.1371/journal.pone.0196216.

[80] H. Patel, Y. Huang, D. Dengiz, M. Pravdivtseva, O. Jansen, E. Quandt, and J. Aizenberg. "Fluid dynamics model of the cerebral ventricular system." *Proc. Natl. Acad. Sci. U. S. A.* (2025). DOI: 10.1073/pnas.2426067122.

[81] S. Lee, N. Kwok, J. Holsapple, T. Heldt, and L. Bourouiba. "Enhanced wall shear stress prevents obstruction by astrocytes in ventricular catheters." *J. R. Soc. Interface.* (2020). DOI: 10.1098/rsif.2019.0884.

[82] J. Lin, M. Morris, W. Olivero, Boop. F., and R. Sanford. "Computational and experimental study of proximal flow in ventricular catheters." *J. Neurosurg.* (2003). DOI: 10.3171/jns.2003.99.2.0426.

[83] U. Thomale, H. Hosch, A. Koch, M. Schulz, G. Stoltenburg, E. Haberl, and C. Sprung. "Perforation holes in ventricular catheters—is less more?": *Childs Nerv. Syst.* (2010). DOI: 10.1007/s00381-009-1055-8.

[84] M. Galarza, Á. Giménez, J. Valero, O. Pellicer, and J. Amigó. "Computational fluid dynamics of ventricular catheters used for the treatment of hydrocephalus: a 3D analysis." *Childs Nerv. Syst.* (2014). DOI: 10.1007/s00381-013-2226-1.

[85] M. Galarza, Á. Giménez, J. Valero, O. Pellicer, J. Martínez-Lage, and J. Amigó. "Basic cerebrospinal fluid flow patterns in ventricular catheters prototypes." *Childs Nerv. Syst.* (2015). DOI: 10.1007/s00381-015-2651-4.

[86] M. Galarza, Á. Giménez, O. Pellicer, J. Valero, and J. Amigó. "New designs of ventricular catheters for hydrocephalus by 3-D computational fluid dynamics." *Childs Nerv. Syst.* (2015). DOI: 10.1007/s00381-014-2477-5.

[87] Á. Giménez, M. Galarza, U. Thomale, M. Schuhmann, J. Valero, and J. Amigó. "Pulsatile flow in ventricular catheters for hydrocephalus". *Philos. Trans. R. Soc. A Math. Phys. Eng. Sci.* (2017). DOI: 10.1098/rsta.2016.0294.

[88] M. Galarza, A. Giménez, O. Pellicer, J. Valero, and J. Amigó. "Parametric study of ventricular catheters for hydrocephalus." *Acta Neurochir.* (2016). DOI: 10.1007/s00701-015-2618-y.

[89] M. Galarza, A. Giménez, O. Pellicer, J. Valero, and J. Amigó. "Ventricular Catheters for Hydrocephalus". *Pediatric Hydrocephalus*. Ed. by G. Cinalli, M. Ozek, and C. Sainte-Rose. Springer International Publishing, 2018. ISBN: 978-3-319-31889-9. DOI: 10.1007/978-3-319-31889-9_72-1.

[90] M. Galarza, V. Etus, F. Sosa, R. Argañaraz, B. Mantese, R. Gazzeri, C. Montoya, P. de la Rosa, A. Guerrero, G. Chaban, Á. Giménez, and J. Amigó. "Flow ventricular catheters for shunted hydrocephalus: initial clinical results." *Childs Nerv. Syst.* (2021). DOI: 10.1007/s00381-020-04941-8.

[91] B. Good, J. Killeffer, and S. TerMaath. "The effects of ventricle geometries and boundary conditions on computational modeling of ventriculoperitoneal catheters". *Comput. Biol. Med.* (2025). DOI: doi.org/10.1016/j.compbiomed.2025.109776.

[92] C. Schwerk and H. Schroten. "In vitro models of the choroid plexus and the blood-cerebrospinal fluid barrier: advances, applications, and perspectives." *Human Cell* (2024). DOI: 10.1007/s13577-024-01115-5.

[93] A. Goriely, M. G. Geers, G. A. Holzapfel, J. Jayamohan, A. Jérusalem, S. Sivaloganathan, W. Squier, J. A. van Dommelen, S. Waters, and E. Kuhl. "Mechanics of the brain: perspectives, challenges, and opportunities." *Biomech. Model. Mechanobiol.* (2015). DOI: 10.1007/s10237-015-0662-4.

[94] F. Morin, M. Chabanas, H. Courtecuisse, and Y. Payan. "Biomechanical modeling of brain soft tissues for medical applications". *Biomechanics of Living Organs*. Academic Press, 2017. DOI: 10.1016/B978-0-12-804009-6.00006-7.

[95] L. Bilston. *Biomechanics of the Brain*. Springer New York, 2019. ISBN: 978-3-030-04995-9.

[96] X. Zhang and J. Weickenmeier. "Brain Stiffness Follows Cuprizone-Induced Variations in Local Myelin Content". *Acta Biomater.* (2023). DOI: 10.1016/j.actbio.2023.08.033.

[97] S. Budday, T. Ovaert, G. Holzapfel, P. Steinmann, and E. Kuhl. "Fifty Shades of Brain: A Review on the Mechanical Testing and Modeling of Brain Tissue". *Arch. Computat. Methods Eng.* (2019). DOI: 10.1007/s11831-019-09352-w.

[98] C-Y. Lin. "Alternative Form of Standard Linear Solid Model for Characterizing Stress Relaxation and Creep: Including a Novel Parameter for Quantifying the Ratio of Fluids to Solids of a Viscoelastic Solid". *Front. Mater. Sci.* (2020). DOI: 10.3389/fmats.2020.00011.

[99] J-C. Petiteau, E. Verron, R. Othman, and H. Le Sourne. "Large strain rate-dependent response of elastomers at different strain rates: Convolution integral vs. internal variable formulations". *Mech. Time Depend. Mater.* (2013). DOI: 10.1007/s11043-012-9188-7.

[100] M. Kohandel, S. Sivaloganathan, and G. Tenti. "Estimation of the quasi-linear viscoelastic parameters using a genetic algorithm". *Math. Comput. Model.* (2008). DOI: 10.1016/j.mcm.2007.04.006.

[101] L. Solamen, M. McGarry, J. Fried, J. Weaver, S. Lollis, and K. Paulsen. "Poroelastic Mechanical Properties of the Brain Tissue of Normal Pressure Hydrocephalus Patients During Lumbar Drain Treatment Using Intrinsic Actuation MR Elastography." *Acad. Radiol.* (2021). DOI: 10.1016/j.acra.2020.03.009.

[102] D. Sowinski, M. McGarry, E. Van Houten, S. Gordon-Wylie, J. Weaver, and K. Paulsen. "Poroelasticity as a Model of Soft Tissue Structure: Hydraulic Permeability Reconstruction for Magnetic Resonance Elastography in Silico". *Front. Phys.* (2021). DOI: 10.3389/fphy.2020.617582.

[103] L. Miller, A. Ramírez-Torres, R. Rodríguez-Ramos, and R. Penta. "Effective Governing Equations for Viscoelastic Composites." *J. Mater.* (2023). DOI: 10.3390/ma16144944.

[104] Y. Feng, Y. Chen, Y. Yao, X. Li, A. Zhang, and G. Genin. "The brain as a structure: A model of how fluid–structure interactions stiffen brain tissue after injury". *Eng. Struct.* (2022). DOI: 10.1016/j.engstruct.2022.113960.

[105] J. Vardakis, L. Guo, T. Peach, T. Lassila, M. Mitolo, D. Chou, Z. Taylor, S. Varma, A. Venneri, A. Frangi, and Y. Ventikos. "Fluid-Structure Interaction for Highly Complex, Statistically Defined, Biological Media: Homogenisation and a 3D Multi-Compartmental Poroelastic Model for Brain Biomechanics". *J. Fluids Struct.* (2019). DOI: 10.1016/j.jfluidstructs.2019.04.008.

[106] M. Almudarra and A. Ramírez-Torres. "Examining avascular tumour growth dynamics: A variable-order non-local modelling perspective." *Math. Mech. Solids* (2024). DOI: 10.1177/10812865241230269.

[107] T. Lee, M. Holland, J. Weickenmeier, A. Gosain, and A. Tepole. "The geometry of incompatibility in growing soft tissues: Theory and numerical characterization". *J. Mech. Phys.Solids* (2021). DOI: 10.1016/j.jmps.2020.104177.

[108] S. Payne. *Lecture notes in multi-scale biomechanics.* 2021.

[109] O. Zienkiewicz, R. Taylor, and P. Nithiarasu. "Fluid–Structure Interaction". *The Finite Element Method for Fluid Dynamics (Seventh Edition).* Butterworth-Heinemann, 2014. ISBN: 978-1-85617-635-4.

[110] G. Cardillo and C. Camporeale. "Modeling fluid–structure interactions between cerebro-spinal fluid and the spinal cord". *J. Fluids Struct.* (2021). DOI: 10.1016/j.jfluidstructs.2021.103251.

[111] L. Fin and R. Grebe. "Three dimensional modeling of the cerebrospinal fluid dynamics and brain interactions in the aqueduct of sylvius." *Comput. Method Biomec.* (2003). DOI: 10.1080/1025584031000097933.

[112] N. Masoumi, D. Bastani, S. Najarian, F. Ganji, F. Farmanzad, and Seddighi A. "Mathematical modeling of CSF pulsatile hydrodynamics based on fluid-solid interaction." *IEEE Trans. Biomed. Eng.* (2010). DOI: 10.1109/TBME.2009.2037975.

[113] N. Smorzhenkov and E. Ignatova. "The use of generative design for the architectural solutions synthesis in the typical construction of residential buildings". *E3S Web Conf.* (2021). DOI: 10.1051/e3sconf/202128104008.

[114] S. Krish. "A practical generative design method". *Comput. Aided. Des.* (2011). DOI: 10.1016/j.cad.2010.09.009.

[115] L. Gradišar, M. Dolenc, and R. Klinc. "Towards machine learned generative design". *Autom. Constr.* (2024). DOI: 10.1016/j.autcon.2024.105284.

[116] L. Han, W. Du, Z. Xia, B. Gao, and M. Yang. "Generative Design and Integrated 3D Printing Manufacture of Cross Joints." *J. Mater.* (2022). DOI: 10.3390/ma15144753.

[117] R. Jaisawal and V. Agrawal. "Generative Design Method (GDM) – A State of Art". *IOP Conf. Ser. Mater. Sci. Eng.* (2021). DOI: 10.1088/1757-899X/1104/1/012036.

[118] M. Tanveer, M. Azad, D. Kim, S. Khalid, and H. Kim. "Generative Design for Engineering Applications: A State-of-the-Art Review". *Arch. Comput. Method Eng.* (2025). DOI: 10.1007/s11831-025-10302-y.

[119] Dassault Systemes. *Innovative Generative Design Solutions*. URL: www.3ds.com/store/cad/generative-design (visited on 06/20/2025).

[120] Autodesk Inc. *Autodesk Revit: BIM software to design and make anything*. URL: www.autodesk.com/uk/products/revit/overview (visited on 12/30/2025).

[121] Autodesk Inc. *Autodesk Fusion: More than CAD, it's the future of design and manufacturing*. URL: www.autodesk.com/uk/products/fusion-360/overview (visited on 12/30/2025).

[122] M. Bracken. "Why animal studies are often poor predictors of human reactions to exposure." *J. R. Soc. Med.* (2009). DOI: 10.1258/jrsm.2008.08k033.

[123] M. Price, W. Zhang, I. Friel, Trevor Robinson, Roisin McConnell, Declan Nolan, Peter Kilpatrick, Sakil Barbhuiya, and Stephen Kyle. "Generative design for additive manufacturing using a biological development analogy". *J. Comput. Des. Eng* (2022). DOI: 10.1093/jcde/qwac016.

[124] S. Kanagalingam, C. Dalton, P. Champneys, T. Boutefnouchet, M. Fernandez-Vicente, D. Shepherd, D. Wimpenny, and L. Thomas-Seale. "Detailed design for additive manufacturing and post processing of generatively designed high tibial osteotomy fixation plates." *Prog. Addit. Manuf.* (2022). DOI: 10.1007/s40964-022-00342-2.

[125] D. Hernandez-Aristizabal, S. Arroyave-Tobón, K. Marquez-Florez, and J-M. Linares. "Bio-inspired generative design of contact interfaces subjected to time-dependent loading conditions". *Results Eng.* (2025). DOI: 10.1016/j.rineng.2025.104340.

[126] V. Ricotta, R. Campbell, T. Ingrassia, and V. Nigrelli. "A new design approach for customised medical devices realized by additive manufacturing." *Int. J. Interact. Des. Manuf.* (2020). DOI: 10.1007/s12008-020-00705-5.

[127] P. Naharro, P. Toharia, A. LaTorre, and J-M. Peña. "Comparative study of regression vs pairwise models for surrogate-based heuristic optimisation". *Swarm Evol. Comput.* (2022). DOI: 10.1016/j.swevo.2022.101176.

[128] J-M. Peña, A. LaTorre, and A. Jérusalem. "SoftFEM: The Soft Finite Element Method". *Int. J. Numer. Methods Eng.* (2019). DOI: 10.1002/nme.6029.

[129] S. Fischer, J. De Oliveira, J. Mumford, and L. Kell. "Using a genetic algorithm to optimize a data-limited catch rule". *ICES J. Mar. Sci.* (2021). DOI: 10.1093/icesjms/fsab018.

[130] M. Malek, M. Guruswamy, and M. Pandya. "Serial and parallel simulated annealing and tabu search algorithms for the traveling salesman problem." *Ann. Oper. Res.* (1989). DOI: 10.1007/BF02022093.

[131] S. Ruder. *An overview of gradient descent optimization algorithms*. 2017. arXiv: 1609.04747.

[132] D. Liu and J. Nocedal. "On the limited memory BFGS method for large scale optimization." *Math. Program.* (1989). DOI: 10.1007/BF01589116.

[133] L-Y. Tseng and C. Chen. "Multiple Trajectory Search for Large Scale Global Optimization". *IEEE Trans. Evol. Comput.* (2008). DOI: 10.1109/CEC.2008.4631210.

[134] X-S. Yang, S. Koziel, and L. Leifsson. "Computational optimization, modelling and simulation: Recent advances and overview". *Procedia Comput. Sci.* (2011). DOI: 10.1016/j.procs.2011.04.132.

[135] J. Larson, M. Menickelly, and S. Wild. "Derivative-free optimization methods". *Acta Numerica* (2019). DOI: 10.1017/s0962492919000060.

[136] G. Venter. "Review of Optimization Techniques". *J. Aerosp. Eng.* (2010). DOI: 10.1002/9780470686652.EAE495.

[137] A. LaTorre, S. Muelas, and J-M. Peña. "A MOS-based dynamic memetic differential evolution algorithm for continuous optimization: a scalability test". *Soft Comput.* (2011). DOI: 10.1007/s00500-010-0646-3.

[138] S. Behera, S. Sahoo, and B. Pati. "A review on optimization algorithms and application to wind energy integration to grid." *Renewable Sustainable Energy Rev.* (2015). DOI: 10.1016/j.rser.2015.03.066.

[139] A. Kumar, S. Dutta, and A. Gandomi. "Surrogate model-driven bio-inspired optimization algorithms for large-scale and high-dimensional problems". *Biomimicry for Aerospace*. Elsevier, 2022. ISBN: 978-0-12-821074-1. DOI: 10.1016/B978-0-12-821074-1.00005-0.

[140] M. Georgioudakis and V. Plevris. "A Comparative Study of Differential Evolution Variants in Constrained Structural Optimization." *Front. Built. Environ.* (2020). DOI: 10.3389/fbuil.2020.00102.

[141] R. Tanabe and A. Fukunaga. "Evaluating the performance of SHADE on CEC 2013 benchmark problems". *IEEE Trans. Evol. Comput.* 2013. DOI: 10.1109/CEC.2013.6557798.

[142] R. Tanabe and A. Fukunaga. "Success-history based parameter adaptation for Differential Evolution". *IEEE Trans. Evol. Comput.* 2013. DOI: 10.1109/CEC.2013.6557555.

[143] P. Larrañga and J. Lozano. *Estimation of Distribution Algorithms*. Springer, 2001.

[144] Z.-Q. Chen, R.-L. Wang, R.-V. Sanchez, J. De Oliveira, and C. Li. "An adaptive genomic difference based genetic algorithm and its application to memetic continuous optimization". *Intel. Data Anal.* (2018). DOI: 10.3233/IDA-173402.

[145] C. Holloman, H. Lee, and D. Higdon. "Multiresolution genetic algorithms and Markov chain Monte Carlo". *J. Comput. Graph. Stat.* 15.4 (2006), pp. 861–79.

[146] Y. Sáez. "Optimization Using Genetic Algorithms with Micropopulations". *Optimization Techniques for Solving Complex Problems* (2009). DOI: 10.1002/9780470411353.ch3.

[147] S. Chen, J. Ding, Z. Shao, and Z. Shi. "Neural surrogate-driven modelling, optimisation, and generation of engineering designs: A concise review". *Mater. Res. Proc.* (2024). DOI: 10.21741/9781644903254-53.

[148] K-A. Norton, D. Bergman, H. Jain, and T. Jackson. "Advances in Surrogate Modeling for Biological Agent-Based Simulations: Trends, Challenges, and Future Prospects". *J. Math. Biol.* (2026). DOI: 10.1007/s00285-025-02318-6.

[149] G. Padula, M. Girfoglio, and G. Rozza. "A brief review of Reduced Order Models using intrusive and non-intrusive techniques". *P. A. M. M.* (2024). DOI: 10.1002/pamm.202400210.

[150] M. van Aalst, T. Nies, T. Pfennig, and A. Matuszyńska. "MxlPy - Python Package for Mechanistic Learning in Life Science". *bioRxiv* (2025). DOI: 10.1101/2025.05.06.652335.

[151] S. Liu, H. Wang, W. Peng, and W. Yao. "Surrogate-assisted evolutionary algorithms for expensive combinatorial optimization: a survey." *Complex Intell. Syst.* (2024). DOI: 10.1007/s40747-024-01465-5.

[152] Y. Jin, M. Olhofer, and B. Sendhoff. "Managing approximate models in evolutionary aerodynamic design optimization". *IEEE Trans. Evol. Comput.* (2001). DOI: 10.1109/CEC.2001.934445.

[153] I. Tzruia, T. Halperin, M. Sipper, and A. Elyasaf. "Fitness Approximation Through Machine Learning with Dynamic Adaptation to the Evolutionary State." *IEEE Trans. Evol. Comput.* (2024). DOI: 10.3390/info15120744.

[154] A. Almutairi and J. Fieldsend. "Automated and surrogate multi-resolution approaches in genetic algorithms". *IEEE S.S.C.I.* (2019). DOI: 10.1109/SSCI44817.2019.9002659.

[155] E. Sinha and B. Minsker. "Multiscale island injection genetic algorithms for groundwater remediation". *Adv. Water Resour.* (2007). DOI: 10.1016/j.advwatres.2007.03.006.

[156] D. Teng, Y-W. Feng, C. Lu, B. Keshtegar, and X-F. Xue. "Generative adversarial surrogate modeling framework for aerospace engineering structural system reliability design". *Aerosp. Sci. Technol.* (2024). DOI: 10.1016/j.ast.2023.108781.

[157] H. Morita, K. Shintani, C. Yuan, and F. Permenter. "VehicleSDF: A 3D generative model for constrained engineering design via surrogate modeling". *arXiv* (2024). DOI: 2410.18986.

[158] M. Barzegar-Gerdroodbary and S. Salavatidezfouli. "A predictive surrogate model based on linear and nonlinear solution manifold reduction in cardiovascular FSI: A comparative study". *Comput. Biol. Med.* (2025). DOI: 10.1016/j.compbiomed.2025.109959.

[159] M. Wu, D. Kamensky, C. Wang, A. Herrema, F. Xu, Marco S. Pigazzini, A. Verma, A. Marsden, Y. Bazilevs, and M.-C. Hsu. "Optimizing fluid–structure interaction systems with immersogeometric analysis and surrogate modeling: Application to a hydraulic arresting gear". *C.M.A.M.E.* (2017). DOI: 10.1016/j.cma.2016.09.032.

[160] M. Raissi, P. Perdikaris, and G. Karniadakis. "Physics-informed neural networks: A deep learning framework for solving forward and inverse problems involving nonlinear partial differential equations". *J. Comput. Phys.* (2019). DOI: 10.1016/j.jcp.2018.10.045.

[161] P. Naharro, A. Latorre, and J-M. Peña. "Surrogate-based optimisation for a hospital simulation scenario using pairwise classifiers". *Proceed. GECCO 21*. 2021, pp. 15–16. DOI: 10.1145/3449726.3463283.

[162] Z-H. Han and K-S. Zhang. "Surrogate-Based Optimization". *Real-World Applications of Genetic Algorithms*. IntechOpen, 2012. ISBN: 978-953-51-0146-8. DOI: 10.5772/36125.

[163] C. Cipriano, S. Noce, S. Mereu, and M. Santini. "Algorithms going wild – A review of machine learning techniques for terrestrial ecology". *Ecol. Model.* (2025). DOI: 10.1016/j.ecolmodel.2025.111164.

[164] I. Sarker. "Machine Learning: Algorithms, Real-World Applications and Research Directions." *S. N. Comput. Sci.* (2021). DOI: 10.1007/s42979-021-00592-x.

[165] R. Baker, J-M. Peña, J. Jayamohan, and A. Jérusalem. "Mechanistic models versus machine learning, a fight worth fighting for the biological community?": *Biol. Lett.* (2018). DOI: 10.1098/rsbl.2017.0660.

[166] K. Kolasa, B. Admassu, M. Hołownia-Voloskova, K. Kedzior, J. Poirrier, and S. Perni. "Systematic reviews of machine learning in healthcare: a literature review." *Expert Rev. Pharmacoecon. Outcomes Res.* (2023). DOI: 10.1080/14737167.2023.2279107.

[167] A. Géron. *Hands-On Machine Learning with Scikit-Learn and TensorFlow*. O'Reilly Media, Inc., 2017. ISBN: 978-1-491-96229-9.

[168] R. Woodman and A. Mangoni. "A comprehensive review of machine learning algorithms and their application in geriatric medicine: present and future." *Aging Clin. Exp. Res.* (2023). DOI: 10.1007/s40520-023-02552-2.

[169] V-D. Nguyen, P. Sanchez Naharro, J-M. Pena, and A. Jerusalem. "Soft-Finite-Element-Method-Driven Multiphysics Airfoil Optimization". *Amer. Inst. Aeronautics Astronautics* (2025). DOI: 10.2514/1.J063262.

[170] V-D. Nguyen, C. Kirchhelle, A. Abdollahi, J. García Grajales, D. Li, K. Benatia, K. Gorbunov, S. Bielle, A. Goriely, and A. Jérusalem. "A numerical framework coupling finite element and meshless methods in sequential and parallel simulations". *Finite Elem. Anal. Des.* (2023). DOI: 10.1016/j.finel.2023.103927.

[171] J. Siggers, S. Waters, J. Wattis, and L. Cummings. "Flow dynamics in a stented ureter." *Math Med Biol.* (2009). DOI: 10.1093/imammb/dqn020.

[172] L. Cummings, S. Waters, J. Wattis, and et al. "The effect of ureteric stents on urine flow: Reflux." *J. Math. Biol.* (2004). DOI: /10.1007/s00285-003-0252-4.

[173] A. Schuh, A. Makropoulos, E. Robinson, L. Cordero-Grande, E. Hughes, J. Hutter, A. Price, M. Murgasova, Rui Pedro A. G. Teixeira, Nora Tusor, Johannes K. Steinweg, Suresh Victor, Mary A. Rutherford, Joseph V. Hajnal, A. David Edwards, and Daniel Rueckert. "Unbiased construction of a temporally consistent morphological atlas of neonatal brain development". *bioRxiv* (2018). DOI: 10.1101/251512.

[174] L. Su, M. Wang, J. Yin, F. Ti, J. Yang, C. Ma, S. Liu, and T. Lu. "Distinguishing poroelasticity and viscoelasticity of brain tissue with time scale". *Acta Biomater.* (2023). DOI: 10.1016/j.actbio.2022.11.009.

[175] H. Brydon, R. Hayward, W. Harkness, and R. Bayston. "Physical properties of cerebrospinal fluid of relevance to shunt function. 2: The effect of protein upon CSF surface tension and contact angle." *Br. J. Neurosurg.* (1995). DOI: 10.1080/02688699550040936.

[176] C. Geuzaine and J-F. Remacle. *Gmsh*. Version 4.6.0. URL: http://gmsh.info/ (visited on 06/22/2020).

[177] J. Gilmore, R. Knickmeyer, and W. Gao. "Imaging structural and functional brain development in early childhood." *Nat. Rev. Neurosci.* (2018). DOI: 10.1038/nrn.2018.1.

[178] L. Feng, S. Li, and S. Feng. "Preparation and characterization of silicone rubber with high modulus via tension spring-type crosslinking". *RSC Adv.* (2017). DOI: 10.1039/C7RA00293A.

[179] H. Weller, G. Tabor, H. Jasak, and C. Fureby. "A tensorial approach to computational continuum mechanics using object-oriented techniques". *Comput. Phys.* (1998). DOI: 10.1063/1.168744.

[180] Open Cascade SAS. *OpenCASCADE Technology*. www.opencascade.com. 2022.

[181] P-L. George and P. Frey. *Mesh generation*. Hermes, 2000. ISBN: 978-1903398005.

[182] S. Patankar and D. Spalding. "A calculation procedure for heat, mass and momentum transfer in three-dimensional parabolic flows". *Int. J. Heat Mass Transfer* (1972). DOI: 10.1016/0017-9310(72)90054-3.

[183] H. Jasak. "Error Analysis and Estimation for the Finite Volume Method With Applications to Fluid Flows". PhD thesis. Imperial College, 1996. URL: www.researchgate.net/publication/230605842_Error_Analysis_and_Estimation_for_the_Finite_Volume_Method_With_Applications_to_Fluid_Flows.

[184] F. Moukalled, L. Mangani, and M. Darwish. *The Finite Volume Method in Computational Fluid Dynamics: An Advanced Introduction with OpenFOAM® and Matlab®*. 2015. DOI: 10.1007/978-3-319-16874-6.

[185] S. Bauer, M. Schäfer, P. Grammenoudis, and Ch. Tsakmakis. "Three-dimensional finite elements for large deformation micropolar elasticity". *Comput. Methods Appl. Mech. Eng.* (2010). DOI: 10.1016/j.cma.2010.05.002.

[186] H-J. Bungartz, F. Lindner, B. Gatzhammer, M. Mehl, K. Scheufele, A. Shukaev, and B. Uekermann. "preCICE – A fully parallel library for multi-physics surface coupling". *Comput. Fluids* (2016). DOI: 10.1016/j.compfluid.2016.04.003.

[187] C. Förster, W. Wall, and E. Ramm. "Artificial added mass instabilities in sequential staggered coupling of nonlinear structures and incompressible viscous flows". *Comput. Methods Appl. Mech. Eng.* 196.7 (2007), pp. 1278–1293. ISSN: 0045-7825. DOI: 10.1016/j.cma.2006.09.002.

[188] J. Ahrens, B. Geveci, and C. Law. *ParaView: An End-User Tool for Large Data Visualization, Visualization Handbook*. Elsevier, 2005. ISBN: 9780123875822.

[189] A. Collier, P. Haste, E. Hayman, F. Rezayaraghi, T. Lam, S. Waters, M. Kurt, and A. Jerusalem. "Computational model of cardiac cycle driven brain pulsation: a novel tool for brain disease exploration". *Comput. Biol. Med.* (2025).

[190] E. Hayman, J.-M. Peña, J. Jayamohan, J-M. Peña Sánchez, A. Jerusalem, and S. Waters. "Validation of a permeable wall model in medical catheters." *J. Eng. Math.* (2026). Under review.

[191] E. Hayman, J.-M. Peña, J. Jayamohan, J-M. Peña Sánchez, S. Waters, and A. Jerusalem. "Generalised surrogate-aided optimisation methodology: application to hydrocephalus shunt system design." *J. Mech. Des.* (2026). Under review.

[192] M. Renardy, L. Joslyn, J. Millar, and D. Kirschner. "To Sobol or not to Sobol? The effects of sampling schemes in systems biology applications". *Math. Biosci.* (2021). DOI: 10.1016/j.mbs.2021.108593.

[193] H. Ockendon and J. Ockendon. *Viscous Flow*. Cambridge University Press, 1995. ISBN: 9781139174206.

[194] X. Yang, A. Mosayyebi, and D. Carugo. "Computational simulation of the flow dynamic field in a porous ureteric stent." *Med. Biol. Eng. Comput.* (2022). DOI: 10.1007/s11517-022-02620-1.

[195] Y. Xue, S. Payne, and S. Waters. "Stokes flows in a two-dimensional bifurcation". *R. Soc. Open Sci.* (2025). DOI: 10.1098/rsos.241392.

[196] F. Smith. "Pipeflows distorted by non-symmetric indentation or branching". *Mathematika* (1976). DOI: 10.1112/S0025579300006161.

[197] I. Sobey. "Laminar boundary-layer flow past a two-dimensional slot." *J. Fluid Mech.* (1977). DOI: 10.1017/S0022112077001025.

[198] O. Tutty. "Flow in a tube with a small side branch." *J. Fluid Mech.* (1988). DOI: 10.1017/S0022112088001521.

[199] A. Samagaio and N. Vlachos. "Calculation of three-dimensional laminar flows in T-shaped junctions". *C.M.A.M.E.* (1989). DOI: 10.1016/0045-7825(89)90038-8.

[200] S. Blonski, D. Zaremba, M. Jachimek, T. Jakiela S. Wacławczyk, and P. Korczyk. "Impact of inertia and channel angles on flow distribution in microfluidic junctions." *Microfluid. Nanofluid.* (2020). DOI: 10.1007/s10404-020-2319-6.

[201] F. Pedregosa, G. Varoquaux, A. Gramfort, V. Michel, B. Thirion, O. Grisel, M. Blondel, P. Prettenhofer, R. Weiss, V. Dubourg, J. Vanderplas, A. Passos, D. Cournapeau, M. Brucher, M. Perrot, and E. Duchesnay. "Scikit-learn: Machine Learning in Python". *J. Mach. Learn. Res.* (2011). DOI: 10.48550/arXiv.1201.0490.

[202] T. Chen and C. Guestrin. "XGBoost: A Scalable Tree Boosting System". *J.A.C.M.* (2016). DOI: 10.1145/2939672.2939785.

[203] G. James, D. Witten, T. Hastie, and R. Tibshirani. *Introduction to Statistical Learning : with Applications in R.* Springer, 2013.

[204] T. Lai, H. Robbins, and C. Wei. "Strong consistency of least squares estimates in multiple regression II". *J. Multivar. Anal.* (1979). DOI: 10.1016/0047-259X(79)90093-9.

[205] A. Hoerl and R. Kennard. "Ridge Regression: Applications to Nonorthogonal Problems". *Technometrics* (1970). DOI: 10.2307/1267352.

[206] R. Tibshirani. "Regression Shrinkage and Selection Via the Lasso". *J. R. Stat. Soc. Ser. B Stat. Methodol.* (2018). DOI: 10.1111/j.2517-6161.1996.tb02080.x.

[207] H. Drucker, C. Burges, L. Kaufman, A. Smola, and V. Vapnik. "Advances in Neural Information Processing Systems". MIT Press, 1996. Chap. Support Vector Regression Machines.

[208] D. MacKay. "Bayesian Interpolation". *Neural Comput.* (1992). DOI: 10.1162/neco.1992.4.3.415.

[209] L. Breiman, J. Friedman, R. Olshen, and C. Stone. *Classification And Regression Trees*. Routledge, 1984. DOI: 10.1201/9781315139470.

[210] L. Breiman. "Random Forests." *Mach. Learn.* (2001). DOI: 10.1023/A:1010933404324.

[211] G. Hinton. "Connectionist learning procedures." *Mach. Learn.* (1990). DOI: 10.1016/0004-3702(89)90049-0.

[212] A. Maćkiewicz and W. Ratajczak. "Principal components analysis (PCA)". *Comput. Geosci.* (1993). DOI: 10.1016/0098-3004(93)90090-R.

[213] A. Draganov and S. Dohn. *Relating tSNE and UMAP to Classical Dimensionality Reduction*. 2024. URL: arxiv.org/abs/2306.11898.

[214] A. Latorre. "A Framework for Hybrid Dynamic Evolutionary Algorithms: Multiple Offspring Sampling (MOS)". PhD thesis. University of Tennessee, 2009. URL: oa.upm.es/2169/1/ANTONIO_LATORRE_DE_LA_FUENTE.pdf.

[215] S. Weisenberg, S. TerMaath, C. Barbier, J. Hill, and J. Killeffer. "A computational fluid dynamics simulation framework for ventricular catheter design optimization." *J. Neurosurg.* (2018). DOI: 10.3171/2017.5.JNS161882.

[216] M. Galarza, A. Giménez, J. Amigó, M. Schuhmann, R. Gazzeri, U. Thomale, and J. McAllister. "Next generation of ventricular catheters for hydrocephalus based on parametric designs." *Childs Nerv. Syst.* (2018). DOI: 10.1007/s00381-017-3565-0.

[217] C. Geuzaine and J-F. Remacle. "Gmsh: a three-dimensional finite element mesh generator with built-in pre- and post-processing facilities". *Int. J. Numer. Meth. Eng.* (2009). DOI: 10.1002/nme.2579.

[218] S. Rebay. "Efficient unstructured mesh generation by means of Delaunay triangulation and Bowyer-Watson algorithm". *J. Comput. Phys.* (1993). DOI: 10.1006/jcph.1993.1097.

[219] J-F. Remacle, F. Henrotte, T. Carrier-Baudouin, E. Bchet, E. Marchandise, C. Geuzaine, and T. Mouton. "A frontal Delaunay quad mesh generator using the Linf norm". *Int. J. Numer. Meth. Eng.* (2013). DOI: 10.1002/nme.4458.

[220] X. Luo, B. Calderhead, H. Liu, and W. Li. "On the initial configurations of collapsible channel flow". *Comput. Struct.* 85 (2007). ISSN: 0045-7949. DOI: 10.1016/j.compstruc.2006.11.010.

[221] X. Chen. "Numerical Modeling of Fluid-Structure Interaction with Rheologically Complex Fluids." Thesis submission. Technische Universität Darmstadt, 2014. URL: tuprints.ulb.tu-darmstadt.de/4216/1/Thesis_XingyuanChen.pdf.

Appendix A

This appendix contains further details on the methods used to create the 3D FSI model, including a non-dimensional analysis which is used to motivate the choice of solvers. It also contains the validation studies confirming that the model is sufficiently accurate for use.

A.1 Non-dimensional analysis

In this section, a non-dimensional analysis of the FSI model governing equations is performed to justify the steady solvers. Parameter values in Table 3.1 show that the scale of the time derivatives in both the fluid and solid problems are negligible, and can be excluded from the governing equations. This justifies the use of equilibrium solvers for the FSI model.

The non-dimensionalisation uses the following scalings:

$$\{x, y, z\} = L\{\tilde{x}, \tilde{y}, \tilde{z}\}, \quad t = T\tilde{t}, \quad \boldsymbol{v} = V\tilde{\boldsymbol{v}}, \quad p = \frac{\mu V}{L}\tilde{p},$$
$$\boldsymbol{u} = U\tilde{\boldsymbol{u}}, \quad \boldsymbol{\sigma} = E\tilde{\sigma},$$

where the capital letter denotes a constant, characteristic value of the variable, and the tilda denotes the non-dimensional counterpart. Length scales in the domain range from 0.2 mm (ChP width) to 1.5 mm (catheter diameter) to 30 mm (domain length). Therefore a characteristic value L =1 mm is chosen. The largest velocities in the domain are seen at the catheter outlet, where the total flux Q passes through a cross-section of area πr^2, where $r = 0.75$ mm (the internal radius of the catheter). This gives a maximum velocity scale $V \approx Q/(\pi r^2) \approx 3$ mm/s. A timescale $T = 10^5$ s ($\sim$1 day) is chosen as the minimum period post-surgery for a successfully inserted catheter to become blocked. Catheter implant surgery takes over an hour to perform, and any immediate ChP blockage that

occurs during the surgery is expected to be noticed and corrected. The model therefore focusses on the period post-surgery where the catheter-ventricle system settles into a new equilibrium. The viscous pressure scale $\mu V/L$ is chosen so that viscous terms balance the pressure gradient in the Navier-Stokes equations. In occlusion scenarios, the ChP deforms sufficiently to collide with the catheter so $U = L =$1 mm. The solid stress tensor $\boldsymbol{\sigma}$ is scaled with E, the Young's modulus of the ChP.

Substituting and rearranging Equations (3.1), (3.2) and (3.3) leads to

$$\nabla \cdot \boldsymbol{v} = 0, \tag{A.1}$$

$$\underbrace{\frac{\rho_f V L}{\mu}}_{:=\mathrm{Re}} \left(\underbrace{\frac{L}{VT}}_{:=\epsilon} \frac{\partial \boldsymbol{v}}{\partial t} + (\boldsymbol{v} \cdot \nabla)\boldsymbol{v} \right) = -\nabla p + \Delta \boldsymbol{v}, \tag{A.2}$$

$$\underbrace{\frac{\rho_s L}{ET^2}}_{\beta} \frac{D^2 \boldsymbol{u}}{Dt^2} = \nabla \cdot \boldsymbol{\sigma}, \tag{A.3}$$

where the tildes have been omitted for readability. Here, the Reynolds number, $\mathrm{Re} = \rho_f V L/\mu$, is the ratio of inertial to viscous forces in a flow and ϵ (resp. $\beta^{1/2}$) is the ratio of the natural timescale of the fluid (resp. solid) to the timescale of interest. The natural timescale of the fluid is L/U, the time it takes for a fluid particle with velocity U to travel length L. The natural timescale of the solid is the period of elastic vibration with no external loading. With the parameter estimates in Table 3.1, the flow has a Reynolds number of approximately four, well within the laminar flow region ($Re < 2,000$). The dimensionless parameters ϵ and β are both on the order of $\approx 10^{-6}$, justifying the decision to neglect time-dependent terms in both the solid and fluid equations.

A.2 Mesh creation

This section contains further detail on standard methods used in mesh creation, style choice and mesh quality analysis.

A.2.1 Geometry creation

To create finite element (FE) meshes, the codebase `gmsh` [176] is used, as it contains the ability to build or import model geometries and algorithms to create

meshes from a given geometry. Geometries can be created in two ways: `gmsh`'s inbuilt kernel allows a bottom-up approach with points defined in space, and lines defined between specific points. Surfaces can be created from closed loops of lines, and volumes from groups of surfaces. B-splines (polynomial curves) through multiple points can be defined as well as simple linear line segments. This allows considerable configurability, with the ability to create arbitrarily complex surfaces. For greater speed, `gmsh` is also compatible with the `openCascade` kernel [180], which enables simple volumes (boxes, spheres and cylinders) to be introduced fully formed, with all associated surfaces, lines and points. `openCascade` allows complex geometries to be created quickly by taking intersections and unions of the simple building blocks, but is limited by the initial shapes of the building blocks. Together, the two kernels can be used with their respective strengths complementing each other.

`gmsh` is used via a C-based scripting language in an ASCII file with .geo extension, with visualisation possible in the inbuilt graphical user interface (GUI).

A.2.2 Mesh styles

Once a geometry has been created in `gmsh`, internal meshing algorithms are used to transform the geometry into a 3D mesh. `gmsh` allows for a great deal of configurability in mesh design, with various options allowing for changes in mesh style, size, and refinement of the mesh in specific areas.

An important quality for any FE mesh is ensuring that the mesh is conforming: the condition that no elements overlap. This is enforced in `gmsh` by meshing the lowest dimension entities first and using these to form the boundaries of higher order elements. This ensures that neighbouring elements do not overlap as they are defined by their common boundary.

A FE mesh will never completely match a curved surface as the mesh is composed of elements with straight edges. The mesh needs to be small enough to capture any curves on the geometry boundary but not so small that the computational simulations take too long to run. Mesh size is prescribed on each point in a `gmsh` geometry, with the command `Characteristic Length{Point{:}} = meshSize;` enforcing a uniform size on all points in the geometry. For meshing areas with a high curvature (such as a small radius tube), the command `Mesh.CharacteristicLengthFromCurvature = k;` enforces at least $\mathtt{k} \cdot \theta / 2\pi$ mesh

elements around an arc of angle θ (and so `k` elements around a full circle). This is a useful command to enforce a smaller mesh around critical areas of high curvature, without reducing the mesh size of the whole domain.

A key feature of any mesh is the shape of the elements created. In 3D, the simplest element available is a tetrahedron (in 2D, a triangle) and `gmsh` creates all its meshes initially with tetrahedra, as these elements are the most able to capture a complex geometry. However, non-quadratic tetrahedral elements are not always advisable in FE simulations, as their shape can introduce an artificial increase in stiffness. Often FVM, including `openFOAM`, are designed with a hexahedral mesh in mind, and methods to approximate partial derivatives assume that elements are arranged in a regular pattern. `Gmsh` has the capability to create a hexahedral (cube) mesh by using the `Recombine` command to post-process a tetrahedral mesh into a hexahedral mesh.

Mesh styles can be subdivided into structured and unstructured. Unstructured meshes place elements wherever the algorithm determines the best position. These algorithms are more flexible, and can cope with more complex geometries. Structured algorithms place elements in a regular pattern and produce more reliable regular elements, but are harder to generate due to their stricter requirements. To implement a structured mesh style in `gmsh`, the key word `Transfinite` is applied to each boundary surface. For this research, the complex geometry of the biological domain (even in an idealised setting) necessitates unstructured algorithms. Figure A.1 shows examples of triangular and quadrilateral, structured and unstructured mesh on a 2D disc. Note, in Figure A.1 d), the structured elements experience greater deformation near the curved boundary as it is harder to maintain the regular pattern.

The meshing algorithms used in `gmsh` are based on adaptions of the Delaunay triangulation. As noted above, `gmsh` always meshes 2D surfaces first, before extending the surface mesh to mesh the 3D volume. This ensures all volume elements are conforming.

Meshing algorithms first apply the Delaunay triangulation to all existing nodes in the geometry. The triangulation is then subdivided to create smaller mesh elements until the mesh size constraint is reached. `gmsh` contains different methods to optimally subdivide the triangulation when creating the final mesh, either by locally refining the mesh through edge splitting and swapping (MeshAdapt [217]) or sequentially inserting new nodes into the circumcentre of the largest triangle

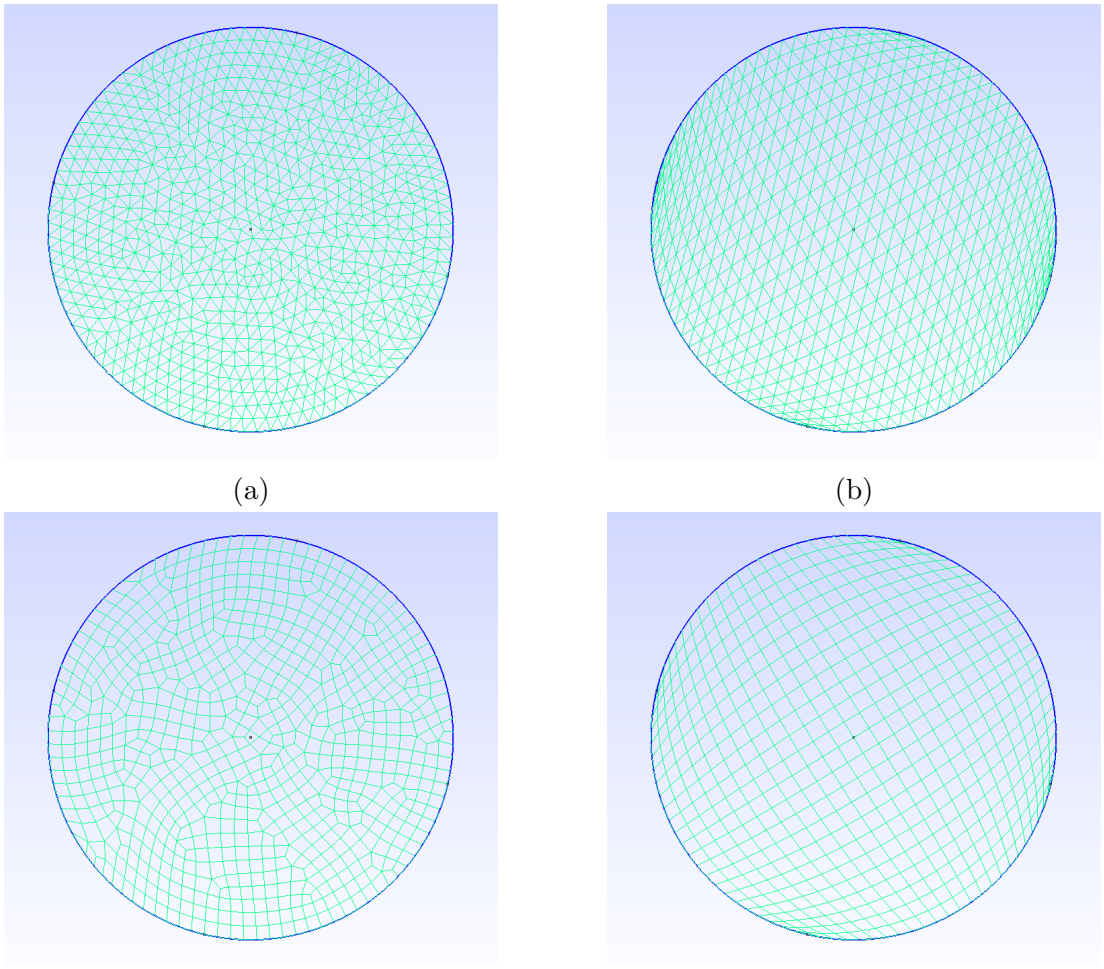

Figure A.1: Example of mesh styles on a 2D surface: (a) unstructured triangular; (b) structured triangular; (c) unstructured quadrilateral; and (d) structured quadrilateral.

(Delaunay [181]). In this project, the Delaunay method is used as recommended by `gmsh`. Adaptations of the Delaunay meshing algorithm to ensure triangles are close to equilateral (Frontal-Delaunay [218]), or close to right-angled (Frontal-Delaunay for Quads [219]), also exist, but are not used here.

A.2.3 Mesh quality

For the numerical solvers to give an accurate solution to the model the mesh must be of sufficiently good quality. Deformed or misshaped elements will add errors which may cause non-convergence of the solver or non-physical results. Solvers often have mesh requirements to ensure a compatible, good quality mesh is accepted: for example `OpenFOAM` will only parse meshes containing simple tetrahedral or hexahedral elements.

`OpenFOAM` uses the command `checkMesh` to evaluate the quality of a mesh, producing a set of summary statistics for the user and highlighting any mesh characteristic metrics which do not indicate a good quality mesh. It is worth noting that `checkMesh` often records the maximum or "worst-case" for each metric, and a failure of a small number of isolated elements to satisfy a criterion does not mean the overall mesh is of poor quality.

Two key metrics which determine the quality of a mesh are non-orthogonality and skew. These metrics can take slightly different forms in different computational solvers. In `OpenFOAM` non-orthogonality describes how far from a perfect cuboid element (2D, rectangle) a cell is. This is measured as the angle between the vector joining neighbouring cell centres, and the vector normal to their shared face, illustrated in Figure A.2 a) with vectors $\boldsymbol{c}_i$ and $\boldsymbol{b}_i$ respectively, where i indexes the neighbours of a specific cell. Non-orthogonality is expressed as an acute angle in degree between 0° and 90°, where 0° is a perfectly orthogonal mesh. Meshes with non-orthogonality greater than 70° require additional non-orthogonality corrector loops, and those with non-orthogonality greater than 85° often fail.

A second measure of mesh quality is skewness, which in `OpenFOAM` is defined as the deviation of the face centre between two elements from the vector connecting their centroids, normalised by the length of the centroids vector (see Figure A.2 b)). Skewness provides a measure of how regularly packed elements are, with zero

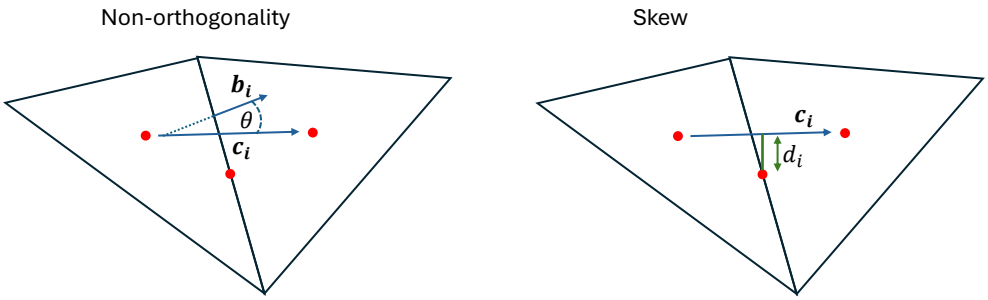

Figure A.2: Visual description of (a) non-orthogonality given by the angle between $\boldsymbol{c}_i$ and $\boldsymbol{b}_i$, (b) skewness measure: $d_i/|\boldsymbol{c_i}|$. i indexes the neighbours of any one cell.

skewness if elements pack in a regular grid pattern, and a high skew measure if the elements are significantly offset.

A.2.4 Mesh postprocessing

In Section A.2.2, it was noted that it is easiest to create an irregular tetrahedral mesh for a general, curved geometry, and that enforcing regular hexahedral meshes on a curved geometry will cause distortion of elements close to the curved boundary. However, in Section A.2.3, it was seen that the optimal mesh for the fluid solver is a regular hexahedral mesh.

To reconcile the flexibility of a tetrahedral mesh with the numerical regularity of a hexahedral one, the `OpenFOAM` postprocess command `polyDualMesh` is applied to a tetrahedral mesh. This generates the mesh dual, transforming tetrahedra into polyhedra by replacing the centroid of each tetrahedron with a node and placing each original node at the centre of a new element. This is shown graphically in Figure A.3. `polyDualMesh` requires one numerical parameter between 0 and 90, which refines the mesh dual near sharp corners of the domain boundary.

As `polyDualMesh` postprocesses an existing tetrahedral mesh, the polyhedral dual always exists and is inherently a good approximation to the domain geometry. Polyhedra are additionally superior to tetrahedrons as they have more neighbours, which ensures a better approximation to gradients as calculated by the fluid solver (see Section 3.4.2.2). Polyhedral meshes also contain a smaller number of elements making them faster to solve compared with a tetrahedral mesh.

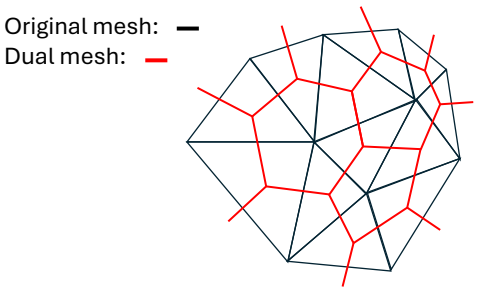

Figure A.3: `polyDualMesh` creates the dual (red) of an existing tetrahedral mesh (black).

The mesh quality analysis discussed above is focussed on `OpenFOAM`'s methods, relevant for the fluid part of the model. The solid solver `MuPhiSim` will also benefit from a good quality mesh (quantified using the same metrics) but does not have the in-built methods to assess mesh quality.

A.3 OpenFOAM folder structure

`OpenFOAM` requires a run directory that contains a specific layout of subdirectories and files containing the information necessary for a fluid simulation. This folder structure is shown below.

```
simulation folder
├── constant
│   ├── transportProperties
│   └── turbulenceProperties
├── 0
│   ├── U
│   └── p
├── system
│   ├── controlDict
│   ├── decomposeParDict
│   ├── fvSchemes
│   └── fvSolutions
├── fluidGeometry.geo
└── run.sh
```

The three subfolders `0`, `constant` and `system` contain information on the boundary conditions, mesh geometry and numerical parameters, respectively.

The `controlDict` contains simulation parameters, such as which solver to use, maximum allowed iterations, and how to write output data. `decomposeParDict` contains parallelisation information on splitting the domain if the simulation is run on $n > 1$ cores. `fvSchemes` and `fvSolutions` contain the numerical parameters and approximations used by the solver, discussed in Section 3.4.2.2. The folder `0` contains the boundary conditions, discussed in Section 3.4.2.3.

The folder `constant` contains the physical parameters and geometry mesh of the simulation. Here, the kinematic viscosity is the only physical parameter value required to solve the incompressible, laminar fluid simulation, and is written in `transportProperties`. `turbulenceProperties` contains any turbulence models required by the simulation. In this project, the fluid is modelled as non-turbulent, so only the line `simulationType:laminar` is written here as a placeholder. In the pipeline created for this project, an additional two files are necessary: the `fluidGeometry.geo` file which contains the `gmsh` geometry with configurable catheter, and `run.sh` which contains the terminal commands needed to execute the fluid part of the FSI pipeline.

A.4 FSI model validation

A.4.1 Fluid validation

A validation study is performed to test the choices of fluid mesh style and size, and the numerical parameters and schemes used in the fluid solver. This study is performed for both the 3D and 2D models.

This study calculates the pressure gradient needed to drive a fluid flux of Q and viscosity μ through a cylindrical tube of radius $a = 0.75$ mm and length $L =$ 10 mm. The tube is oriented with its centreline along the z axis. These lengths and flux are chosen to be close in magnitude to the hydrocephalus fluid domain, ensuring all the modelling assumptions made above are still relevant here. This problem has the well-known Poiseuille flow solution for pressure p, that is

$$Q = \frac{\pi a^4}{8\mu}\frac{dp}{dz}. \tag{A.4}$$

In 2D the pipe is interpreted as a rectangle domain of height $2a$ =2 $\times$ 0.75 mm = 1.5 mm, and length 10 mm and has solution

$$Q = \frac{2a^3}{3\mu}\frac{dp}{dz}. \tag{A.5}$$

At the inlet a total fluid flux of $Q = 6$ mm^3/s is imposed with parabolic inlet flow profile in the normal direction. A reference pressure of 0 Pa is imposed on the outlet. No-slip conditions are imposed at all other walls.

The Poiseuille solution establishes that the pressure field is constant across the cross section of the tube, but to negate the effect of numerical fluctuations, the average pressure over the tube cross section is extracted. To establish agreement with the analytic Poiseuille solution the relative percentage error (RPE) is calculated as

$$100\frac{(x_{\text{CFD}} - x_{\text{analytic}})}{x_{\text{analytic}}} \tag{A.6}$$

where here x_{CFD} and x_{analytic} are the (constant) pressure gradient along the tube as evaluated, respectively, by the CFD model and analytic solution.

Figure A.4 shows the RPE for a) 3D and b) 2D mesh styles. Different mesh styles are analysed (colours), at characteristic mesh lengths between 0.05 mm and 0.2 mm (x-axis). Depending on the style of the mesh, the same characteristic length leads to different numbers of mesh elements. RPE of less than 1% is considered acceptable (blue shaded region). Figure A.4 a) shows results for the 3D study. Both unstructured meshes styles have relative percentage errors above 15 %, and the structured tetrahedral mesh has errors above 1 % which is not acceptable. The structured hexahedral mesh has good agreement with the analytic solution for meshes with over 100,000 elements, as expected. The cylindrical domain is a sufficiently simple geometry to admit a regular mesh which is not the case in the more complex geometry of the hydrocephalus scenario so this is not a useful mesh style despite the accuracy. The polyhedral mesh style has excellent accuracy even for very small numbers of mesh elements, and is flexible enough to capture the complex hydrocephalus geometry. The polyhedral mesh has far less elements for the same characteristic mesh size as it is created by merging multiple neighbouring tetrahedra. Simulations on this mesh are therefore faster and more efficient.

A.4.2 Fluid time dependence study

In Section 3.3 the model equations are shown to be time independent, which motivates the use of static solvers in the computational framework. To show that dynamic effects are not present in the fluid part of the model, a dynamic simulation run on a long timescale is shown to give results indistinguishable from

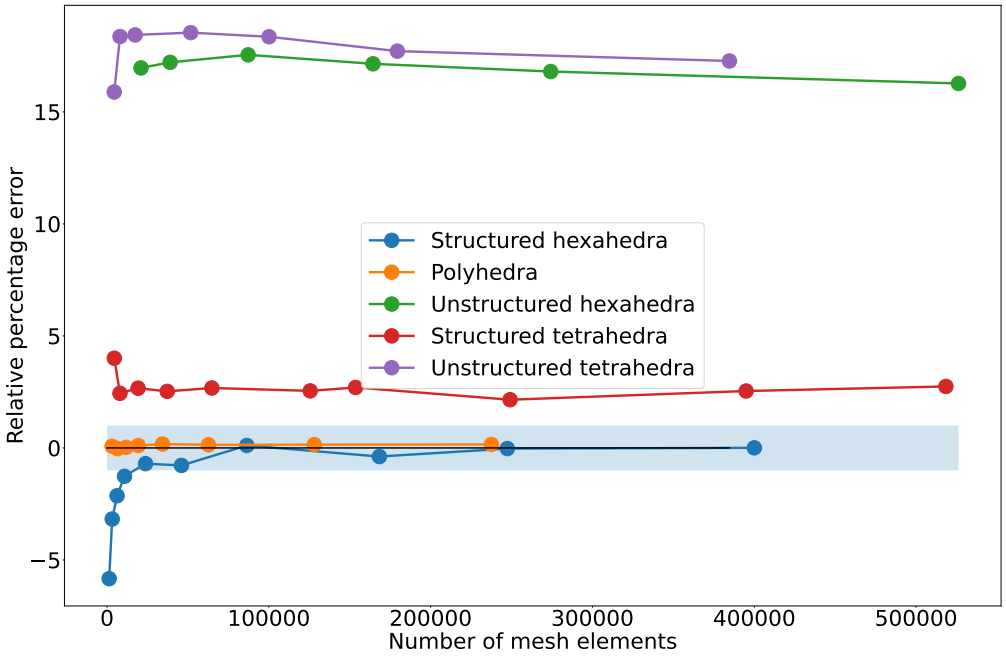

(a)

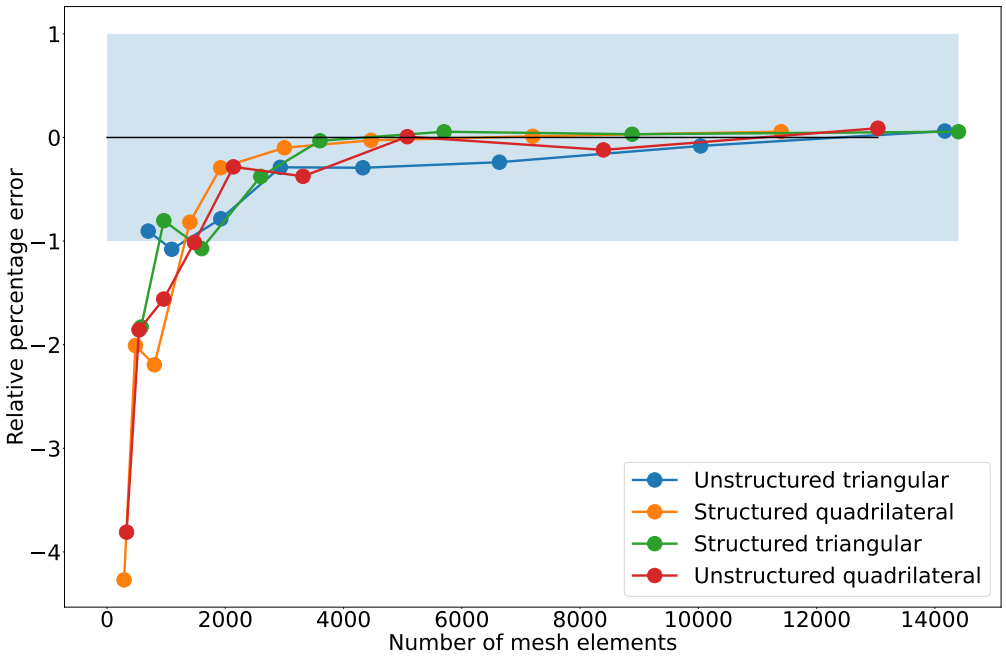

(b)

Figure A.4: Fluid validation study for (a) 3D and (b) 2D domains.

those of a static solver. The timescale considered in Section A.1 is one day, but the fluid evolves to equilibrium on a much faster time scale so it is sufficient to consider a smaller time interval.

The static simpleFoam solver is compared to results from pimpleFoam (one of `openFOAM`'s time dependent solver options). A time step of 0.01 s is used for the time dependent problem, and the initial velocity of the fluid set to $\mathbf{0}$, and the pressure to 0 everywhere. The problem is run for a total length of 1 s, after which the steady equilibrium has been found. Figure A.5 compares the results of the simpleFOAM (lower axis, iterations) and pimpleFOAM (top axis, physical time) solvers. The first 0.4 s of the time dependent solution is shown as this is sufficient to reach the steady state. The fluid velocity at the outlet of the catheter is extracted and the average (solid line) and interquartile range (shading) are plotted. This region is chosen as it has the highest velocities and so will take the longest to reach equilibrium. The solvers show good agreement between the equilibrium solutions after the initial period of fluctuation. An additional benefit of static solvers is a generally faster runtime: in this study simpleFoam took 14 minutes to run on one core of an i7 laptop while pimpleFoam took 2 hours.

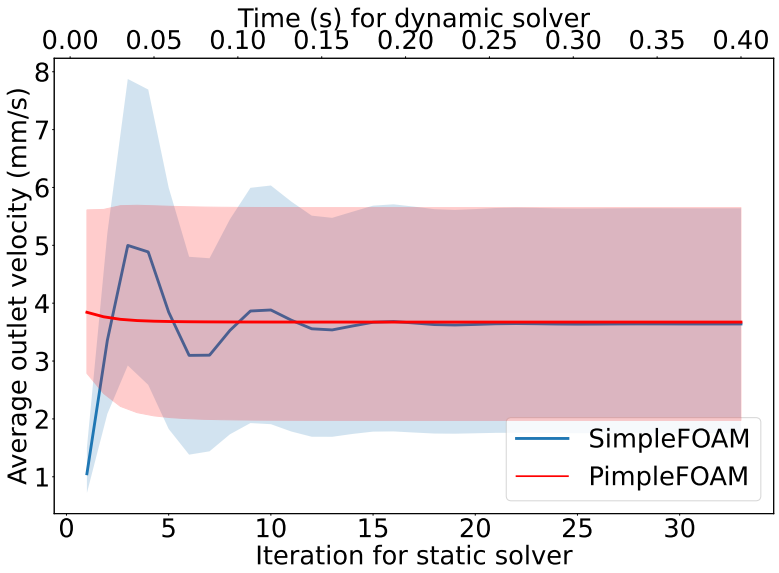

Figure A.5: Comparison of fluid evolution with a static (lower axis) and dynamic (upper axis) solver.

A.4.3 Solid validation

To validate the static solver used by `MuPhiSim` a benchmark study is performed on a cylindrical cavity embedded in an infinite elastic material. The cavity has length 10 mm and radius 1 mm. The geometry of this problem is shown in Figure A.6, with the infinite area modelled as a cube with side length 50 mm. The solid deformation is driven by a constant internal pressure p_0.

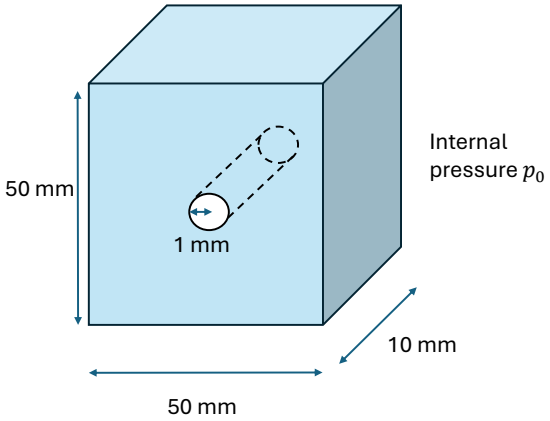

Figure A.6: Geometry of the solid validation study.

A linear elastic constitutive model is used which permits analytic solutions, testing the accuracy as well as the convergence of the solver. A Young's modulus of $E = 50$ Pa and Poisson's ratio of $\nu = 0.3$ are used. A pressure $p_0 = 5$ Pa is imposed on the interior of the cavity and a zero displacement condition imposed on the "infinite" boundaries. In 3D, the geometry has boundaries on the end faces. Here, zero tangential stress and zero normal displacement are imposed. In 2D, a cross section of the geometry is modelled and an additional assumption of plane strain is used. These modelling choices mean that the 2D and 3D models lead to the same solution, which in 3D is independent of the z coordinate. `MuPhiSim` is used to find the equilibrium configuration of the problem.

This problem has an analytical solution. The cavity is modelled as a hollow cylinder with radius $a = 1$ mm. Cylindrical polar coordinates are used with the z axis oriented with the centreline of the cylinder. The problem is axisymmetric and independent of z which motivates an axisymmetric deformation field $\boldsymbol{u} = u(r)\boldsymbol{e}_r$, and stress fields independent of z.

The equation for the equilibrium deformation of the solid is

$$\frac{d\sigma_r}{dr} + \frac{\sigma_r - \sigma_\theta}{r} = 0 \tag{A.7}$$

where σ_r is the radial component of the stress tensor, and σ_θ is the circumferential component. For a linear elastic constitutive model, the relation between the stress tensor and the deformation field is

$$\sigma_r = \frac{E}{(1+\nu)(1-2\nu)}\left((1-\nu)\frac{du}{dr} + \nu\frac{u}{r}\right) \tag{A.8}$$

$$\sigma_\theta = \frac{E}{(1+\nu)(1-2\nu)}\left((1-\nu)\frac{u}{r} + \nu\frac{du}{dr}\right). \tag{A.9}$$

This gives a governing equation with corresponding boundary condition of

$$\frac{d}{dr}\left(\frac{du}{dr} + \frac{u}{r}\right) = 0 \tag{A.10}$$

$$\sigma_r = 0 \quad \text{as} \quad r \to \infty, \quad \sigma_r = -p_0 \quad \text{at} \quad r = a \tag{A.11}$$

where p_0 is the constant interior pressure. This system gives a solution

$$u(r) = \frac{p_0 a^2(1+\nu)}{Er}. \tag{A.12}$$

The displacement at $r = a$ is then

$$u(a) = \frac{p_0 a(1+\nu)}{E} = 0.13 \tag{A.13}$$

in both the 2D and 3D formulations.

Figure A.7 shows the relative percentage error of the solid solver compared to the analytical solution for the 3D (lower axis) and 2D (upper axis) formulations. The relative percentage error is defined as in Equation (A.6), for $u(a)$. Only tetrahedral meshes are tested as these are the most configurable. Relative percentage errors of 1% (blue shading) are acceptable, and are achieved in both dimensions when the characteristic mesh size is less than 0.15 mm.

A.4.4 Solid time dependence study

As with the fluid part, a time dependence study is performed for the solid part. The implicit dynamic and implicit static solvers available in MuPhiSim are compared.

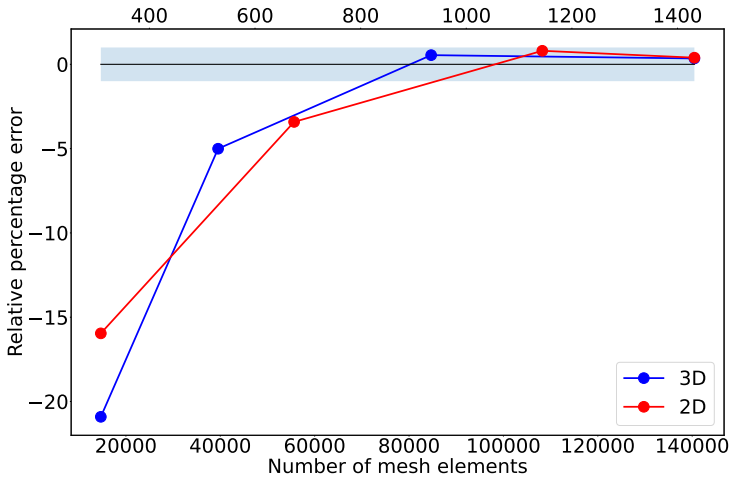

Figure A.7: Solid validation study for the 3D (lower axis) and 2D (upper axis) domains.

In the FSI codebase, the stress boundary condition is imposed as a linear ramp from 0 to allow the deformation of the ChP to evolve in a numerically stable way. Figure A.8 shows the comparison between static and dynamic implementations. In Figure A.8 a) the stress is imposed over a time of 5 s, and in Figure A.8 the stress is imposed over a time of 100 s. In all cases 1000 sub-iterations are used, which in the dynamic solvers should be interpreted as a time step (of $5 \cdot 10^{-4}$ s in Figure A.8 a), and 0.1 s in Figure A.8 b)), and in the static solver is non-physical. In both subfigures, the static curve is the same, a straight line, as the solver is independent of the time parameters. In Figure A.8 a) the expected dynamic oscillations can be seen, whereas in Figure A.8 b) the amplitude of the oscillations is minimal as timescale of 100 s is suitably long compared to the natural timescale of elastic oscillations. 100 s is short compared with a day, the timescale of interest, meaning the static solver is sufficient for this problem. As seen in the fluid simulations, the dynamic solver is more time consuming than the static solver.

Figure A.8 b) shows the dynamic and static implementations are interchangeable with a sufficiently long time scale of 100 s as the deformation profile is indistinguishable.

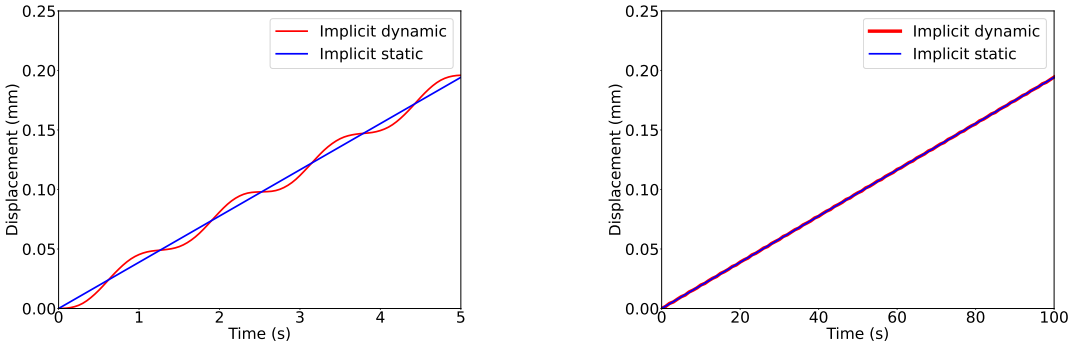

(a) (b)

Figure A.8: A comparison of solid deformation using static and dynamic solvers. A simulation time of (a) 5 s and (b) 100 s is used.

A.4.5 FSI validation

The FSI model was validated against a standard benchmark in the literature [220, 221] to ensure model accuracy. This benchmark considers a 2D fluid channel, rigid except for one section of the top wall which is modelled as a deformable solid. The wall has thickness 0.1 cm with a pressure external to the channel of 1.755 Pa. The fluid flow is driven by a parabolic velocity profile on the left boundary with average velocity of 3 cm/s. The geometry of the problem is shown in Figure A.9. Material parameters are taken from Ref. [221], page 113: $\rho_f = 1$ g/cm^3, $\mu_f = 1$ mPa s. In Ref. [221] the solid is modelled with a compressible St Venant-Kirchhoff hyperelastic model in plane strain with Young's Modulus 35.9 kPa and Poisson's ratio 0.45. A 2D FSI model and a 3D counterpart for a rectangular channel with depth 1 cm are developed for comparison against these results. To ensure that the 3D interpretation replicates the 2D system, additional constraints of zero out-of-plane displacement for the solid, and planar flow with no z-dependence for the fluid, are enforced on the system.

The equilibrium displacement of the FSI interface in this system is found and compared with values extracted from Ref. [221]. Figure A.9 b) shows excellent agreement with the benchmark.

This concludes the model validation, with both the fluid and solid solvers separately validated against analytic problems, and both shown to be time independent. The FSI code as a whole was then validated against a problem from the literature, and excellent agreement seen.

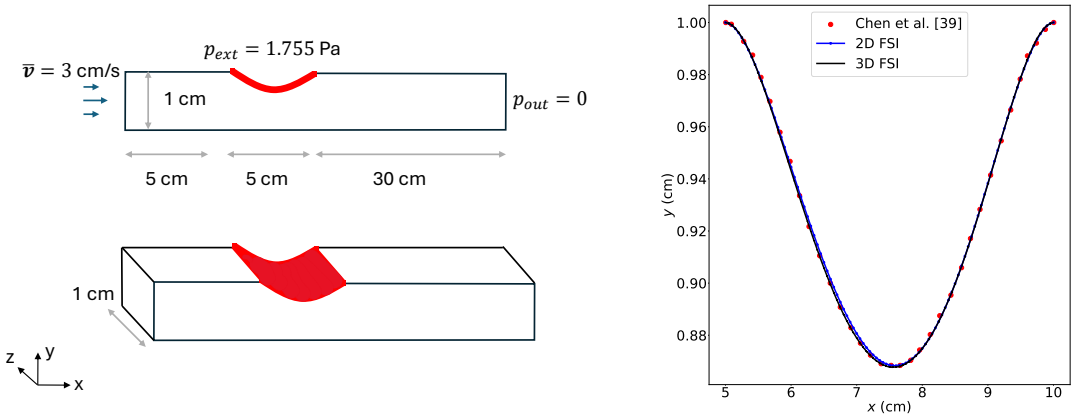

(a) (b)

Figure A.9: (a) Geometry of the FSI benchmark problem, with the deformable solid shown in red, for 2D (upper) and 3D (lower). The driving velocity is indicated on the left boundary. All other fluid boundaries have a no-slip fluid condition imposed and all solid boundaries have zero displacement. (b) Comparison of equilibrium boundary position between the FSI model and results given in Ref. [221].

A.5 Model parameters sensitivity study

When building the 3D FSI model, physical parameters were taken from the literature to best replicate the biological scenario. However, in many cases, there was significant uncertainty in the value of the parameter either due to measurement error, inter-patient variability, or a lack of existing research. In particular, the dimensions and shape of the ventricle and ChP and the Young's modulus of the ChP were taken from large ranges of values. To ensure the model is not sensitive to these specific choices of parameter value, a parameter sensitivity study is performed. Each parameter is varied by 20% of its value (i.e., for a parameter with value p, values of $0.8p$ and $1.2p$ are tested). This considers a large degree of variation in each parameter while ensuring that the geometry remains physically coherent. Adjusting parameter values will change the results of the simulation, however it is only important that the adjusted model provides the same ranking of catheter designs. As the aim of the model is to compare catheter designs, it therefore is sufficient to use a single choice of parameter value going forward.

Table A.1 summarises the model parameters investigated in this parameter sensitivity study and gives the parameter values used. For each test, only one

parameter is varied and all others are held constant at the base value. For computational efficiency, the 2D FSI model is used to investigate the effects of changing the parameter value. Six of the seven parameters under investigation are characteristic lengths of the domain. The last parameter is the Young's Modulus of the ChP. As this is a parameter expected to have a significant effect on the deformation of the ChP a larger range of values are tested.

Table A.1: Model parameters.

Parameter	**Base value**	**Lower value**	**Upper value**
Domain width	8 mm	6.4 mm	9.6 mm
Domain height	6 mm	4.8 mm	7.2 mm
ChP width	0.2 mm	0.16 mm	0.24 mm
ChP height	3.5 mm	2.8 mm	4.2 mm
Catheter to ChP horizontal distance	2 mm	1.6 mm	2.4 mm
Catheter to ChP vertical distance	2.5 mm	2 mm	3 mm
ChP Young's modulus	50 Pa	30 Pa	150 Pa

In each study three different catheter designs are simulated in the FSI model. The three catheter designs are shown in Figure A.10 a), b) and c). In Figure A.11, design a) corresponds to blue results, design b) to orange, and design c) to green. The results of the parameter study are shown in Figure A.11 a) and b). Each subplot shows the effect of varying one design parameter by 20% of its base value. For each combination of parameter values the model successfully and consistently discriminates between the three catheter designs tested: green is always ranked best, followed by orange, then blue.

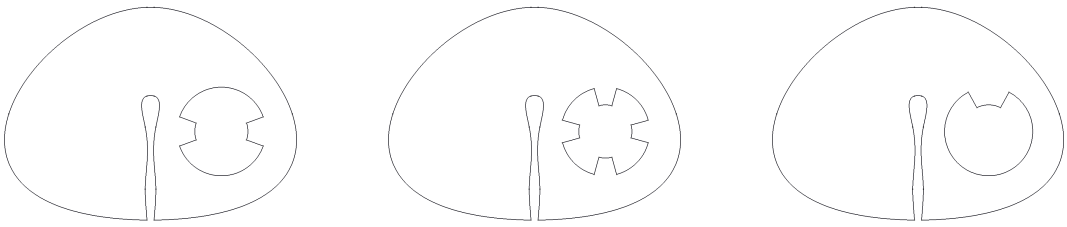

(a) (b) (c)

Figure A.10: (a), (b), (c) Catheter designs used in parameter variation study.

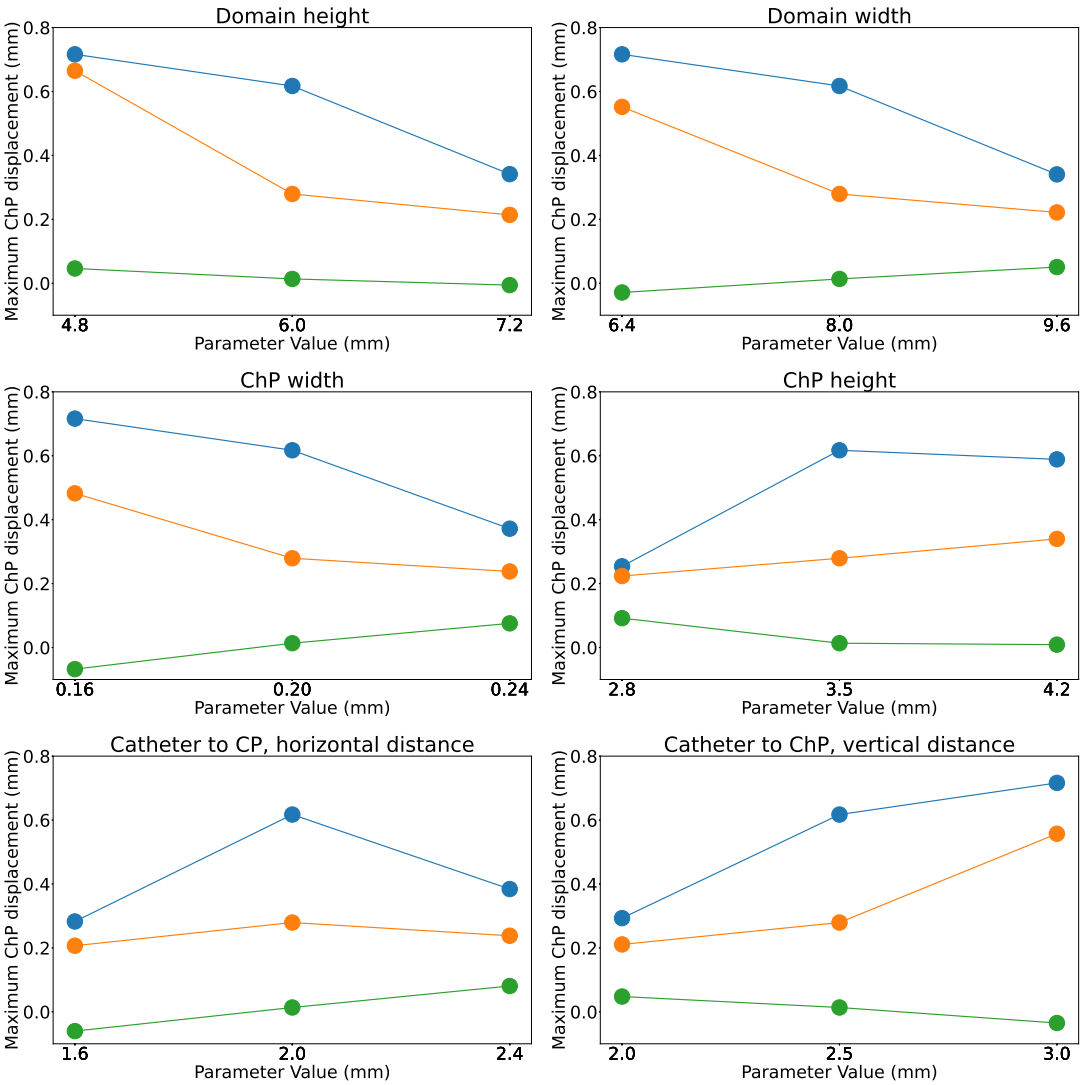

(a)

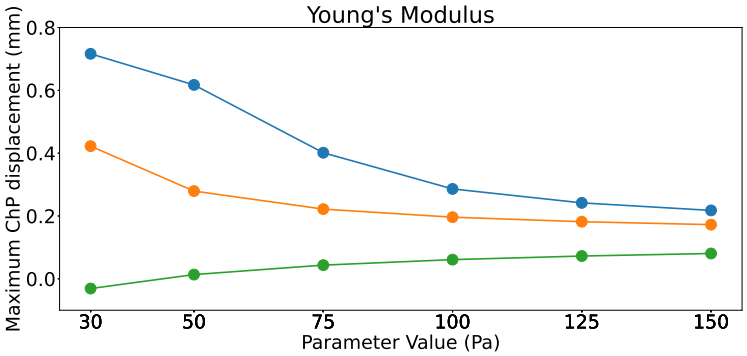

(b)

Figure A.11: (d) Maximum equilibrium ChP displacement for different design parameter values. (e) Maximum equilibrium ChP displacement for different Young's Modulus values.

Appendix B

This chapter contains further results on the reduced-order models (ROMs) presented in Chapters 4 and 5, which are separately presented in Ref. [50] and (shortly) in Ref. [190]. The first section directly compares the maximum equilibrium ChP displacement for the 2D and 3D FSI models. The second section contains further detail on the formation of the expression for permeability used in Section 5.2.

B.1 Reconciling 2D and 3D FSI models

To quantify the agreement between the 3D and 2D FSI models, the maximum equilibrium ChP deformation for a range of hole sizes is compared. For this study, a 3D catheter design with ten rows of four holes of variable radius positioned symmetrically around the catheter circumference is used. This inlet hole placement corresponds to the 3D design shown in Figure 2.2 b), and here the constant radius of the inlet holes is allowed to vary. This geometry interpreted in 2D is shown in Figure 4.5.

To directly compare the models, a measure of hole proportion is introduced, defined as the proportion of catheter surface that is hole. In 3D the catheter surface means only the cylindrical walls, and not the circular faces on each end. In 2D, the hole proportion takes a simple expression of $\arctan(r/r_o)/45°$ where r is the radius (of the conical base) of an inlet hole (see Figure 3.2), r_o is the exterior radius of the catheter ($r_o = 1.25$ mm here). In 3D, a closed analytical expression is not available and so the hole proportion is extracted from surface area calculations in `ParaView`.

In both models, the maximum equilibrium displacement of the ChP occurs along the top of the ChP (see examples in Figures 4.2, 4.5). In 2D, the x component of displacement is extracted from the top of the ChP. To reconcile the extra dimension of the 3D model, a line average of the x component of the displacement field, extracted from the top line of the ChP, is used: $= \left(\int_{\text{line}} \boldsymbol{u} \cdot \boldsymbol{e}_x \, ds\right) / L_z$. The computational speed of the 2D model is leveraged to extract displacement data for values of α between 0° and 90° (appreciating the four-fold rotational symmetry of the design) to give a range of displacements for each hole proportion.

Displacements in the 2D model of 0.71 mm indicate a collision between ChP and catheter.

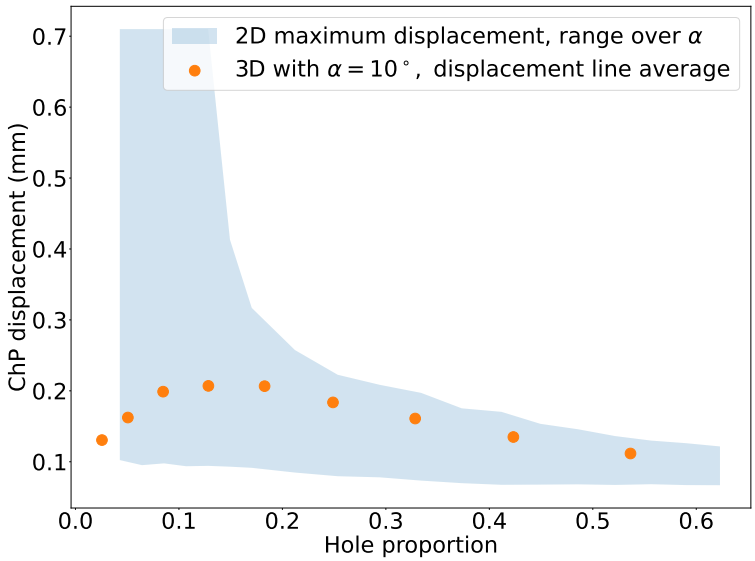

Figure B.1: ChP displacement against hole proportion, 2D: blue shading, 3D: orange markers. Image reproduced from Ref. [50] under a Creative Commons Attribution 4.0 International License (CC BY 4.0 [32]).

Figure B.1 shows that the line average of the 3D FSI is contained within the range of 2D FSI model displacements for each hole proportion. This is qualitatively acceptable, and lends confidence to the use of the 2D FSI as a ROM for the 3D FSI, despite the 3D model containing more detail than the cross-section.

B.2 Adjusted permeability expression

This section provides further exploration and results for the permeable wall ROM introduced in Section 5.2, with particular focus on the factor of $r_h/2$ used in the heuristic adjustment to the permeability factor in Equation (5.19). Equation (5.18) is referred to as the initial permeability factor and Equation (5.19) is the adjusted permeability factor. The results presented here will be published in Ref. [190].

To assess the agreement of the ROM to the full model, and the effect of using the adjusted versus initial permeability expression, a sweep over a range of inlet hole designs and geometries is performed. To isolate the effect of the permeability factor, the "full model" used in this analysis is defined by Equations (5.2) – (5.4), with the geometry shown in Figure 5.4 a). This model is fluid-only, resolving only the flow within the catheter, and neglecting the ventricular domain and fluid–structure interaction effects associated with the Choroid Plexus. Fluid ex-

ternal to the catheter is modelled as being at a spatially constant value p_0 in both the full model and ROM. The full model is solved using the simpleFOAM solver and the ROM is solved using standard integration functions from the `scipy` package.

For this hole geometry sweep, all inlet holes are modelled as cylindrical with circular cross-sections. This differs from the ventricular catheter designs considered in all earlier parts of this thesis, which use conical inlet holes, in line with physical examples. The choice of circular inlet holes in this section is chosen to better align the full model with the assumptions of the ROM.

Each tested geometry has a constant hole radius and a regular hole arrangement. As a result, three design parameters define the geometry. The non-dimensional hole radius satisfies $r_h \in [0.1, 0.5]$, spanning values observed in existing catheter examples. Holes are arranged in $n_c \in \{1, \ldots, 5\}$ circumferential rows, with $n_a \in \{1, \ldots, 20\}$ holes per row. The parameter n_c controls the circumferential distribution of holes, while n_a controls their axial distribution. Rows are placed uniformly around the catheter circumference, and holes within each row are distributed uniformly along the catheter axis.

The full model and ROM are solved for all combinations of n_a, n_c, and r_h, with r_h sampled at nine equally spaced values. For the case $n_c = 5$ and $r_h = 0.5$, inlet holes overlap circumferentially and the corresponding geometries are therefore excluded from the analysis.

Model accuracy for each geometry is quantified using the relative percentage error (RPE) metric defined in Equation (5.20). Figure B.2 b) shows the RPE between the ROM and full model for each catheter design using the initial permeability factor. Figure B.2 b) shows the RPE for the same geometries with adjusted form of the permeability factor with the additional heuristic of $r_h/2$.

Figure B.2 b) has RPE ranging between 0% (excellent agreement) and -20%. There is a significant trend that increasing the hole radius r_h leads to larger discrepancies, as does increasing the number of axial hole rings n_a, arguably because error in the permeability accumulates across a larger number of permeable regions, amplifying discrepancies in axial flux and pressure. In contrast, varying the number of circumferential hole rows n_c has little effect on RPE, suggesting that non-axisymmetric effects are negligible and that the catheter flow is well approximated as axisymmetric.

The adjusted permeability factor used in Figure B.2 c) gives a much better agreement between the ROM and full model, with the RPE now bounded by -6% in all cases, a three-fold reduction in error compared to the unadjusted Figure B.2 b). There is still some dependence between RPE and parameters controlling the catheter inlet hole geometry: low r_h and n_a still correlate to better RPE, showing the adjustment to the permeability measure does not completely capture the complex flow near the inlet holes. It is likely that the model could be further improved by incorporating either dependence on the n_a and n_c parameters. However, each extra complexity added to the model needs to be quantified,

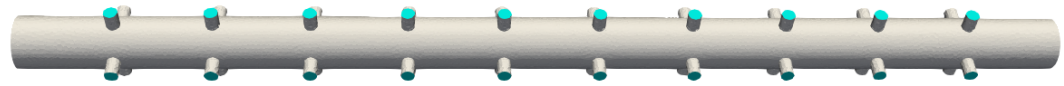

(a)

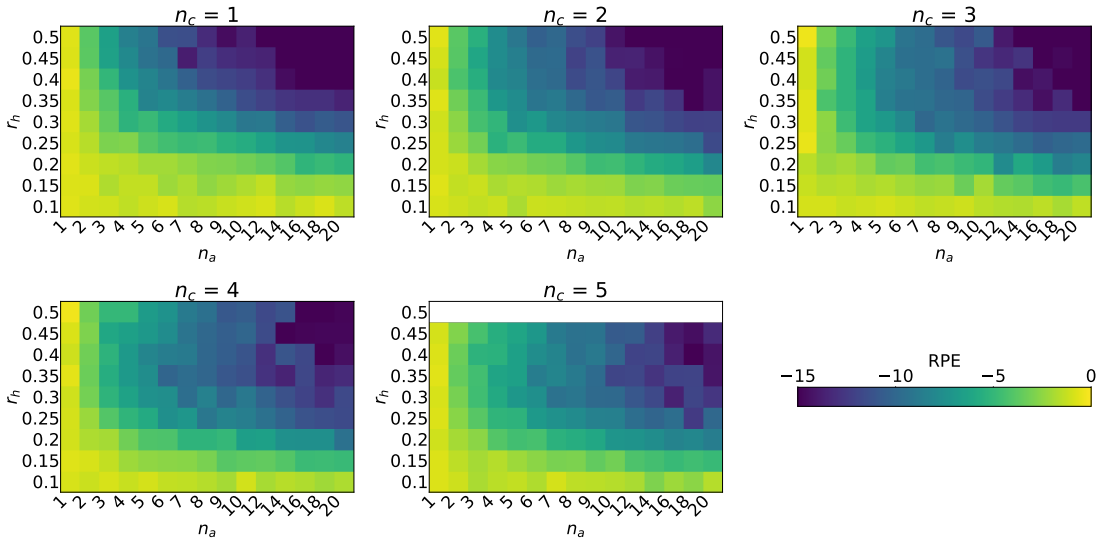

(b)

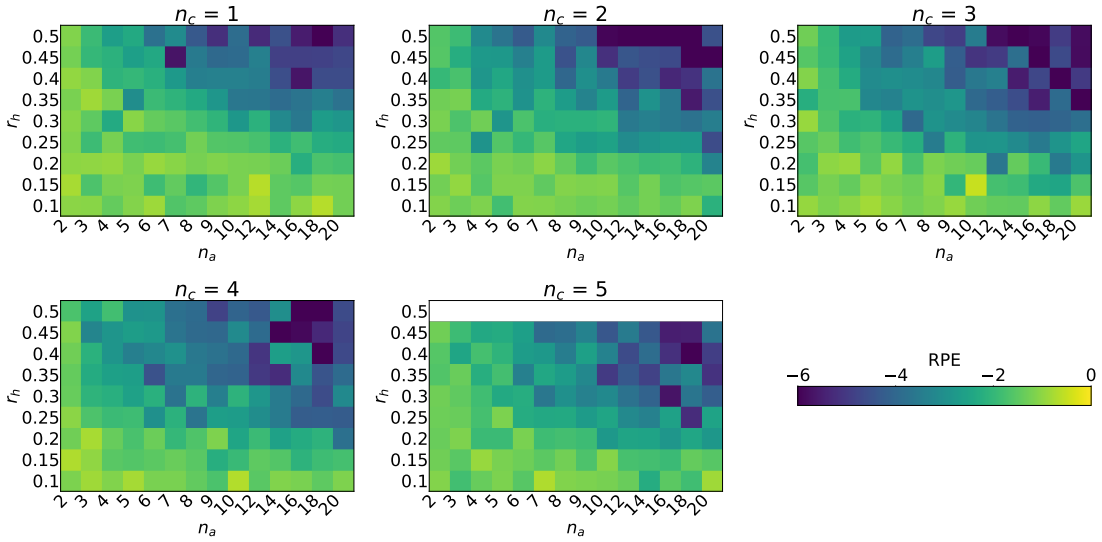

(c)

Figure B.2: (a) Example catheter geometry used in this sweep of inlet hole configurations, this example with $r_h = 0.2$, $n_c = 4$ and $n_a = 10$. (b) and (c) RPE for each catheter design using, respectively, the initial and adjusted permeability factors. Different subplots: different n_c, r_h rows and n_a columns. Yellow shows good agreement between the full and reduced models and dark colours show poor agreements. Note the different scale of the different subfigures. The largest hole radius $r_h = 0.5$ mm is excluded from the plot with $n_c = 5$, as these designs have overlapping holes.

either requiring detailed mathematical treatment of higher order effects, or a large quantity of data for calibration and parameter fitting. The factor of $r_h/2$ is therefore considered a simple adjustment that has mitigated the largest source of error, and is sufficient in this ROM.

B.3 Permeable model visualisation parameters

This section lists the design parameters of the catheters used for example visualisations in Chapter 5. The catheter designs presented in Chapter 5 are parameterised with three variables for each inlet hole, as described in Section 5.1. The following three tables give the parameter used by the catheter shown in Figure 5.6. The catheter design of Table B.2 is also used in the visualisation of Figure 5.9.

Table B.1: Design parameters for Figure 5.6 a)

Hole radius (mm)	z position (mm)	ϕ (°)	Hole radius (mm)	z position (mm)	ϕ (°)
0.553	6.139	197.602	0.552	9.511	314.777
0.544	23.329	193.0	0.529	9.218	9.475
0.522	22.346	60.054	0.516	26.389	158.221
0.511	22.018	342.344	0.496	20.392	192.584
0.493	14.656	70.723	0.492	15.91	290.896
0.477	18.923	132.991	0.476	8.595	110.875
0.455	22.595	330.829	0.455	5.401	128.026
0.452	16.888	286.047	0.452	2.873	86.953
0.425	21.592	47.129	0.403	25.332	193.765
0.403	1.596	115.464	0.386	10.521	46.091
0.367	26.379	295.967	0.357	8.593	240.931
0.344	27.41	96.792	0.326	6.235	292.711
0.319	15.729	140.292	0.314	2.727	355.679
0.302	16.065	13.361	0.237	21.096	125.578
0.213	23.509	148.591	0.195	13.434	332.128
0.179	13.068	162.748	0.176	16.812	327.972
0.174	24.934	213.029	0.158	4.219	263.644
0.154	10.005	125.715	0.147	14.672	173.397
0.146	12.133	213.64	0.127	2.947	65.795
0.126	24.536	216.175	0.104	28.103	57.869

Table B.2: Design parameters for Figure 5.6 c)

Hole radius (mm)	z position (mm)	ϕ (°)
0.445	16.674	159.396
0.423	9.066	185.092
0.348	6.631	67.264
0.347	1.188	254.235
0.286	5.629	286.16
0.239	4.369	204.183
0.166	5.559	87.68
0.116	11.248	302.956
0.111	19.327	320.071
0.1	25.879	100.104

Table B.3: Design parameters for Figure 5.6 e)

Hole radius (mm)	z position (mm)	ϕ (°)	Hole radius (mm)	z position (mm)	ϕ (°)
0.567	15.0	270.69	0.561	20.0	311.96
0.551	10.0	277.817	0.535	25.0	152.22
0.521	15.0	261.801	0.52	15.0	274.331
0.466	15.0	4.353	0.455	10.0	164.678
0.443	25.0	22.399	0.436	15.0	94.207
0.423	15.0	86.476	0.421	10.0	0.964
0.416	25.0	93.089	0.406	25.0	166.212
0.402	15.0	26.45	0.371	20.0	258.543
0.335	20.0	214.879	0.316	5.0	266.911
0.3	20.0	160.274	0.252	15.0	326.741
0.248	25.0	333.96	0.214	15.0	139.703
0.205	20.0	93.303	0.203	10.0	119.263
0.188	5.0	35.588	0.18	15.0	353.887
0.18	15.0	118.179	0.169	15.0	346.042
0.126	25.0	259.322	0.106	15.0	17.96
0.077	25.0	112.962	0.072	5.0	156.747

Appendix C

This chapter of the appendix gives further detail on the development of the machine learning layer used in the surrogate fitness function, with further accuracy metrics and the hyperparameters explored during training.

C.1 Hyperparameter optimisation

Tables C.1 and C.2 give a brief summary of each hyperparameter for each ML model, and the values tested in the gridsearch. The three graph based models: random forest, gradient boost and XGBoost share several hyperparameters due to their similar structure.

The values chosen for investigation are taken from a small range around default values.

C.2 Further accuracy metrics

In this section figures analogous to Figure 6.3 are shown, for the other machine learning (ML) accuracy metrics discussed in Chapter 5: mean absolute error (MAE), root mean squared error (RMSE) and Spearman's correlation coefficient ρ. In all cases yellow indicates a good accuracy score, and purple a poor score. Values of RMSE and MAE are clipped at an upper bound of 1, and Spearman's ρ at a lower bound of 0 to aid visualisation (any model with values outside this range performs very poorly).

All the metrics identify the same tree-based models as the most promising for further investigation: the random forest and the gradient boosted regressors. This is in agreement with the models identified by considering the R^2 metric in Section 6.5, which increases confidence in this choice of model as it is robust to all metrics.

Table C.1: Hyperparameter optimisation (part one).

ML model	Hyperparameter	Values tested
Linear regression	`fit_intercept`: Whether to include intercept	true, false
	`positive`: Restrict coefficients to be positive	false
Ridge	`alpha`: Regularisation strength	0.01, 0.1, 1.0, 10.0, 100.0
	`fit_intercept`: Whether to include intercept	true, false
	`solver`: Optimisation algorithm	auto, svd, cholesky, lsqr, sag, saga
Lasso	`alpha`: Regularisation strength	1e-4, 1e-3, 1e-2, 1e-1, 1.0
	`fit_intercept`: Whether to include intercept	true, false
	`selection`: Coordinate descent update order	cyclic, random
Decision tree	`max_depth`: Maximum depth of tree	none, 2, 3, 5, 7, 10
	`min_samples_split`: Minimum samples to split node	2, 5, 10
	`min_samples_leaf`: Minimum samples at each leaf	1, 2, 4, 8
	`max_features`: Features considered at each split	none, sqrt, log2
	`splitter`: Split selection strategy	best, random
upport vector regressor	C: Regularisation strength	0.1, 0.5, 1
	γ: Influence of individual samples	1e-5, 1e-4, 0.001
	ϵ: Width of the no-penalty region	0.1, 0.3, 0.5
Random forest	`n_estimators`: Number of trees	100, 200, 300
	`max_depth`: Maximum depth of trees	2, 3, 5
	`max_features`: Features considered at each split	sqrt, log2
	`min_samples_split`: Minimum samples to split node	2, 3, 5
	`min_samples_leaf`: Minimum samples at each leaf	1, 2, 4

Table C.2: Hyperparameter optimisation (part two).

ML model	**Hyperparameter**	**Values tested**
Gradient boost	`n_estimators`: Number of trees	100, 200, 300
	`learning_rate`: Contribution of each tree	0.05, 0.1, 0.15
	`max_depth`: Maximum depth of trees	2, 3, 5
	`subsample`: Fraction of samples per tree	0.8, 0.9, 1.0
	`min_samples_leaf`: Minimum samples at each leaf	1, 2, 4
XGBoost	`n_estimators`: Number of trees	100, 200, 300
	`learning_rate`: Contribution of each tree	0.05, 0.1, 0.15
	`max_depth`: Maximum depth of trees	2, 3, 5
	`subsample`: Fraction of samples per tree	0.8, 0.9, 1.0
	`colsample_bytree`: Fraction of features per tree	0.8, 0.9, 1.0
MLP	`hidden_layer_sizes`: Number/size of hidden layers	(50,), (100,), (100,50), (50,50,50)
	`activation`: Hidden layer activation function	relu, tanh
	`solver`: Optimisation algorithm	adam, lbfgs
	`alpha`: Regularisation strength	1e-5, 1e-4, 1e-3, 1e-2
	`learning_rate`: Learning rate schedule	constant, adaptive
	`learning_rate_init`: Initial learning rate	1e-3, 1e-2
	`early_stopping`: Use validation to stop training	True, False

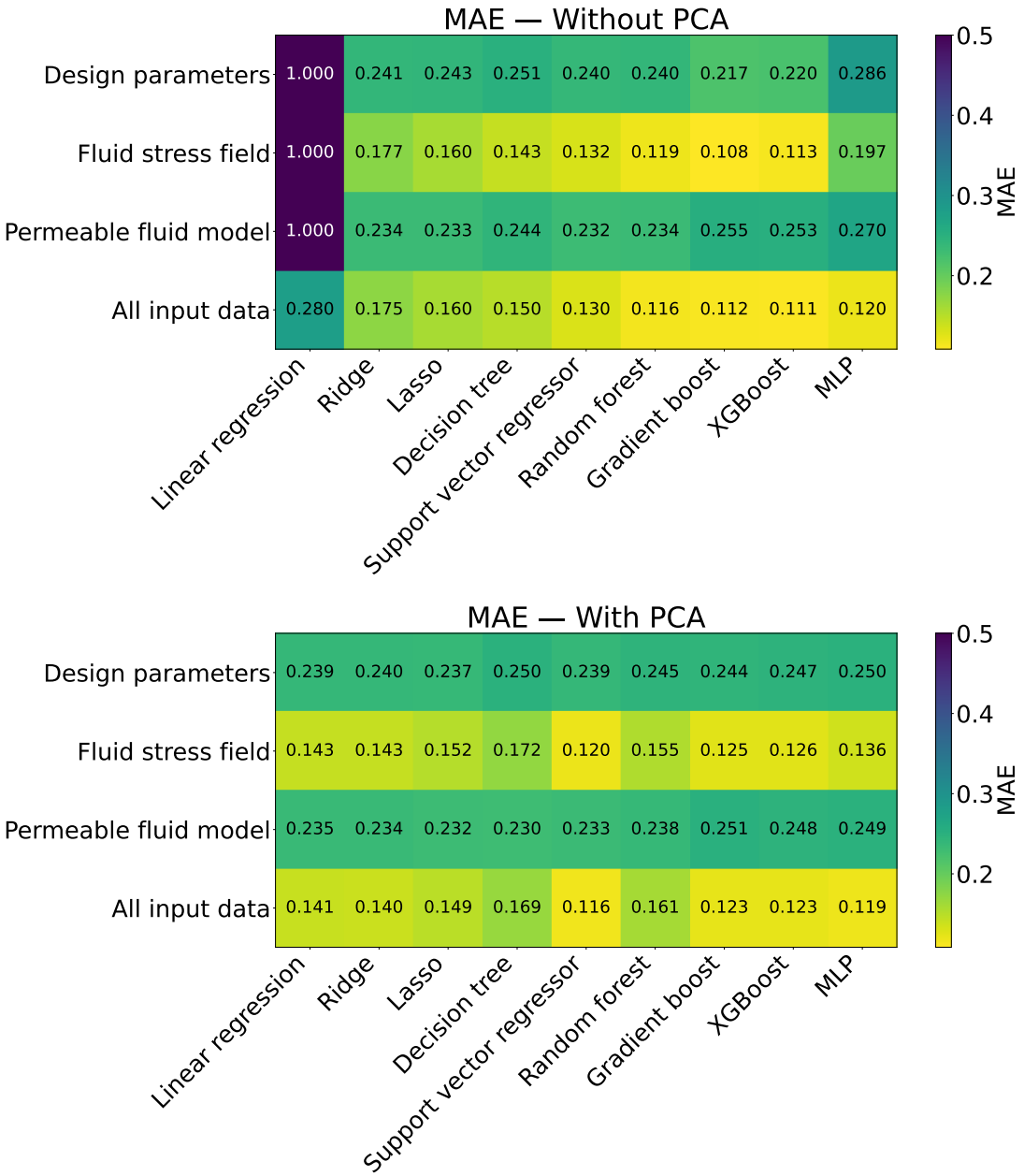

Figure C.1: Average MAE score for each ML model applied to each dataset, without (a), and with (b) PCA preprocessing.

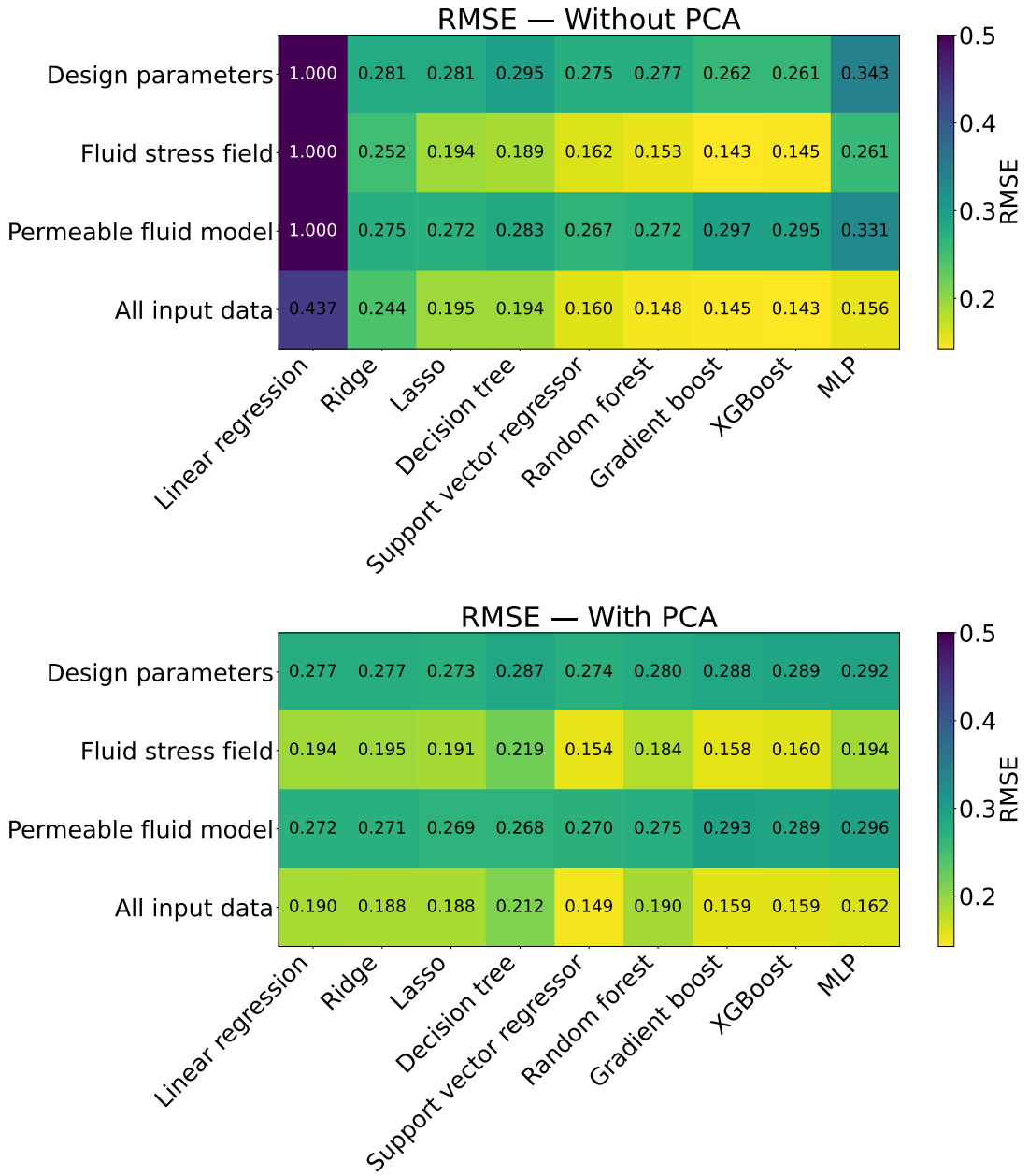

Figure C.2: Average RMSE score for each ML model applied to each dataset, without (a), and with (b) PCA preprocessing.

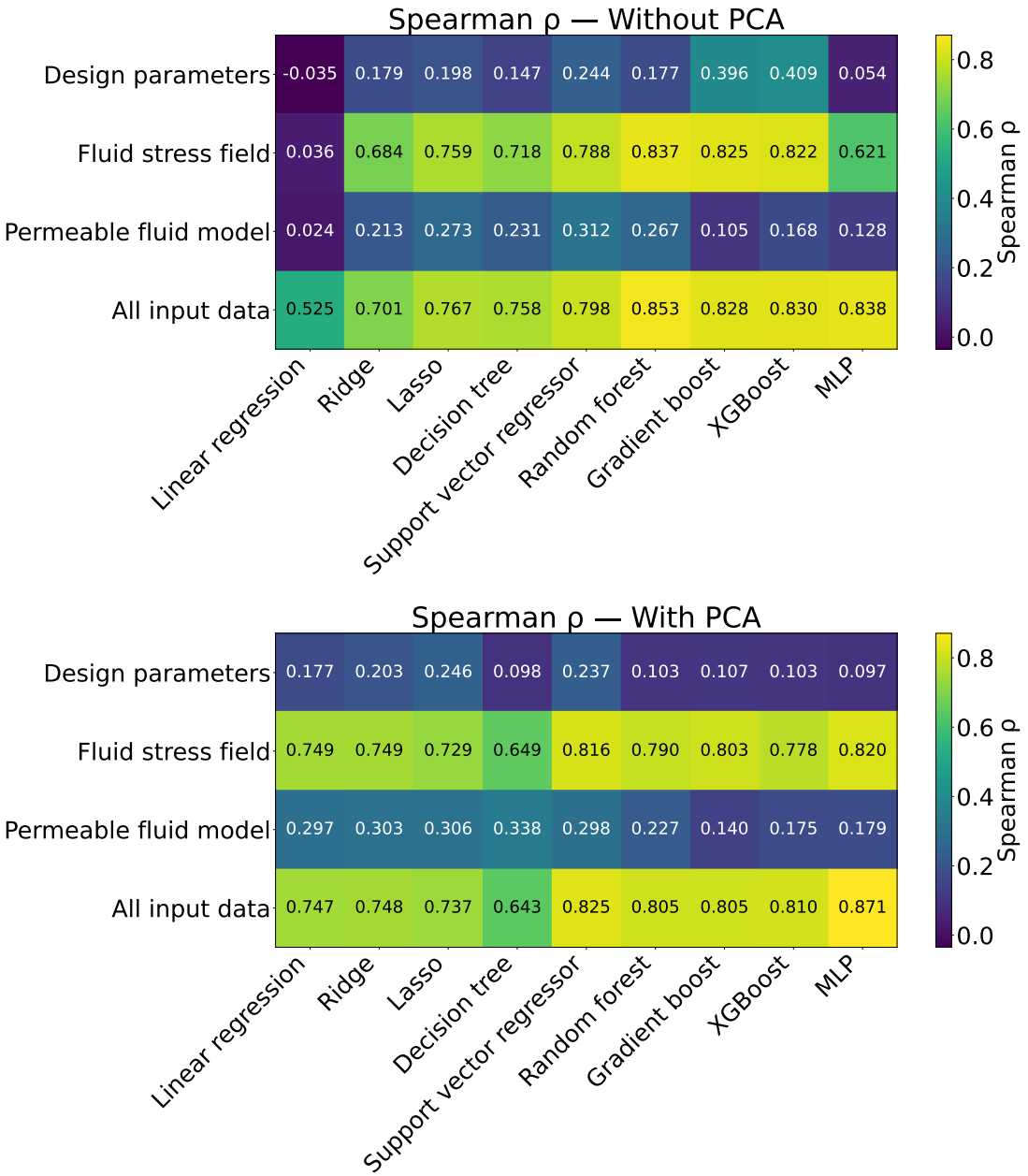

Figure C.3: Average Spearman's ρ score for each ML model applied to each dataset, without (a), and with (b) PCA preprocessing.

Appendix D

This appendix lists the design parameters of the optimised catheter designs, which are then explored in the full 3D fluid-structure interaction model in Chapter 7.

D.1 Optimised design parameters

The tables in the section give the design parameters for catheters identified as optimal in the optimisation work of Chapter 7, which are visualised in Figures 7.4, 7.7 and 7.10. As described in Section 7.1.2, each circumferential ring of inlet holes is described by four parameters.

Table D.1: Design shown in Figure 7.4 a).

Row number i	**Radius** r_i	**Number of holes** n_i	**Pitch length** $zPos_i$	**Offset** ϕ_i
Row 1	0.235 mm	6	2.31 mm	219.3°
Row 2	0.411 mm	6	0.765 mm	214.6°
Row 3	0.345 mm	4	1.173 mm	169.7°
Row 4	0.148 mm	3	1.1768 mm	103.7°
Row 5	0.216 mm	8	4.298 mm	147.8°
Row 6	0.269 mm	9	0.549 mm	140.3°

Table D.2: Design shown in Figure 7.4 b).

Row number i	**Radius** r_i	**Number of holes** n_i	**Pitch length** $zPos_i$	**Offset** ϕ_i
Row 1	0.22 mm	10	2.860 mm	158.7°
Row 2	0.135 mm	4	0.796 mm	163.4°
Row 3	0.149 mm	5	1.110 mm	89.7°
Row 4	0.105 mm	3	1.499 mm	114.6°
Row 5	0.126 mm	2	4.973 mm	152.6°
Row 6	0.226 mm	9	1.135 mm	291.5°

Table D.3: Design shown in Figure 7.4 c).

Row number i	**Radius** r_i	**Number of holes** n_i	**Pitch length** $zPos_i$	**Offset** ϕ_i
Row 1	0.119 mm	10	2.860 mm	66.8°
Row 2	0.381 mm	9	0.796 mm	326.1°
Row 3	0.119 mm	9	1.110 mm	28.0°
Row 4	0 mm	0	1.499 mm	276.6°
Row 5	0.25 mm	7	4.973 mm	230.6°
Row 6	0.427 mm	5	1.135 mm	337.2°

Table D.4: Design shown in Figure 7.7 a).

Row number i	**Radius** r_i	**Number of holes** n_i	**Pitch length** $zPos_i$	**Offset** ϕ_i
Row 1	0.47 mm	4	1.187 mm	0°
Row 2	0.485 mm	4	0.854 mm	0°
Row 3	0.231 mm	4	3.228 mm	0°
Row 4	0.146 mm	4	1.193 mm	0°
Row 5	0.365 mm	4	3.543 mm	0°
Row 6	0.443 mm	4	0.356 mm	0°

Table D.5: Design shown in Figure 7.7 b).

Row number i	**Radius** r_i	**Number of holes** n_i	**Pitch length** $zPos_i$	**Offset** ϕ_i
Row 1	0.41 mm	4	0.858 mm	0°
Row 2	0.494 mm	4	1.646 mm	0°
Row 3	0.248 mm	4	3.228 mm	0°
Row 4	0.132 mm	4	0.627 mm	0°
Row 5	0.456 mm	4	3.231 mm	0°
Row 6	0.278 mm	4	0.787 mm	0°

Table D.6: Design shown in Figure 7.10 a).

Row number i	**Radius** r_i	**Number of holes** n_i	**Pitch length** $zPos_i$	**Offset** ϕ_i
Row 1	0.4 mm	6	0.341 mm	254.3°
Row 2	0.205 mm	4	0.697 mm	3.5°
Row 3	0.194 mm	0	3.929 mm	260.5°
Row 4	0 mm	3	2.14 mm	0.2°
Row 5	0.255 mm	0	0.643 mm	332.7°
Row 6	0.247 mm	10	3.883 mm	358.1°

Table D.7: Design shown in Figure 7.10 b).

Row number i	**Radius** r_i	**Number of holes** n_i	**Pitch length** $zPos_i$	**Offset** ϕ_i
Row 1	0.365 mm	5	0.496 mm	9.733°
Row 2	0 mm	2	1.692 mm	35.487°
Row 3	0 mm	2	5.047 mm	48.386°
Row 4	0.128 mm	7	0.95 mm	61.835°
Row 5	0 mm	8	2.006 mm	141.903°
Row 6	0.281 mm	9	2.136 mm	56.236°